Alma Mater Studiorum – Università di Bologna

DOTTORATO DI RICERCA IN

CHIMICA

Ciclo XXVI

Settore Concorsuale di afferenza: 03/A2

Settore Scientifico disciplinare: CHIM/02

Study of molecules of astrochemical, astrophysical and atmospheric interest by means of High – Resolution Infrared Spectroscopy

Presentata da: MATTIA VILLA

Coordinatore Dottorato **Relatore**

Prof. Aldo Roda **Prof. Luciano Fusina**

Esame finale anno 2014

Dottorando: Mattia Villa

Tutor: Prof. Luciano Fusina

Curriculum, indirizzo: Scienze Chimiche, Chimica Fisica

Titolo tesi: Study of molecules of astrochemical, astrophysical and atmospheric interest by means of High – Resolution Infrared Spectroscopy

Il lavoro di ricerca del Dott. Mattia Villa nel triennio di frequenza del Dottorato in Chimica si è concentrato sulla registrazione di spettri infrarossi ad alta risoluzione di molecole in fase gassosa e sulla loro interpretazione sulla base di idonei modelli teorici. Le molecole oggetto di studio rivestono particolare rilevanza nel campo della fisica e chimica dell'atmosfera e del mezzo interstellare. Sono state utilizzate per la registrazione degli spettri sia tecniche spettroscopiche convenzionali, come la spettroscopia a trasformata di Fourier, sia tecniche più avanzate come la spettroscopia laser in molecole a temperatura criogenica. Sono state studiate molecole lineari (diversi isotopologhi dell'acetilene: $^{12}C_2D_2$, $^{12}C^{13}CD_2$, $H^{12}C^{13}CD$, $D^{12}C^{13}CH$, DCCF e diacetilene DC_4H) e rotatori simmetrici (CH_3CCH, $^{15}ND_3$ e CF_3Br). Alcune di queste molecole rivestono inoltre particolare interesse spettroscopico in quanto rappresentano molecole modello di un'intera classe di composti. L'acetilene è infatti la più semplice molecola lineare tetratomica con un elevato numero di derivati isotopicamente sostituiti che presentano comportamento differente a seconda della presenza o dell'assenza del centro di simmetria. $^{15}ND_3$ è caratterizzato dalla vibrazione di inversione che si manifesta in modo del tutto singolare negli spettri vibrazionali.
La fase preliminare di registrazione degli spettri è stata completata dalla loro analisi consistente nell'assegnazione dei numeri quantici delle transizioni vibrorotazionali e nell'identificazione degli stati vibrazionali coinvolti. Opportuni programmi di calcolo costruiti sulla base di idonei modelli teorici sono stati quindi utilizzati per ottenere dalle assegnazioni i parametri spettroscopici caratterizzanti gli stati coinvolti nelle transizioni. L'analisi ha permesso l'osservazione di numerose perturbazioni che modificano l'andamento spettrale sia in termini di frequenze che di intensità. Le interazioni tra i livelli vibrorotazionali, che a volte coinvolgono numerosi stati vibrazionali, sono state in questi casi espressamente considerate nel modello, ottenendo quindi valori precisi dei parametri di interazione, importanti per studi di dinamica molecolare. Le informazioni spettroscopiche ottenute per ciascuna molecola possono inoltre essere utilizzate per calcoli della geometria all'equilibrio e per la determinazione del campo di forza anarmonico per via sperimentale.
La realizzazione dell'attività di ricerca ha permesso al dottorando di collaborare con diversi gruppi di ricerca quali ad esempio il Dipartimento di Chimica "G. Ciamician" di Bologna, l'Università Cà Foscari di Venezia, l'Université Libre de Bruxelles e la Bergische Universität di Wuppertal.
Infatti, nel corso del dottorato, il Dott. Mattia Villa ha trascorso un periodo di tre mesi presso l'Université Libre de Bruxelles, sotto la supervisione del Prof. Michel Herman. Durante tale soggiorno, egli ha avuto modo di utilizzare tecniche innovative, quali l'espansione supersonica, la Cavity Ring Down Spectroscopy e la Cavity Enhanced Absorption Spectroscopy, per la registrazione di spettri in particolari condizioni, grazie all'utilizzo di cammini ottici molto elevati, di bassissime temperature e di elevata risoluzione e sensibilità.
L'attività svolta si è concretizzata nella realizzazione di 9 articoli scientifici pubblicati su riviste internazionali, quali Molecular Physics, Journal of Chemical Physics, Journal of Quantitative Spectroscopy & Radiative Transfer, and Astronomy&Astrophysics. I risultati più recenti, attualmente in corso di completamento, saranno oggetto di ulteriori pubblicazioni. Inoltre, il Dott. Mattia Villa ha partecipato a 3 convegni internazionali e a un workshop esclusivamente dedicato agli studi spettroscopici e teorici sulla molecola di acetilene, organizzato da International Solvay Institutes a Bruxelles, presentando e discutendo i risultati salienti della ricerca svolta, complessivamente 7 poster.
Durante il periodo di tesi il Dott. Villa ha sempre dimostrato grande interesse per l'attività di ricerca svolta apportando il proprio contributo originale nelle varie fasi della ricerca. Ha inoltre dimostrato attitudine al lavoro di gruppo necessario per sviluppare fruttuosamente le collaborazioni nazionali e internazionali. La preparazione di base acquisita durante gli studi e i lavori di tesi precedenti, si è via via raffinata affrontando e risolvendo in modo brillante le numerose situazioni molto complesse legate all'analisi di spettri particolarmente ricchi di informazioni. Assiduità nell'impegno di lavoro e notevole entusiasmo sono altre positive caratteristiche del Dott. Villa.

Abstract

The spectroscopic investigation of the gas–phase molecules relevant for the chemistry of the atmosphere and of the interstellar medium has been performed.

Two types of molecules have been studied, linear and symmetric top. Several experimental high–resolution techniques have been adopted, exploiting the spectrometers available in Bologna, Venezia, Brussels and Wuppertal: Fourier–Transform–Infrared Spectroscopy, Cavity–Ring–Down Spectroscopy, Cavity–Enhanced–Absorption Spectroscopy, Tunable–Diode–Laser Spectroscopy. Concerning linear molecules, the spectra of a number of isotopologues of acetylene, $^{12}C_2D_2$, $H^{12}C^{13}CD$, $H^{13}C^{12}CD$, $^{13}C^{12}CD_2$, of DCCF and monodeutero–diacetylene DC_4H, have been studied, from 320 to 6800 cm^{-1}. This interval covers bending, stretching, overtone and combination bands, the focus on specific ranges depending on the molecule. In particular, the analysis of the bending modes has been performed for $^{12}C_2D_2$ (450–2200 cm^{-1}), $^{13}C^{12}CD_2$ (450–1700 cm^{-1}), DCCF (320–850cm^{-1}) and DC_4H (450–1100 cm^{-1}), of the stretching–bending system for $^{12}C_2D_2$ (450–5500 cm^{-1}) and of the $2\nu_1$ and combination bands up to four quanta of excitation for $H^{12}C^{13}CD$, $H^{13}C^{12}CD$ and $^{13}C^{12}CD_2$ (6130–6800 cm^{-1}). In case of symmetric top molecules, CH_3CCH has been investigated in the $2\nu_1$ region (6200–6700 cm^{-1}), which is particularly congested due to the huge network of states affected by Coriolis and anharmonic interactions. The bending fundamentals of $^{15}ND_3$ (450–2700 cm^{-1}) have been studied for the first time, characterizing completely the bending states, $v_2 = 1$ and $v_4 = 1$, whereas the analysis of the stretching modes, which evidenced the presence of several perturbations, has been started. Finally, the fundamental band ν_4 of CF_3Br in the 1190–1220 cm^{-1} region has been investigated. Transitions belonging to the $CF_3{}^{79}Br$ and $CF_3{}^{81}Br$ molecules have been identified since the spectra were recorded using a sample containing the two isotopologues in natural abundance. This allowed the characterization of the $v_4 = 1$ state for both isotopologues and the evaluation of the bromine isotopic splitting.

TABLE OF CONTENTS

Abstract			V
List of Figures			IX
List of Tables			XI
List of Publications			XIII
PART I	THEORY		1
Chapter 1	INTRODUCTION		3
	References		7
Chapter 2	THEORY		9
	2.1	LINEAR MOLECULES	10
		2.1.1 Vibrational Energy	10
		2.1.2 Rotational Energy	13
		2.1.3 Rovibrational Energy and essential resonances	14
	2.2	SYMMETRIC TOPS	20
		2.2.1 Vibrational and rotational energies	20
		2.2.2 Rovibrational energy	21
	2.3	ACCIDENTAL RESONANCES	25
		2.3.1 Anharmonic interactions	25
		2.3.2 Coriolis interactions	27
	2.4	SELECTION RULES AND TRANSITIONS	27
		2.4.1 Linear molecules	28
		2.4.2 Symmetric molecules	33
	References		37
PART II	ANALYSIS		39
Chapter 3	ANALYSIS OF LINEAR MOLECULES		41
	3.1	$^{12}C_2D_2$	42
		3.1.1 Experiment	42
		3.1.2 Description of the spectra	44
		3.1.3 Analysis	47
		3.1.4 Results and Discussion	55
	3.2	$^{13}C^{12}CD_2$	66
		3.2.1 Experiment	66
		3.2.2 Description of the spectra	67
		3.2.3 Analysis	71
		3.2.4 Results and Discussion	74

	3.3	$H^{12}C^{13}CD$, $H^{13}C^{12}CD$, $^{13}C^{12}CD_2$: 6200 – 6800 cm^{-1}	79
		3.3.1 Experiment	80
		3.3.2 Analysis, Results and Discussion	82
	3.4	DCCF	87
		3.4.1 Experiment	88
		3.4.2 Description of the spectra	89
		3.4.3 Analysis	93
		3.4.4 Results and Discussion	95
	3.5	DC_4H	99
		3.5.1 Experiment	100
		3.5.2 Description of the spectra	101
		3.5.3 Analysis, Results and Discussion	102
	References		106
Chapter 4	ANALYSIS OF SYMMETRIC TOP MOLECULES		110
	4.1	CH_3CCH	110
		4.1.1 Experiment	111
		4.1.2 Description of the spectra	114
		4.1.3 Analysis	116
		4.1.4 Results and Discussion	122
	4.2	$^{15}ND_3$	126
		4.2.1 Experiment	127
		4.2.2 Description of the spectra	128
		4.2.3 Analysis	135
		4.2.4 Results and Discussion	139
	4.3	CF_3Br	142
		4.3.1 Experiment	143
		4.3.2 Description of the spectrum	145
		4.3.3 Analysis, Results and Discussion	149
	References		154
Chapter 5	CONCLUSIONS AND PERSPECTIVES		157
	5.1	Conclusions	157
		5.1.1 Linear molecules	157
		5.1.2 Symmetric top molecules	159
	5.2	Future perspectives	160
	References		162
APPENDIX			163
	APPENDIX A – CHARACTER TABLES		165

List of Figures

2.1	Coriolis components for a triatomic linear molecule	15
2.2	Splitting of energy levels of the state $v_t = 2$	19
2.3	Splitting of energy levels of the state $v_t = v_{t'} = 1$	19
2.4	Rotational energy levels of a prolate symmetric top	22
2.5	Symmetry properties of the rotational levels of a prolate top molecule	24
2.6	Anharmonic resonance scheme	26
2.7	Selection rules for transitions in linear molecules	32
2.8	Structure of a parallel band in a symmetric top	35
2.9	Structure of a perpendicular band in a symmetric top	36
3.1	Normal modes of vibration of acetylene	41
3.2	Portion of the spectrum of $^{12}C_2D_2$ in the range 2100 – 2200 cm^{-1}	44
3.3	Portion of the spectrum of $^{12}C_2D_2$ in the range 2300 – 2650 cm^{-1}	45
3.4	Portion of the spectrum of $^{12}C_2D_2$ in the range 3205 – 3235 cm^{-1}	46
3.5	Portion of the spectrum of $^{12}C_2D_2$ in the range 4120 – 4250 cm^{-1}	47
3.6	Portion of the spectrum of $^{13}C^{12}CD_2$ in the range 460 – 600 cm^{-1}	68
3.7	Portion of the spectrum of $^{13}C^{12}CD_2$ in the range 530.4 – 534.4 cm^{-1}	69
3.8	Portion of the spectrum of $^{13}C^{12}CD_2$ in the range 970 – 1170 cm^{-1}	70
3.9	Portion of the spectrum of $^{13}C^{12}CD_2$ in the range 1550 – 1650 cm^{-1}	71
3.10	Femto–FT–CEAS experimental setup	80
3.11	Portion of the spectrum of $^{13}C^{12}CD_2$ in the range 6275 – 6370 cm^{-1}	82
3.12	Portion of the spectrum of $H^{12}C^{13}CD$ and $H^{13}C^{12}CD$ in the range 6400 – 6640 cm^{-1}	83
3.13	Portion of the spectrum of $^{13}C^{12}CD_2$ in the range 6720 – 6800 cm^{-1}	84
3.14	Portion of the spectrum of DCCF in the range 364 – 370 cm^{-1}	89
3.15	Portion of the spectrum of DCCF in the range 431.5 – 437.5 cm^{-1}	90
3.16	Portion of the spectrum of DCCF in the range 440.5 – 446.5 cm^{-1}	91
3.17	Portion of the spectrum of DCCF in the range 601 – 605 cm^{-1}	92
3.18	Portion of the spectrum of DCCF in the range 780 – 840 cm^{-1}	92
3.19	Overview of the spectrum of DC_4H	101
3.20	Vibrational energy levels diagram of DC_4H	104
4.1	FANTASIO+ experimental setup	111
4.2	Overview of the spectrum of CH_3CCH in the range 6200 – 6800 cm^{-1}	114
4.3	Comparison between CEAS, FTIR and CRDS spectra	115
4.4	Detail of the CRDS spectrum of $\nu_1 + \nu_2$ of CH_3CCH	116
4.5	Detail of the CRDS spectrum of $2\nu_1$ of CH_3CCH	117
4.6	Potential energy curve of ammonia	126
4.7	Overview of the spectrum of $^{15}ND_3$ in the range 550 – 1600 cm^{-1}	128
4.8	Detail of the *Q* branch of ν_2 of $^{15}ND_3$	129
4.9	Detail of the *P* and *R* branches of ν_2 of $^{15}ND_3$	130
4.10	Detail of the *Q* branch of ν_4 of $^{15}ND_3$	131
4.11	Detail of the ${}^{p}P_K(7)$ and *R* branches of ν_4 of $^{15}ND_3$	132
4.12	Portion of the spectrum of $^{15}ND_3$ in the range 2300 – 2700 cm^{-1}	133

4.13 Detail of the Q branch of ν_1 of $^{15}ND_3$ 134
4.14 Detail of the Q branch of ν_3 of $^{15}ND_3$ 135
4.15 Overview of the ν_4 band of CF_3Br 145
4.16 Portion of the Q branches of CF_3Br the range 1208.5 – 1209.8 cm^{-1} 146
4.17 Portion of the ^{p}P branches of CF_3Br the range 1204.50 – 1204.75 cm^{-1} 147
4.18 Portion of the ^{p}Q branches of CF_3Br the range 1209.7 – 1210.3 cm^{-1} 148
4.19 Portion of the ^{r}R branches of CF_3Br the range 1213.5 – 1213.7 cm^{-1} 149
5.1 Structure of the energy states of $^{14}NH_3$ in the range 3000 – 4000 cm^{-1} 160

List of Tables

2.1	Classification of vibrational symmetry levels	11
2.2	Selection rules for linear molecules	29
2.3	Assignment of nuclear spin quantum number	30
2.4	Selection rules for transitions in a symmetric top	33
2.5	Selection rules for transitions in a C_{3V} molecule	33
3.1	Normal modes of $^{12}C_2D_2$	42
3.2	Experimental conditions of C_2D_2 spectra	43
3.3	List of bands of $^{12}C_2D_2$	48
3.4	Block–diagonalized matrices used for interacting states	54
3.5	Spectroscopic parameters of bending modes of $^{12}C_2D_2$	55
3.6	Spectroscopic parameters of ν_1 of $^{12}C_2D_2$	58
3.7	Spectroscopic parameters of ν_2 of $^{12}C_2D_2$	59
3.8	Spectroscopic parameters of ν_3 of $^{12}C_2D_2$	60
3.9	Spectroscopic parameters of $\nu_1 + \nu_3$ and $\nu_2 + \nu_3$ of $^{12}C_2D_2$	61
3.10	Spectroscopic parameters of $\nu_1 + \nu_2$ of $^{12}C_2D_2$	62
3.11	Vibrational term values of $^{12}C_2D_2$	63
3.12	Experimental conditions of $^{13}C^{12}CD_2$ spectra	67
3.13	List of bands of $^{13}C^{12}CD_2$	72
3.14	Spectroscopic parameters of bending modes of $^{13}C^{12}CD_2$ with $v_4 + v_5 = 2$	75
3.15	Spectroscopic parameters of bending modes of $^{13}C^{12}CD_2$ with $v_4 + v_5 = 3$	77
3.16	Vibrational term values of $^{13}C^{12}CD_2$	79
3.17	Experimental conditions of femto–FT–CEAS spectra	81
3.18	List of bands of $H^{12}C^{13}CD$, $H^{13}C^{12}CD$ and $^{13}C^{12}CD_2$	84
3.19	Spectroscopic parameters of $H^{12}C^{13}CD$, $H^{13}C^{12}CD$ and $^{13}C^{12}CD_2$	86
3.20	Normal modes of DCCF	87
3.21	Experimental conditions of DCCF spectra	88
3.22	List of bands of DCCF	93
3.23	Spectroscopic parameters of bending modes and of $v_3 = 1$ of DCCF	96
3.24	Vibrational term values of DCCF	98
3.25	Normal modes of DC_4H	99
3.26	Experimental conditions of DC_4H spectra	100
3.27	List of bands of DC_4H	102
3.28	Spectroscopic parameters of bending modes of DC_4H	105
4.1	Normal modes of CH_3CCH	110
4.2	Experimental conditions of CH_3CCH cryogenic spectra	112
4.3	Experimental conditions of CH_3CCH FTIR spectra	113
4.4	List of bands of CH_3CCH	119
4.5	Ground state parameters of CH_3CCH	120
4.6	Off–diagonal matrix elements of the Hamiltonian used for CH_3CCH analysis	121
4.7	Spectroscopic parameters of the global analysis of CH_3CCH	123
4.8	Polyad matrix for CH_3CCH	124
4.9	Spectroscopic parameters for other bands of CH_3CCH	125

4.10	Experimental conditions of $^{15}ND_3$ spectra	127
4.11	Off–diagonal matrix elements of the vibration-rotation-inversion Hamiltonian	137
4.12	Ground state parameters of $^{15}ND_3$	138
4.13	Spectroscopic parameters of bending modes of $^{15}ND_3$	140
4.14	Spectroscopic parameters of stretching modes of $^{15}ND_3$	141
4.15	Normal modes of CF_3Br	143
4.16	Experimental conditions of CF_3Br spectra	144
4.17	Spectroscopic parameters of $\upsilon_4 = 1$ of $CF_3{}^{79}Br$	151
4.18	Spectroscopic parameters of $\upsilon_4 = 1$ of $CF_3{}^{81}Br$	152
I	Character table: $D_{\infty h}$ point group	165
II	Character table: $C_{\infty v}$ point group	165
III	Character table: C_{3V} point group	165

List of publications

1- "The infrared spectrum of propyne in the range 6200 – 6700 cm^{-1}"
M. Villa, L. Fusina, G. Nivellini, K. Didriche, X. De Ghellinck d'Elseghem Vaernewijck and M. Herman,
Chem. Phys. **402**, 14 (2012).

2- "Accurate ro–vibrational rest frequencies of DC_4H at infrared and millimetre wavelengths"
F. Tamassia, L. Bizzocchi, C. Degli Esposti, L. Dore, M. Di Lauro, L. Fusina, M. Villa and E. Cané,
A&A **549**, A38 (2013).

3- "Infrared spectroscopy of $^{15}ND_3$: the ν_2 and ν_4 bending fundamental bands"
E. Cané, G. Di Lonardo, L. Fusina, G. Nivellini, F. Tamassia and M. Villa,
JQRST **119**, 1 (2013).

4- "The infrared spectrum of $^{12}C_2D_2$: the stretching–bending band system up to 5500 cm^{-1}"
M. Villa, E. Cané, F. Tamassia, G. Di Lonardo and L. Fusina,
J. Chem. Phys. **138**, 134312 (2013).

5- "Femto–FT–CEAS investigation of rare acetylene isotopologues ($H^{12}C^{13}CD$, $D^{12}C^{13}CH$ and $D^{12}C^{13}CD$)"
M. Villa, L. Fusina, G. Di Lonardo, X. De Ghellinck d'Elseghem Vaernewijck and M. Herman,
Mol. Phys. **111**, 14-15, 1972 (2013).

6- "The high–resolution infrared spectrum of DC_4H from 450 to 1100 cm^{-1}: overtone, combination and hot bands"
L. Bizzocchi, F. Tamassia, C. Degli Esposti, L. Dore, L. Fusina, M. Villa and E. Cané,
J. Chem. Phys. **139**, 154308 (2013).

7- “The infrared spectrum of DCCF in the 320 – 850 cm^{-1} region: bending states up to $v_{tot} = 3$”
M. Villa, E. Cané, L. Fusina, H. Bürger and M. Litz,
Mol. Phys. (2013), doi:10.1080/00268976.2013.830787.

8- “High resolution infrared spectroscopy of $^{13}C^{12}CD_2$: the bending states with $v_4 + v_5$ up to 3”
L. Fusina, E. Cané, F. Tamassia, M. Villa and G. Di Lonardo,
Mol. Phys. (2013), doi:10.1080/00268976.2013.834086.

9- "The ro–vibrational analysis of the nu4 fundamental band of CF_3Br from jet–cooled diode laser and FTIR spectra in the 8.3 μm region"
E. Cané, M. Villa, R. Tarroni, F. Tamassia, A. Pietropolli Charmet, N. Tasinato, P. Stoppa and S. Giorgianni,
Mol. Phys. (2014), doi:10.1080/00268976.2013.872310.

PART I

THEORY

CHAPTER 1

INTRODUCTION

Rotational and vibrational spectroscopies, besides being techniques widely used to infer information on molecular structure [1], have a very important role in the investigation of the atmospheric chemistry and of the interstellar medium. Since the second half of the 1900, the study of Earth's and planetary atmospheres and of the interstellar medium by means of spectroscopic techniques has greatly increased, due to the availability of data detected by radio–telescopes or by instruments on board of satellites, stratospheric balloons, aircrafts, and spacecrafts. Nowadays, remote sensing techniques are widely used to probe the atmosphere and to retrieve the concentration profiles for a number of species. Molecular spectroscopy has made three major contributions to projects for studying the atmosphere of the Earth: 1) the determination of the energy balance of the Earth associated with radiative gain and loss, in relation to the greenhouse effect; 2) the detection of naturally occurring trace molecules in the atmosphere; 3) the assessment of the impact of human activities on the atmospheric composition, in particular the introduction of harmful, anthropogenic gases [2,3]. In fact, composition changes of the Earth's atmosphere, mainly due to various anthropogenic factors occurring in the last decades, are considered responsible for several adverse climate and environmental impacts. Climate change studies need the temporal trend of hazardous atmospheric pollutants, i.e. of both greenhouse and ozone depleting gases. Among them, particularly relevant are halogenated hydrocarbons, due to their role in stratospheric ozone depletion as well as in global warming.

In the last decades the investigation of remote environments has been extended to the interstellar medium and to the atmosphere of other planets [4–6]. Nowadays, there is an increasing interest towards the detection and the determination of the abundance of organic and inorganic molecules, ions, and radicals in interstellar space to provide data for understanding the formation of the stars and the origin of living matter [3]. Several space missions have led to the identification of a large variety of chemical compounds in the space as well as in the planetary atmospheres by means of spectroscopic techniques. A classic example is the Voyager Programme, aimed to the exploration of the external solar system, which started in 1977 with the launch of the Voyager 1 and 2 spatial probes and is still in progress. Afterwards, the Infrared Space Observatory (ISO) mission (1997) and the Cassini spacecrafts (2004) have provided a

huge amount of spectroscopic data. More recently, laboratory studies have been greatly stimulated by three recent research projects: Herschel (previously named FIRST, Far Infra–Red and Sub–millimeter Telescope), ALMA (Atacama Large Millimeter/sub–millimeter Array) and SOFIA (Stratospheric Observatory For Infrared Astronomy). These extend the range of observable frequencies from the millimeter–wave region to the infrared.

Despite the enormous work already carried out, many information are still lacking and numerous molecular species still need to be characterized. To fully exploit the considerable potential of spectroscopic techniques in the investigation of Earth's and planetary atmospheres as well as of the interstellar medium, it is necessary to know accurately the values of several spectroscopic parameters for the investigated molecules. In particular, these parameters are the frequency and the intensity of the rotational, vibrational or rovibrational transitions, the corresponding pressure broadening coefficients and their temperature dependence. For the relevant species, these parameters obtained by experimental laboratory studies are collected in databases which are continuously updated and improved [7,8]. From the spectroscopic point of view, the whole characterization of molecules of either atmospheric or astrochemical interest relies on the determination of the above mentioned parameters.

Many polyatomic molecules discovered in space are carbon chains with an acetylenic structure, i.e. featuring alternating single and triple C–C bonds. The simplest members of the family are acetylene (C_2H_2) and diacetylene (C_4H_2) which play a major role in the synthesis of complex interstellar molecules. Ion–neutral or neutral–neutral reactions between these moieties and C^+ or CN lead to the production of larger hydrocarbons (C_mH_n) or cyanopolyynes ($HC_{2n}CN$) [9]. In particular, the study of different isotopologues can provide a valuable piece of information about the isotopic composition in different environments. Various perdeuterated molecules have already been observed in many different sources [10 and refs. therein]: the study of multiply deuterated species provides much stronger constraints to discriminate between a gas–phase or a grain–surface reaction, and therefore to understand the interstellar chemistry. As far as non linear molecules are concerned, ammonia is undoubtedly one of the most important and extensively studied. In fact it collects the interest of spectroscopists, astrophysicists and theoretical scientists. It is abundant in a wide variety of objects throughout the universe. It has been detected in the interstellar medium [11], in remote stars [12], and in the atmospheres of the giant planets of the solar system and of their moons. The $^{14}N/^{15}N$ isotopic ratio in Jupiter's atmosphere from observation of NH_3 transitions has been recently reported [13]. It has been detected also in low mass brown dwarfs [14–16] and is expected in extrasolar planets [17,18]. In

particular, in recent publications [19,20] it has been highlighted the need for precise spectroscopic data for the less abundant ammonia isotopologues.

Another important molecule is methylacetylene, or propyne. It has been detected in the atmosphere of Titan [21,22], in the interstellar clouds [23], in the northern auroral region of Jupiter [24], and tentatively identified at the south pole of Saturn [21]. It was also observed in the Earth atmosphere by ACE mission in biomass burning plumes [25].

Finally, for what concerns terrestrial atmosphere, a large variety of gases are responsible for greenhouse effects and ozone depletion. The brominated compounds, which include the long–lived anthropogenic Halons and methylbromide, are highly dangerous pollutants of the Earth's atmosphere, being the source of bromine radical which is so efficient as a catalyst of stratospheric ozone depletion to be considered responsible for about 25% of the ozone loss in the Antarctic ozone hole [26,27]. The catalytic cycle of destruction of ozone can be summarized in this way:

$$X + O_3 \rightarrow XO + O_2$$
$$XO + O \rightarrow X + O_2$$
$$\overline{O_3 + O \rightarrow 2\,O_2}$$

where X is a radical species, the most important being H, N, Cl or Br. In particular, the last one is the most aggressive as its reservoir species (i.e. molecules that deactivate the radicals responsible for this process in the stratosphere) are not stable and all the bromine present in the stratosphere is active against the ozone layer.

Furthermore, besides being a powerful destructor of the ozone layer, CF_3Br is a relevant greenhouse gas since its infrared spectrum is characterized by strong absorptions mainly due to the ν_1 and ν_4 fundamentals in the region of the atmospheric transparency (between ca. 8 and 12 μm). Its radiative efficiency amounts to 0.32 W m^{-2} ppb^{-1} with a global warming potential (GWP) equal to 7140 over a 100–year horizon [28]. CF_3Br was banned from use in December 2003 since its ozone depletion potential, ODP, is the worst one among the bromine sources, being equal to 10 referred to CFC–11, a chlorinated compound. Its effects are quite important considering that bromine is up to 45–70 times more efficient than chlorine as a catalyst of the stratospheric ozone depletion and that is characterized by a long stratospheric lifetime, about 65 years [26].

This thesis is thus devoted to retrieve spectroscopic information for species of atmospheric and astrochemical importance. Accurate values of vibrational and rotational parameters, i.e. energies, anharmonicity constants, vibrational dependences of rotational

parameters obtained from rovibrational analysis, provide very valuable information for the determination of an accurate quartic anharmonic force field, which is very useful to predict for example the position of absorptions not yet detected or previously characterized.

The thesis is essentially based on the list of publications reported at the beginning. It is structured as follows: in the first part the theoretical quanto–mechanics aspects are reported and the general theory of vibrational and rotational motions in linear and symmetric top molecules is described. In the second part the analysis of the molecules is discussed. The experimental techniques employed for the registration of the spectra are reported and the Hamiltonian model used for each specific molecule is detailed. Finally, in Chapter 5 the conclusions are presented.

References

[1] G.H. Herzberg, Molecular spectra and molecular structure, vol. II, Infrared and Raman spectra of polyatomic molecules, Kriekger publishing company, Malabar, 1991.

[2] G. Duxbury, Infrared vibration–rotation spectroscopy. From free radicals to the infrared sky, John Wiley & Sons, Chichester, 2000.

[3] G. Winnewisser, E. Herbst and H. Ungerechts, Spectroscopy of the Earth's atmosphere and Interstellar Medium, edited by K.N. Rao and A. Weber, Academic Press, San Diego, 1992.

[4] V. Formisano, S.K. Atreya, T. Encrenaz, N. Ignatiev, M. Giuranna, *Science* **306**, 1758 (2004).

[5] F. Lefèvre, F. Forget, *Nature* **460**, 7200 (2009).

[6] G. Tinetti, M. –C. Liang, A. Vidal–Madjar, D. Ehrenreich, A. Lecavalier Des Etangs, Y.L. Yung, *Astrophys. J.* **654**, L99 (2007).

[7] L.S. Rothman, I.E. Gordon, Y. Babikov, A. Barbe, D. Chris Benner, P.F. Bernath, M. Birk, L. Bizzocchi, V. Boudon, L.R. Brown, A. Campargue, K. Chance, E.A. Cohen, L.H. Coudert, V.M. Devi, B.J. Drouin, A. Fayt, J. –M. Flaud, R.R. Gamache, J.J. Harrison, J. –M. Hartmann, C. Hill, J.T. Hodges, D. Jacquemart, A. Jolly, J. Lamouroux, R.J. Le Roy, G. Li, D.A. Long, O.M. Lyulin, C.J. Mackie, S.T. Massie, S. Mikhailenko, H.S.P. Müller, O.V. Naumenko, A.V. Nikitin, J. Orphal, V. Perevalov, A. Perrin, E.R. Polovtseva, C. Richard, M.A.H. Smith, E. Starikova, K. Sung, S. Tashkun, J. Tennyson, G.C. Toon, V.G. Tyuterev, G. Wagner, *JQRST*, http://dx.doi.org/10.1016/j.jqsrt.2013.07.002i.

[8] H.M. Pickett, R.L. Poynter, E.A. Cohen, M.L. Delitsky, .J.C. Pearson, H.S.P. Müller, Submillimiter, millimiter, and microwave spectral line catalog., *JQSRT* **96**, 883 (1998).

[9] I. Cherchneff and A.E. Glassgolf, *ApJ* **419**, L41 (1993).

[10] S. Yu, B.J. Drouin, J.C. Pearson, H.M. Pickett, V. Lattanzi and A. Walters, *Astrophys. J.* **698**, 2114 (2009).

[11] A.C. Ceung, D.M. Rank, C.H. Townes, D.D. Thornton and W.J. Welch, *Phys. Rev. Lett.* **21**, 1701 (1968).

[12] T.L. Wilson, C. Henkel and S. Hüttemeister, *Astron. Astrophys.* **460**, 533 (2006).

[13] M.M. Abbas, A. LeClair, T. Owen, B.J. Conrath, F.M. Flasar, V.G. Kunde, C.A. Nixon, R.K. Achterberg, G. Bjoraker, D.J. Jennings, G. Orton and P.N. Roman, *Astrophys. J.* **602**, 1063 (2004).

[14] D. Saumon, M.S. Marley, S.K. Leggett, T.R. Geballe, D. Stephens, D.A. Golimowski, M.C. Cushing, X. Fan, J.T. Rayner, K. Lodders and R.S. Freedman, *Astrophys. J.* **656**, 1136 (2007).

[15] S.K. Leggett, M.C. Cushing, D. Saumon, M.S. Marley, T.L. Roellig, S.J. Warren, B. Bumingham, H.R.A. Jones, J.D. Kirkpatrick, N. Lodieu, P.E. Lucas, A.K. Mainzer, E.L. Martin, M.J. McCaughrean, D.J. Pinfield, G.C. Sloan, R.L. Smart, M. Tamura and J. Van Cleve, *Astrophys. J.* **695**, 1517 (2009).

[16] S.K. Leggett, M.S. Marley, R.S. Freedman, D. Saumon, D. Liu, T.R. Geballe, D.A. Golimowski and D. Stephens, *Astrophys. J.* **667**, 537 (2007).

[17] D. Sudarsky, A. Burrows and I. Hubeny, *Astrophys. J.* **538**, 1121 (2003).

[18] M.R. Line, G. Vasisht, P. Chen, D. Angerhausen and Y.L. Yung, *Astrophys. J.* **738**, 32 (2011).

[19] X. Huang, D.W. Schwenke, and T.J. Lee, *J. Chem. Phys.* **134**, 044320–15 (2011).

[20] X. Huang, D.W. Schwenke, and T.J. Lee, *J. Chem. Phys.* **134**, 044321–18 (2011).

[21] R. Hanel, B. Conrath, F.M. Flasar, V. Kunde, W. Maguire, J. Pearl, J. Pirraglia, R. Samuelson, L. Heralth, M. Allison, D. Cruikshank, D. Gautier, P. Gierasch, L. Horn, R. Koppany, and C. Ponnamperuma, *Science* **212**, 192 (1981).

[22] A. Coustenis, D.E. Jennings, C.A Nixon, R.K. Achterberg, P. Lavvas, S. Vinatier, N.A. Teanby, G.L. Bjoraker, R.C. Carlson, L. Piani, G. Bampasidis, F.M. Flasar, P.N. Romani, *Icarus* **207**, 461 (2010).

[23] T.B.H. Kuiper, E.N. Rodriguez Kuiper, D.F. Dickinson, B.E. Turner, B. Zuckermann, *Astrophys. J.* **276**, 211 (1984) and references therein.

[24] S. J. Kim, J. Caldwell, A. Rivolo, R. Wagner, G.S. Orton, *Icarus* **64**, 233 (1985).

[25] P.F. Coheur, H. Herbin, C. Clerbaux, D. Hurtmans, C. Wespes, M. Carleer, S. Turquety, C.P. Rinsland, J. Remedios, D. Hauglustaine, C.D. Boone and P.F. Bernath, *Atmos. Chem. Phys.* **7**, 5437 (2007).

[26] B. –M. Sinnhuber, N. Sheode, M. Sinnhuber, M.P. Chipperfield and W. Feng, Atmos. Chem. Phys. Discuss. **6**, 6497 (2006).

[27] M.B. McElroy, R.J. Salawitch and K. Minschwaner, Planet. Space Sci. **40**, 373 (1992).

[28] Scientific Assessment of Ozone Depletion 2010, Report 52 of the World Meteorological Association's Global Ozone Research and Monitoring Project, National Oceanic and Atmospheric Administration, National Aeronautics and Space Administration, United Nations Environment Programme, World Meteorological Organization, European Commission.

CHAPTER 2

THEORY

Molecules can be classified according to their principal moments of inertia. A molecule contains a set of nuclei, each of which is taken to be a point mass m_i with coordinates x_i, y_i, z_i with respect to a set of cartesian axes whose origin is fixed onto the centre of mass of the set of nuclei. The moments of inertia about x, y, z are given by

$$I_x = \sum_i m_i \left(y_i^2 + z_i^2 \right)$$

$$I_y = \sum_i m_i \left(x_i^2 + z_i^2 \right) \qquad (2.1)$$

$$I_z = \sum_i m_i \left(x_i^2 + y_i^2 \right)$$

A more convenient labelling scheme for the axes is based upon the magnitude of the moments of inertia. These axes are the principal inertial axes a, b, c and they correspond to x, y, z cartesian axes in order to ensure the following inequality

$$I_A \le I_B \le I_C \qquad (2.2)$$

so that I_C is always the largest moment of inertia and I_A is the smallest one.

On the basis of the values of I_A, I_B, I_C, a molecule can be classified as [1–3]:

- Linear molecule, $I_B = I_C, I_A = 0$;
- Spherical top, $I_A = I_B = I_C$;
- Prolate symmetric top, $I_A < I_B = I_C$;
- Oblate symmetric top, $I_A = I_B < I_C$;
- Asymmetric top, $I_A < I_B < I_C$.

2.1 LINEAR MOLECULES

2.1.1 Vibrational energy

Linear molecules belong to either the $D_{\infty h}$ or $C_{\infty v}$ point groups, depending on whether they do or do not have a centre of inversion [2]. The character tables for $D_{\infty h}$ and $C_{\infty v}$ point groups are reported in Appendix A, Tables I and II.

The vibrational degrees of freedom are $3N-5$ in a N–atomic linear molecule, where N is the number of nuclei: there are $(N-1)$ non degenerate stretching vibrations and $(N-2)$ two–dimensional degenerate bending vibrations [4]. The last ones can be treated using the bidimensional harmonic oscillator model. If the two components of a degenerate bending vibration with a phase shift of 90° are superimposed, a simple motion of the same frequency is obtained, in which, however, not all the atoms move in phase and in straight line, although they do move with the same frequency. Each atom will swing along the axes x and y producing a circular movement around z and giving rise to a vibrational angular momentum ℓ about the internuclear axis of the molecule [1]. In this case, the Schrödinger equation can be solved by using cylindrical coordinates, as a function of r (distance of the oscillator from the origin) and θ (angle between r and one of the Cartesian axes) [5].

The wavefunction for degenerate modes, expressed as a function of υ and ℓ quantum numbers (vibrational quantum number and vibrational angular momentum quantum number, respectively), is eigenfunction of the equations

$$H\psi_{\upsilon,\ell} = \hbar\upsilon(\upsilon+1)\psi_{\upsilon,\ell} \qquad (2.3)$$

and

$$L\psi_{\upsilon,\ell} = \hbar\ell\,\psi_{\upsilon,\ell} \qquad (2.4)$$

where H is the energy Hamiltonian operator and L is the vibrational angular momentum operator, defined as

$$L = q_x p_y + q_y p_x \qquad (2.5)$$

with q_i and p_i being the normal coordinate and the conjugate momentum operator, respectively.

Once υ is known, it is possible to calculate the eigenvalue ℓ, according to:

$$\ell = \upsilon, \upsilon-2, ..., -\upsilon+2, -\upsilon \qquad (2.6)$$

It is possible to classify the vibrational levels by using the combination of v and ℓ quantum numbers. In case of v–multiple excitation of a doubly degenerate mode, there are several degenerated states, corresponding to $(v+1)$ values of ℓ, obtained from Eq. (2.6). These states are designated on the basis of irreducible representations of the $C_{\infty v}$ or $D_{\infty h}$ point groups using the value of $|\ell|$ [1], as reported in Table 2.1.

Table 2.1: Classification of vibrational symmetry levels as a function of $|\ell|$

$\lvert\ell\rvert$	Symmetry		Degeneration
	$C_{\infty V}$	$D_{\infty h}$	
0	Σ^+	$\Sigma^+_{g/u}$	1
0	Σ^-	$\Sigma^-_{g/u}$	1
1	Π	$\Pi_{g/u}$	2
2	Δ	$\Delta_{g/u}$	2
3	Φ	$\Phi_{g/u}$	2
…	…		…

If a centre of symmetry is present ($D_{\infty h}$ point group), all the levels in Table 2.1 have the adequate *g/u* subscript, corresponding to the symmetry of the wavefunction with respect to the inversion point group symmetry operation (with $g \times g = g$, $u \times u = g$, and $g \times u = u \times g = u$).

In case of multiple v excitation of non degenerate stretching states, only a Σ^+ or Σ^- symmetry state is obtained, the latter symmetry corresponding to an odd excitation of a Σ^- mode, whereas if in addition bending modes are excited, more levels are present. For example, if the double vibrational excitation of the same bending mode is considered, three sublevels are generated: one of Σ^+ symmetry and one of double degenerate Δ symmetry, for $\ell = 0$ and $\ell = \pm 2$, respectively. Differently, the combination of two different bending modes (t and t') leads to four vibrational levels: for $\ell = \ell_t(\pm 1) + \ell_{t'}(\mp 1) = 0$ Σ^+ and Σ^- levels are obtained, respectively, and one double degenerate Δ level for $\ell = \ell_t(\pm 1) + \ell_{t'}(\pm 1) = \pm 2$ [4]. Within the harmonic oscillator approximation, the energy is independent of ℓ. When vibrational levels are generated by triple, or even higher, simultaneous excitation of bending modes, two states can

have the same ℓ value. In this case, I or II are used as left superscript, and for convention I refers to the higher energy state, II to the lower one.

The degeneracy of sublevels with the same υ and different ℓ values is removed by diagonal anharmonic terms, while the one between $+\ell$ and $-\ell$ components is affected when considering vibration–rotation interactions (see Section 2.1.3). In fact, the harmonic oscillator model is inadequate to describe in detail the vibrational energy of a molecule and the expression of the energy must be corrected taking into account anharmonicity contributions, by using a polynomial expansion that is function of $\left(\upsilon+\frac{d}{2}\right)^n$, where υ is the vibrational quantum number, d is the degeneracy of the mode and $n \geq 2$.

The Schrödinger equation in its more general formulation is:

$$H_{vib}\Psi_{vib\ \upsilon,\ell} = E_{vib}\Psi_{vib\ \upsilon,\ell} \tag{2.7}$$

Its solution in terms of quantum numbers υ and ℓ gives the vibrational energy, represented by the spectroscopic vibrational term value G. The diagonal vibrational terms of the Hamiltonian in term of the Dunham expansion for a linear molecule with two degenerate bending vibrations is the following:

$$\begin{aligned}\frac{E}{hc} = G(\upsilon,\ell) = &\sum_i \omega_i\left(\upsilon_i+\frac{d_i}{2}\right)+\sum_{i\leq j} x_{ij}\left(\upsilon_i+\frac{d_i}{2}\right)\left(\upsilon_j+\frac{d_j}{2}\right)+\sum_{t\leq t'} g_{bb'}\ell_b\ell_{b'} \\ &+\sum_{i\leq j\leq k} y_{ijk}\left(\upsilon_i+\frac{d_i}{2}\right)\left(\upsilon_j+\frac{d_j}{2}\right)\left(\upsilon_k+\frac{d_k}{2}\right)+\sum_i\sum_{t\leq t'} y_i^{bb'}\left(\upsilon_i+\frac{d_i}{2}\right)\ell_b\ell_{b'}+.....\end{aligned} \tag{2.8}$$

where:

i, j, k = index of the normal modes of the molecule

b, b' = bending degenerate modes

ω_i = zeroth order vibrational frequencies (harmonic frequencies)

x_{ij} , y_{ijk}, $y_i^{bb'}$ = anharmonicity constants

$g_{bb'}$ = anharmonicity constants relative to ℓ, responsible of the partial removal of the degeneration

$y_i^{bb'}$ = higher anharmonicity constants as a function of υ e ℓ

d_i = degree of degeneracy of the vibration

Off–diagonal terms are responsible for removing completely the degeneracy between levels. They will be taken into consideration below, in Section 2.1.3.

2.1.2 Rotational energy

The simplest model used to describe the rotation of a molecule is that of the rigid rotor. The rotational term value is a function of *J*, which is the quantum number of the total angular momentum, according to:

$$F(J) = \frac{hJ(J+1)}{8\pi^2 cI} = BJ(J+1) \tag{2.9}$$

where both *F*(*J*) and the rotational constant *B* have the dimension of wavenumbers [2]. However, Eq. (2.9) is not sufficient to describe the effects of the non–rigidity of the molecule. It is therefore necessary to introduce higher order correction terms containing the distortion constants *D*, *H*, *L*, *P*, … . They represent the influence of the centrifugal force which results in a very slight increase of the internuclear distances when the molecule is rotating. In addition, in case of a bending state, the structure is much more distorted. As explained before, if a degenerate vibration is excited, an angular momentum around the internuclear axis is generated and represented by the quantum number ℓ. The rotational term assumes the form of the symmetric top one (see Section 2.2.2) as a function of *J* and ℓ, where ℓ is replaced by *k* in symmetric tops. For a molecule with two degenerate bending vibrations is:

$$\begin{aligned} F_\upsilon(J) = &\left[B_\upsilon + \sum_{b\le b'} \gamma^{bb'} \ell_b \ell_{b'} + \sum_i \sum_{i\le j} \gamma_i^{bb'} \left(\upsilon_i + \frac{d_i}{2} \right) \ell_b \ell_b \right] \left(M - \ell^2 \right) \\ &- \left(D_\upsilon + \sum_{b\le b'} \delta^{bb'} \ell_b \ell_{b'} \right) \left(M - \ell^2 \right)^2 + H_\upsilon \left(M - \ell^2 \right)^3 + ... \end{aligned} \tag{2.10}$$

with

$$\begin{aligned} B_\upsilon = &B_e - \sum_i \alpha_i \left(\upsilon_i + \frac{d_i}{2} \right) + \sum_{i\le j} \gamma_{ij} \left(\upsilon_i + \frac{d_i}{2} \right) \left(\upsilon_j + \frac{d_j}{2} \right) \\ &+ \sum_{i\le j\le k} \gamma_{ijk} \left(\upsilon_i + \frac{d_i}{2} \right) \left(\upsilon_j + \frac{d_j}{2} \right) \left(\upsilon_k + \frac{d_k}{2} \right) + ... \end{aligned} \tag{2.11}$$

$$D_\upsilon = D_e + \sum_i \beta_i \left(\upsilon_i + \frac{d_i}{2} \right) + \sum_{i\le j} \delta_{ij} \left(\upsilon_i + \frac{d_i}{2} \right) \left(\upsilon_j + \frac{d_j}{2} \right) + ... \tag{2.12}$$

$$H_\upsilon = H_e + \sum_i h_i \left(\upsilon_i + \frac{d_i}{2} \right) + ... \tag{2.13}$$

where $M = J(J+1)$ and $J \ge |\ell|$, being ℓ the projection of *J* along the internuclear axis.

The constants appearing in the Eq. (2.10) – (2.13) are:

B_υ = rotational constant

D_υ = quartic centrifugal distortion constant

H_υ = sextic centrifugal distortion constant

…..

B_e = rotational constant for the equilibrium configuration of the molecule (equilibrium point of the potential energy function)

$\alpha, \gamma_{ij}, \gamma_{ijk}$ = rovibrational interaction constants underlining the vibrational dependance of B

D_e, H_e = centrifugal distortion constants at the equilibrium configuration of the molecule

β_i, δ_{ij}, h_i = higher order centrifugal distortion taking into account the D e H dependence from the vibrational state

$\gamma^{ss'}, \delta^{ss'}$ = vibrational constants as function of ℓ

$\gamma_i^{ss'}$ = vibrational constants as function of υ and ℓ

2.1.3 Rovibrational energy and essential resonances

In molecules rotation can take place simultaneously with a vibration, giving rise to the rotational structure of infrared vibration bands [1]. The energy of the rotational levels belonging to a vibrational state is described as the sum of vibrational (2.8) and rotational (2.9) contributions. Taking into account Eqs. (2.11), (2.12) and (2.13), the rovibrational term T is obtained:

$$T(\upsilon, \ell, J) = G(\upsilon, \ell) + F(\upsilon, \ell, J) \qquad (2.14)$$

In Eq. (2.14) the G and F terms are supposed to be independent, even if there is the rovibrational coupling given by α constants. This means that the vibration is referred to a coordinates system fixed onto the molecule and uniformly rotating with her.

In such a system, it must be taken into account the presence of two apparent forces: the centrifugal force and the Coriolis force [1]. The magnitude of these forces is given by:

$$F_{centrifugal} = m r \omega^2 \qquad (2.15)$$

$$F_{Coriolis} = 2 m \mathrm{v}_a \omega \sin\varphi \qquad (2.16)$$

where:

m = mass of the nuclei

v_a = apparent velocity with respect to the moving coordinate system

r = distance from the axis of rotation

ω = angular velocity of the coordinate system with respect to a fixed coordinate system

φ = angle between the axis of rotation and the direction of v_a

The introduction of the centrifugal force in the rovibrational Hamiltonian involves the inclusion of centrifugal distortion constants, as reported in Eq. (2.14), which are effective even if the system is not vibrating.

The introduction of the Coriolis force leads to an additional coupling between rotation and vibration (Coriolis coupling), which is in general stronger than the effect of the centrifugal force, since the velocity due to the vibration (v_a) is usually much larger than that due to rotation ($r\omega$). However, this interaction occurs only when the molecule is vibrationally excited ($v_a \neq 0$) and additional vibrational angular momenta appear. This is due to the fact that, in the rotating coordinates system, the nuclei will not move in straight lines, but in ellipses around the equilibrium position of each atom, inducing in bending vibrations a non zero additional vibrational angular momentum around the axis of the ellipses. This is described for a triatomic linear molecule in Figure 2.1.

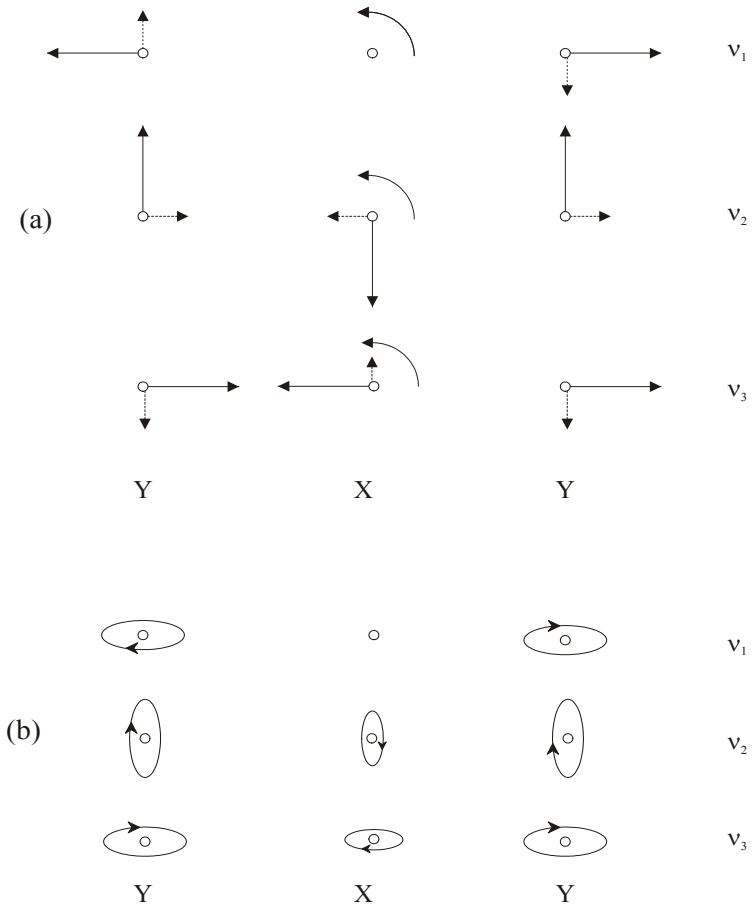

Figure 2.1: Coriolis components for a triatomic linear molecule XY_2.

(a) Continuous lines: nuclei motion; dashed lines: apparent Coriolis forces.

(b) Motion of nuclei on account of Coriolis interaction

The Coriolis coupling is distinguished as *First order* and *Second order*. In the *First order Coriolis interaction* the interaction is between the two components of the same degenerate vibrational mode, whereas in the second case it occurs between two different vibrational modes. This will be discussed later in Section 2.3.

The effect of a first order Coriolis interaction is the removal of the degeneracy between rovibrational levels of a degenerate state. The splitting between rotational levels in a vibrational state with $\ell = 1$ (ℓ – type splitting) is given by:

$$\Delta\nu = q(\upsilon+1)J(J+1) \qquad (2.17)$$

where $q \cong \frac{B_e}{\omega_e}$ is called ℓ – type doubling constant and ω_e is the harmonic frequency of the specific normal mode.

In case of absence of resonances, the rovibrational term gives the energies of the rotational levels of a vibrational state, corresponding to diagonal Hamiltonian matrix elements with basis function $|\upsilon, \ell, J\rangle$, whose elements are obtained from Eq. (2.14).

The off–diagonal matrix elements are:

- off–diagonal in ℓ, responsible for ℓ – type rotational splitting and for other resonances arising in bending modes;
- off–diagonal in ℓ, responsible for ℓ – type vibrational splitting and for other resonances arising in bending modes;
- off–diagonal in υ, representing Fermi, Darling–Dennison and higher anharmonic interaction (strictly speaking, a Fermi resonance occurs between vibrational levels with $\Delta\upsilon_i = \pm 2$ and $\Delta\upsilon_j = \mp 1$, so between a fundamental mode and an overtone or a combination band; a Darling–Dennison resonance occurs between vibrational levels with $\Delta\upsilon_i = \pm 2$ and $\Delta\upsilon_j = \mp 2$; in other cases they are generally called anharmonic interactions).

They will be discussed later in Section 2.3.

Usually these terms include higher order contributions as a function of υ, ℓ, and J, i.e. diagonal cubic and quartic terms of vibrational energy (y and γ).

The discussion about this item will be focused on acetylene and its isotopologues.

In order to calculate the energies of bending levels, the Amat and Nielsen model for linear molecules [6], subsequently modified [7–14], is applied.

The energy levels of bending vibrations ν_4 and ν_5 can be numerically obtained as eigenvalues of the rovibrational energy matrix with basis eigenfunctions $|\upsilon_4, \ell_4, \upsilon_5, \ell_5, J, \ell\rangle$. In

some cases of ℓ – type interaction, ℓ_4 and ℓ_5 are not good quantum numbers useful for the classification, but their sum is. Rovibrational levels are classified *e* or *f* in function of their parity. For a molecule in a singlet electronic state, the parity is:

$+(-1)^J$ for *e* levels

$-(-1)^J$ for *f* levels

Using the convention of the Watson basis, if the rovibrational eigenfunctions are chosen following the symmetry with respect the inversion operation:

$$E^*\left|\upsilon,\ell,J\right\rangle = (-1)^{J-\ell}\left|\upsilon,-\ell,J\right\rangle \tag{2.18}$$

the symmetrised eigenfunctions, called Wang basis, are defined as follows:

$$\ell_4 = \ell_5 = 0 \qquad \left|\upsilon,0,J,e\right\rangle = \left|\upsilon,0,J\right\rangle \tag{2.19}$$

$$\ell_4 + \ell_5 \geq 0 \qquad \left|\upsilon,\ell,J,e\right\rangle = \sqrt{\frac{1}{2}}\left[\left|\upsilon,\ell,J\right\rangle + (-1)^{\ell}\left|\upsilon,-\ell,J\right\rangle\right] \tag{2.20}$$

with

$$\ell_4 \neq 0 \text{ and/or } \ell_5 \neq 0 \quad \left|\upsilon,\ell,J,f\right\rangle = \sqrt{\frac{1}{2}}\left[\left|\upsilon,\ell,J\right\rangle - (-1)^{\ell}\left|\upsilon,-\ell,J\right\rangle\right] \tag{2.21}$$

Because of ℓ – type perturbations, the energies of the levels for bending modes of the molecule cannot be described by using closed algebraic expressions. These energy levels have to be obtained in a numerical way, diagonalizing appropriated rovibrational energy matrices. It is therefore necessary to build a matrix for every group of interacting states involved in the observed transitions, characterized by the same value of $\upsilon_{tot} = \upsilon_4 + \upsilon_5$, and to consider each time the off–diagonal matrix elements relative to the perturbations affecting these states.

Since bending modes are involved, Wang eigenfunctions are used, in order to have a factorization of Hamiltonian matrices: off–diagonal elements are responsible only for the coupling between *e* states or between *f* states. In this way the obtained matrices are smaller and easier to diagonalize. Perturbation matrices involving states with different υ_{tot} (including stretching and stretching–bending states) with off–diagonal elements for both ℓ – type perturbations and anharmonic resonances, can be constructed.

Diagonal matrix elements determine the energy order of ℓ sublevels for each vibrational state and they are obtained from the rovibrational term *T*. For bending states with υ_{tot} up to 3, when the energy of the levels and the relative vibrational constants are referred to the ground

state (υ = 0) and not to the minimum of the well of the potential energy surface, the matrix elements are:

$$G^0(\upsilon_4^{\ell_4},\upsilon_5^{\ell_5}) + F^0(\upsilon_4^{\ell_4},\upsilon_5^{\ell_5},M) \tag{2.22}$$

$$\begin{aligned} G^0(\upsilon_4^{\ell_4},\upsilon_5^{\ell_5}) = {} & \omega_4^0\upsilon_4 + \omega_5^0\upsilon_5 + x_{44}^0\upsilon_4^2 + x_{55}^0\upsilon_5^2 + x_{45}^0\upsilon_4\upsilon_5 \\ & + g_{44}^0\ell_4^2 + g_{55}^0\ell_5^2 + g_{45}^0\ell_4\ell_5 + y_{444}^0\upsilon_4^3 + y_{555}^0\upsilon_5^3 + y_{445}^0\upsilon_4^2\upsilon_5 + y_{455}^0\upsilon_4\upsilon_5^2 \\ & + y_4^{44}\upsilon_4\ell_4^2 + y_4^{45}\upsilon_4\ell_4\ell_5 + y_4^{55}\upsilon_4\ell_5^2 + y_5^{44}\upsilon_5\ell_4^2 + y_5^{45}\upsilon_5\ell_4\ell_5 + y_5^{55}\upsilon_5\ell_5^2 \end{aligned} \tag{2.23}$$

$$\begin{aligned} F^0(\upsilon_4^{\ell_4},\upsilon_5^{\ell_5},M) = {} & (B_\upsilon + \gamma^{44}\ell_4^2 + \gamma^{45}\ell_4\ell_5 + \gamma^{55}\ell_5^2 + \gamma_4^{44}\upsilon_4\ell_4^2 \\ & + \gamma_4^{45}\upsilon_4\ell_4\ell_5 + \gamma_4^{55}\upsilon_4\ell_5^2 + \gamma_5^{44}\upsilon_5\ell_4^2 + \gamma_5^{45}\upsilon_5\ell_4\ell_5 + \gamma_5^{55}\upsilon_5\ell_5^2)(M-\ell^2) \\ & - (D_\upsilon + \delta^{44}\ell_4^2 + \delta^{45}\ell_4\ell_5 + \delta^{55}\ell_5^2)(M-\ell^2)^2 + H_\upsilon(M-\ell^2)^3 \end{aligned} \tag{2.24}$$

where

$$\begin{aligned} B_\upsilon = {} & B_0 - \alpha_4\upsilon_4 - \alpha_5\upsilon_5 + \gamma_{44}\upsilon_4^2 + \gamma_{45}\upsilon_4\upsilon_5 + \gamma_{55}\upsilon_5^2 \\ & + \gamma_{444}\upsilon_4^3 + \gamma_{445}\upsilon_4^2\upsilon_5 + \gamma_{455}\upsilon_4\upsilon_5^2 + \gamma_{555}\upsilon_5^3 \end{aligned} \tag{2.25}$$

$$D_\upsilon = D_0 + \beta_4\upsilon_4 - \beta_{55} + \delta_{44}\upsilon_4^2 + \delta_{45}\upsilon_4\upsilon_5 + \delta_{55}\upsilon_5^2 \tag{2.26}$$

$$H_\upsilon = H_0 + h_4\upsilon_4 + h_5\upsilon_5 \tag{2.27}$$

with B_0, D_0 and H_0 being the rotational and centrifugal distorsion constants of the ground state.

Off–diagonal vibrational ℓ terms, responsible of resonances and vibrational doublings, and rotational ℓ – type of bending modes are also present in the matrix. They are:

$$\left\langle \upsilon_4^{\ell_4},\upsilon_5^{\ell_5},J,\ell \left| H_2' \right| \upsilon_4^{\ell_4\pm2},\upsilon_5^{\ell_5\mp2},J,\ell \right\rangle = \frac{1}{4} r_{45} \left\{ (\upsilon_4 \mp \ell_4)(\upsilon_4 \pm \ell_4 + 2)(\upsilon_5 \pm \ell_5)(\upsilon_5 \mp \ell_5 + 2) \right\}^{1/2} \tag{2.28}$$

where r_{45} is the vibrational ℓ – type doubling constant [15], whose effect is to split Σ^+ and Σ^- states belonging, together with a Δ state, to the vibrational sublevel of the combination $\upsilon_4 = 1, \upsilon_5 = 1$;

$$\left\langle \upsilon_t^{\ell_t},J,\ell \left| H_2' \right| \upsilon_t^{\ell_t\pm2},J,\ell\pm2 \right\rangle = \frac{1}{4} q_t \left\{ (\upsilon_t \pm \ell_t)(\upsilon_t \pm \ell_t + 2)\left[M - \ell(\ell\pm1)\right]\left[M - \ell(\ell\pm1)(\ell\pm2)\right] \right\}^{1/2} \tag{2.29}$$

where q_t is the rotational ℓ–type doubling constant [15], whose effect is to split the two components *e* and *f* of a double degenerate state. It also represents the resonance between states of different symmetry with the same υ, as for example between the different components of the states Σ and Δ or Π and Φ;

$$\left\langle \upsilon_t^{\ell_t}, J, \ell \middle| H_2' \middle| \upsilon_t^{\ell_t \pm 4}, J, \ell \pm 2 \right\rangle = \frac{1}{4}\rho_t \{ \ (\upsilon_t \pm \ell_t)(\upsilon_t \pm \ell_t + 2)(\upsilon_t \pm \ell_t)(\upsilon_t \pm \ell_t + 4)$$
$$[M - \ell(\ell \pm 1)][M - \ell(\ell \pm 1)(\ell \pm 2)] \qquad (2.30)$$
$$[M - \ell(\ell \pm 2)(\ell \pm 3)][M - \ell(\ell \pm 3)(\ell \pm 4)] \ \}^{1/2}$$

where ρ_t is a rotational constant important at high J values and in case of at least a double excitation of the same bending mode, as illustrated in Fig. 2.2;

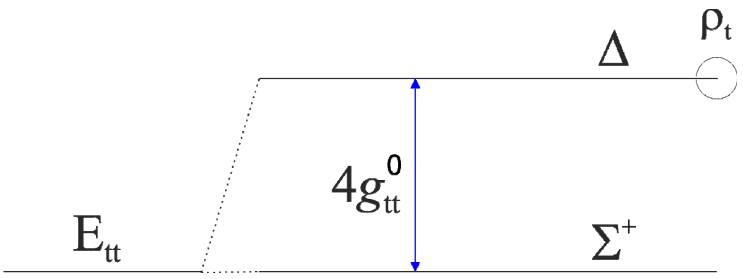

Figure 2.2: Splitting of energy levels of the state $\upsilon_t = 2$, with t = 4 or 5.

$$\left\langle \upsilon_4^{\ell_4}, \upsilon_5^{\ell_5}, J, \ell \middle| H_2' \middle| \upsilon_4^{\ell_4 \pm 2}, \upsilon_5^{\ell_5 \pm 2}, J, \ell \pm 4 \right\rangle = \frac{1}{16}\rho_{45}$$
$$\{ \ (\upsilon_4 \pm \ell_4)(\upsilon_5 \pm \ell_5)(\upsilon_4 \pm \ell_4 + 2)(\upsilon_5 \pm \ell_5 + 2)[M - \ell(\ell \pm 1)] \qquad (2.31)$$
$$[M - \ell(\ell \pm 1)(\ell \pm 2)][M - \ell(\ell \pm 2)(\ell \pm 3)][M - \ell(\ell \pm 3)(\ell \pm 4)] \ \}^{1/2}$$

where ρ_{45} is the analogous of ρ_t in the case that both the bending modes are excited simultaneously [12], as illustrated in Fig. 2.3.

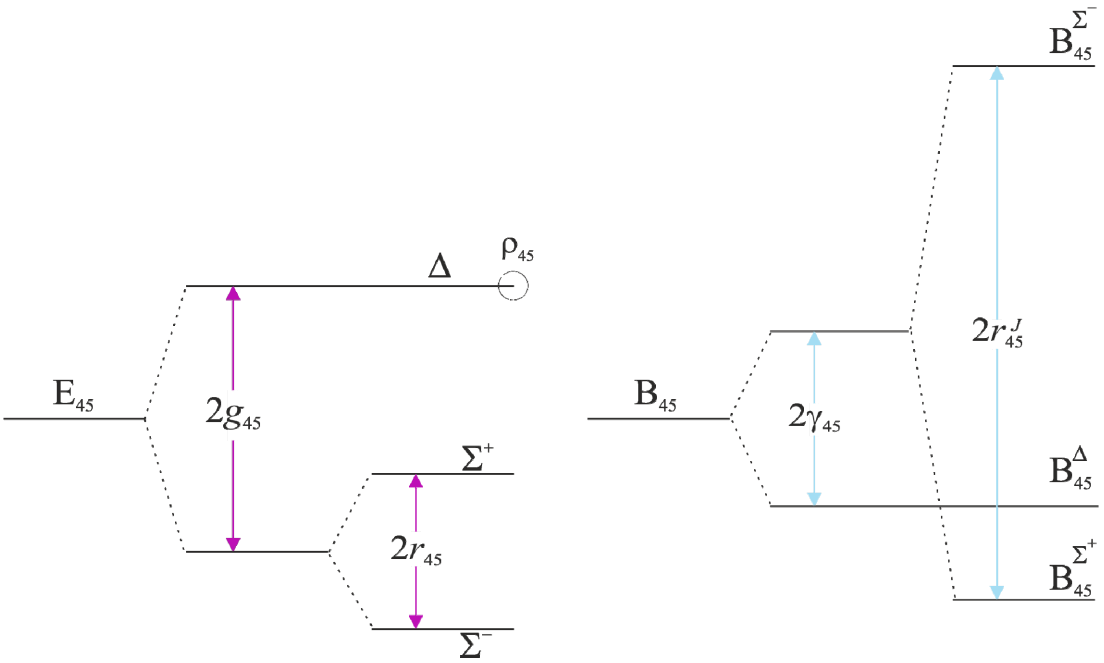

Figure 2.3: Splitting of energy levels and of B_υ of the state $\upsilon_4 = \upsilon_5 = 1$.
g is the vibrational diagonal term
r is the vibrational off–diagonal term
γ is the rotational diagonal term
r^J is the rotational off–diagonal term

The interaction constants present in the off–diagonal matrix elements are well represented by expressions containing a term of zeroth order and other terms of higher order which express the dependence from the quantum numbers J and υ. Their general expressions are:

$$r_{45} = r_{45}^{0} + r_{45}^{J} J(J+1) + r_{45}^{JJ} J^2 (J+1)^2 + r_{445}(\upsilon_4 + 1) + r_{455}(\upsilon_5 + 1) + ... \tag{2.32}$$

$$q_t = q_t^0 + q_{tt}\upsilon_t + q_{tt'}\upsilon_{t'} + q_t^J J(J+1) + q_t^{JJ} J^2 (J+1)^2 + q_t^{\ell}(\ell \pm 1)^2 ... \tag{2.33}$$

$$\rho_t = \rho_t^0 + \rho_{tt}\upsilon_t + \rho_{tt'}\upsilon_{t'} + \rho_t^J J(J+1) + ... \tag{2.34}$$

In Eqs. (2.32) – (2.34) the first term is the zeroth order term. Off–diagonal interactions in ℓ are all diagonal in υ, being effective between rovibrational levels with the same value of υ_{tot}.
As far as off–diagonal terms in υ are concerned, they will be discussed in Section 2.3.

2.2 SYMMETRIC TOPS

2.2.1 Vibrational and rotational energies

In contrast to linear molecules, all the other molecules, including symmetric tops, have $3N–6$ vibrational degrees of freedom, where N is the number of the atoms.

As far as the vibrational energy is concerned, symmetric tops are described by the same expression used for linear molecules, see Eq. (2.8). The situation is different for the rotational motion. In a symmetric top two inertia moments must be taken into account: I_A and I_B for a prolate top, I_B and I_C for an oblate top. The J quantum number is no more sufficient, and the component of the angular momentum about the axis of higher symmetry, k, must be taken into account. It can take $2J + 1$ values from $–J$ to $+J$ including 0 ($–J \le k \le J$). In the expression of the energy, the quantum number K ($K = |k|$) is introduced. K assumes $J + 1$ values form 0 to J. All rotational levels with $K > 0$ possess a double degeneracy which can be thought of, classically, as being due to the clockwise or anti – clockwise rotation about the top axis. For $K = 0$ there is no angular momentum about the top axis and therefore no K degeneracy. For a prolate top:

$$F(J,K) = B_{\upsilon}\left[J\left(J+1\right)\right] + \left(A_{\upsilon} - B_{\upsilon}\right)K^2 \tag{2.35}$$

where

$$B_\upsilon = B_e - \sum_i \alpha_i^B \left(\upsilon_i + \frac{d_i}{2} \right) + \ldots \tag{2.36}$$

$$A_\upsilon = A_e - \sum_i \alpha_i^A \left(\upsilon_i + \frac{d_i}{2} \right) + \ldots \tag{2.37}$$

$B_e = \frac{h}{8\pi^2 c I_B}$ and $A_e = \frac{h}{8\pi^2 c I_A}$ correspond to the value of B and A at equilibrium position, and α_i are the rovibrational interaction constants underlining the vibrational dependence of rotational constants.

If the top is oblate, the rotation constant C replaces A in Eq. (2.35) with

$$C_\upsilon = C_e - \sum_i \alpha_i^C \left(\upsilon_i + \frac{d_i}{2} \right) + \ldots \tag{2.38}$$

where $C_e = \frac{h}{8\pi^2 c I_C}$.

Taking into account the non rigidity of the molecule, as already seen for linear molecules, centrifugal distortion constants must be considered.

2.2.2 Rovibrational energy

The first order Coriolis interaction is effective between the two components of a E degenerate vibrational state, and it is stronger than that active between non – degenerate states or degenerate states of linear molecules [1]. The result is a splitting of the degenerate vibrational levels into two levels whose separation increases with increasing rotation (K) about the top axis and is 0 for $K = 0$ (the same ℓ – doubling already seen for linear molecules). This is illustrated in Figure 2.4 for a prolate symmetric top. In addition, as already seen in Section 2.1.3, Coriolis force is produced by interaction of two vibrations of different species, which increases with increasing rotation and results in a contribution to the rotational constant α.

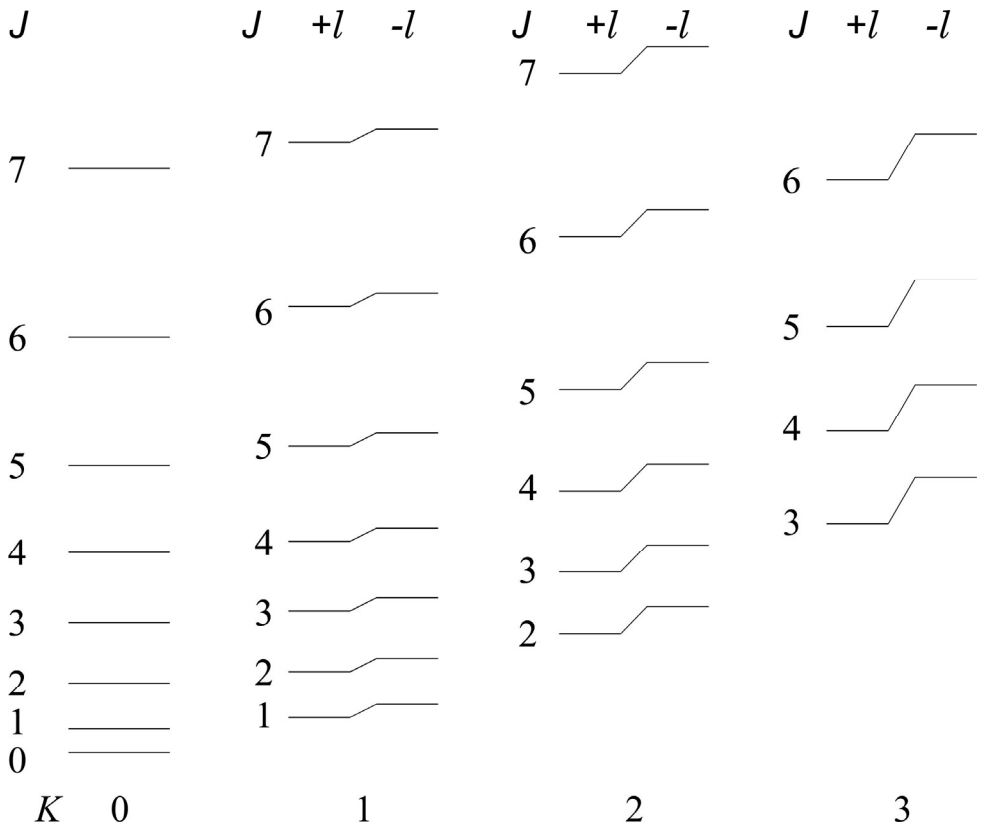

Figure 2.4: Rotational energy levels of a prolate symmetric top molecule in a doubly degenerate vibrational state.

The magnitude of the vibrational angular momentum in a degenerate vibrational state in which only one degenerate vibration ν_i is singly excited is $\zeta_i(h/2\pi)$, where $0 \le |\zeta_i| \le 1$. So, the expression of the rotational energy for a prolate symmetric top is:

$$\begin{aligned} F(\upsilon,J,K,\ell) = {} & B_\upsilon\left[J(J+1)-k^2\right]+A_\upsilon k^2-2(A\zeta)_\upsilon k\ell-D_{\upsilon J}\left[J(J+1)\right]^2 \\ & -D_{\upsilon JK}\left[J(J+1)\right]k^2-D_{\upsilon K}k^4+\eta_{\upsilon J}\left[J(J+1)\right]k\ell+\eta_{\upsilon K}k^3\ell \\ & +H_{\upsilon J}\left[J(J+1)\right]^3+H_{\upsilon JK}\left[J(J+1)\right]^2k^2+H_{\upsilon KJ}\left[J(J+1)\right]k^4+H_{\upsilon K}k^6 \\ & +\tau_{\upsilon J}\left[J(J+1)\right]^2k\ell+\tau_{\upsilon JK}\left[J(J+1)\right]k^3\ell+\tau_{\upsilon K}k^5\ell+\tau_{\upsilon K*}k^3\ell^3 \end{aligned} \tag{2.39}$$

D and *H* are centrifugal distortion constants, and

$$(A\zeta)_\upsilon = (A\zeta)_e - \sum_i \alpha_i^{A\zeta}(\upsilon_i+\frac{d_i}{2})+\ldots \tag{2.40}$$

$2\alpha_i^{A\zeta}$ is the coefficient of $k\ell_t\left(\upsilon_i+\frac{d_i}{2}\right)$. Maes introduced η_J and η_K constants [16] using the relationship

$$2\alpha_i^{A\zeta} = \eta_{i,r} \tag{2.41}$$

the τ constants are higher order dependences of η_J and η_K.

The rovibrational term value T is the sum of the vibrational and rotational term values, as explained above in Section 2.1.3 for linear molecules. In this case it is function of both J and K quantum numbers:

$$T(\upsilon,\ell,J,K) = G(\upsilon,\ell) + F(\upsilon,\ell,J,K) \tag{2.42}$$

In case of symmetric top molecules, there are three rotational $\ell-$ doubling interactions, involving three different $\ell-$ doubling constants. The differences between them are associated to selection rules in k and ℓ which govern the nonzero off–diagonal matrix elements. These are as follows:

- $\Delta\ell = \pm 2$, $\Delta k = \pm 2$, denoted $q_t^{(+)}-$ type interaction
- $\Delta\ell = \pm 2$, $\Delta k = \mp 2$, denoted $q_t^{(-)}-$ type interaction
- $\Delta\ell = \pm 2$, $\Delta k = \mp 1$, denoted r_t – type interaction.

The last two occur only in certain symmetry point groups, owing to symmetry restrictions [17]. The first one is the most familiar type and the $\ell-$ doubling constant $q_t^{(+)}$ defines the magnitude of the off–diagonal matrix elements according to equation:

$$\begin{aligned}\left\langle \upsilon_t,\ell_t+1,J,k+1\left|H_{22}+H_{24}/hc\right|\upsilon_t,\ell_t-1,J,k-1\right\rangle = \\ -\frac{1}{4}q_t^{(+)}\left\{\left[\left(\upsilon_t+1\right)^2-\ell^2\right]\left[J\left(J+1\right)-k\left(k+1\right)\right]\left[J\left(J+1\right)-k\left(k-1\right)\right]\right\}^{1/2}\end{aligned} \tag{2.43}$$

In a symmetric top additional symmetry properties of the rotational eigenfunctions have to be considered, since certain rotations are symmetry operations, depending on the point group to which the molecule belongs. Let us consider the case of C_{3V} molecules. The character table for C_{3V} point group is reported in Appendix A, Table III.

The eigenfunction of the symmetric top may be written, as pointed out by Dennison [18] and Mulliken [19]

$$\psi_r = \Theta_{JKM}(\vartheta)e^{iM\chi}e^{\pm iK\varphi} \tag{2.44}$$

where φ is the angle of rotation about the top axis. If φ increases by $2\pi/3$ the rotational eigenfunction is unchanged if K is a multiple of 3. So the rotational eigenfunction for $K= 3n$ ($n=$ 1, 2 ,3,…) are of species A_1 and A_2. This holds for both components of a doubly degenerate rotational levels when $K \neq 0$. If K is not a multiple of 3, ($K= 3n \pm 1$) the rotational eigenfunction does not remain unchanged, that is, it is of species E [1]. This is illustrated in Figure 2.5.

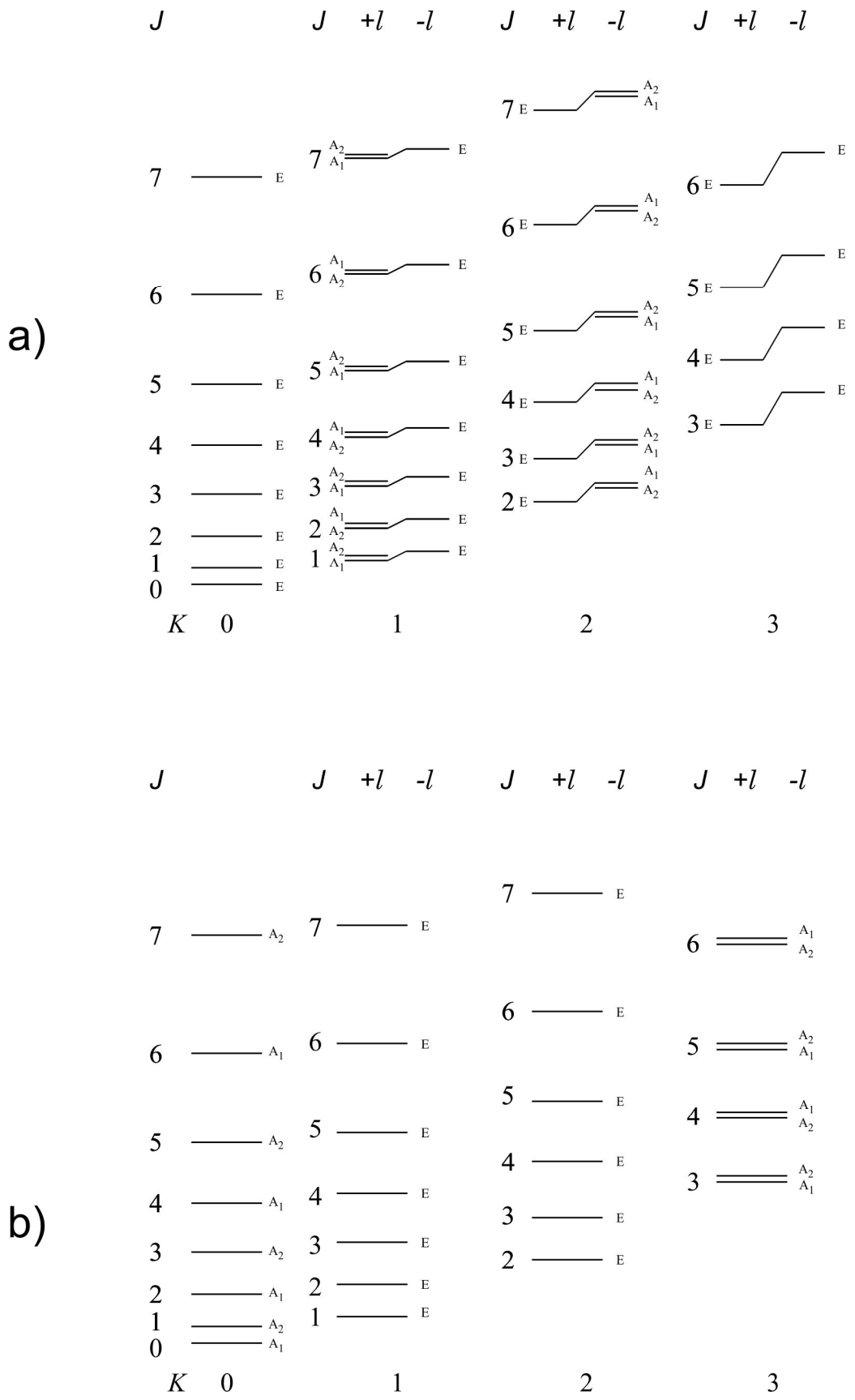

Figure 2.5: Symmetry properties of the rotational levels of a prolate top molecule for a) degenerate vibrational state, b) totally symmetric vibrational state.

2.3 ACCIDENTAL RESONANCES

A resonance is called accidental if the two resonanting vibrational states have close energy by chance. In such cases, the coupling matrix element is off–diagonal with respect to at least two quantum numbers v. These resonances are:

– Fermi interactions (or more generally anharmonic interactions)

– Coriolis interactions (or better second order Coriolis interactions)

These two effects are frequently considered in order to explain changes in band origin positions, in rotational constants, in intensities and breakdown of selection rules.

2.3.1 Anharmonic interactions

An anharmonic resonance is a purely vibrational interaction in origin, occurring between levels of the same symmetry species. The term "Fermi resonance" is used to describe the interaction between an overtone or a combination level and a fundamental one that have nearly coincident energies. This interaction is called first type or second type Fermi resonance, respectively [20]. An anharmonic resonance between two overtone levels is called Darling–Dennison interaction. In all the other cases it is called more generally anharmonic interaction.

The energy matrix representing the interaction is:

$$\begin{vmatrix} E_1^0 - \Delta E & W \\ W & E_2^0 - \Delta E \end{vmatrix} = 0 \tag{2.45}$$

with

$$\begin{gathered} \left\langle 1 \middle| H^{(0)} \middle| 1 \right\rangle = E_1^0 \qquad\qquad \left\langle 2 \middle| H^{(0)} \middle| 2 \right\rangle = E_2^0 \\ \left\langle 1 \middle| H^{(i)} \middle| 2 \right\rangle = \left\langle 2 \middle| H^{(i)} \middle| 1 \right\rangle = W_{12} = W_{21} = W \end{gathered} \tag{2.46}$$

1,2 being the unperturbed eigenfunctions, E_1^0, E_2^0 the unperturbed energies of the two states, ΔE their energy separation induced by the perturbation and W is the interaction containing the coupling constant between the two levels. The energy difference between the unperturbed and the perturbed state is obtained from the solution of the secular determinant:

$$\Delta E = \left\langle E^* \right\rangle \pm \frac{\left[\left(\delta^0 \right)^2 + 4W^2 \right]^{1/2}}{2} \tag{2.47}$$

where

$\left\langle E^* \right\rangle = \frac{1}{2}\left(E_1^* + E_2^*\right)$ is the barycentre of the perturbed or unperturbed levels

$\delta^0 = E_1^0 - E_2^0$ is the energy difference between the two unperturbed levels.

This interaction occurs only between two levels having identical rotational wavefunction, i.e. identical rotational quantum numbers and identical symmetry species [1–3, 21]. In fact, as the *H* operator is totally symmetric with respect to every symmetry operation undergone by the molecule, the unperturbed eigenfunctions ψ_1^0 and ψ_2^0 must have the right symmetry to make the elements W_{12} of the matrix

$$W_{12} = \int \psi_1^0 \hat{H} \psi_2^{*0} d\tau \tag{2.48}$$

different from zero, i.e. their direct product must contain the totally symmetric representation.

The vibrational eigenfunctions of the two interacting states are linear combinations of the two unperturbed eigenfunctions:

$$\begin{aligned} \psi_1 &= a\psi_1^0 - b\psi_2^0 \\ \psi_2 &= b\psi_1^0 + a\psi_2^0 \end{aligned} \tag{2.49}$$

with $a^2 + b^2 = 1$.

As illustrated in Fig. 2.6, the smaller the energy difference between the two unperturbed levels, the larger the observed energy shifts from the expected values.

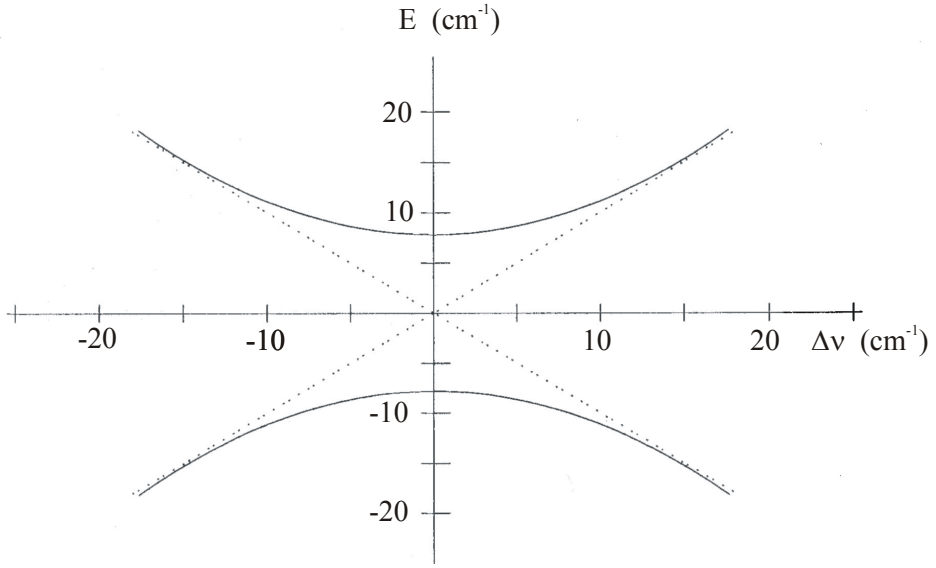

Figure 2.6 : Anharmonic resonance scheme. Dashed lines represent unperturbed (ψ_m^0 *e* ψ_n^0); continuous lines represent real functions.

2.3.2 Coriolis interactions

The second order Coriolis interaction is a rovibrational interaction occurring between two vibrational levels of different symmetry. It is caused by terms of the rotation vibration kinetic energy operator H_{rv} that depend linearly on both a rotational angular momentum operator and a vibrational angular momentum operator [21]. This interaction can be foreseen by using Jahn rule [22]: a Coriolis interaction can occur between two levels A and B if the product of their symmetry species leads to an irreducible representation containing the species of a rotation around the axis x, y or z:

$$\Gamma_A \otimes \Gamma_B \supset R_x, R_y \text{ or } R_z \tag{2.50}$$

Similarly to Fermi resonances, when two vibrational states are perturbed by a Coriolis interaction, near the point of intersection of the term curves a shift of the energy levels from the unperturbed positions is observed, that is, a rotational perturbation results. The Coriolis interaction matrix elements vanish when the rotational quantum numbers are zero, so that the band origin positions are not changed by this effect. Furthermore, since the Coriolis interaction increases with increasing J, the shift from the unperturbed position does not go back to zero for large J, even thought the energy difference between levels of the same J is then fairly large [1].

2.4 SELECTION RULES AND TRANSITIONS

In the process of absorption or emission of radiation involving transitions between a pair of vibrational states, usually the molecule interacts with the electric, rather than the magnetic component of the electromagnetic radiation. For this reason, the active selection rules are known as electric dipole selection rules or, simply, dipole selection rules [2]. These rules are based on symmetry criteria and vibrational transitions are observable only when they induce a variation of the dipole moment of the molecule. The equation of the transition moment is:

$$R = \int \psi' \mu \psi^{*"} d\tau \neq 0 \tag{2.51}$$

where ψ' and $\psi"$ are the vibrational functions of the states involved in the transition and μ is the electric dipole moment operator

$$\mu = \mu_e + \left(\frac{d\mu}{d\tau}\right)_e \tau + \frac{1}{2!}\left(\frac{\partial^2 \mu}{\partial \tau^2}\right)_e \tau^2 + ... \tag{2.52}$$

The intensity of the transition is proportional to the square of the magnitude of the transition moment $|R|^2$. The requirement for the Eq. (2.51) to be satisfied, and for the transition to be allowed, is that the symmetry of the quantity to be integrated is totally symmetric (Σ^+ for a linear molecule, *A* for a symmetric top)

$$\Gamma\left(\Psi_{\upsilon}^{'}\right)\otimes\Gamma\left(\mu\right)\otimes\Gamma\left(\Psi_{\upsilon}^{''}\right)\subset A \tag{2.53}$$

(*A* is used to denote the totally symmetric group of any point group).

In addition, only transitions with $\Delta\upsilon = \pm 1$ are allowed. This condition is obtained from the harmonic approximation, by breaking off of the Eq. (2.52) at the second term. By adding higher order terms this rule falls down, and transitions involving $\Delta\upsilon = \pm 2, \pm 3, \ldots$ (overtones) are allowed, even if the intensity decreases with increasing $\Delta\upsilon$ [2].

The transitions are classified depending on the direction of the variation of the transition moment during the vibration: if it is parallel to the principal axis of symmetry the transition is parallel, if perpendicular to it the transition is called perpendicular.

2.4.1 Linear molecules

Linear molecules belong either to the $D_{\infty h}$ or $C_{\infty v}$ point group, depending on whether they do or do not have a centre of inversion. Adapting Eq. (2.53), the vibrational transitions are allowed if

$$\Gamma\left(\psi'\right)\otimes\Gamma\left(\mu\right)\otimes\Gamma\left(\psi''\right)\supseteq\Sigma_u^+ \text{ or } \Pi_u \text{ for } D_{\infty h} \tag{2.54}$$

$$\Gamma\left(\psi'\right)\otimes\Gamma\left(\mu\right)\otimes\Gamma\left(\psi''\right)\supseteq\Sigma^+ \text{or } \Pi \text{ for } C_{\infty v} \tag{2.55}$$

From the point of view of the parity of rotational eigenfunctions, the only allowed transitions are those for which $+\leftrightarrow-$.

Combining these results, the selection rules reported in Table 2.2 are obtained, as a function of quantum numbers *J* and ℓ.

Table 2.2: Selection rules for transitions in linear molecules

PARALLEL BANDS: $\Delta\ell = 0$	
$\Sigma \leftrightarrow \Sigma$	$\Delta J = \pm 1$
$\Pi \leftrightarrow \Pi$, $\Delta \leftrightarrow \Delta$	$\Delta J = 0,\ \pm 1$

PERPENDICULAR BANDS: $\Delta\ell = \pm 1$	
$\Sigma \leftrightarrow \Pi$, $\Pi \leftrightarrow \Delta$, $\Delta \leftrightarrow \Phi$	$\Delta J = 0,\ \pm 1$

It must be pointed out that in case of parallel transitions ($\Delta\ell = 0$), the spectral lines corresponding to transitions with $\Delta J = 0$ have low intensity and can be observed only for low J values.

In addition, the mixing of the eigenfunctions of two or more perturbed states can lead to the observation of "perturbation allowed" transitions according to the rules mentioned above, as for example transitions $\Sigma \leftrightarrow \Delta$.

Another restriction follows from Eq. (2.53), for centrosymmetric molecules: only transitions $g \leftrightarrow u$ are allowed.

As a consequence of the convention for the parity of the levels explained in Section 2.1.3, the following selection rules in terms of "e, f" are obtained:

$e \leftrightarrow f$	$\Delta J = 0$	Q branches
$e \leftrightarrow e$, $f \leftrightarrow f$	$\Delta J = \pm 1$	P, R branches

To predict the intensity of rovibrational lines, it is important to consider the symmetry of the molecule. If the molecule belongs to the point group $C_{\infty v}$, the statistical weight of a rotational level in a totally symmetric electronic state is given by the number of possible orientations of J in a magnetic field, that is $2J+1$. The intensity of the lines is governed principally by Boltzmann factors. On the other hand, if the molecule belongs to the point group $D_{\infty h}$, the rotational eigenfunctions change sign with respect to the exchange of identical particles (nuclei). In fact the total eigenfunction is:

$$\psi = \psi_e \psi_v \psi_r \psi_{ns} \tag{2.56}$$

where ψ_e, ψ_v, ψ_r and ψ_{ns} are the electronic, vibrational, rotational and the nuclear spin eigenfunctions. If ψ_e and ψ_v are totalsymmetric, the sign of the total eigenfunction when all nuclei on one side of the centre are simultaneously exchanged with the corresponding ones on the other side depends on the behaviour of ψ_r and ψ_{ns}. $\psi_r\, \psi_{ns}$ can change or maintain unaltered

its sign, and correspondingly the rotational levels are symmetric or antisymmetric with respect to the exchange of identical nuclei. The eigenfunctions have different statistical weights, depending on ψ_{ns} and on the type of statistic they follow. If the molecule has an even number of fermions (half integer spin) on one side of the centre of symmetry it is subjected to the Bose – Einstein statistics, as it behaves as a boson (integer spin). Vice versa if the number of fermions is odd the Fermi – Dirac statistic is followed. The nuclear spin is half integer for nuclei with an odd mass number, integer for nuclei with even mass number and odd charge number, and it is zero for nuclei with even mass number and charge number. This is summarized in Table 2.3:

Table 2.3: Assignment of nuclear spin quantum number to the nuclei as a function of their mass and charge number

I	Mass Number	Charge number
0	Even	Even
$\frac{1}{2}$	Odd	Odd
1	Even	Odd

If the spin of all the nuclei is zero, with the possible exception of the one at the centre of symmetry, the antisymmetric rotational levels are missing entirely, that is, for Σ_g^+ electronic states the odd rotational levels are absent, assuming Bose – Einstein statistic for nuclei of spin zero [1].

In the other cases the ratio of statistical weights of the symmetric and antisymmetric rotational levels is $\frac{I+1}{I}$ or $\frac{I}{I+1}$, depending on whether the nuclei follow the Bose – Einstein or Fermi – Dirac statistic, respectively.

For $^{12}C_2H_2$ the total eigenfunction follows Fermi – Dirac statistic as the nuclear spin quantum number is half integer $\left[I(\mathrm{H}) = 1/2, I(^{12}\mathrm{C}) = 0 \right]$. This leads to an intensity alternation of 1:3 for even and odd J values respectively, as the antisymmetric rotational levels have three times the statistical weight of the symmetric ones. For $^{12}C_2D_2$ Bose – Einstein statistic is followed, as $\left[I(\mathrm{D}) = 1, I(^{12}\mathrm{C}) = 0 \right]$. In this case the intensity alternation is 6:3.

As a consequence the infrared bands have the following characteristics:

- $\Sigma \leftrightarrow \Sigma$ parallel bands → they have two branches, *R* and *P*, with single rovibrational lines with $\Delta J = +1$ and $\Delta J = -1$, respectively. Transition can be $\Sigma^+ \leftrightarrow \Sigma^+$ $(e \leftrightarrow e)$ or $\Sigma^- \leftrightarrow \Sigma^-$ $(f \leftrightarrow f)$, while $\Sigma^+ \leftrightarrow \Sigma^-$ $(e \leftrightarrow f)$ are forbidden (see Figure 2.7 (a)).

- $\Pi \leftrightarrow \Pi$, $\Delta \leftrightarrow \Delta$, $\Phi \leftrightarrow \Phi$ parallel bands → they have three branches, *R* ($\Delta J = +1$), *P* ($\Delta J = -1$) and *Q* ($\Delta J = 0$), and double rovibrational lines. *Q* branches are doublets of $(e \leftrightarrow f)$ type, while *P* and *R* are doublets of $(e \leftrightarrow e)$ and $(f \leftrightarrow f)$ type. In absence of strong perturbations, the *Q* transitions are much weaker than the *P* and the *R* (see Figure 2.7 (b)). It is important to underline that for Π states *J* = 0 levels do not exist, as well as for Δ, Φ, ... states the lowest value for *J* are 2, 3, ... respectively, because $J \geq \ell$.

- $\Sigma \leftrightarrow \Pi$ perpendicular bands → they present three branches: *R* ($\Delta J = +1$), *P* ($\Delta J = -1$) and *Q* ($\Delta J = 0$) of single rovibrational lines. They can be:
    - $\Pi \leftrightarrow \Sigma^-$ → *Q* $(e \leftrightarrow f)$ type, *P* and *R* $(f \leftrightarrow f)$ type
    - $\Pi \leftrightarrow \Sigma^+$ → *Q* $(f \leftrightarrow e)$ type, *P* and *R* $(e \leftrightarrow e)$ type (Figure 2.7 (c))

- $\Pi \leftrightarrow \Delta$, $\Delta \leftrightarrow \Phi$ perpendicular bands → they have three branches *R* ($\Delta J = +1$), *P* ($\Delta J = -1$) and *Q* ($\Delta J = 0$) formed by doublets of rovibrational lines. *Q* are $(e \leftrightarrow f)$ type, *P* and *R* are $(e \leftrightarrow e)$ and $(f \leftrightarrow f)$ type (Figure 2.7 (d)). In this case the *Q* lines are slightly more intense than the *P* and *R* ones. In addition, transition of $\Delta \leftrightarrow \Sigma$ type, which are forbidden by the selection rules, can be observed as a consequence of the mixing of the eigenfunctions of the excited levels which are affected by a rovibrational interaction.

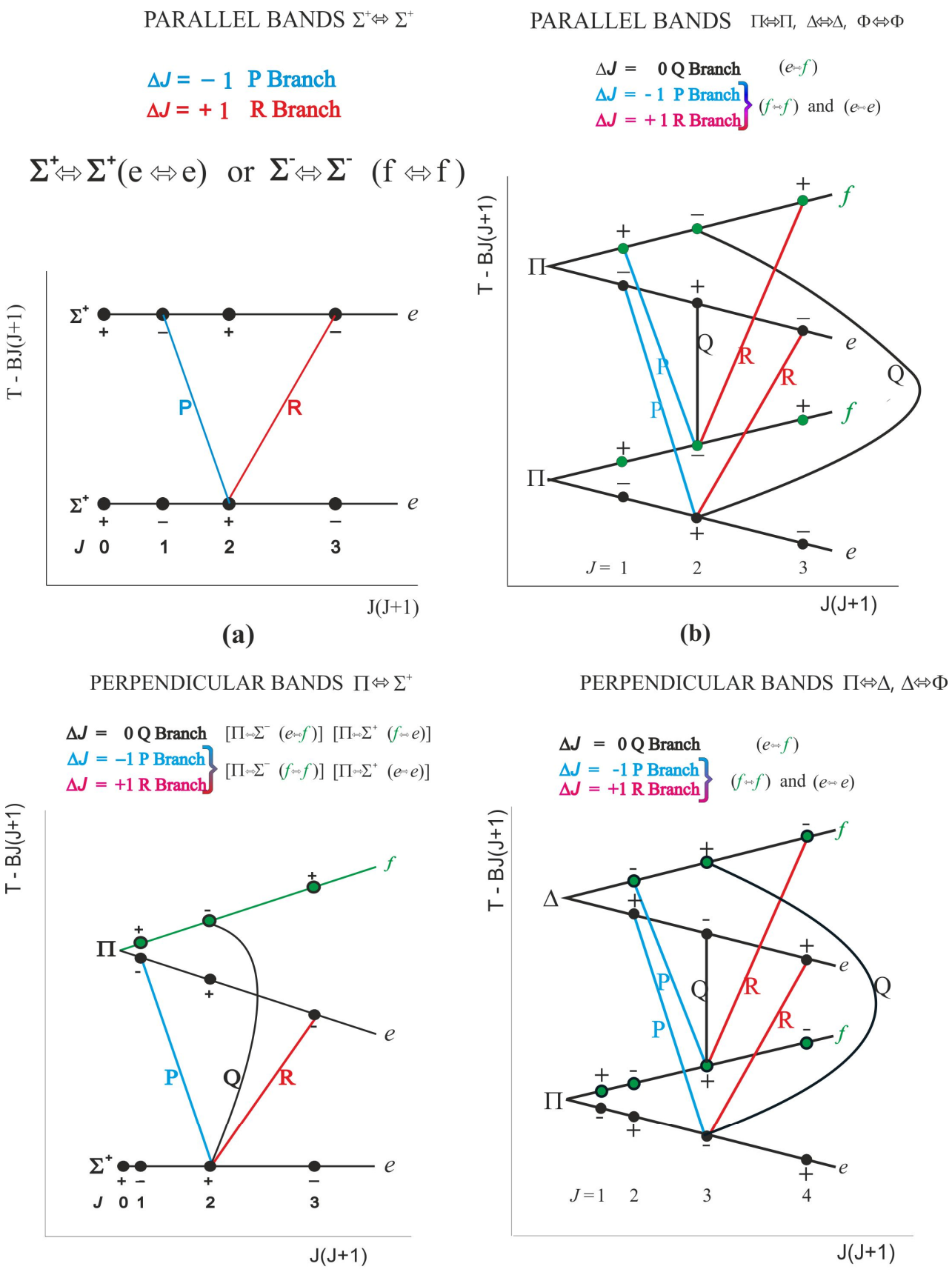

Figure 2.7: Selection rules for transitions of linear molecules; (a) Σ–Σ parallel band, (b) Π–Π or Δ–Δ parallel band, (c) Π–Σ perpendicular band, (d) Π–Δ or Δ–Φ perpendicular band.

2.4.2 Symmetric top molecules

The selection rules for rovibrational transitions of a symmetric top are reported in Table 2.4.

Table 2.4: Selection rules for a symmetric top

Parallel Bands: $\left\langle \upsilon' \middle\| \mu_z \middle\| \upsilon'' \right\rangle \neq 0,\ \Gamma(\psi_{\upsilon'}) \otimes \Gamma(\psi_{\upsilon''}) \supset \Gamma(\mu_z)$	
Vibrational selection rule: $\psi_{\upsilon'} \leftarrow \psi_{\upsilon''}$ A←A $E_s(\pm\ell) \leftarrow E_s(\pm\ell)$	Rotational selection rule: $K = 0;\ \Delta K = 0,\ \Delta J = \pm 1$ $K \neq 0;\ \Delta K = 0,\ \Delta J = 0, \pm 1$
Perpendicular Bands: $\left\langle \upsilon' \middle\| \mu_{xy} \middle\| \upsilon'' \right\rangle \neq 0,\ \Gamma(\psi_{\upsilon'}) \otimes \Gamma(\psi_{\upsilon''}) \supset \Gamma(\mu_{xy})$	
Vibrational selection rule: $\psi_{\upsilon'} \leftarrow \psi_{\upsilon''}$ $E(\pm\ell) \leftarrow A$ $E_s(\pm\ell) \leftarrow E_s(\pm\ell)$	Rotational selection rule: $\Delta K = \pm 1,\ \Delta J = 0, \pm 1$

The rovibrational transitions are usually labelled with the values of J and K of the lower energy state and the ΔJ and ΔK of the transitions. This notation is ${}^{\Delta K}\Delta J_{J''}(K'')$ to identify a parallel transition, ${}^{\Delta K}\Delta J_{K''}(J'')$ for a perpendicular transition, and the nomenclature is reported in Table 2.5.

Table 2.5: Selection rules in J and K for rovibrational transitions of a C_{3v} molecule

PARALLEL BAND		
$\Delta J = -1$	$\Delta K = 0$	${}^{q}P_{J''}(K'')$
$\Delta J = 0$	$\Delta K = 0,\ K \neq 0$	${}^{q}Q_{J''}(K'')$
$\Delta J = +1$	$\Delta K = 0$	${}^{q}R_{J''}(K'')$
PERPENDICULAR BAND		
$\Delta J = -1$	$\Delta K = -1$	${}^{p}P_{k''}(J'')$
$\Delta J = -1$	$\Delta K = +1$	${}^{r}P_{K''}(J'')$
$\Delta J = 0$	$\Delta K = -1$	${}^{p}Q_{K''}(J'')$
$\Delta J = 0$	$\Delta K = +1$	${}^{r}Q_{K''}(J'')$
$\Delta J = +1$	$\Delta K = -1$	${}^{p}R_{K''}(J'')$
$\Delta J = +1$	$\Delta K = +1$	${}^{r}R_{K''}(J'')$

As explained in Section 2.4.1 for linear molecules, the intensity of the lines is governed both by Boltzmann factors and by statistical weights. In fact, the levels with $K = 3n$ (n = 0, 1, 2, 3,…) have a larger statistical weight than those with $K = 3n \pm 1$, resulting an alternation of the type: strong, weak, weak, strong, weak, weak, and so on. For molecules of the point group C_{3V}, the general case in which the spin of the three identical nuclei is I, the weight factors due to the spin are:

$$\text{For } K = 3n \qquad \frac{1}{3}(2I+1)\left(4I^2+4I+3\right) \tag{2.57}$$

$$\text{For } K = 3n\pm 1 \qquad \frac{1}{3}(2I+1)\left(4I^2+4I\right) \tag{2.58}$$

The shape of parallel and perpendicular bands are reported in Figs. 2.8 and 2.9, respectively. In parallel bands only levels with the same K value are connected by transitions. So for each K value, a sub–band made of three branches P, Q and R is obtained. The band is obtained by the addition of many sub–bands, corresponding to the various K values populated at the temperature of observation, as shown in Fig. 2.8.

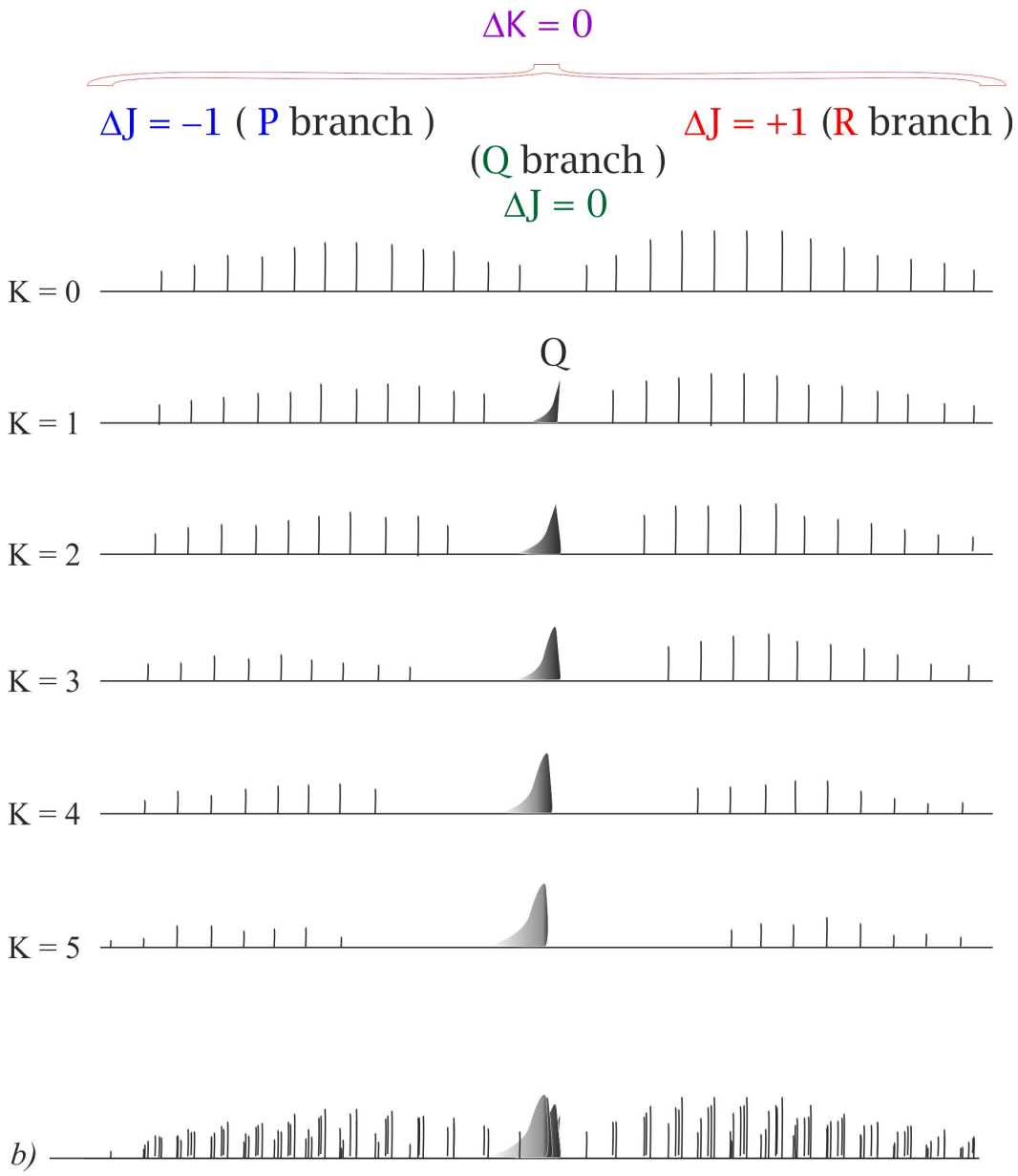

Figure 2.8: Structure of *K* sub–bands of a parallel band for a symmetric top. In *b*) the total structure of the parallel band is shown.

The overall shape of a parallel band is similar to that of a perpendicular band of a linear molecule, being characterized by sub–bands with a strong line–like *Q* branch and the *P* and *R* branches to lower and higher wavenumbers, respectively. For what concerns intensity, as discussed before in Section 2.2.2 and above, the sub–bands with $K = 3n$ (with $n = 1, 2, 3,\ldots$) are stronger than the others.

A perpendicular band consists of two series of sub–bands with $\Delta K = \pm 1$ for each *K"* value $\neq 0$. The intensity of the *Q* branch in a sub–band is about the sum of the intensity of the *P* and *R* branches, therefore the series of lines formed by the *Q* branches in the sub–bands form the

most prominent feature of a perpendicular band. Usually, when $\Delta J = \Delta K$ the branch is stronger than in the case $\Delta J \neq \Delta K$. This is shown in Fig. 2.9.

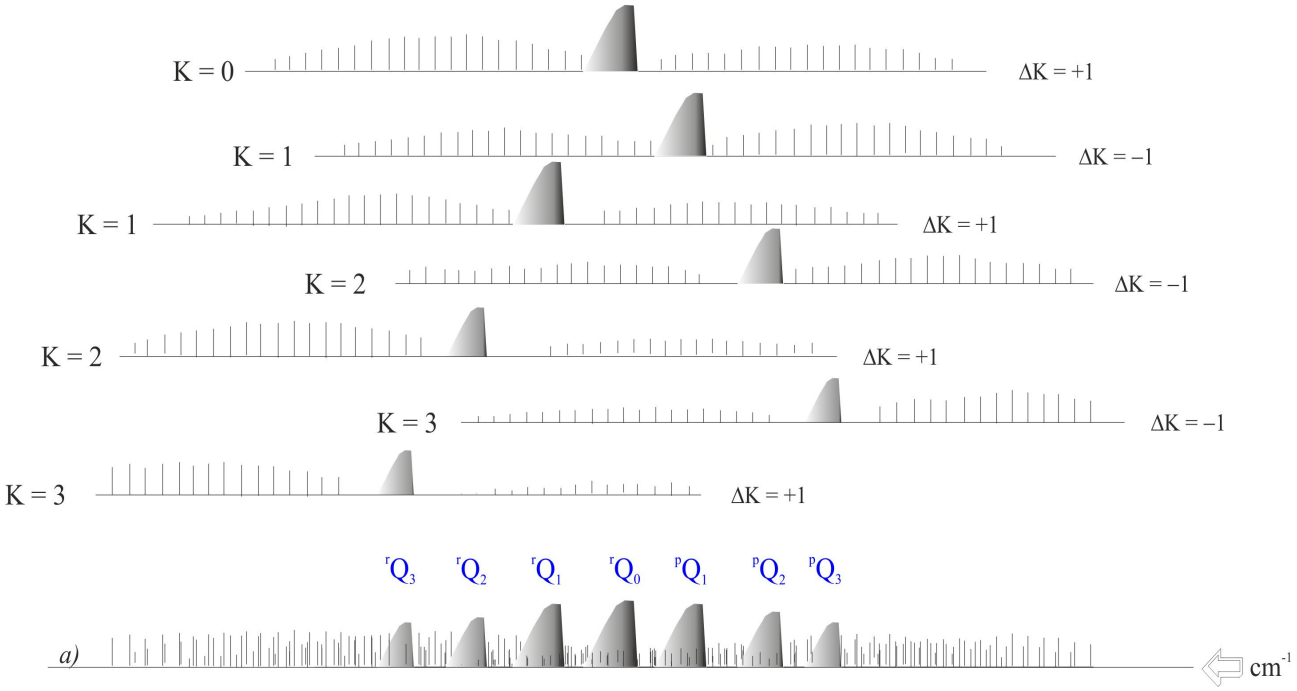

Figure 2.9: Structure of *K* sub–bands of a perpendicular band for a prolate symmetric top. In *a*) the total structure of the perpendicular band is shown.

References

[1] G.H. Herzberg, Molecular spectra and molecular structure, vol. II, Infrared and Raman spectra of polyatomic molecules, Kriekger publishing company, Malabar, 1991.

[2] J.M. Hollas, High Resolution Spectrocopy, John Wiley & Sons, Chichester, 1998.

[3] P.F. Bernath, Spectra of Atoms and Molecules, Oxford University Press, 1995.

[4] M. Herman, J. Liévin, J.V. Auwera and A. Campargue, Advances in Chemical Physics vol. **108**, John Wiley & Sons, New York, 1999.

[5] L. Pauling and E.B. Wilson Jr., Introduction to Quantum Mechanics, Mc Graw−Hill Book Co., New York, 1935.

[6] G. Amat and H.H. Nielsen, *J. Mol. Spectrosc.* **2**, 152 (1958).

[7] J. Pliva, *J. Mol. Spectrosc.* **44**, 165 (1972).

[8] J.K. Watson, *J. Mol. Spectrosc.* **101**, 83 (1983).

[9] M. Winnewisser and B.P. Winnewisser, *J. Mol. Spectrosc.* **41**, 143 (1972).

[10] K.M.T. Yamada, F.V. Briss and M.R. Aliev, *J. Mol. Spectrosc.* **112**, 347 (1985).

[11] M. Herman, T. Huet, Y. Kabbadj and J.V. Auwera, *Mol. Phys.* **72**, 75 (1991).

[12] J. Hientanen, *Mol. Phys.* **49**, 1029 (1983).

[13] G. Amat, H.H. Nielsen and G. Tarrago, Rotation−Vibration of Polyatomic Molecules, M. Dekkar, New, York, 1971.

[14] D. Papousek and M.R. Aliev, Molecular Vibrational−Rotational Spectra, Elsevier Sc.Pub.Cy., 1982.

[15] J. Hientanen and D.M. Dennison, *Phys Rev.* **57**, 128 (1940).

[16] S. Maes, *Cah. Phys*. **14**, 125, 164 (1960).

[17] N. Rao and C.W. Mathews, Molecular Spectroscopy: Modern Research, Academic Press, New York, 1972.

[18] D.M. Dennison, *Rev. Mod. Phys.* **3**, 280 (1930).

[19] R.S. Mulliken, *Phys Rev.* **59**, 873 (1941).

[20] G. Graner, *J. Mol. Spectrosc.* **161**, 58 (1993).

[21] J.T. Hougen, Physical Chemistry An Advanced Treatise, volume IV/Molecular properties, chapter 7, edited by Douglas Henderson, Academic Press, New York, 1970.

[22] H.A. Jahn, *Phys. Rev.* **56**, 680 (1939).

PART II

EXPERIMENT

&

ANALYSIS

CHAPTER 3

ANALYSIS OF LINEAR MOLECULES

Acetylene is one of the most studied molecules, both theoretically and experimentally, since it represents the simplest model of linear tetratomic species. The spectroscopic studies on this molecule have a great importance in the fields of molecular dynamics, astrophysics, quantum – theoretical calculations and molecular spectroscopy. It has been identified in the terrestrial [1] and planetary [2] atmospheres and in the interstellar medium [3]. Diacetylene too is of great interest, as it plays, with acetylene, a major role in the synthesis of complex interstellar molecules. Nowadays, the study of isotopically substituted species has attracted the attention of both spectroscopists and astrophysicists. In particular, the deuterated molecules can provide information on the H/D ratio in various regions of the interstellar medium and in planetary atmospheres. That is why a very detailed study of some acetylene isotopologues has been carried out.

The overview of the normal modes of vibration of acetylene is shown in Fig. 3.1, together with their symmetry for both the $C_{\infty v}$ or $D_{\infty h}$ isotopologues.

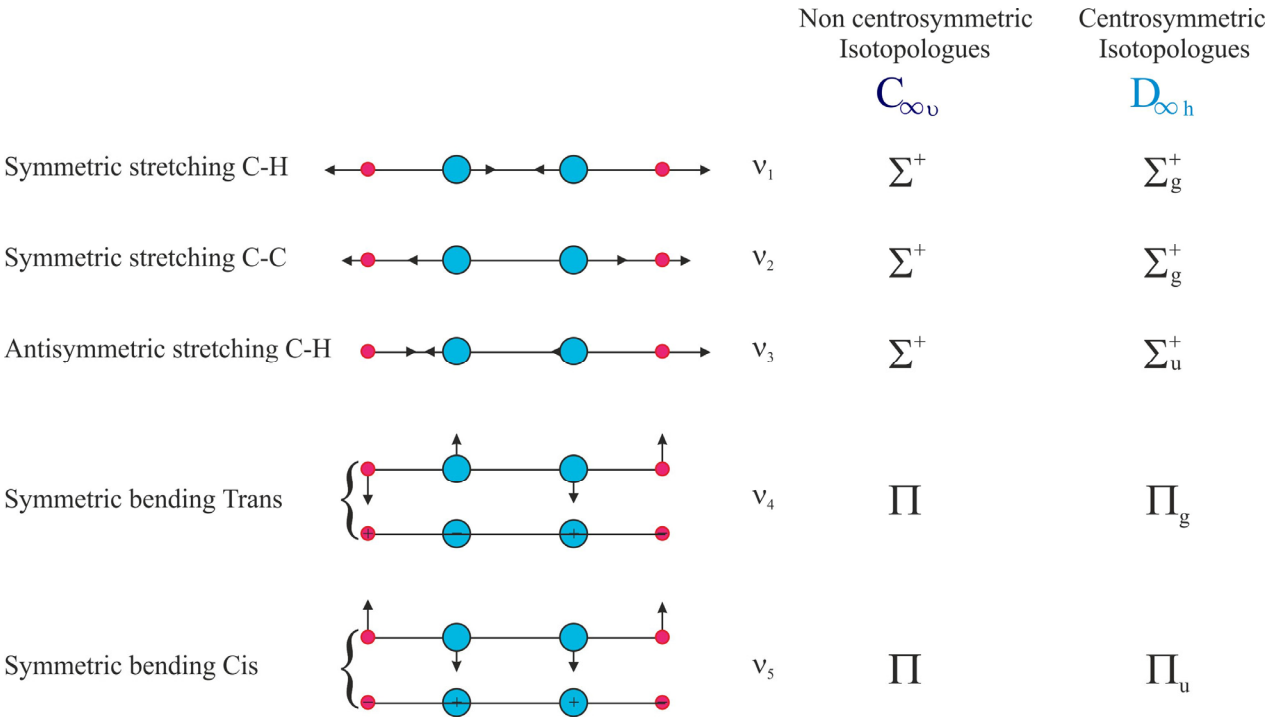

Figure 3.1: Normal modes of vibration of acetylene

3.1 $^{12}C_2D_2$

The ground electronic state of the perdeuterated acetylene, $^{12}C_2D_2$, has been extensively investigated by infrared (IR) and Raman spectroscopy [4–19]. However, few studies of the spectrum below 5000 cm^{-1} were reported more than forty years ago [8,9,11,16]. The most recent investigations have been published by Bermejo *et al*. [17], concerning the stimulated Raman spectrum of the ν_2 stretching fundamental and associated bending modes, by Yu *et al*. [18] on a re–analysis of the bending modes based on spectra recorded in the THz region, and by Weirauch *et al*. [19] on the analysis of the bands in the 10000 – 12500 cm^{-1} range. For this reason an intensive and systematic analysis of the stretching modes has been accomplished from 900 to 5500 cm^{-1}, taking into account their associated first overtones, combinations and hot bands involving bending modes. The wavenumbers of the normal modes of $^{12}C_2D_2$ are reported in Table 3.1. As this molecule has a centre of symmetry, it belongs to the $D_{\infty h}$ point group.

Table 3.1: Normal modes of $^{12}C_2D_2$

Band	Symmetry	Band centre (cm^{-1})
ν_1	Σ_g^+	2705.22201
ν_2	Σ_g^+	1764.80624
ν_3	Σ_u^+	2439.24673
ν_4	Π_g	510.68219
ν_5	Π_u	537.78665

3.1.1 Experiment

The spectra were recorded in Bologna, between 900 and 5500 cm^{-1}, using a Bomen DA3.002 Fourier transform (FT) spectrometer. In the region 900 – 2400 cm^{-1}, a Globar source, a KBr beam splitter and a high sensitivity HgCdTe detector operating at liquid nitrogen temperature were used. In the interval 2400 – 5500 cm^{-1}, the same source and beam splitter were used, whereas the detector was an InSb type. In both ranges, optical path from 0.18 to 10 m were adopted. The achieved resolution ranged from 0.004 to 0.009 cm^{-1}. $^{12}C_2D_2$ was purchased from Cambridge Isotope Labs, with a purity of 99%. Different pressure conditions, from 26.6 Pa to 1333.2 Pa, were used for recording the spectra. An overview about the general conditions for each recording are reported in Table 3.2. Rovibration transitions of H_2O [20,21], CO_2 [22] and

OCS [23], which was added in the sample cell, were used to calibrate the spectra. The calibration of the region 3800 – 5000 cm^{-1} was performed by adding a small amount of N_2O to the sample [24]. Particular care was devoted to the calibration of the spectra since consistent results had to be obtained from the analysis of different bands reaching the same excited state, which were observed in different spectral regions.

Table 3.2: Experimental conditions for the recording of $^{12}C_2D_2$ spectra

Spectrum	Pressure of the sample (Pa)	Range (cm^{-1})	Source	Detector	Resolution (cm^{-1})	#Scans	Optical pathlength (m)
a	26.6	900 – 1800	Globar	MCT*	0.004	220	0.18
b	266.6	900 – 2300	Globar	MCT*	0.006	300	9
c	29.0	2300 – 3900	Globar	InSb	0.006	800	0.18
d	266.6	2300 – 3900	Globar	InSb	0.006	800	10
e	1333.2	3800 – 4800	Globar	InSb	0.009	800	10
f	1333.2	3800 – 5000	Globar	InSb	0.009	850	10
g	1333.2	4500 – 5600	Globar	InSb	0.009	1400	10
h	66.6	4900 – 5500	Globar	InSb	0.009	500	10
i	133.3	4900 – 5500	Globar	InSb	0.009	500	10
l	266.6	4900 – 5500	Globar	InSb	0.009	500	10

* MCT is a HgCdTe detector

The estimated wavenumber accuracy and the precision of the measured transitions range between 0.0002 and 0.0006 cm^{-1}, depending on the signal–to–noise ratio and on the Doppler width of the lines. This can be calculated according to the following equation:

$$\Delta\nu = 7.162\times10^{-7}\times\nu_0\sqrt{\frac{T}{M}} \qquad (3.1)$$

where T is the temperature in Kelvin and M the molecular mass in atomic units. It may be noted that the Doppler broadening is proportional to the wavenumber (ν_0).

3.1.2 Description of the spectra

In the region from 900 to 5500 cm^{-1} of the $^{12}C_2D_2$ vibrational spectrum, the most evident features are the fundamental bands of the stretching motions and their first overtone and combination bands. In total, 92 bands were assigned, 44 of which were newly observed. The 48 bands already present in the literature and recorded at medium resolution (see Table I of Ref. [15]) were measured anew at high resolution and the assignments were extended to higher *J* values.

a) The 900 – 2200 cm^{-1} region

This region contains the difference bands of the three stretching vibrations, namely $\nu_1 - \nu_5$ at 2167.43 cm^{-1}, $\nu_2 - \nu_5$ at 1227.02 cm^{-1}, $\nu_3 - \nu_4$ at 1928.56 cm^{-1}, and associated bands involving the bending modes. A difference band is a transition with $\Delta v = 1$ arising from an excited state. In the same region the Raman spectrum displays the very intense ν_2 band and all the related hot bands. Fig. 3.2 shows the $\nu_1 - \nu_5$ band and five accompanying hot bands of very low intensity with centres between 2151 and 2164 cm^{-1}. Some very weak bands with $\upsilon_{tot} = \upsilon_4 + \upsilon_5 = 3$ or 4 of the pure bending excited states were also identified.

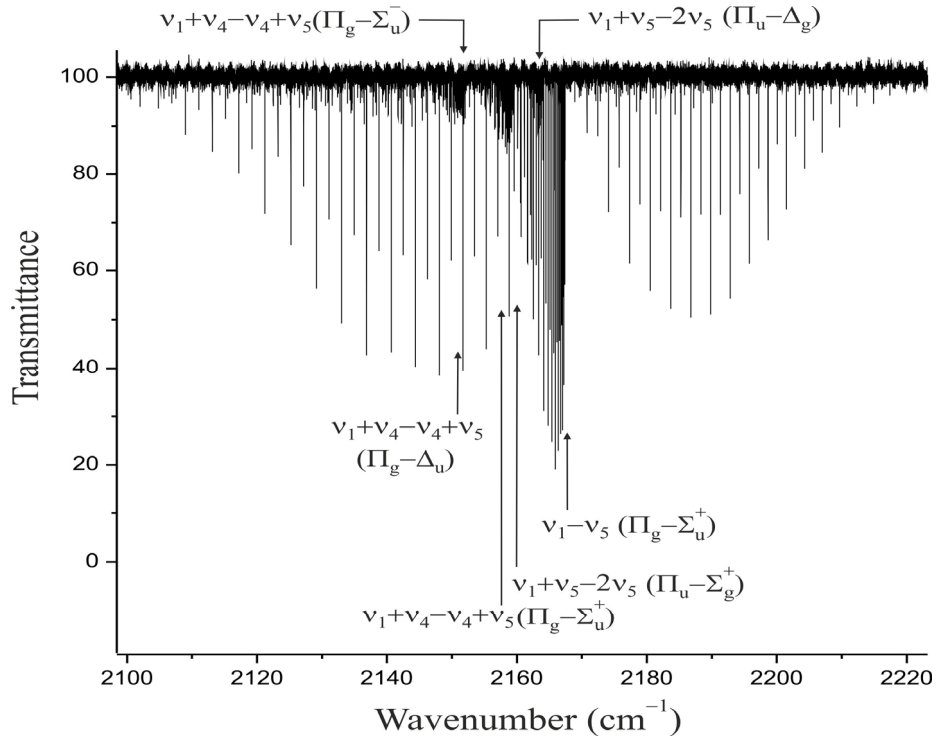

Figure 3.2: Portion of the infrared spectrum of $^{12}C_2D_2$ in the range 2100 – 2200 cm^{-1} showing the difference band $\nu_1 - \nu_5$ and associated hot bands. Experimental conditions are those of spectrum *d* in Table 3.2.

b) The 2200 – 2700 cm^{-1} region

This region of the spectrum is dominated by the most intense band, $\nu_3 \leftarrow$ GS at 2439.25 cm^{-1}. A large number of hot bands can be observed in the same region, namely $\nu_3 + \nu_4 \leftarrow \nu_4$, $\nu_3 + \nu_5 \leftarrow \nu_5$ and all the bands of the kind $\nu_3 + [(\nu_4 + \nu_5) = 2] \leftarrow [(\nu_4 + \nu_5) = 2]$, where the two states in parenthesis are identical. A few bands having very low intensity with $(\nu_4 + \nu_5) = 4$ excited states can also be identified but they were not taken into consideration. Figure 3.3 shows the ν_3 band recorded at low pressure and short path length.

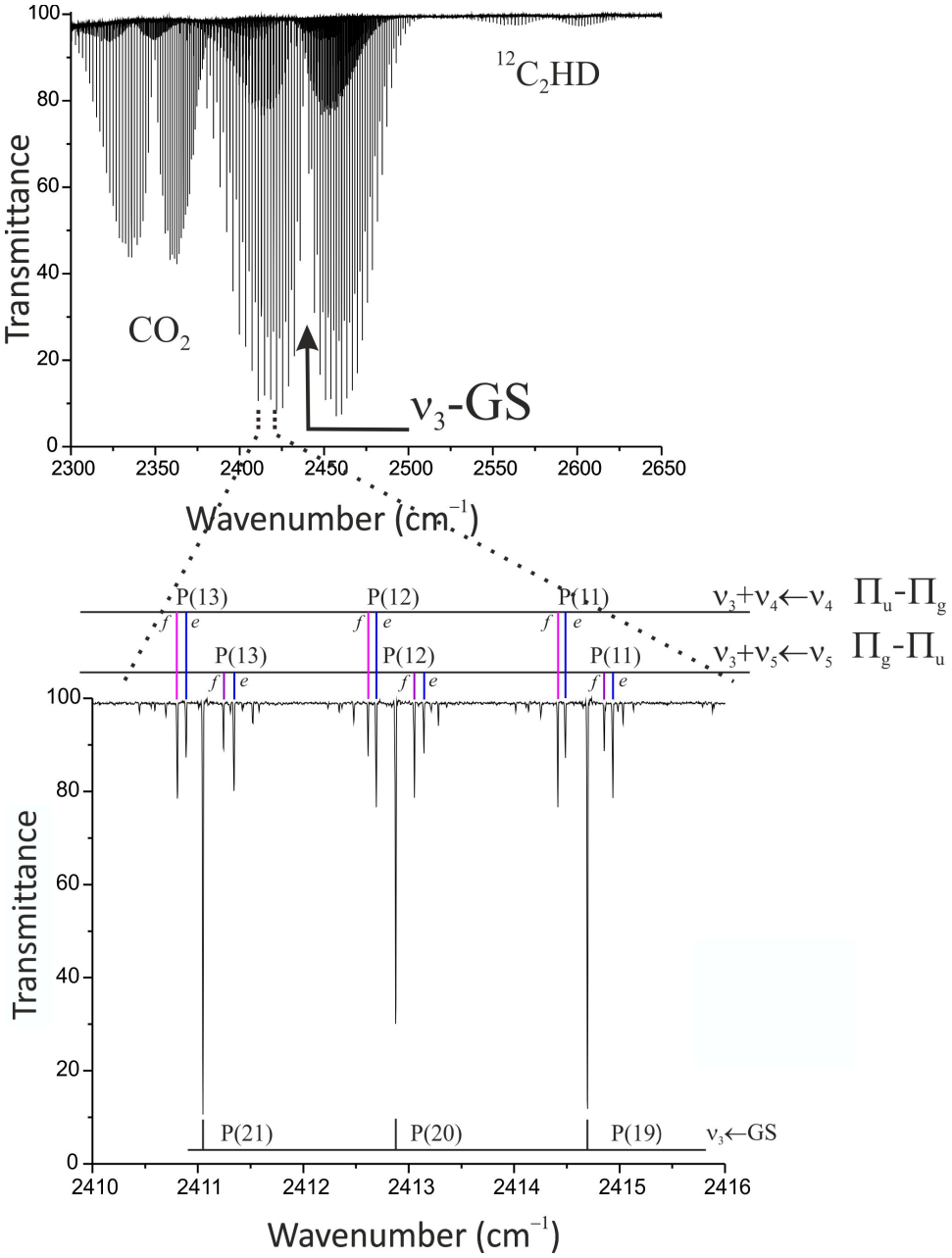

Figure 3.3: Portion of the infrared spectrum of $^{12}C_2D_2$ in the range 2300 – 2650 cm^{-1} showing the ν_3 parallel band, with a detail of the hot bands structures. Experimental conditions are those of spectrum *c* in Table 3.2.

c) The 2700 – 3500 cm^{-1} region

Two bands of medium–low intensity are present in this region of the spectrum: $\nu_3 + \nu_4 \leftarrow$ GS at 2944.32 cm^{-1} and $\nu_1 + \nu_5 \leftarrow$ GS at 3234.78 cm^{-1}. Each band is accompanied by few hot bands from both ν_4 and ν_5. The $\nu_1 + \nu_5$ (Π_u) state can also be characterised by means of the weak $(\Pi_u - \Pi_g)$ band from ν_4 (Π_g) at 2724.10 cm^{-1}. In the $\nu_1 + \nu_4 + \nu_5(\Delta_u) \leftarrow \nu_4(\Pi_g)$ band only the $P_{f\text{-}f}$, $R_{f\text{-}f}$, and $Q_{f\text{-}e}$ branches have been identified. Doublets absorptions were expected, but no transitions involving the *e* levels of the Δ_u state were observed. Probably, this is due to a strong ℓ–type interaction between the *f* levels of the Σ_u^- and Δ_u states of the $\nu_1 + \nu_4 + \nu_5$ manifold which allows an intensity borrowing from the $\Sigma_u^- - \Pi_g$ to the $\Delta_u - \Pi_g$ band (in both cases the Π_g state is ν_4). Other very weak bands are present in this region, namely $\nu_2 + \nu_4 + \nu_5 \leftarrow$ GS $(\Sigma_u^+ - \Sigma_g^+)$, at 2803.96 cm^{-1}, $\nu_3 + 2\nu_4 \leftarrow$ GS $(\Sigma_u^+ - \Sigma_g^+)$ and $(\Delta_u - \Sigma_g^+)$ at 3452.73 and 3452.20 cm^{-1}, respectively, and $\nu_3 + 2\nu_5 \leftarrow$ GS $(\Sigma_u^+ - \Sigma_g^+)$ at 3499.87 cm^{-1}. In Figure 3.4 an overview of the spectral region between 3205 and 3235 cm^{-1} is shown, where the *Q* branches of the combination band $\nu_1 + \nu_5$ and associated hot bands are identified.

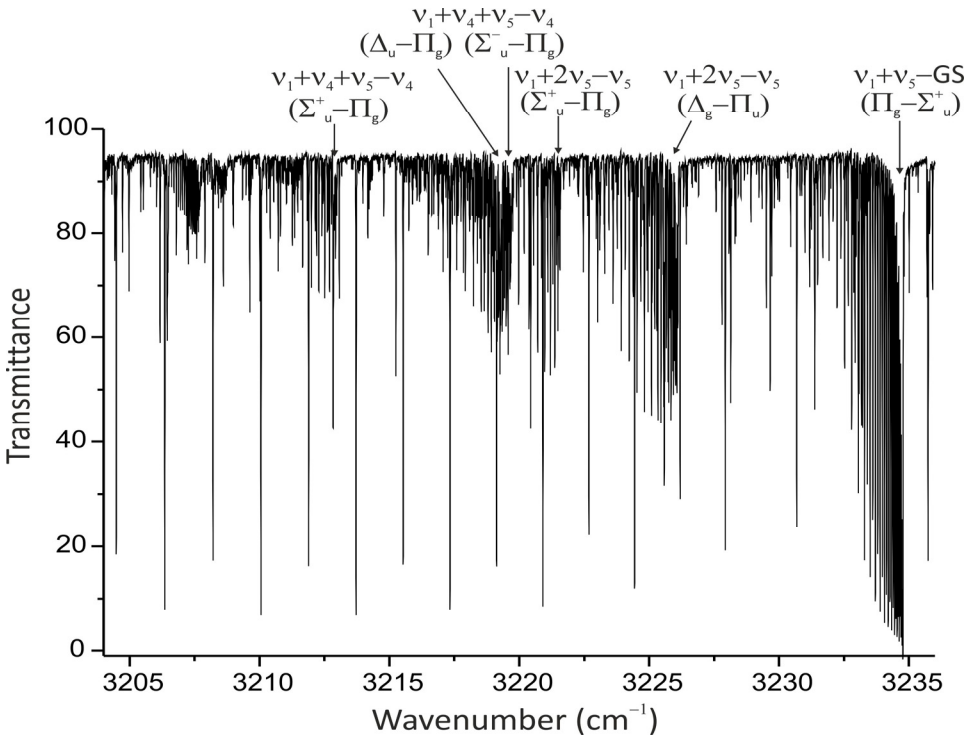

Figure 3.4: Portion of the infrared spectrum of $^{12}C_2D_2$ showing the *Q* branches of the $\nu_1 + \nu_5$ band and associated hot bands. Experimental conditions are those of spectrum *d* in Table 3.2.

d) The 3500 – 5500 cm^{-1} region

Two bands are prominent in this region of the spectrum: the medium–weak $\nu_2 + \nu_3 \leftarrow$ GS ($\Sigma_u^+ - \Sigma_g^+$) at 4190.64 cm^{-1} and the medium–strong $\nu_1 + \nu_3 \leftarrow$ GS ($\Sigma_u^+ - \Sigma_g^+$) at 5145.47 cm^{-1}. Both bands are associated with hot bands from ν_4 and ν_5. Two other rather weak bands are observed, namely $2\nu_3 \leftarrow \nu_5$ at 4311.40 cm^{-1} and $2\nu_1 \leftarrow \nu_5$ at 4848.40 cm^{-1}. The inclusion of these bands in the analysis allowed the determination of the x_{33} and x_{11} anharmonicity constants. Figure 3.5 shows the $\nu_2 + \nu_3$ parallel band with the associated hot bands from ν_4 and ν_5.

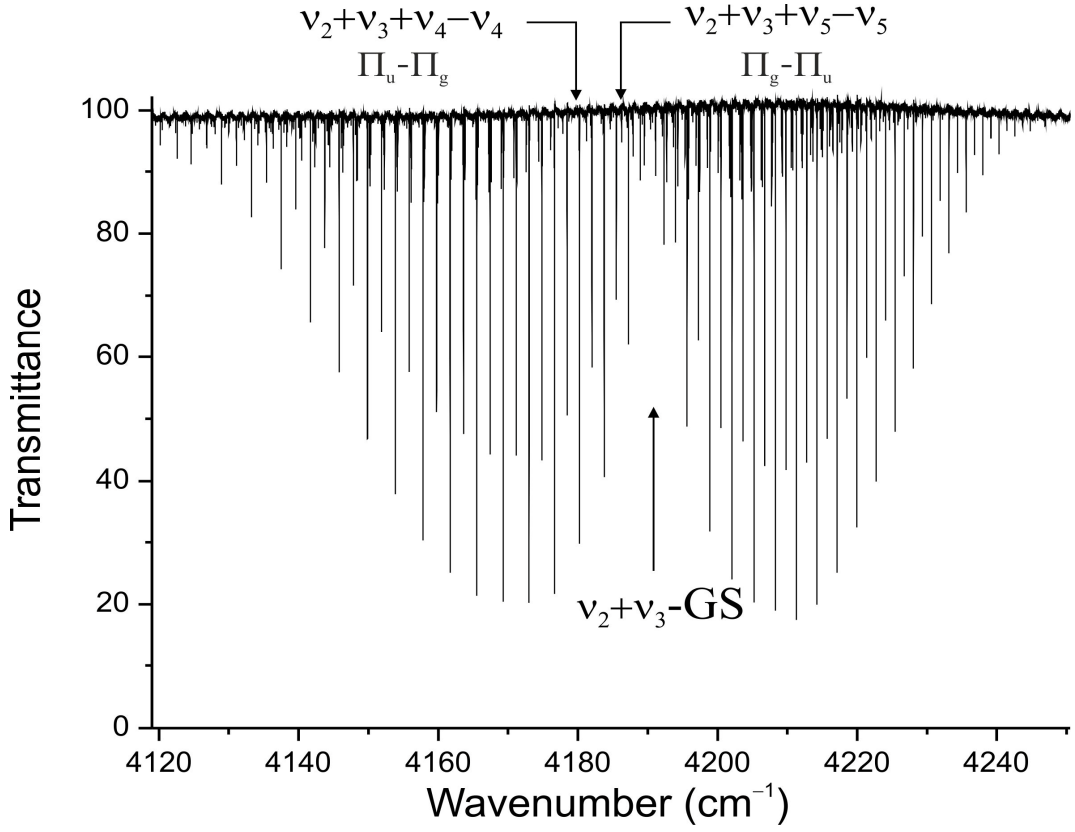

Figure 3.5: Portion of the infrared spectrum of $^{12}C_2D_2$ in the range 4120 – 4250 cm^{-1} showing the $\nu_2+\nu_3$ combination parallel band. Experimental conditions are those of spectrum *l* in Table 3.2.

3.1.3 Analysis

All the 92 bands analysed are collected in Table 3.3, together with the symmetry of the vibrational states involved in the transition, the band centre, the observed range of *J"* values for the various branches, the number of the fitted and assigned lines and the RMS error resulting from the simultaneous least – squares analysis described below. In the same Table are listed also

the 11 Raman bands involving ν_2 reported in [17] and the pure bending bands observed for the first time.

Table 3.3: Bands of $^{12}C_2D_2$ included in the least–squares fitting procedures

Transition	Symmetry	ν_C [a]	P, R, Q (J_{min}, J_{max})	σ ($\times 10^4$) [b]	n. fitted/ assign. lines
(*a*) 900 – 2200 cm^{-1}					
		Pure bending modes			
$\nu_4 + \nu_5 \leftarrow$ GS	$^{1}\Sigma_u^+ \leftarrow {}^{1}\Sigma_g^+$	1048.4893	$P_{e\text{-}e}$ (1-41); $R_{e\text{-}e}$ (0-40)	2.44	82/83
$\nu_4 + 2\nu_5 \leftarrow \nu_5$	$^{II}\Pi_g \leftarrow {}^{1}\Pi_u$	1036.1751	$P_{e\text{-}e}$ (2-49); $R_{e\text{-}e}$ (1-43); $Q_{f\text{-}e}$ (1-22) $P_{f\text{-}f}$ (2-50); $R_{f\text{-}f}$ (1-44); $Q_{e\text{-}f}$ (10-27)	4.05	160/224
$2\nu_4 + \nu_5 \leftarrow \nu_4$	$^{II}\Pi_u \leftarrow {}^{1}\Pi_g$	1041.2146	$P_{e\text{-}e}$ (2-44); $R_{e\text{-}e}$ (1-44); $Q_{f\text{-}e}$ (1-18) $P_{f\text{-}f}$ (2-44); $R_{f\text{-}f}$ (1-43); $Q_{e\text{-}f}$ (11-18)	4.06	134/199
$2\nu_4 + \nu_5 \leftarrow$ GS	$^{II}\Pi_u \leftarrow {}^{1}\Sigma_g^+$	1551.8973	$P_{e\text{-}e}$ (4-22); $R_{e\text{-}e}$ (4-16); $Q_{f\text{-}e}$ (1-22)	4.56	39/56
	$^{I}\Pi_u \leftarrow {}^{1}\Sigma_g^+$	1561.6080	$Q_{f\text{-}e}$ (1-21)	6.65	19/21
$4\nu_5 \leftarrow \nu_5$	$^{1}\Sigma_g^+ \leftarrow {}^{1}\Pi_u$	1594.6866	$P_{e\text{-}e}$ (3-23); $R_{e\text{-}e}$ (1-23); $Q_{e\text{-}f}$ (1-18)	5.39	47/61
	$^{1}\Delta_g \leftarrow {}^{1}\Pi_u$	1598.5331	$P_{e\text{-}e}$ (10-14); $R_{e\text{-}e}$ (3-14);$Q_{f\text{-}e}$ (2-22); $P_{f\text{-}f}$ (10-14); $R_{f\text{-}f}$ (3-14);$Q_{e\text{-}f}$ (2-21)	5.45	55/75
$3\nu_5 \leftarrow$ GS	$^{1}\Pi_u \leftarrow {}^{1}\Sigma_g^+$	1603.6858	$P_{e\text{-}e}$ (1-35); $R_{e\text{-}e}$ (1-34); $Q_{e\text{-}f}$ (1-35)	4.86	87/99
$3\nu_4 + \nu_5 \leftarrow$ GS	$^{1}\Sigma_u^+ \leftarrow {}^{1}\Sigma_g^+$	2064.4858	$P_{e\text{-}e}$ (2-22); $R_{e\text{-}e}$ (0-22)	5.54	35/44
		Stretching – bending modes			
$\nu_2 + \nu_4 \leftarrow \nu_4 + \nu_5$	$^{1}\Pi_g \leftarrow {}^{1}\Sigma_u^-$	1222.8899	$P_{f\text{-}f}$ (2-22); $R_{f\text{-}f}$ (0-22); $Q_{e\text{-}f}$ (1-24)	4.38	50/67
	$^{1}\Pi_g \leftarrow {}^{1}\Delta_u$	1223.1834	$P_{e\text{-}e}$ (2-21); $R_{e\text{-}e}$ (2-21); $Q_{f\text{-}e}$ (2-23); $P_{f\text{-}f}$ (2-21); $R_{f\text{-}f}$ (2-20); $Q_{e\text{-}f}$ (2-24)	4.00	102/124
	$^{1}\Pi_g \leftarrow {}^{1}\Sigma_u^+$	1230.0653	$P_{e\text{-}e}$ (3-23); $R_{e\text{-}e}$ (1-21); $Q_{f\text{-}e}$ (1-21)	4.57	50/63
$\nu_2 \leftarrow \nu_5$	$^{1}\Sigma_g^+ \leftarrow {}^{1}\Pi_u$	1227.0196	$P_{e\text{-}e}$ (1-35); $R_{e\text{-}e}$ (1-34); $Q_{e\text{-}f}$ (1-35)	3.06	102/104
$\nu_2 + \nu_5 \leftarrow 2\nu_5$	$^{1}\Pi_u \leftarrow {}^{1}\Delta_g$	1229.0972	$P_{e\text{-}e}$ (2-18); $R_{e\text{-}e}$ (2-19); $Q_{f\text{-}e}$ (2-26); $P_{f\text{-}f}$ (2-17); $R_{f\text{-}f}$ (3-16); $Q_{e\text{-}f}$ (2-25);	3.88	102/113
	$^{1}\Pi_u \leftarrow {}^{1}\Sigma_g^+$	1233.3727	$P_{e\text{-}e}$ (1-24); $R_{e\text{-}e}$ (1-26); $Q_{f\text{-}e}$ (1-26)	4.04	70/76
$\nu_2 + \nu_4 \leftarrow \nu_5$	$^{1}\Pi_g \leftarrow {}^{1}\Pi_u$	1733.7679	$P_{e\text{-}e}$ (3-24); $R_{e\text{-}e}$ (1-21); $P_{f\text{-}f}$ (2-24); $R_{f\text{-}f}$ (1-24)	4.29	85/89
$\nu_2 + 2\nu_4 \leftarrow \nu_4 + \nu_5$	$^{1}\Sigma_g^+ \leftarrow {}^{1}\Sigma_u^+$	1741.6427	$P_{e\text{-}e}$ (1-19); $R_{e\text{-}e}$ (5-15)	8.72	24/28
$2\nu_2 \leftarrow \nu_2$ [c]	$^{1}\Sigma_g^+ \leftarrow {}^{1}\Sigma_g^+$	1756.0056	$Q_{e\text{-}e}$ (1-28)	2.95	27/28
$\nu_2 + 2\nu_4 \leftarrow 2\nu_4$ [c]	$^{1}\Delta_g \leftarrow {}^{1}\Delta_g$	1757.1101	$Q_{e\text{-}e}$ (2-26); $Q_{f\text{-}f}$ (2-24)	8.94	26/48
	$^{1}\Sigma_g^+ \leftarrow {}^{1}\Sigma_g^+$	1758.3197	$Q_{e\text{-}e}$ (2-26)	5.84	18/23
$\nu_2 + \nu_4 \leftarrow \nu_4$ [c]	$^{1}\Pi_g \leftarrow {}^{1}\Pi_g$	1760.8724	$Q_{e\text{-}e}$ (1-36); $Q_{f\text{-}f}$ (1-37)	5.06	58/73
$\nu_2 + \nu_4 + \nu_5 \leftarrow \nu_4 + \nu_5$ [c]	$^{1}\Delta_u \leftarrow {}^{1}\Delta_u$	1762.3767	$Q_{e\text{-}e}$ (2-20); $Q_{f\text{-}f}$ (2-20)	9.31	14/38
	$^{1}\Sigma_u^- \leftarrow {}^{1}\Sigma_u^-$	1762.3865	$Q_{f\text{-}f}$ (1-20)	9.07	13/20
	$^{1}\Sigma_u^+ \leftarrow {}^{1}\Sigma_u^+$	1762.4767	$Q_{e\text{-}e}$ (1-21)	8.29	11/19
$\nu_2 \leftarrow$ GS [c]	$^{1}\Sigma_g^+ \leftarrow {}^{1}\Sigma_g^+$	1764.8062	$Q_{e\text{-}e}$ (1-46)	4.96	43/44
$\nu_2 + \nu_5 \leftarrow \nu_5$ [c]	$^{1}\Pi_u \leftarrow {}^{1}\Pi_u$	1766.4458	$Q_{e\text{-}e}$ (1-33); $Q_{f\text{-}f}$ (1-34)	4.49	52/62
$\nu_2 + 2\nu_5 \leftarrow 2\nu_5$ [c]	$^{1}\Sigma_g^+ \leftarrow {}^{1}\Sigma_g^+$	1767.8361	$Q_{e\text{-}e}$ (2-22)	7.52	18/20

	$\Delta_g \leftarrow \Delta_g$	1768.0076	$Q_{e\text{-}e}$ (2-23); $Q_{f\text{-}f}$ (2-23)	8.05	19/42
$\nu_2 + \nu_5 \leftarrow \nu_4$	$\Pi_u \leftarrow \Pi_g$	1793.5502	$P_{e\text{-}e}$ (2-23); $R_{e\text{-}e}$ (1-24); $P_{f\text{-}f}$ (3-25); $R_{f\text{-}f}$ (1-22)	4.65	82/90
$\nu_3 + \nu_4 \leftarrow 2\nu_4$	$\Pi_u \leftarrow \Sigma_g^+$	1919.5060	$Q_{f\text{-}e}$ (1-28)	3.86	27/28
	$\Pi_u \leftarrow \Delta_g$	1920.1117	$P_{e\text{-}e}$ (3-30); $R_{e\text{-}e}$ (2-24); $Q_{f\text{-}e}$ (2-18); $P_{f\text{-}f}$ (3-25); $R_{f\text{-}f}$ (2-23); $Q_{e\text{-}f}$ (2-20)	3.88	117/129
$\nu_3 \leftarrow \nu_4$	$\Sigma_u^+ \leftarrow \Pi_g$	1928.5645	$P_{e\text{-}e}$ (1-35); $R_{e\text{-}e}$ (1-36); $Q_{e\text{-}f}$ (1-31)	2.12	100/100
$\nu_3 + \nu_5 \leftarrow \nu_4 + \nu_5$	$\Pi_g \leftarrow \Sigma_u^-$	1923.2017	$P_{f\text{-}f}$ (3-24); $R_{f\text{-}f}$ (0-22); $Q_{f\text{-}f}$ (1-24)	4.67	55/65
	$\Pi_g \leftarrow \Delta_u$	1923.4952	$P_{e\text{-}e}$ (3-20); $R_{e\text{-}e}$ (6-20); $Q_{f\text{-}e}$ (2-24); $P_{f\text{-}f}$ (2-21); $R_{f\text{-}f}$ (3-21); $Q_{e\text{-}f}$ (3-23)	4.38	93/106
	$\Pi_g \leftarrow \Sigma_u^+$	1930.3771	$P_{e\text{-}e}$ (2-24); $R_{e\text{-}e}$ (0-21); $Q_{f\text{-}e}$ (1-23)	4.65	60/67
$\nu_1 + \nu_4 \leftarrow \nu_4 + \nu_5$	$\Pi_g \leftarrow \Sigma_u^-$	2151.9229	$P_{f\text{-}f}$ (4-22); $R_{f\text{-}f}$ (1-18); $Q_{e\text{-}f}$ (2-22)	4.50	46/50
	$\Pi_g \leftarrow \Delta_u$	2152.2164	$P_{e\text{-}e}$ (3-17); $R_{e\text{-}e}$ (7-13); $Q_{f\text{-}e}$ (4-17); $P_{f\text{-}f}$ (3-23); $R_{f\text{-}f}$ (3-16); $Q_{e\text{-}f}$ (2-22)	4.20	63/70
	$\Pi_g \leftarrow \Sigma_u^+$	2159.0983	$P_{e\text{-}e}$ (7-21); $R_{e\text{-}e}$ (2-21); $Q_{f\text{-}e}$ (3-20)	3.93	43/50
$\nu_1 + \nu_5 \leftarrow 2\nu_5$	$\Pi_u \leftarrow \Delta_g$	2159.6450	$P_{e\text{-}e}$ (2-18); $R_{e\text{-}e}$ (4-19); $Q_{f\text{-}e}$ (2-26); $P_{f\text{-}f}$ (2-19); $R_{f\text{-}f}$ (5-19); $Q_{e\text{-}f}$ (2-27)	3.93	105/116
	$\Pi_u \leftarrow \Sigma_g^+$	2163.9205	$P_{e\text{-}e}$ (6-30); $R_{e\text{-}e}$ (2-16); $Q_{f\text{-}e}$(2-20)	3.97	55/57
$\nu_1 \leftarrow \nu_5$	$\Sigma_g^+ \leftarrow \Pi_u$	2167.4354	$P_{e\text{-}e}$ (1-36); $R_{e\text{-}e}$ (1-33); $Q_{e\text{-}f}$ (1-36)	3.06	104/104

(*b*) 2200 – 2700 cm^{-1}

$\nu_2 + 2\nu_4 \leftarrow \nu_5$	$\Sigma_g^+ \leftarrow \Pi_u$	2245.3453	$Q_{e\text{-}f}$ (6-22);	9.24	11/12
$\nu_2 + \nu_4 + \nu_5 \leftarrow \nu_4$	$\Sigma_u^+ \leftarrow \Pi_g$	2293.2777	$P_{e\text{-}e}$ (1-24); $R_{e\text{-}e}$ (2-25); $Q_{e\text{-}f}$ (1-25);	3.99	66/69
	$\Delta_u \leftarrow \Pi_g$	2300.0457	$P_{e\text{-}e}$ (3-20); $R_{e\text{-}e}$ (1-20); $Q_{f\text{-}e}$ (5-27); $P_{f\text{-}f}$ (5-21); $R_{f\text{-}f}$ (1-27); $Q_{e\text{-}f}$ (2-28)	4.94	105/126
	$\Sigma_u^- \leftarrow \Pi_g$	2300.3690	$P_{f\text{-}f}$ (2-25); $R_{f\text{-}f}$ (1-24); $Q_{f\text{-}e}$ (12-23)	4.46	52/58
$\nu_2 + \nu_5 \leftarrow$ GS	$\Pi_u \leftarrow \Sigma_g^+$	2304.2324	$P_{e\text{-}e}$ (2-35); $R_{e\text{-}e}$ (0-36); $Q_{f\text{-}e}$ (4-40)	3.29	101/107
$\nu_2 + 2\nu_5 \leftarrow \nu_5$	$\Sigma_g^+ \leftarrow \Pi_u$	2300.9092	$P_{e\text{-}e}$ (1-31); $R_{e\text{-}e}$ (1-36); $Q_{e\text{-}f}$ (1-28)	4.14	82/93
	$\Delta_g \leftarrow \Pi_u$	2305.3562	$P_{e\text{-}e}$ (3-21); $R_{e\text{-}e}$ (1-24); $Q_{f\text{-}e}$ (2-36); $P_{f\text{-}f}$ (3-24); $R_{f\text{-}f}$ (1-30); $Q_{e\text{-}f}$ (2-22)	4.01	122/147
$\nu_3 + 2\nu_4 \leftarrow 2\nu_4$	$\Sigma_u^+ \leftarrow \Sigma_g^+$	2427.9171	$P_{e\text{-}e}$ (1-38); $R_{e\text{-}e}$ (0-36)	3.29	73/75
	$\Delta_u \leftarrow \Delta_g$	2427.9926	$P_{e\text{-}e}$ (3-36); $R_{e\text{-}e}$ (2-35); $P_{f\text{-}f}$ (3-35); $R_{f\text{-}f}$ (2-35)	3.15	117/135
$\nu_3 + \nu_4 + \nu_5 \leftarrow \nu_4 + \nu_5$	$\Sigma_g^+ \leftarrow \Sigma_u^+$	2428.1303	$P_{e\text{-}e}$ (2-42); $R_{e\text{-}e}$ (0-41)	3.70	74/83
	$\Delta_g \leftarrow \Delta_u$	2428.1329	$P_{e\text{-}e}$ (3-39); $R_{e\text{-}e}$ (2-39); $Q_{f\text{-}e}$ (2-12); $P_{f\text{-}f}$ (3-43); $R_{f\text{-}f}$ (2-41); $Q_{e\text{-}f}$ (2-12)	3.98	142/178
	$\Sigma_g^- \leftarrow \Sigma_u^-$	2428.7443	$P_{f\text{-}f}$ (1-42); $R_{f\text{-}f}$ (0-43)	2.77	84/86
$\nu_3 + 2\nu_5 \leftarrow 2\nu_5$	$\Delta_u \leftarrow \Delta_g$	2428.8651	$P_{e\text{-}e}$ (3-47); $R_{e\text{-}e}$ (2-46); $P_{f\text{-}f}$ (3-41); $R_{f\text{-}f}$ (2-41)	3.42	157/168
	$\Sigma_u^+ \leftarrow \Sigma_g^+$	2429.0075	$P_{e\text{-}e}$ (1-42); $R_{e\text{-}e}$ (0-41)	2.92	84/84
$\nu_3 + \nu_4 \leftarrow \nu_4$	$\Pi_u \leftarrow \Pi_g$	2433.6361	$P_{e\text{-}e}$ (2-51); $R_{e\text{-}e}$ (1-54); $Q_{f\text{-}e}$ (2-22); $P_{f\text{-}f}$ (2-51); $R_{f\text{-}f}$ (1-52); $Q_{e\text{-}f}$ (1-21)	2.55	233/246
$\nu_3 + \nu_5 \leftarrow \nu_5$	$\Pi_g \leftarrow \Pi_u$	2434.0797	$P_{e\text{-}e}$ (2-51); $R_{e\text{-}e}$ (1-52); $Q_{f\text{-}e}$ (3-22); $P_{f\text{-}f}$ (2-52); $R_{f\text{-}f}$ (1-52); $Q_{e\text{-}f}$ (1-21)	3.29	227/244
$\nu_3 \leftarrow$ GS	$\Sigma_u^+ \leftarrow \Sigma_g^+$	2439.2467	$P_{e\text{-}e}$ (1-58); $R_{e\text{-}e}$ (0-59)	3.01	111/118
$\nu_1 + 2\nu_4 \leftarrow \nu_4 + \nu_5$	$\Sigma_g^+ \leftarrow \Sigma_u^+$	2658.7100	$P_{e\text{-}e}$ (3-15); $R_{e\text{-}e}$ (1-12)	5.09	24/25
$\nu_1 + \nu_4 \leftarrow \nu_5$	$\Pi_g \leftarrow \Pi_u$	2662.8009	$P_{e\text{-}e}$ (2-27); $R_{e\text{-}e}$ (1-25); $P_{f\text{-}f}$ (2-26); $R_{f\text{-}f}$ (1-24)	3.39	92/100

(*c*) 2700 – 3500 cm^{-1}						
$\nu_1 + \nu_5 \leftarrow \nu_4$	Π_u	Π_g	2724.0980	$P_{e\text{-}e}$ (2-30); $R_{e\text{-}e}$ (1-30); $P_{f\text{-}f}$ (2-31); $R_{f\text{-}f}$ (1-28)	3.49	107/115
$\nu_2 + \nu_4 + \nu_5 \leftarrow$ GS	Σ_u^+	Σ_g^+	2803.9599	$P_{e\text{-}e}$ (1-30); $R_{e\text{-}e}$ (0-26)	4.88	51/57
$\nu_3 + \nu_4 + \nu_5 \leftarrow \nu_5$	Σ_g^+	Π_u	2931.8329	$P_{e\text{-}e}$ (1-36); $R_{e\text{-}e}$ (1-34); $Q_{e\text{-}f}$ (1-28)	3.57	95/97
	Δ_g	Π_u	2938.7174	$P_{e\text{-}e}$ (3-28); $R_{e\text{-}e}$ (1-27); $Q_{f\text{-}e}$ (3-27); $P_{f\text{-}f}$ (3-31); $R_{f\text{-}f}$ (3-27); $Q_{e\text{-}f}$ (6-32)	3.09	152/159
	Σ_g^-	Π_u	2939.6223	$P_{f\text{-}f}$ (2-34); $R_{f\text{-}f}$ (1-30); $Q_{f\text{-}e}$ (2-31)	3.91	86/93
$\nu_3 + 2\nu_4 \leftarrow \nu_4$	Δ_u	Π_g	2941.5170	$P_{e\text{-}e}$ (3-42); $R_{e\text{-}e}$ (1-36); $Q_{f\text{-}e}$ (6-29); $P_{f\text{-}f}$ (3-39); $R_{f\text{-}f}$ (1-35); $Q_{e\text{-}f}$ (2-18)	3.96	167/187
	Σ_u^+	Π_g	2942.0472	$P_{e\text{-}e}$ (1-20); $R_{e\text{-}e}$ (3-11); $Q_{e\text{-}f}$ (1-29)	3.01	52/57
$\nu_3 + \nu_4 \leftarrow$ GS	Π_u	Σ_g^+	2944.3182	$P_{e\text{-}e}$ (1-44); $R_{e\text{-}e}$ (0-42); $Q_{f\text{-}e}$ (1-46)	2.13	126/131
$\nu_1 + \nu_4 + \nu_5 \leftarrow \nu_4$	Σ_u^+	Π_g	3212.9892	$P_{e\text{-}e}$ (2-34); $R_{e\text{-}e}$ (1-30); $Q_{e\text{-}f}$ (1-26);	4.48	81/89
	Δ_u	Π_g	3219.3541	$P_{f\text{-}f}$ (3-33); $R_{f\text{-}f}$ (1-23); $Q_{f\text{-}e}$ (2-25)	4.54	64/78
	Σ_u^-	Π_g	3219.7273	$P_{f\text{-}f}$ (3-30); $R_{f\text{-}f}$ (3-27); $Q_{f\text{-}e}$ (3-24)	3.66	67/75
$\nu_1 + 2\nu_5 \leftarrow \nu_5$	Σ_g^+	Π_u	3221.5975	$P_{e\text{-}e}$ (1-37); $R_{e\text{-}e}$ (1-32); $Q_{e\text{-}f}$ (1-27)	4.04	85/96
	Δ_g	Π_u	3226.1345	$P_{e\text{-}e}$ (3-35); $R_{e\text{-}e}$ (1-24); $Q_{f\text{-}e}$ (2-30); $P_{f\text{-}f}$ (3-38); $R_{f\text{-}f}$ (1-30); $Q_{e\text{-}f}$ (2-35)	3.55	145/186
$\nu_1 + \nu_5 \leftarrow$ GS	Π_u	Σ_g^+	3234.7802	$P_{e\text{-}e}$ (2-44); $R_{e\text{-}e}$ (0-38); $Q_{f\text{-}e}$ (2-39)	3.06	114/120
$\nu_3 + 2\nu_4 \leftarrow$ GS[d]	Δ_u	Σ_g^+	3452.1992	$P_{e\text{-}e}$ (9-20); $R_{e\text{-}e}$ (6-17)	4.49	22/24
	Σ_u^+	Σ_g^+	3452.7294	$P_{e\text{-}e}$ (1-28); $R_{e\text{-}e}$ (0-28);	4.14	54/57
$\nu_3 + 2\nu_5 \leftarrow$ GS	Σ_u^+	Σ_g^+	3499.8672	$P_{e\text{-}e}$ (1-28); $R_{e\text{-}e}$ (0-30);	4.70	57/59
(*d*) 3500 –5500 cm^{-1}						
$\nu_1 + \nu_4 + \nu_5 \leftarrow$ GS	Σ_u^+	Σ_g^+	3723.6714	$P_{e\text{-}e}$ (1-32); $R_{e\text{-}e}$ (0-31)	3.56	61/64
$\nu_2 + 3\nu_4 + \nu_5 \leftarrow$ GS	Σ_u^+	Σ_g^+	3821.7771	$P_{e\text{-}e}$ (1-15); $R_{e\text{-}e}$ (0-15)	4.39	26/31
$2\nu_2 + \nu_5 \leftarrow$ GS	Π_u	Σ_g^+	4061.8118	$P_{e\text{-}e}$ (2-26); $R_{e\text{-}e}$ (0-26); $Q_{f\text{-}e}$ (1-33)	4.87	60/84
$\nu_2 + \nu_3 + 2\nu_4 \leftarrow 2\nu_4$	Δ_u	Δ_g	4172.0138	$P_{e\text{-}e}$ (3-30); $R_{e\text{-}e}$ (2-30); $P_{f\text{-}f}$ (3-28); $R_{f\text{-}f}$ (2-27)	4.81	87/108
	Σ_u^+	Σ_g^+	4172.9860	$P_{e\text{-}e}$ (1-29); $R_{e\text{-}e}$ (0-28)	4.63	45/57
$\nu_2+\nu_3+\nu_4+\nu_5 \leftarrow \nu_4+\nu_5$	Δ_g	Δ_u	4177.2083	$P_{e\text{-}e}$ (3-29); $R_{e\text{-}e}$ (2-25); $P_{f\text{-}f}$ (3-30); $R_{f\text{-}f}$ (2-26)	7.92	84/104
	Σ_g^+	Σ_u^+	4177.2950	$P_{e\text{-}e}$ (1-33); $R_{e\text{-}e}$ (0-28)	8.28	50/62
	Σ_g^-	Σ_u^-	4177.8378	$P_{f\text{-}f}$ (1-32); $R_{f\text{-}f}$ (0-30)	7.53	51/63
$\nu_2 + \nu_3 + \nu_4 \leftarrow \nu_4$	Π_u	Π_g	4181.2577	$P_{e\text{-}e}$ (2-40); $R_{e\text{-}e}$ (1-38); $Q_{f\text{-}e}$ (1-5) $P_{f\text{-}f}$ (2-39); $R_{f\text{-}f}$ (1-39); $Q_{e\text{-}f}$ (1-5)	3.75	138/164
$\nu_2 + \nu_3 + 2\nu_5 \leftarrow 2\nu_5$	Σ_u^+	Σ_g^+	4183.3423	$P_{e\text{-}e}$ (1-29); $R_{e\text{-}e}$ (0-27)	4.78	44/57
	Δ_u	Δ_g	4183.3823	$P_{e\text{-}e}$ (3-28); $R_{e\text{-}e}$ (2-28); $P_{f\text{-}f}$ (3-31); $R_{f\text{-}f}$ (2-29)	7.00	80/109
$\nu_2 + \nu_3 + \nu_5 \leftarrow \nu_5$	Π_g	Π_u	4187.0696	$P_{e\text{-}e}$ (2-39); $R_{e\text{-}e}$ (1-37); $Q_{e\text{-}f}$ (1-6) $P_{f\text{-}f}$ (2-39); $R_{f\text{-}f}$ (1-37); $Q_{f\text{-}e}$ (1-4)	3.28	141/160
$\nu_2 + \nu_3 \leftarrow$ GS	Σ_u^+	Σ_g^+	4190.6395	$P_{e\text{-}e}$ (1-46); $R_{e\text{-}e}$ (0-48)	3.14	95/95
$\nu_1 + 3\nu_5 \leftarrow$ GS	Π_u	Σ_g^+	4283.7206	$Q_{f\text{-}e}$ (1-20)	10.56	19/20
$2\nu_3 \leftarrow \nu_5$	Σ_g^+	Π_u	4311.4006	$P_{e\text{-}e}$ (3-21); $R_{e\text{-}e}$ (1-23);$Q_{e\text{-}f}$ (1-26)	4.97	63/68
$\nu_2 + \nu_3 + 2\nu_4 \leftarrow \nu_4$	Σ_u^+	Π_g	4687.0654	$Q_{e\text{-}f}$ (5-19)	3.96	15/15

$\nu_2 + \nu_3 + \nu_4 \leftarrow$ GS	$\Pi_u \leftarrow \Sigma_g^+$	4691.9360	$P_{e\text{-}e}$ (2-30); $R_{e\text{-}e}$ (0-28); $Q_{f\text{-}e}$ (1-32)	4.53	89/90
$2\nu_1 \leftarrow \nu_5$	$\Sigma_g^+ \leftarrow \Pi_u$	4848.4109	$P_{e\text{-}e}$ (1-28); $R_{e\text{-}e}$ (1-21); $Q_{f\text{-}e}$ (1-28)	5.44	52/76
$\nu_1 + \nu_2 + \nu_5 \leftarrow$ GS	$\Pi_u \leftarrow \Sigma_g^+$	4982.1510	$Q_{f\text{-}e}$ (2-26)	3.80	22/24
$\nu_1 + \nu_3 + 2\nu_4 \leftarrow 2\nu_4$	$\Delta_u \leftarrow \Delta_g$	5055.5466	$P_{e\text{-}e}$ (3-31); $R_{e\text{-}e}$ (2-30); $P_{f\text{-}f}$ (1-31); $R_{f\text{-}f}$ (2-30)	4.78	54/116
	$\Sigma_u^+ \leftarrow \Sigma_g^+$	5055.8595	$P_{e\text{-}e}$ (1-32); $R_{e\text{-}e}$ (0-30)	3.85	40/63
$\nu_1+\nu_3+\nu_4+\nu_5 \leftarrow \nu_4+\nu_5$	$\Sigma_g^- \leftarrow \Sigma_u^-$	5062.4808	$P_{f\text{-}f}$ (1-31); $R_{f\text{-}f}$ (0-30)	4.47	54/62
	$\Delta_g \leftarrow \Delta_u$	5063.0325	$P_{e\text{-}e}$ (2-31); $R_{e\text{-}e}$ (2-29); $P_{f\text{-}f}$ (3-30); $R_{f\text{-}f}$ (2-30)	5.34	66/113
	$\Sigma_g^+ \leftarrow \Sigma_u^+$	5063.1806	$P_{e\text{-}e}$ (1-35); $R_{e\text{-}e}$ (0-33)	4.80	43/69
$\nu_1 + \nu_3 + 2\nu_5 \leftarrow 2\nu_5$	$\Sigma_u^+ \leftarrow \Sigma_g^+$	5070.2493	$P_{e\text{-}e}$ (1-25); $R_{e\text{-}e}$ (0-25)	5.24	36/51
	$\Delta_u \leftarrow \Delta_g$	5070.4295	$P_{e\text{-}e}$ (3-30); $R_{e\text{-}e}$ (2-27); $P_{f\text{-}f}$ (3-30); $R_{f\text{-}f}$ (2-29)	5.03	81/110
$\nu_1 + \nu_3 + \nu_4 \leftarrow \nu_4$	$\Pi_u \leftarrow \Pi_g$	5076.1170	$P_{e\text{-}e}$ (2-43); $R_{e\text{-}e}$ (1-41); $P_{f\text{-}f}$ (2-41); $R_{f\text{-}f}$ (1-41)	4.63	118/166
$\nu_1 + \nu_3 + \nu_5 \leftarrow \nu_5$	$\Pi_g \leftarrow \Pi_u$	5083.8130	$P_{e\text{-}e}$ (2-40); $R_{e\text{-}e}$ (1-40); $P_{f\text{-}f}$ (2-37); $R_{f\text{-}f}$ (1-35)	4.28	116/149
$\nu_1 + \nu_3 \leftarrow$ GS	$\Sigma_u^+ \leftarrow \Sigma_g^+$	5097.1857	$P_{e\text{-}e}$ (1-48); $R_{e\text{-}e}$ (0-47)	3.99	82/96
$\nu_2 + \nu_3 + 2\nu_4 + \nu_5 \leftarrow \nu_5$	$\Pi_g \leftarrow \Pi_u$	5193.0072	$P_{e\text{-}e}$ (2-19); $R_{e\text{-}e}$ (2-17); $P_{f\text{-}f}$ (2-19); $R_{f\text{-}f}$ (2-17)	4.85	45/68
$\nu_2 + \nu_3 + 3\nu_4 \leftarrow \nu_4$	$\Pi_u \leftarrow \Pi_g$	5195.4746	$P_{e\text{-}e}$ (2-24); $R_{e\text{-}e}$ (1-19); $P_{f\text{-}f}$ (2-24); $R_{f\text{-}f}$ (1-19)	10.34	52/84
$\nu_2 + \nu_3 + 2\nu_4 \leftarrow$ GS[d]	$\Delta_u \leftarrow \Sigma_g^+$	5196.2204	$P_{e\text{-}e}$ (8-33); $R_{e\text{-}e}$ (8-33)	4.37	42/52
	$\Sigma_u^+ \leftarrow \Sigma_g^+$	5197.7983	$P_{e\text{-}e}$ (1-35); $R_{e\text{-}e}$ (0-37)	4.84	64/73
$\nu_2 + \nu_3 + 2\nu_5 \leftarrow$ GS	$\Sigma_u^+ \leftarrow \Sigma_g^+$	5254.2020	$P_{e\text{-}e}$ (1-22); $R_{e\text{-}e}$ (0-22)	7.59	36/45
$\nu_1+\nu_2+\nu_4+\nu_5 \leftarrow$ GS	$\Sigma_u^+ \leftarrow \Sigma_g^+$	5466.7403	$P_{e\text{-}e}$ (1-26); $R_{e\text{-}e}$ (0-20)	4.65	43/47

[a] In cm^{-1}. For the definition of the band centre ν_C see text.

[b] σ (in cm^{-1}) corresponds to the RMS value of the residuals for the various assigned lines resulting from the simultaneous fit.

[c] Raman and Infrared data from Ref. [17].

[d] Perturbation allowed transition.

As already pointed out in Section 2.4.1, the assignment procedure was carried out taking into account the intensity alternation of adjacent lines due to 6:3 statistical weight ratio of symmetric and antisymmetric levels. Lower state combination differences (LSCD), calculated from the parameters reported in Table 3.5, were used to assign the *J* values of the transitions and to identify the lower vibrational state. The upper state was assigned on the basis of its symmetry, dictated by the selection rules illustrated in Section 2.4.1. Once the identification and characterization of the upper state was accomplished, a systematic search of all the allowed bands reaching the same state from different lower states was performed.

The spectroscopic analysis of the assigned bands was carried out in two steps. First, the transition wavenumbers for each band were fitted separately to effective upper state rovibrational

parameters, to check the correctness of the assignments and to extend the data set to higher J values. The basic Hamiltonian of a linear molecule, with distortion corrections up to high power in the rotational angular momentum was adopted for the analysis. For the transitions involving doubly degenerate states, the $\ell-$ doubling energy contributions were considered. So the rovibrational term values (see Eq. (2.14)) are given by

$$\begin{aligned} T^0(\upsilon,J) = G_c^0(\upsilon) + B_\upsilon J(J+1) - D_\upsilon\left[J(J+1)\right]^2 + H_\upsilon\left[J(J+1)\right]^3 + \ldots \\ \mp \tfrac{1}{2}\left\{q_\upsilon\left[J(J+1)\right] + q_\upsilon^J\left[J(J+1)\right]^2 + q_\upsilon^{JJ}\left[J(J+1)\right]^3\right\} \end{aligned} \tag{3.2}$$

where the – and + signs are related to the *e* and *f* levels, respectively, and the centre energy is

$$G_c^0 = G_\upsilon^0 - B_\upsilon k^2 - D_\upsilon k^4 \tag{3.3}$$

with G_υ^0 being the pure vibrational term value defined in Eq. (2.8) and where $k = \ell_4 + \ell_5$.

The band centre is defined as

$$\nu_C = G_{\upsilon'}^0 - B_{\upsilon'}k^2 - D_{\upsilon'}k^4 - (G_{\upsilon''}^0 - B_{\upsilon''}k^2 - D_{\upsilon''}k^4) \tag{3.4}$$

where $G_{\upsilon'}^0$ and $G_{\upsilon''}^0$ refer to the upper and lower state, respectively.

As a starting point, the calculation of the spectroscopic parameters of the lower states (involving pure bending modes) was accomplished. These were derived from the analysis of the IR data [14], the transition recorded in the THz region [18] and the newly observed $\nu_4 + \nu_5\left(\Sigma_u^+\right) \leftarrow \mathrm{GS}\left(\Sigma_g^+\right)$ band, fitting simultaneously only transitions with $\upsilon_{tot} \le 2$. Since the ν_4 and ν_5 bending mode are separated by about 27 cm^{-1}, vibrational coupling of Darling–Dennison type occurs between levels of identical symmetry, such as $\upsilon_4 = 2$ (Σ_g^+ and Δ_g) and $\upsilon_5 = 2$ (Σ_g^+ and Δ_g). The $\upsilon_{tot} = 3$ states were not included in the dataset since all the hot bands involving stretching modes identified in the spectra are from levels with $\upsilon_{tot} \le 2$. Moreover, the anharmonic interaction between the υ_4 = 3 and υ_4 = 1, υ_5 = 2 levels cannot be properly accounted for, owing to the lack of experimental observations on the former state. The model Hamiltonian for the simultaneous analysis of bending modes is described by Eqs. (2.23) – (2.27) and (2.32) – (2.34). In addition there is also the parameter

$$\rho_{45}^0 + \rho_{45}^J M + \rho_{45}^{JJ} M^2 \tag{3.5}$$

The off–diagonal elements for the Darling – Dennison interaction are reported in Table I of Ref. [14], where $s_{45} = K_{44,55}$:

$$\left\langle \upsilon_4^{\ell_4}, \upsilon_5^{\ell_5} \left| H_2' \right| (\upsilon_4 - 2)^{\ell_4}, (\upsilon_4 + 2)^{\ell_5} \right\rangle = \frac{1}{4} K_{44,55} \left\{ \left(\upsilon_4^2 - \ell_4^2 \right) \left[\left(\upsilon_5^2 + 2 \right) - \ell_5^2 \right] \right\}^{1/2} \tag{3.6}$$

where

$$K_{44,55} = K_{44,55}^0 + K_{44,55}^J M + K_{44,55}^{JJ} M^2 + K_{44,55}^4 \upsilon_4 + K_{44,55}^5 \left(\upsilon_5 + 2 \right) \tag{3.7}$$

and

$$\left\langle \upsilon_4^{\ell_4}, \upsilon_5^{\ell_5} \left| H_2' \right| (\upsilon_4 - 2)^{\ell_4 \mp 2}, (\upsilon_4 + 2)^{\ell_5 \pm 2} \right\rangle = \frac{1}{16} (r_{45} + 2g_{45}) \left\{ \left(\upsilon_4 \pm \ell_4 - 2 \right) \left(\upsilon_4 \pm \ell_4 \right) \left(\upsilon_5 \pm \ell_5 + 2 \right) \left(\upsilon_5 \pm \ell_5 + 4 \right) \right\}^{1/2} \tag{3.8}$$

Once the analysis of the bending states was completed, the second step was started by analysing the stretching – bending system. The band–by–band analysis revealed, as expected, that some bands are affected by perturbations. All the transition wavenumbers relative to a specific stretching mode, i.e. the fundamental band, its first overtone, the hot and combination bands involving bending modes, were fitted together. In this way, three sets of spectroscopic parameters, one for each stretching mode, were obtained from independent fits. In this case, the data were fitted following the Eqs. (2.8), (2.10) – (2.13). Moreover, the *r*, *q*, and ρ parameters are given by the expressions:

$$r_{s45} = r_{s45}^0 + r_{s45}^J M + r_{s45}^{JJ} M^2, \tag{3.9}$$

$$q_{st} = q_{st}^0 + q_{stt} \upsilon_t + q_{stt'} \upsilon_{t'} + q_{ss't} \upsilon_s \upsilon_t + q_{st}^J M + q_{st}^{JJ} M^2, \tag{3.10}$$

$$\rho_{st} = \rho_{st}^0 + \rho_{st}^J M + \rho_{st}^{JJ} M^2 + \rho_{st}^{JJJ} M^3, \tag{3.11}$$

$$\rho_{s45} = \rho_{s45}^0 + \rho_{s45}^J M, \tag{3.12}$$

The Darling – Dennison interaction must be taken into account in the global fit of stretching – bending bands too. The off–diagonal elements (Eq. (3.5), with $s_{s45} = K_{s44,s55}$) contain the parameters in the following equations:

$$K_{s44,s55} = K_{s44,s55}^0 + K_{s44,s55}^J M + K_{s44,s55}^{JJ} M^2 \tag{3.13}$$

where the subscripts s = 1, 2, 3 refer to one of the stretching modes, for the $\Sigma_{g,u}^+$ interacting states. For interacting $\Delta_{g,u}$ states the parameters are g_{45}, r_{45} or r_{s45}, as defined in Eqs. (2.23) for bending states and (2.8) for stretching–bending states, (2.32) and (3.9). The complete block–diagonalized matrices illustrating the $\ell-$ type and the Darling–Dennison interactions between the bending levels in the vibrational manifolds is reported hereafter in Table 3.4:

Table 3.4: Block – diagonalized matrices used for the interactions occurring in acetylene isotopologues

$v_t = 0$	t = 4, 5	$[0^0\ J]$
$v_t = 1$	t = 4, 5	$[1^{\pm 1}\ J]$
$v_4 = 1,\ v_5 = 1$		$\begin{pmatrix} \left[1^{\pm 1}1^{\pm 1}J\right] \pm \frac{1}{4}\rho_{45}M(M-2) & \frac{1}{2}(q_5 \pm q_4)\sqrt{M(M-2)} \\ & \left[1^{\pm 1}1^{\mp 1}J\right] \pm r_{45} \end{pmatrix}$
$v_4 = 2$ and $v_5 = 2$	a)	$\begin{pmatrix} \left[2^{-2}0^0J\right] - \frac{1}{2}\rho_4 M(M-2) & \frac{1}{2}(r_{45} + 2g_{45}) \\ & \left[0^0 2^{-2}J\right] - \frac{1}{2}\rho_5 M(M-2) \end{pmatrix}$
	b)	$\begin{pmatrix} [2^0 0^0 J] & K_{45} & q_4\sqrt{M(M-2)} & 0 \\ & [0^0 2^0 J] & 0 & q_5\sqrt{M(M-2)} \\ & & [2^2 0^0 J] + \frac{1}{2}\rho_4 M(M-2) & \frac{1}{2}(r_{45} + 2g_{45}) \\ & & & [0^0 2^2 J] + \frac{1}{2}\rho_5 M(M-2) \end{pmatrix}$
$v_4 = 2,\ v_5 = 1$ and $v_5 = 3$		$\begin{pmatrix} \left[0^0 3^{\pm 1}J\right] \mp q_5^{(3)}M & \frac{1}{2}(r_{45} + 2g_{45}) & \sqrt{2}K_{44,55} & \frac{\sqrt{3}}{2}\left[q_5^{(3)} \mp \rho_5 M\right]\sqrt{(M-2)(M-6)} & 0 \\ & \left[2^{\pm 2}1^{\mp 1}J\right] & \sqrt{2}\left(r_{45} + \frac{1}{2}q_4 M\right) & 0 & \frac{1}{2}\left[q_5^{(1)} \mp \rho_4 M\right]\sqrt{(M-2)(M-6)} \\ & & \left[2^0 1^{\pm 1}J\right] \mp \frac{1}{2}q_5^{(1)}M & 0 & \frac{1}{\sqrt{2}}\left[q_4 \mp \frac{1}{2}\rho_{45}M\right]\sqrt{(M-2)(M-6)} \\ & & & \left[0^0 3^{\pm 3}\right] & \frac{\sqrt{3}}{2}(r_{45} + 2g_{45}) \\ & & & & \left[2^{\pm 2}1^{\pm 1}\right] \end{pmatrix}$

with $q_5^{(3)}$ for $3\nu_5$, and $q_5^{(1)}$ for ν_5 in $2\nu_4 + \nu_5$.

The stretching – stretching combination bands, $\nu_1 + \nu_2 \leftarrow$ GS, $\nu_1 + \nu_3 \leftarrow$ GS and $\nu_2 + \nu_3 \leftarrow$ GS, with the associated hot and combination bands, were fitted separately. All the parameters related to the $\upsilon_s = 1$ (s = 1, 2, 3) states in Eqs. (2.8) and (2.10), i.e. ω_s^0, $x_{ss'}^0$, α_s^0, β_s^0, *etc.*, were constrained to the values obtained from the analysis of the corresponding stetching band system. In the simultaneous fits the ground state and the pure bending state parameters were held fixed to the values reported in Table 3.5. Identical unitary weights were assigned to all the transitions with the exclusion of the overlapping lines, which were given zero weight. In addition, transition wavenumbers that differed from the corresponding calculated values by more than a chosen limit (0.001 cm^{-1} or 0.0015/0.002 cm^{-1} in few cases) were excluded from the last cycle of the least–squares procedure. The choice of the refined parameters in each fit was dictated by the structure of the data set. An identical strategy has been adopted for the simultaneous fit of the transitions involving each stretching or stretching–stretching mode. First, the bands

corresponding to the $\upsilon_s = 1$ and 2 (s = 1, 2, 3) states were fitted. The transitions to the corresponding associated bending states were successively added in blocks, starting with those involving $\upsilon_4 = 1$ and $\upsilon_5 = 1$, then the manifold $\upsilon_4 = \upsilon_5 = 1$ $\left(\Sigma_u^+,\ \Sigma_u^-,\ \Delta_u\right)$ was added, and, finally, the $\upsilon_4 = 2$ and $\upsilon_5 = 2$, Σ_g^+ and Δ_g states were added, coupled by the Darling – Dennison interaction. The enlargement of the dataset resulted in the refinement of the appropriate higher order parameters, necessary to adequately reproduce the experimental observations, according to some constraints. They must: a) correspond to lower–order ones previously obtained, b) be statistically determined, c) improve the quality of the fit. The adequacy of the Hamiltonian model adopted was tested by comparing the results of the simultaneous analysis to those achieved in the single band fits mentioned above.

3.1.4 Results and Discussion

The quality of the fit for each band in the single band fits or in the simultaneous fits is highlighted by the RMS values listed in the fifth column of Table 3.3: they are all better than 0.0011 cm^{-1}. In the same table, very precise values for the band centres are also reported: their uncertainties are usually of the order of magnitude of a few parts in 10^{-4} cm^{-1}.

The parameters obtained for the bending states, in comparison with those from Ref. [17] (column 3) and Ref. [18] (column 4), are displayed in Table 3.5.

Table 3.5: Spectroscopic parameters (in cm^{-1})[a] of the bending modes of $^{12}C_2D_2$

Parameter	This work	Bermejo *et al.*[b]	Yu *et al.*[c]
ω_4^0	509.23325964(245)	509.2330789(270)	509.2607280(210)
ω_5^0	538.02536058(249)	538.0252188(182)	538.006990(240)
x_{44}^0	1.89165528(278)	1.891696(363)	1.94171(213)
x_{45}^0	–1.7407432(138)	–1.7407768(131)	–1.726368(367)
x_{55}^0	–1.60296682(272)	–1.603037(363)	–1.65901(247)
g_{44}^0	0.40720362(173)	0.407158(363)	–0.52043(213)
g_{45}^0	3.3510743(135)	3.35106236(711)	1.64708977(407)
g_{55}^0	2.21426400(173)	2.214306(363)	1.43786(213)
y_{445}			0.20499(196)
$y_{555} \times 10^3$			0.624(123)
y_5^{44}			–0.22342(230)
r_{45}^0	–3.5876949(270)	–3.58769929(906)	–5.7730(740)

$r_{45}^{J} \times 10^{5}$	8.37963(630)	8.36107(398)	8.37619(340)
$r_{45}^{JJ} \times 10^{8}$	–2.3812(170)	–1.9091(993)	–1.4663(157)
$r_{45}^{JJJ} \times 10^{12}$	0.36743(777)		0.4340(147)
r_{445}			0.18426(600)
r_{455}			0.9086(801)
B_0	0.8478734706(168)	0.847874129(220)	0.8478734840(640)
$\alpha_4^0 \times 10^{3}$	–2.08049802(902)	–2.080753(133)	2.0815510(767)
$\alpha_5^0 \times 10^{3}$	–2.16654528(895)	–2.1664494(722)	2.162834(100)
$\gamma_{44} \times 10^{5}$	–1.929906(813)	–2.1922(251)	–2.07330(987)
$\gamma_{45} \times 10^{5}$	–0.19079(298)	–0.20151(461)	–0.6076(177)
$\gamma_{55} \times 10^{5}$	1.959146(841)	2.2075(256)	2.28485(874)
$\gamma^{(44)} \times 10^{5}$	–0.838506(705)	–0.5951(259)	–0.64161(951)
$\gamma^{(45)} \times 10^{5}$	–7.87940(315)	–7.85862(451)	–9.00656(767)
$\gamma^{(55)} \times 10^{5}$	–5.120826(702)	–5.3617(254)	–4.8080(110)
$\gamma_{445} \times 10^{6}$			–1.324(133)
$\gamma_{555} \times 10^{8}$			–3.74(170)
$\gamma_4^{(45)} \times 10^{6}$			0.1473(107)
$\gamma_5^{(44)} \times 10^{6}$			–6.664(245)
$\gamma_5^{(55)} \times 10^{6}$			–0.7268(200)
$D_0 \times 10^{6}$	0.8023884(490)	0.801900(363)	–0.8025180(940)
$\beta_4 \times 10^{8}$	1.65751(300)	1.744(149)	–1.4633(123)
$\beta_5 \times 10^{8}$	3.09829(298)	2.9604(623)	–0.8496(244)
$\delta_{44} \times 10^{9}$	–3.0382(189)	–4.473(705)	4.7203(543)
$\delta_{45} \times 10^{9}$		–0.0768(310)	–16.612(117)
$\delta_{55} \times 10^{9}$	5.5841(211)	6.484(330)	1.451(117)
$\delta^{(44)} \times 10^{9}$	8.8406(307)	9.79(217)	–12.258(157)
$\delta^{(45)} \times 10^{9}$	–21.566(167)	–19.306(773)	6.841(297)
$\delta^{(55)} \times 10^{9}$	–17.4427(205)	–17.115(945)	–15.681(427)
$\delta_{445} \times 10^{9}$			–5.961(120)
$\delta_{555} \times 10^{9}$			–2.2182(644)
$\delta_4^{(45)} \times 10^{9}$			5.374(193)
$\delta_5^{(44)} \times 10^{9}$			2.261(287)
$\delta_5^{(55)}$ x 10^{9}			6.054(147)
$H_0 \times 10^{12}$	0.8802(564)	0.302(179)	1.0850(470)
$h_4 \times 10^{12}$	0.2861(145)	0.5023(653)	0.1461(190)
$h_5 \times 10^{12}$	0.2850(125)	0.2021(218)	0.1421(163)
$q_4^0 \times 10^{3}$	3.22881354(961)	3.229034(628)	–3.239940(310)
$q_5^0 \times 10^{3}$	3.2614320(190)	3.25890(161)	–3.2338620(175)
$q_{44} \times 10^{5}$	1.301280(917)	1.2822(621)	–4.1048(270)

$q_{45} \times 10^5$	2.1347(780)		–7.95716(450)
$q_{54} \times 10^5$	–1.2411(780)	2.159(362)	–1.1925(117)
$q_{55} \times 10^5$	1.40188(190)	1.661(162)	–4.7145(113)
$q_4^J \times 10^8$	–2.25170 (120)	–2.2459(106)	2.257130(190)
$q_5^J \times 10^8$	–2.25445(132)	–2.25759(678)	2.259100(217)
$q_4^{JJ} \times 10^{12}$	0.16914(826)	0.1814(633)	–0.30728(577)
$q_5^{JJ} \times 10^{12}$	0.15902(958)	0.2353(339)	–0.31228(647)
$q_4^K \times 10^5$			1.9577(117)
$q_5^K \times 10^5$			0.27766(284)
$\rho_4^0 \times 10^8$	–2.35173(951)	–2.252(584)	–3.09100(460)
$\rho_5^0 \times 10^8$	4.22443(401)	3.814(247)	–1.3220(130)
$\rho_4^J \times 10^{12}$	0.1296(295)		–1.1534(844)
$\rho_5^J \times 10^{12}$	0.3769(442)		–0.8866(630)
$\rho_{45}^0 \times 10^8$	8.6567(653)	6.869(405)	5.0770(510)
$\rho_4^{JJ} \times 10^{15}$			0.5023(394)
$\rho_5^{JJ} \times 10^{15}$	–0.1446(138)		0.2695(299)
$\rho_{45}^J \times 10^{12}$	–1.1790(622)		–2.5458(544)
$\rho_{45}^{JJ} \times 10^{15}$			0.3923(247)
$K_{44,55}^0$	–7.3977269(196)	–7.39823(427)	–8.18790(260)
$K_{44,55}^4 \times 10^3$			0.37943(314)
$K_{44,55}^J \times 10^3$	0.1164559(790)	0.14565(315)	0.109410(790)
$K_{44,55}^{JJ} \times 10^6$	0.016560(202)		
N. of fitted / assigned lines	1372 / 1491	1039 / 1158	1938 / 2092
RMS / cm^{-1} (IR data)	0.00013	0.00019	0.00011
RMS / MHz (MW data)	0.092	0.038	0.092

[a] Estimated uncertainties (1σ) are given in parenthesis in units of the last figure quoted.
[b] From Ref. [17].
[c] From Ref. [18].

The comparison between columns 2 and 3 shows that these values are in good agreement between them, with the exception of a few higher order parameters. A large number of spectroscopic parameters were determined more precisely due to the inclusion in the dataset of the measurements in the THz region. An analogous comparison with data in column 4 is more difficult to perform, since the model Hamiltonian adopted by Yu *et al*. [18] differs from the one of the present study in many respects, as for example opposite signs and/or different coefficients in their Hamiltonian. Moreover, some large differences are related to the presence of higher order corrections due to the inclusion in their analysis of $\upsilon_{tot} = 3$ states. For example, the values

of r_{45}^0 in columns 2 and 4 are practically identical if the contributions of r_{445} and r_{455} are taken into account (see Eq. (2.32)). The parameters obtained in the simultaneous fits of each stretching or stretching – stretching system are listed in Tables from 3.6 to 3.10, together with the number of assigned transitions and of those retained in the final fit according to the criterion for rejection, that is also reported.

Table 3.6: Spectroscopic parameters (in cm^{-1}) of $^{12}C_2D_2$ resulting from the simultaneous fit of the ν_1 fundamental and its associated hot bands

Parameter		Parameter	
ω_1^0	2717.345212(123)		
x_{11}^0	–12.1232060(724)	y_1^{45}	–0.1606064(574)
x_{14}^0	–15.623572(183)	y_1^{55}	0.0107148(389)
x_{15}^0	–8.2450668(963)	r_{145}^0	–3.3690433(612)
y_{144}	0.301172(129)	$r_{145}^J \times 10^5$	11.9052(434)
y_{145}	0.1376154(930)	$r_{145}^{JJ} \times 10^8$	–1.0355(579)
$\alpha_1^0 \times 10^3$	5.981994(285)	$\gamma_{145} \times 10^5$	2.1840(397)
$\gamma_{11} \times 10^5$	8.2078(229)	$\gamma_{15} \times 10^5$	–0.5789(109)
$\gamma_{14} \times 10^5$	11.0950(190)	$\gamma_1^{45} \times 10^5$	5.2106(407)
		$\delta_{145} \times 10^9$	6.917(398)
$q_{14}^0 \times 10^3$	3.39571(483)	$q_{14}^J \times 10^8$	–6.256(279)
$q_{15}^0 \times 10^3$	3.326832(350)	$q_{15}^J \times 10^8$	–2.4114(166)
$q_{144} \times 10^5$	–9.500(467)	$q_{14}^{JJ} \times 10^{12}$	49.16(248)
$q_{145} \times 10^5$	–11.710(191)	$\rho_{14}^0 \times 10^8$	-99.0(178)
$q_{155} \times 10^5$	0.8049(278)	$\rho_{15}^0 \times 10^8$	4.5685(355)
$K_{144,155}^0$			–7.678006(650)
$K_{144,155}^J \times 10^3$			0.10910(191)
$K_{144,155}^{JJ} \times 10^6$			0.01889(185)
N. of fitted / assigned data	1308/1471		
St. dev. of the fit (cm^{-1})	0.000392		

Table 3.7: Spectroscopic parameters (in cm^{-1}) of $^{12}C_2D_2$ resulting from the simultaneous fit of the ν_2 fundamental and its associated hot bands

Parameter		Parameter	
ω_2^0	1769.206582(101)	y_{255}^0	–0.0374280(437)
x_{22}^0	–4.4003408(641)	y_2^{44}	–0.2660039(886)
x_{24}^0	–4.014847(153)	y_2^{45}	–0.0425694(572)
x_{25}^0	1.706545(140)	y_{225}	–0.0328287(652)
y_{244}^0	0.3437783(657)	r_{245}^0	–3.5456078(593)
y_{245}^0	–0.020935(181)	$r_{245}^J \times 10^5$	8.2815(243)
$\alpha_2^0 \times 10^3$	3.162298(170)	$\gamma_{25} \times 10^5$	–6.2440(151)
$\gamma_{22} \times 10^5$	–0.3621(134)	$\gamma_2^{44} \times 10^5$	2.6371(747)
$\gamma_{24} \times 10^5$	–9.2327(758)	$\gamma_2^{45} \times 10^5$	–0.4281(451)
$\delta_{24} \times 10^9$	–117.07(288)	$\delta_2^{44} \times 10^9$	116.12(291)
$\delta_{25} \times 10^9$	–11.185(501)	$\delta_2^{55} \times 10^9$	9.914(420)
$q_{24}^0 \times 10^3$	3.34499(184)	$q_{24}^J \times 10^8$	–2.1745(411)
$q_{25}^0 \times 10^3$	3.240958(935)	$q_{25}^J \times 10^8$	–2.1220(296)
$q_{244} \times 10^5$	–8.087(179)	$q_{225} \times 10^5$	4.4298(433)
$q_{245} \times 10^5$	–2.460(216)	$\rho_{24}^0 \times 10^8$	–35.85(103)
$q_{254} \times 10^5$	8.538(111)	$\rho_{25}^0 \times 10^8$	1.281(147)
$q_{255} \times 10^5$	2.9874(884)	$\rho_{24}^J \times 10^9$	0.2808(149)
$K_{244,255}^0$	–7.576259(388)		
$K_{244,255}^J \times 10^3$	0.10303(239)		
N. of fitted / assigned data	1614/1924		
St. dev. of the fit (cm^{-1})	0.000481		

Table 3.8: Spectroscopic parameters (in cm^{-1}) of $^{12}C_2D_2$ resulting from the simultaneous fit of the ν_3 fundamental and its associated hot bands

Parameter		Parameter	
ω_3^0	2453.8998296(796)		
x_{33}^0	–14.6531002(498)	y_{355}^0	–0.0192250(383)
x_{34}^0	–5.5854373(583)	y_3^{44}	–0.0255495(247)
x_{35}^0	–5.1522200(713)	y_3^{45}	–0.1610476(266)
y_{344}^0	–0.0041588(306)	r_{345}^0	–3.8946969(355)
y_{345}^0	–0.1838570(444)	$r_{345}^J \times 10^5$	8.6213(130)
$\alpha_3^0 \times 10^3$	4.491143(178)	$\gamma_{345} \times 10^5$	0.24981(468)
$\gamma_{33} \times 10^5$	–0.9277(135)	$\gamma_{35} \times 10^5$	5.1303(160)
$\gamma_{34} \times 10^5$	2.56605(648)	$\gamma_3^{45} \times 10^5$	0.4399(105)
		$\gamma_3^{55} \times 10^5$	
$\beta_3^0 \times 10^8$			
$\delta_{34} \times 10^9$		$\delta_{35} \times 10^9$	0.1756(332)
$q_{34}^0 \times 10^3$	3.228778(142)	$q_{354} \times 10^5$	–8.4142(309)
$q_{35}^0 \times 10^3$	3.175816(195)	$q_{355} \times 10^5$	1.4161(162)
$q_{344} \times 10^5$	1.62145(636)	$q_{34}^J \times 10^8$	–2.24553(471)
$q_{345} \times 10^5$	14.7020(347)	$q_{35}^J \times 10^8$	–2.22975(508)
$\rho_{34}^0 \times 10^8$	–2.3054(120)	$\rho_{345}^0 \times 10^8$	–0.7197(354)
$\rho_{35}^0 \times 10^8$	4.5264(227)		
$K_{344,355}^0$	–7.898610(231)		
$K_{344,355}^J \times 10^3$	0.103326(790)		
$K_{344,355}^{JJ} \times 10^6$	0.023998(608)		
N. of fitted / assigned data	2636 / 2844		
St. dev. of the fit (cm^{-1})	0.000352		

Table 3.9: Spectroscopic parameters (in cm^{-1}) of $^{12}C_2D_2$ resulting from the simultaneous fit of $\nu_1 + \nu_3$ or $\nu_2 + \nu_3$ and their associated hot bands

Parameter [a]	$\nu_1 + \nu_3$	$\nu_2 + \nu_3$
x^0_{i3}	–47.2829951(888)	–13.4135050(932)
y^0_{i34}	–0.416912(182)	–0.182626(178)
y^0_{i35}	0.059782(203)	–0.016131(188)
y^0_{i344}	0.2903226(853)	0.2852376(789)
y^0_{i345}	0.233812(138)	–0.0957096(994)
y^0_{i355}	–0.0131750(926)	–0.0420135(857)
$y^{(44)}_{i3}$	–0.0149052(408)	0.0601886(437)
$y^{(45)}_{i3}$	0.4020405(626)	0.0093238(510)
$y^{(55)}_{i3}$	–0.0239856(320)	–0.0169411(437)
$\gamma_{i3} \times 10^5$	–7.6196(227)	8.5203(227)
$\gamma_{i34} \times 10^5$	0.3432(229)	2.9434(710)
$\gamma_{i35} \times 10^5$	1.7896(528)	1.4850(573)
$\gamma_{i344} \times 10^5$	–0.2963(132)	9.922(198)
$\gamma_{i345} \times 10^5$	–1.8891(229)	
$\gamma_{i355} \times 10^5$	–0.1208(203)	–11.307(225)
$\gamma^{(44)}_{i3} \times 10^5$		–12.543(189)
$\gamma^{(45)}_{i3} \times 10^5$	–5.3231(154)	
$\gamma^{(55)}_{i3} \times 10^5$		10.540(201)
$\delta_{i3} \times 10^9$	–1.311(122)	–1.084(111)
$\delta_{i34} \times 10^9$		44.746(623)
$\delta_{i35} \times 10^9$	–2.761(249)	2.035(208)
$\delta_{i344} \times 10^9$		–43.630(531)
$q^0_{i34} \times 10^3$	3.275240(747)	3.34103(110)
$q^0_{i35} \times 10^3$	3.20992(101)	3.17004(141)
$q^0_{i344} \times 10^5$	1.1315(226)	–6.7208(949)
$q^0_{i345} \times 10^5$		4.9936(902)
$q^0_{i355} \times 10^5$	1.5291(422)	6.771(130)
$q^J_{i34} \times 10^8$	–3.297(116)	–1.9919(329)

$q^{J}_{i35}\times10^{8}$	–4.008(189)	–2.1525(408)
$q^{JJ}_{i34}\times10^{12}$	3.289(508)	
$q^{JJ}_{i35}\times10^{12}$	10.371(954)	
$\rho^{0}_{i34}\times10^{8}$	–0.8652(495)	–30.950(386)
$\rho^{0}_{i35}\times10^{8}$	4.4426(604)	–2.254(170)
$\rho^{J}_{i34}\times10^{12}$		29.75(314)
$\rho^{0}_{i345}\times10^{8}$	10.2297(836)	6.610(124)
r^{0}_{i345}	–3.2377758(955)	–3.859076(102)
$r^{J}_{i345}\times10^{5}$	7.7172(513)	8.6751(629)
$r^{JJ}_{i345}\times10^{8}$	–2.2712(543)	–1.7699(720)
$K^{0}_{i344,i355}$	−7.898610 [b]	−7.898610 [b]
$K^{J}_{i344,i355}\times10^{3}$		–1.3957(280)
N. of fitted / assigned lines	690/995	1061/1254
St. dev. of the fit (cm^{-1})	0.000474	0.000544

[a] i = 1 or 2, respectively.

[b] Fixed to the value of $K^{0}_{344,355}$ in Table 3.8.

Table 3.10: Spectroscopic parameters (in cm^{-1}) of $^{12}C_2D_2$ resulting from the simultaneous fit of the $\nu_1+\nu_2$ and associated hot bands

Parameter	
x^{0}_{12}	–17.20[a]
y_{125}	–1.907831(204)
y_{1245}	–3.752246(235)
$\gamma_{1245}\times10^{5}$	19.608(143)
$\delta_{1245}\times10^{9}$	651.98(265)
$q^{0}_{125}\times10^{3}$	3.57484(324)
$q^{J}_{125}\times10^{8}$	–5.744(495)
N. of fitted / assigned data	65/71
St. dev. of the fit (cm^{-1})	0.000460

[a] Fixed to value from Ref.[10]

The number of data for ν_1 is smaller than that for the other stretching systems since transitions from the GS to the excited states of "*g*" symmetry are not allowed in IR and, differently from ν_2 [17], they are too weak to be observed in Raman. In total, 8762 transitions were fitted, 1246 of them (about 14%) were discarded because they were overlapping or exceeded the limit for rejection.

Thirty one parameters for ν_1, 36 for ν_2 and 35 for ν_3 were determined with high precision. The standard deviation of each fit is smaller than 0.0006 cm^{-1}, of the same order of magnitude of the estimated uncertainty of the experimental measurements. A comparison between the leading terms of the rotational and vibrational ℓ – type and Darling – Dennison interactions shows that the values in ν_1, ν_2 and ν_3 differ from the corresponding ones in the bending states by less than 10%. As far as the stretching – stretching combinations are concerned, in the case of $\nu_1 + \nu_2$ only 6 parameters were determined, because only two bands, namely $\nu_1 + \nu_2 + \nu_5\,(\Pi_u) \leftarrow$ GS and $\nu_1 + \nu_2 + \nu_4 + \nu_5\,(\Sigma_u^+) \leftarrow$ GS, were observed. For $\nu_1 + \nu_3$ and $\nu_2 + \nu_3$ more than 30 parameters were determined, whereas all the vibrations and rotational constants of each stretching mode present in the stretching – stretching combination bands were constrained to the values listed in Tables 3.5 – 3.8. In particular, in the global fits for $\nu_1 + \nu_3$ and $\nu_2 + \nu_3$, the $K^0_{44,55}$ Darling – Dennison interaction constant was constrained to the value obtained from the analysis of the ν_3 system, whereas $K^J_{44,55}$ was refined for the $\nu_2 + \nu_3$ system. For most of the parameters the estimated uncertainties are several orders of magnitude smaller than their values and, generally, low internal correlations are observed between them. The centre term values G^0_C, defined in Eq. (3.3), of the vibrationally excited states involved in the analysed bands are collected in Table 3.11.

Table 3.11: Vibrational term values (in cm^{-1}) of the levels involving stretching and bending modes in $^{12}C_2D_2$

υ_1	υ_2	υ_3	υ_4	υ_5	ℓ_4	ℓ_5	Sym.	G^0_C
0	0	0	1	0	±1	0	Π_g	510.68219
0	0	0	0	1	0	±1	Π_u	537.78665
0	0	0	2	0	±2	0	Δ_g	1024.20659
0	0	0	2	0	0	0	Σ_g^+	1024.81229
0	0	0	1	1	1	–1	Σ_u^+	1041.48926
0	0	0	1	1	±1	±1	Δ_u	1048.37117
0	0	0	1	1	–1	1	Σ_u^-	1048.66465

0	0	0	0	2	0	0	Σ_g^+	1070.85970
0	0	0	0	2	0	±2	Δ_g	1075.13524
0	0	0	2	1	0	±1	$^{II}\Pi_u$	1551.89730
0	0	0	2	1	±2	∓1	$^{I}\Pi_u$	1561.60795
0	0	0	1	2	±1	0	Π_g	1573.96161
0	0	0	0	3	0	±1	Π_u	1603.68581
0	1	0	0	0	0	0	Σ_g^+	1764.80624
0	0	0	3	1	1	−1	Σ_u^+	2064.48581
0	0	0	0	4	0	0	Σ_g^+	2132.47325
0	0	0	0	4	0	±2	Δ_g	2136.31979
0	1	0	1	0	±1	0	Π_g	2271.55459
0	1	0	0	1	0	±1	Π_u	2304.23241
0	0	1	0	0	0	0	Σ_u^+	2439.24673
1	0	0	0	0	0	0	Σ_g^+	2705.22201
0	1	0	2	0	±2	0	Δ_g	2781.31663
0	1	0	2	0	0	0	Σ_g^+	2783.13199
0	1	0	1	1	1	−1	Σ_u^+	2803.95993
0	1	0	1	1	±1	±1	Δ_u	2810.72784
0	1	0	1	1	−1	1	Σ_u^-	2811.05117
0	1	0	0	2	0	0	Σ_g^+	2838.69581
0	1	0	0	2	0	±2	Δ_g	2843.14287
0	0	1	1	0	±1	0	Π_u	2944.31825
0	0	1	0	1	0	±1	Π_g	2971.86638
1	0	0	1	0	±1	0	Π_g	3200.58759
1	0	0	0	1	0	±1	Π_u	3234.78021
0	0	1	2	0	±2	0	Δ_u	3452.19924
0	0	1	2	0	0	0	Σ_u^+	3452.72943
0	0	1	1	1	1	−1	Σ_g^+	3469.61959
0	0	1	1	1	±1	±1	Δ_g	3476.50406
0	0	1	1	1	−1	1	Σ_g^-	3477.40899
0	0	1	0	2	0	0	Σ_u^+	3499.86718
0	0	1	0	2	0	±2	Δ_u	3504.00033
0	2	0	0	0	0	0	Σ_g^+	3520.81180
1	0	0	2	0	0	0	Σ_g^+	3700.19928
1	0	0	1	1	−1	1	Σ_u^+	3723.67139
1	0	0	1	1	±1	±1	Δ_u	3730.03632
1	0	0	1	1	1	−1	Σ_u^-	3730.40948
1	0	0	0	2	0	0	Σ_g^+	3759.38414
1	0	0	0	2	0	±2	Δ_g	3763.92113
0	1	0	3	1	1	−1	Σ_u^+	3821.77710
0	2	0	0	1	0	±1	Π_u	4061.81183
0	1	1	0	0	0	0	Σ_u^+	4190.63947
1	0	0	0	3	0	±1	Π_u	4283.72062

0	1	1	1	0	±1	0	Π_u	4691.93986
0	1	1	0	1	0	0	Π_g	4724.85628
0	0	2	0	0	0	0	Σ_g^+	4849.18726
1	1	0	0	1	0	±1	Π_u	4982.15096
1	0	1	0	0	0	0	Σ_u^+	5097.18574
0	1	1	2	0	±2	0	Δ_u	5196.22036
0	1	1	2	0	0	0	Σ_u^+	5197.79829
0	1	1	1	1	1	−1	Σ_g^+	5218.78431
0	1	1	1	1	±1	±1	Δ_g	5225.57948
0	1	1	1	1	−1	1	Σ_g^-	5226.50246
0	1	1	0	2	0	0	Σ_u^+	5254.20203
0	1	1	0	2	0	±2	Δ_u	5258.51755
2	0	0	0	0	0	0	Σ_g^+	5386.19760
1	1	0	1	1	1	−1	Σ_u^+	5466.74027
1	0	1	1	0	±1	0	Π_u	5586.79923
1	0	1	0	1	±1	0	Π_g	5621.59962
0	1	1	3	0	±1	0	Π_u	5706.15675
0	1	1	2	1	0	±1	Π_g	5730.79388
1	0	1	2	0	±2	0	Δ_u	6079.75319
1	0	1	2	0	0	0	Σ_u^+	6080.67181
1	0	1	1	1	1	−1	Σ_g^+	6104.66989
1	0	1	1	1	−1	1	Σ_g^-	6111.14544
1	0	1	1	1	±1	±1	Δ_g	6111.40371
1	0	1	0	2	0	0	Σ_u^+	6141.10897
1	0	1	0	2	0	±2	Δ_u	6145.56472

Sixteen term values are related to pure bending states and 59 to stretching–bending levels. Some local perturbations have been observed during the analysis. In the fit of the $2\nu_1 \leftarrow \nu_5$ band, the discrepancies between observed and calculated wavenumbers increased with increasing *J*. The interacting state could be $\upsilon_1 = \upsilon_2 = 1$, $\upsilon_4 = 2$, lying approximately 50 cm^{-1} apart, through the 1/244 anharmonic resonance as already pointed out by Weirauch *et al*. [19]. Another perturbation has been evidenced in the analysis of the $\nu_1 + \nu_3 + \nu_5\,(\Pi_g) \leftarrow \nu_5\,(\Pi_u)$ band, localized between *J* = 33 and 34 *e* levels, while in $\nu_1 + \nu_3 + \nu_4\ (\Pi_u) \leftarrow \nu_4\ (\Pi_g)$ it is observed between the *J* = 22 and 23 *f* levels. Again, the latter perturbation can be explained by the 1/244 interaction between the upper state and $\upsilon_2 = \upsilon_3 = 1$, $\upsilon_4 = 3$. However, because the energy separation is larger, about 85 cm^{-1}, its effects are not as strong and evident as they are in case of several dyads at higher energies.

3.2 $^{13}C^{12}CD_2$

In recent years, the bending states of all the 10 isotopologues of acetylene have been characterized up to v_{tot} = 2, 3, or 4, depending on the molecule [25–32], with the exception of $^{13}C^{12}CD_2$ which, so far, received little attention. The accurate characterization of the bending rotation – vibration levels of any isotopologue of acetylene using high resolution IR spectroscopy is certainly the starting point for an extensive investigation of the vibrationally excited states of the molecule up to high energies. So, for the first time, a high – resolution study of the bending states with v_{tot} up to 3 for $^{13}C^{12}CD_2$ was performed. The obtained results will give a better insight into the isotopic dependence of the parameters characterising the bending states for all the fully deuterated acetylene isotopologues.

3.2.1 Experiment

Two samples were synthesised using different amounts of the reagents. In particular, the sample #1 was synthesised as described in [33], aiming to obtain the maximum possible amount of the partially deuterated species, $H^{12}C^{13}CD$ and $H^{13}C^{12}CD$. The reaction sequence is summarized hereafter:

$$\left[Si(CH_3)_3\right]_2 NLi \xrightarrow[2.\ CH_3CO_2D]{1.\ BrH_2{}^{12}C{}^{13}CH_2Br} \underset{\approx 30\%}{D^{12}C^{13}CD} + \underset{\approx 20\%}{H^{12}C^{13}CD} + \underset{\approx 20\%}{H^{13}C^{12}CD} + \underset{\approx 30\%}{H^{12}C^{13}CH}$$

The precursor $BrH_2{}^{12}C^{13}CH_2Br$ was prepared starting from $^{12}CH_3{}^{13}CH_2OH$ as detailed in [27] and reported hereafter:

$$^{12}CH_3{}^{13}CHOH \xrightarrow{P_4O_{10}} H_2{}^{12}C = {}^{13}CH_2 \xrightarrow{Br_2} BrH_2{}^{12}C{}^{13}CH_2Br$$

More recently, another sample, #2, was prepared using a larger amount of deuterated acetic acid and the percentage of $^{13}C^{12}CD_2$ in the mixture rose to about 60%.

The spectra were recorded in the region 450 – 1900 cm^{-1} using a Bomem DA3.002 Fourier transform spectrometer in Bologna, equipped with a Globar source, a KBr beam splitter and two types of HgCdTe detectors operating at the liquid nitrogen temperature. The first (MCT1, see Table 3.12) was adopted in the low frequency region to record the ν_4 and ν_5 fundamentals and associated hot bands. The other (MCT2), with a detectivity D* about 50 times higher than that used in the low wavenumber region, operating from 800 cm^{-1}, was used to

record overtones and combination bands from the ground state. The optical path, ranging from 0.18 to 10 m, was obtained using a multipass White–type cell. Several scans, up to 1280, were co–added in order to improve the signal–to–noise ratio and the quality of the spectra. The achieved resolution ranged from 0.004 to 0.006 cm^{-1}. Different pressure conditions, from 133.3 Pa to 1333.3 Pa, were adopted. Detailed conditions for each spectrum are collected in Table 3.12.

Table 3.12: Experimental conditions for the recording of $^{13}C^{12}CD_2$ spectra

Spectrum	Pressure of the sample (Pa)	Range (cm^{-1})	Source	Detector	Resolution (cm^{-1})	#Scans	Optical pathlenght (m)
a	133.3	450 – 1100	Globar	MCT1	0.004	880	0.18
b	1333.3	950 – 1700	Globar	MCT2	0.004	880	0.18
c	1333.3	450 – 1900	Globar	MCT1	0.006	300	0.18
d	360.0	450 – 850	Globar	MCT1	0.006	1280	6
e	360.0	800 – 1800	Globar	MCT2	0.006	1280	10

Rotation – vibration transitions of H_2O [20] and CO_2 [22] were used for calibration. Particular care was devoted to the calibration of the spectra since consistent results had to be obtained from the analysis of bands observed in different spectral regions reaching the same excited state.

3.2.2 Description of the spectra

The spectra, which appear very congested due to the presence of transitions belonging to four different isotopologues, show absorptions in two different regions, namely 450 – 600 cm^{-1} and 950 – 1900 cm^{-1}. The low wavenumber region contains the bending fundamentals ν_4 and ν_5 and associated hot bands. Figure 3.6 shows the ν_5 band of the isotopologue under analysis together with the ν_4 fundamental of $H^{12}C^{13}CD$ and $H^{13}C^{12}CD$. The ν_4 band of $^{13}C^{12}CD_2$, with centre at 504.97 cm^{-1}, cannot be observed in Fig. 3.6 since its intensity is at least two orders of magnitude smaller than that of ν_5.

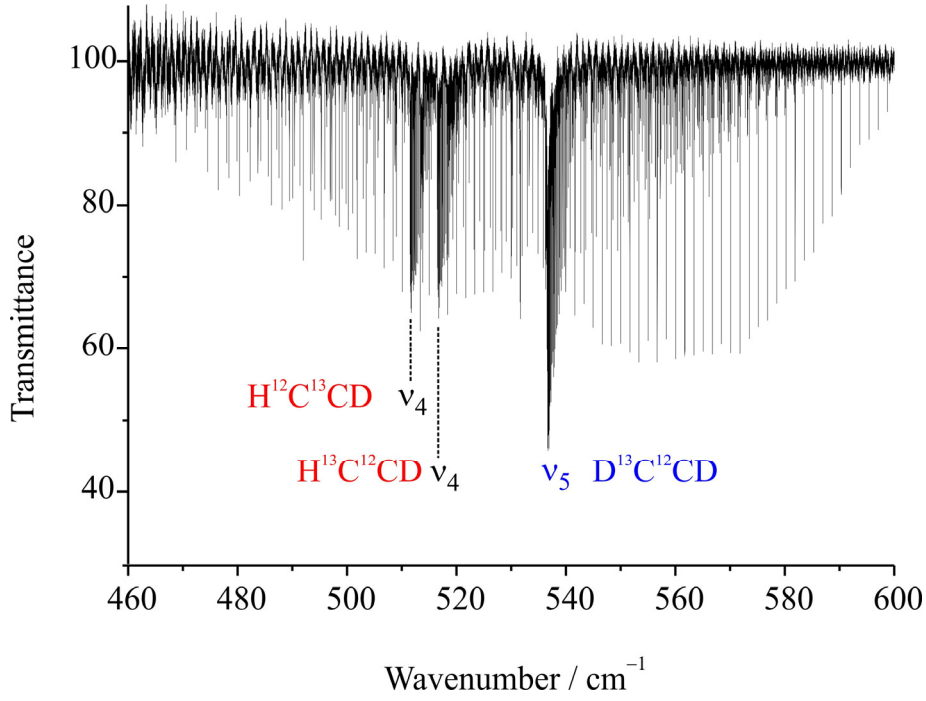

Figure 3.6: Portion of the spectrum between 460 and 600 cm^{-1} showing the ν_5 band of $^{13}C^{12}CD_2$ and the ν_4 band of $H^{12}C^{13}CD$ and $H^{13}C^{12}CD$. Experimental conditions: sample #1, condition of spectrum *a* in Table 3.12.

The spectrum appears very crowded. As an example, three *Q* branches related to hot bands involving states with v_{tot} = 2 or 3 are shown in Fig. 3.7. The assignments are further complicated by the presence of lines due to other isotopologues. Nevertheless, the identification of transitions for the partially deuterated species, $H^{12}C^{13}CD$ and $H^{13}C^{12}CD$, was facilitated by the accurate knowledge of their spectrum in the investigated region [30].

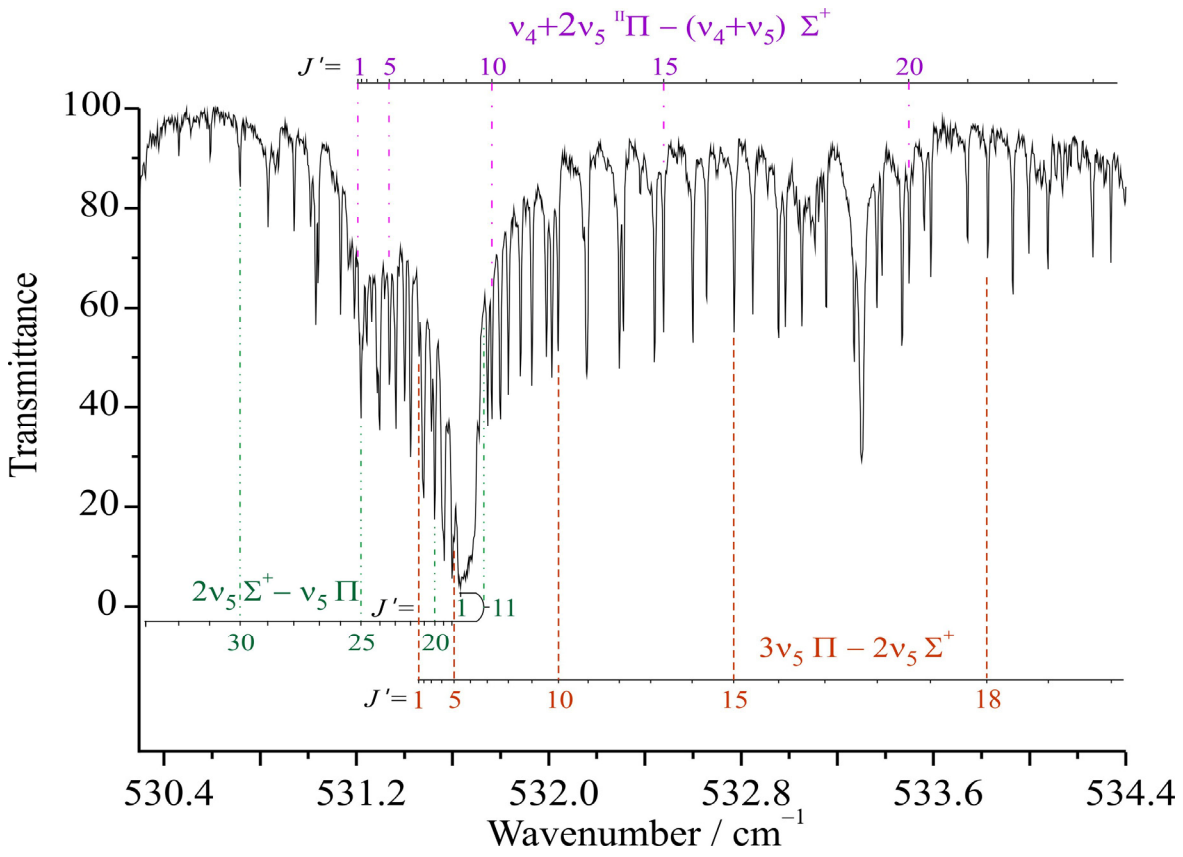

Figure 3.7: Portion of the infrared spectrum between 530.4 and 534.4 cm^{-1} showing the *Q* branches of three hot bands of ν_5. Experimental conditions: sample #2, condition of spectrum *c* in Table 3.12.

The region of the spectrum 950 – 1110 cm^{-1} contains the strong $\nu_4 + \nu_5$ (Σ^+) ← GS band at 1013.22 cm^{-1}, illustrated in Figure 3.8, and the hot bands, $2\nu_4 + \nu_5$ ($^{II}\Pi$) ← ν_4 (Π) and $\nu_4 + 2\nu_5$ ($^{II}\Pi$) ← ν_5 (Π). They are centred at 1035.61 and 1029.72 cm^{-1}, respectively. It is worth noting that the two strong bands centred at 1020.5 and 1030.3 cm^{-1} are the $2\nu_4$ (Σ^+) ← GS overtones of $H^{12}C^{13}CD$ and $H^{13}C^{12}CD$, respectively, indicated in red in the figure. The same band for $^{13}C^{12}CD_2$ is observed at 1013.22 cm^{-1}. The very weak $2\nu_5$ (Σ^+) ← GS overtone is detected at 1068.29 cm^{-1}.

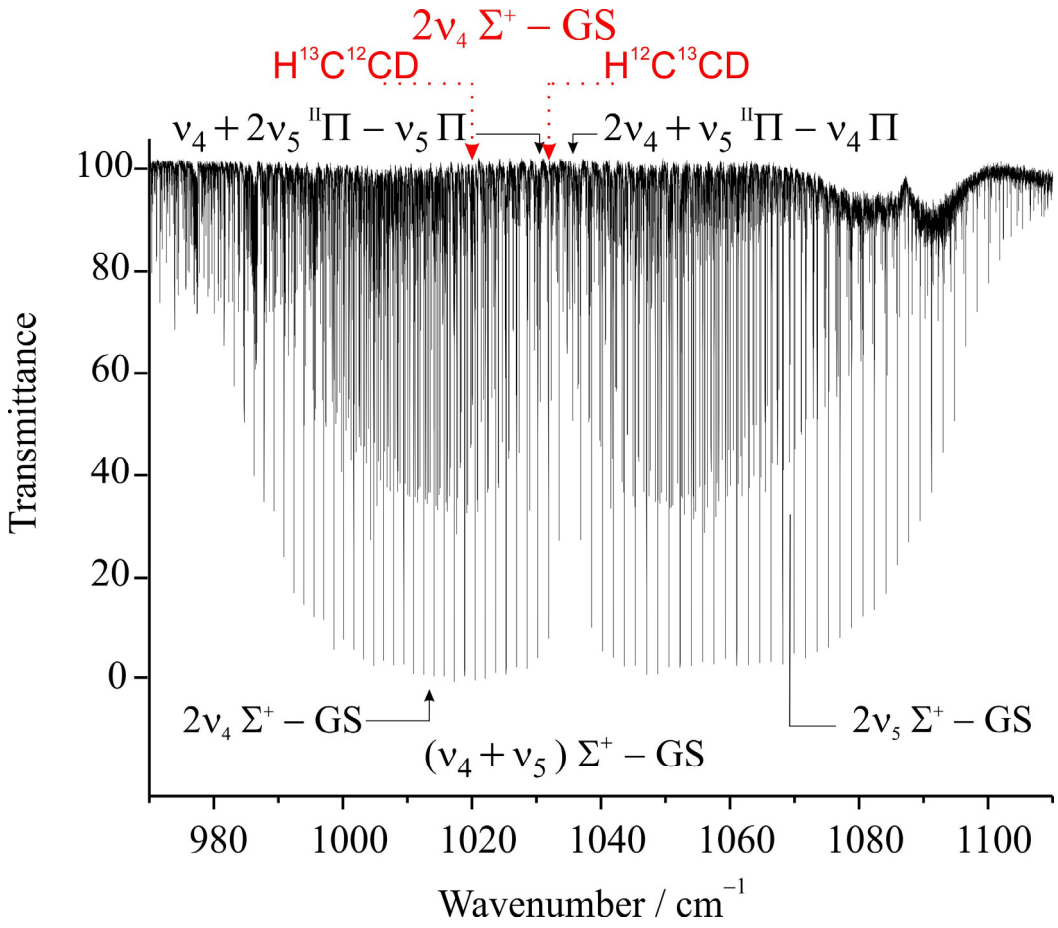

Figure 3.8: Portion of the infrared spectrum between 970 and 1110 cm^{-1} showing the bands present in this range for the different isotopologues. Experimental conditions: sample #2, condition of spectrum *b* in Table 3.12.

The intensity pattern is different from what observed in the fundamental bands, since the intensity of the $\nu_5 \leftarrow$ GS band is at least two orders of magnitude higher than that of the $\nu_4 \leftarrow$ GS band. In addition, the $3\nu_5 \leftarrow \nu_5$ band and the 'perturbation allowed' $\Delta(\ell_4 + \ell_5) = 2$, $2\nu_4$ (Δ_e) $\leftarrow$ GS and $\nu_4 + \nu_5$ (Δ_e) $\leftarrow$ GS bands were detected, whereas $2\nu_5$ (Δ_e) $\leftarrow$ GS is too weak to be observed in the adopted experimental conditions.

Finally, in the region between 1500 and 1900 cm^{-1} two $\Pi \leftarrow \Sigma^+$ transitions are detected, namely $2\nu_4 + \nu_5$ ($^{II}\Pi$) $\leftarrow$ GS and $3\nu_5$ (Π) $\leftarrow$ GS; the last one is illustrated in Figure 3.9. The strong lines randomly distributed in the figure correspond to ν_2 absorptions of water, which was used for calibration [20].

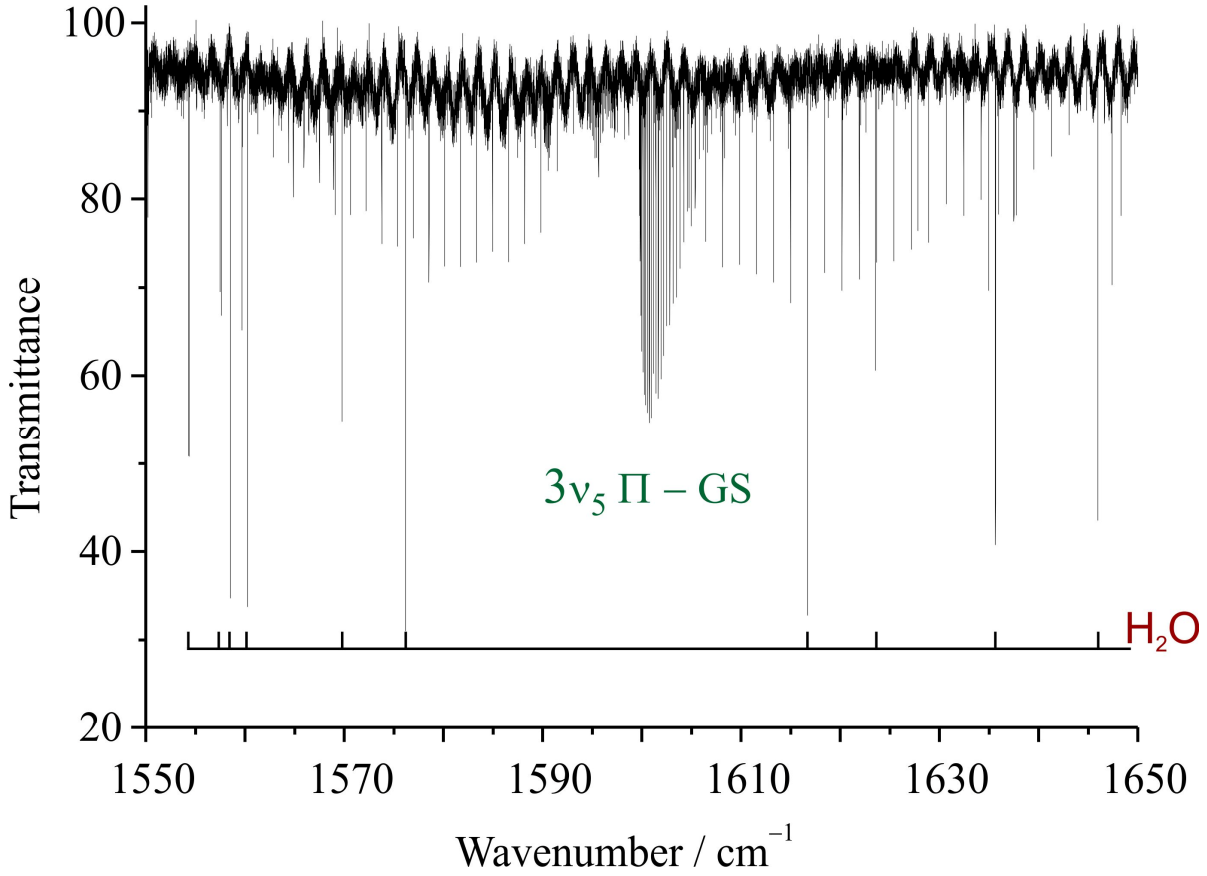

Figure 3.9: Portion of the infrared spectrum in the range 1550 – 1650 cm^{-1} showing the $3\nu_5$ Π overtone. Experimental conditions: sample #2, condition of spectrum *e* in Table 3.12.

3.2.3 Analysis

Di Lonardo *et al.* reported in Ref. [34] on the high resolution IR and Raman spectra of ν_2 and associated combination and hot bands for the molecule under study, together with a set of parameters for the ground and bending states with $v_{tot} \leq 2$, obtained from the simultaneous fit of 1361 IR transitions. During this work an extension of the observation and analysis of the pure bending transitions with v_{tot} up to 3 has been realised.

Table 3.13 collects all the analysed bending bands, together with the symmetry of the vibrational states involved in the transitions, the band centre, the observed range of *J"* values for the various branches, the RMS error resulting from the simultaneous least–squares analysis described below, and the number of fitted and assigned lines. In total, 27 vibrational bands have been characterized for $^{13}C^{12}CD_2$.

Table 3.13: Bands of $^{13}C^{12}CD_2$ included in the least–squares fitting procedures

Transition	Symmetry	ν_c [a]	P, R, Q (J_{min}, J_{max})	$\sigma(\times 10^5)$ [b]	number fitted/ assigned lines
(*a*) 450 – 600 cm^{-1}					
$\nu_4 \leftarrow$ G.S.	$\Pi \leftarrow \Sigma^+$	504.9732	$P_{e\text{-}e}$ (2-36); $R_{e\text{-}e}$ (0-42); $Q_{f\text{-}e}$ (1-37)	42	108/114
$\nu_5 \leftarrow$ G.S.	$\Pi \leftarrow \Sigma^+$	536.6340	$P_{e\text{-}e}$ (2-51); $R_{e\text{-}e}$ (0-51); $Q_{f\text{-}e}$ (1-51)	28	151/153
$2\nu_4 \leftarrow \nu_5$	$\Sigma^+ \leftarrow \Pi$	476.5902	$P_{e\text{-}e}$ (1-21); $R_{e\text{-}e}$ (1-29); $Q_{e\text{-}f}$ (1-29)	42	68/79
	$\Delta \leftarrow \Pi$	476.0933	$R_{e\text{-}e}$ (11-16); $Q_{e\text{-}f}$ (2-31)	41	33/36
$\nu_4 + \nu_5 \leftarrow \nu_4$	$\Sigma^+ \leftarrow \Pi$	530.2057	$P_{e\text{-}e}$ (1-44); $R_{e\text{-}e}$ (1-46); $Q_{e\text{-}f}$ (6-38)	43	113/124
	$\Sigma^- \leftarrow \Pi$	536.8154	$P_{f\text{-}f}$ (1-42); $R_{f\text{-}f}$ (1-45); $Q_{f\text{-}e}$ (1-42)	35	119/127
	$\Delta \leftarrow \Pi$	536.5953	$P_{e\text{-}e}$ (3-39); $R_{e\text{-}e}$ (1-37); $Q_{e\text{-}f}$ (2-36) $P_{f\text{-}f}$ (3-42); $R_{f\text{-}f}$ (1-44); $Q_{f\text{-}e}$ (2-41)	37	221/232
$2\nu_5 \leftarrow \nu_5$	$\Sigma^+ \leftarrow \Pi$	531.6524	$P_{e\text{-}e}$ (1-44); $R_{e\text{-}e}$ (1-46); $Q_{e\text{-}f}$ (1-39)	33	119/129
	$\Delta \leftarrow \Pi$	536.2430	$P_{e\text{-}e}$ (3-37); $R_{e\text{-}e}$ (1-40); $Q_{e\text{-}f}$ (2-41) $P_{f\text{-}f}$ (3-44); $R_{f\text{-}f}$ (1-45); $Q_{f\text{-}e}$ (2-43)	32	236/244
$2\nu_4 + \nu_5 \leftarrow 2\nu_4$	$^{II}\Pi \leftarrow \Sigma^+$	527.3632	$P_{e\text{-}e}$ (2-18); $R_{e\text{-}e}$ (0-13); $Q_{f\text{-}e}$ (1-27)	42	46/58
	$^{II}\Pi \leftarrow \Delta$	527.8602	$P_{e\text{-}e}$ (2-32); $R_{e\text{-}e}$ (2-30); $Q_{e\text{-}f}$ (4-30) $P_{f\text{-}f}$ (2-32); $R_{f\text{-}f}$ (2-36); $Q_{f\text{-}e}$ (2-26)	46	152/176
$\nu_4 + 2\nu_5 \leftarrow \nu_4 + \nu_5$	$^{II}\Pi \leftarrow \Sigma^+$	531.1800	$P_{e\text{-}e}$ (2-37); $R_{e\text{-}e}$ (0-39); $Q_{e\text{-}f}$ (1-29)	40	79/105
	$^{II}\Pi \leftarrow \Sigma^-$	524.5703	$P_{f\text{-}f}$ (3-25); $R_{f\text{-}f}$ (8-25); $Q_{e\text{-}f}$ (4-24)	45	47/62
	$^{II}\Pi \leftarrow \Delta$	524.7903	$P_{e\text{-}e}$ (2-24); $R_{e\text{-}e}$ (2-23); $Q_{e\text{-}f}$ (2-29) $P_{f\text{-}f}$ (2-28); $R_{f\text{-}f}$ (2-36); $Q_{f\text{-}e}$ (2-30)	44	125/164
$3\nu_5 \leftarrow 2\nu_5$	$\Pi \leftarrow \Sigma^+$	531.4496	$P_{e\text{-}e}$ (2-40); $R_{e\text{-}e}$ (0-41); $Q_{f\text{-}e}$ (1-27)	40	103/108
	$\Pi \leftarrow \Delta$	526.8590	$P_{e\text{-}e}$ (2-26); $R_{e\text{-}e}$ (2-26); $Q_{e\text{-}f}$ (2-31) $P_{f\text{-}f}$ (2-35); $R_{f\text{-}f}$ (2-35); $Q_{f\text{-}e}$ (2-32)	41	150/175
	$\Phi \leftarrow \Delta$	535.8696	$P_{e\text{-}e}$ (4-34); $R_{e\text{-}e}$ (2-36); $Q_{e\text{-}f}$ (3-16) $P_{f\text{-}f}$ (5-33); $R_{f\text{-}f}$ (2-36); $Q_{f\text{-}e}$ (3-13)	47	140/154
(*b*) 950 – 1700 cm^{-1}					
$2\nu_4 \leftarrow$ G.S.	$\Sigma^+ \leftarrow \Sigma^+$	1 013.2242	$P_{e\text{-}e}$ (1-35); $R_{e\text{-}e}$ (0-34)	33	65/70
	($\Delta \leftarrow \Sigma^+$) [c]	1 012.7272	$P_{e\text{-}e}$ (5-35); $R_{e\text{-}e}$ (4-35)	39	61/63
$\nu_4 + \nu_5 \leftarrow$ G.S.	$\Sigma^+ \leftarrow \Sigma^+$	1 035.1790	$P_{e\text{-}e}$ (1-50); $R_{e\text{-}e}$ (0-47)	34	87/98
	($\Delta \leftarrow \Sigma^+$) [c]	1 041.5685	$P_{e\text{-}e}$ (7-41); $R_{e\text{-}e}$ (4-38)	30	66/70
$2\nu_5 \leftarrow$ G.S.	$\Sigma^+ \leftarrow \Sigma^+$	1 068.2864	$P_{e\text{-}e}$ (1-33); $R_{e\text{-}e}$ (0-33)	37	64/67
$2\nu_4 + \nu_5 \leftarrow \nu_4$	$^{II}\Pi \leftarrow \Pi$	1 035.6142	$P_{e\text{-}e}$ (2-41); $R_{e\text{-}e}$ (1-35); $Q_{e\text{-}f}$ (10-20) $P_{f\text{-}f}$ (2-38); $R_{f\text{-}f}$ (1-35); $Q_{f\text{-}e}$ (1-15)	34	147/173
$\nu_4 + 2\nu_5 \leftarrow \nu_5$	$^{II}\Pi \leftarrow \Pi$	1 029.7250	$P_{e\text{-}e}$ (2-40); $R_{e\text{-}e}$ (1-35), $Q_{e\text{-}f}$ (2-20) $P_{f\text{-}f}$ (2-41); $R_{f\text{-}f}$ (1-40); $Q_{f\text{-}e}$ (1-17)	34	143/190
$3\nu_5 \leftarrow \nu_5$	$\Pi \leftarrow \Pi$	1 063.1021	$P_{e\text{-}e}$ (2-26); $R_{e\text{-}e}$ (1-25); $Q_{e\text{-}f}$ (1) $P_{f\text{-}f}$ (2-27); $R_{f\text{-}f}$ (1-22)	47	71/99
$2\nu_4 + \nu_5 \leftarrow$ G.S.	$^{II}\Pi \leftarrow \Sigma^+$	1 540.5874	$P_{e\text{-}e}$ (7-25); $R_{e\text{-}e}$ (7-14); $Q_{f\text{-}e}$ (5-25)	52	40/48
$3\nu_5 \leftarrow$ G.S.	$\Pi \leftarrow \Sigma^+$	1 599.7360	$P_{e\text{-}e}$ (2-30); $R_{e\text{-}e}$ (0-30); $Q_{f\text{-}e}$ (1-32)	39	90/92

[a] $\nu_C = G^0_{v'} - B_{v'}k^2 - D_{v'}k^4 - (G^0_{v''} - B_{v''}k^2 - D_{v''}k^4)$, as defined by Eq. (3.4).

[b] σ (in cm^{-1}) corresponds to the RMS value of the residuals for the various assigned lines resulting from the simultaneous fit.

[c] Perturbation allowed transition.

First, the spectrum below 600 cm^{-1} was analyzed and the assignment of the transitions belonging to the bands previously reported, namely $\nu_4 + \nu_5$ (Σ^+) ← ν_5 (Π), ν_5 (Π) ← GS, and $2\nu_5$ (Σ^+) ← ν_5 (Π) [35–37], was extended to higher J values. Then, transitions involving states not yet characterized were searched for, including the ν_4 fundamental. The assignment of the hot bands with v_{tot} up to 2 was accomplished using the ground, $v_4 = 1$ and $v_5 = 1$ state combination differences, which unambiguously defined the low energy vibrational state of the transitions. Once precise values of the LSCD for the $v_{tot} = 2$ states were determined, the search for transitions involving bending states with $v_{tot} = 3$ was undertaken. The assignment of the upper state was done by comparison of the band centres with those of the corresponding bands of $^{12}C_2D_2$ [31] and $^{13}C_2D_2$ [32]. All the components, Π and Φ, of the $v_5 = 3$ manifold were identified from $v_5 = 2$ (Σ^+ and Δ) in the region below 600 cm^{-1}, and the Π component was observed also from ν_5 at 1063.10 cm^{-1} and from the ground state at 1599.74 cm^{-1}. Differently, no transitions to the $v_4 = 3$, Π and Φ, states nor to the $^1\Pi$ and Φ states of the $v_4 = 1$, $v_5 = 2$ or $v_4 = 2$, $v_5 = 1$ manifolds could be identified, either in the low or in the high wavenumber region. The effects of strong ℓ–type interactions between rotation – vibration levels are evident in the intensity of the Q branch of the $2\nu_4$ (Δ) ← ν_5 (Π) band. In fact, only $Q_{e\text{-}f}$ transitions were observed, the $Q_{f\text{-}e}$ components being too weak to be detected. A similar behaviour was already pointed out for $^{12}C_2D_2$ [14] and for $^{13}C_2D_2$ [32].

The analysis was carried out in the same way as described in Section 3.1.3 for the bending modes of $^{12}C_2D_2$. At first the transition wavenumbers for each band were fitted separately to the upper state rotation–vibration parameters, in order to check the correctness of the assignments and to extend the data set. The data were analysed using the basic Hamiltonian of a linear molecule, with centrifugal distortion corrections up to the sextic power and ℓ – doubling energy contributions containing q_v, q_v^J and q_v^{JJ} coefficients. Afterwords, simultaneous fits of the experimental data were performed. The data set contains the rotation–vibration transitions listed in Table 3.13. The energies of the levels involved were obtained by diagonalizing the appropriate energy matrix containing the vibration (G^0), Eq. (2.8), and rotation (F), Eqs. from (2.10) to (2.13), diagonal contributions. Vibrational and rotational ℓ – type resonances are expressed by Eqs. (2.32), (2.33), (2.34) and (3.5). In addition, because

the ν_4 and ν_5 bending modes are separated by about 32 cm^{-1}, vibrational coupling of Darling–Dennison type is expected between levels of identical symmetry, such as $\upsilon_4 = 2$ (Σ^+ and Δ) and $\upsilon_5 = 2$ (Σ^+ and Δ), $\upsilon_4 = 1, \upsilon_5 = 2$ ($^{II}\Pi$, $^{I}\Pi$ and Φ) and $\upsilon_4 = 3$ (Π and Φ), $\upsilon_4 = 2, \upsilon_5 = 1$ ($^{II}\Pi$, $^{I}\Pi$ and Φ) and $\upsilon_5 = 3$ (Π and Φ). These interactions, which have been treated in detail for $^{12}C_2D_2$ [14] and in the previous Section 3.1 of this thesis, were taken into account in the global fitting procedures. Unfortunately, due to the lack of experimental data for the $\upsilon_4 = 3$ state, only the ℓ – type interactions were considered for the levels of the $\upsilon_4 = 1, \upsilon_5 = 2$ manifold. That is why, also the off–diagonal matrix elements expressed by Eq. (3.7) have been taken into account for interacting Σ^+ and Π states, and the parameters g_{45}^0 and r_{45}, as defined in Eqs. (2.23) and (2.32), for interacting Δ and Φ states. (The complete block–diagonalized matrices illustrating the ℓ – type and the Darling–Dennison interactions between the bending levels in the various vibrational manifolds are reported in Table 3.4, Section 3.1.3).

The weights of the experimental data were chosen proportional to the inverse of their squared estimated uncertainties, with the exclusion of the overlapping lines which were given zero weight. An uncertainty equal to 4.0×10^{-4} cm^{-1}, was assigned to each IR measurement, despite the fact that the lines had different S/N depending on their intensity and on the different experimental conditions of the recorded spectra. Finally, all the transition wavenumbers that differed from the corresponding calculated values by more than 0.001 cm^{-1} (2.5 times their estimated uncertainties) were excluded from the data set in the final cycle of the refinement.

3.2.4 Results and Discussion

In total, 3210 rotation vibration transitions were assigned to 27 bands involving bending states with $\upsilon_4 + \upsilon_5$ and $|\ell_4 + \ell_5|$ up to 3. Two separate global fits were performed, fit #1 and fit #2. Fit #1 has been realised taking into account only transitions involving states with υ_{tot} up to 2, while fit #2 includes also states with $\upsilon_{tot} = 3$. Fit #1 is necessary to obtain a consistent set of parameters before including in the dataset transitions with $\upsilon_{tot} = 3$. In addition, all bending states involving υ_{tot} up to 2 were experimentally characterised, allowing a thorough analysis of the Darling–Dennison interaction. Furthermore, in the future perspective of analysing the stretching–bending system, hot bands originate mostly from levels of the $\upsilon_{tot} \leq 2$ manifold. In total, 1512 out of 1606 transitions are retained in the final cycle of fit #1. 94 lines are rejected because they were overlapping, 75 of them, or exceeded the chosen limit for rejection of 0.001

cm^{-1}, 19. Unfortunately, some of the refined constants, i.e. x_{44}^0, x_{55}^0, g_{44}^0, g_{55}^0, and $K_{44,55}^0$ resulted 100% correlated. They were anyway refined since, if anyone of these parameters is constrained to zero and not refined, the fit quality degrades severely since the number of rejected lines as well as the RMS value increase substantially. Thirty–three statistically well–determined parameters obtained from fit #1 are listed in Table 3.14.

Table 3.14: Spectroscopic parameters (in cm^{-1}) resulting from simultaneous fit of all the levels with $v_4 + v_5 = 2$ of $^{13}C^{12}CD_2$

Parameter				Parameter			
ω_4^0		503.5590227	(916)	g_{44}^0		0.528580	(783)
ω_5^0		536.8457377	(553)	g_{45}^0		3.2164363	(295)
x_{44}^0		1.720677	(801)	g_{55}^0		2.168679	(799)
x_{45}^0		–1.5771690	(479)	r_{45}^0		–3.3048301	(407)
x_{55}^0		–1.545358	(798)	r_{45}^J	$\times 10^3$	0.086777	(129)
B_0		0.833118618	(476)				
α_4	$\times 10^3$	–1.942591	(479)	α_5	$\times 10^3$	–2.075082	(100)
γ_{44}	$\times 10^3$	–0.0127577	(719)	γ^{44}	$\times 10^3$	–0.011627	(460)
γ_{45}	$\times 10^3$	–0.001626	(128)	γ^{45}	$\times 10^3$	–0.079089	(105)
γ_{55}	$\times 10^3$	0.0092852	(365)	γ^{55}	$\times 10^3$	–0.0399346	(652)
D_0	$\times 10^6$	0.772401	(191)	δ_{45}	$\times 10^9$	–1.2342	(691)
β_4	$\times 10^6$	0.0208169	(752)	δ^{45}	$\times 10^9$	–1.3781	(975)
β_5	$\times 10^6$	0.0169939	(348)				
q_4^0	$\times 10^3$	3.167414	(118)	q_4^J	$\times 10^6$	–0.0214603	(918)
q_5^0	$\times 10^3$	3.1675169	(839)	q_5^J	$\times 10^6$	–0.0206686	(497)
q_{45}	$\times 10^3$	0.21576	(340)	q_5^k	$\times 10^3$	0.030631	(149)
ρ_5^0	$\times 10^6$	–0.002577	(104)				
ρ_{45}^0	$\times 10^6$	–0.005038	(322)	$K_{44,55}^0$		–6.49161	(132)
Number of fitted / assigned lines		1512 / 1606					
St. dev. of the fit $\times 10^4$		3.5					

These results can be compared with those obtained for $^{12}C_2D_2$, column 2 of Table 3.15, and $^{13}C_2D_2$, Table 2 in Ref. [32]. All the common parameters, but γ_{45}, ρ_5^0 and ρ_{45}^0, agree both in sign and order of magnitude. The differences between the parameters of the three molecules are in the range 0.2 – 10 %, with the exception of g_{44}^0 whose values differ by about 20 %. In addition, the leading vibrational and rotational parameters, ω_t^0, B_0, α_t, D_0, and the interaction constants q_t^0 show the expected trend associated with the increased molecular masses due to the isotopic substitution.

The parameters in Table 3.14 were chosen as a starting point for fit #2. The inclusion in the data set of transitions with $v_{tot} = 3$ made it necessary to refine additional constants, which are higher order dependences of the vibration and rotation parameters in Table 3.14. The Darling–Dennison interaction has been taken into account for the interacting $v_5 = 3$ and $v_4 = 2$, $v_5 = 1$ levels, despite the fact that the $^{I}\Pi$ and Φ states of the latter manifold were not detected. As a consequence, some of the refined parameters in fit #2 are effective. Several least–squares fits were performed with different choices of parameters which had to meet the following requirements. The parameters have to: a) correspond to lower–order ones previously refined; b) be statistically determined; c) adopt the correct order of magnitude; d) improve the quality of the fit; e) show low correlation. After each fit, the statistical significance of the obtained parameters was checked as well as their correlation coefficients.

In total, 2450 out of 2689 transition wavenumbers were retained in the final cycle of the least–squares procedure. Two hundred and thirty–nine lines were excluded from the fit, because they were overlapping (187) or exceeded the chosen limit for rejection (52). The standard deviation of the fit, equal to 3.9×10^{-4} cm^{-1}, is again very close to the estimated precision of the measurements.

The lack of experimental observations involving $v_4 = 3$ prevented the treatment of the Darling–Dennison interaction with $v_4 = 1$, $v_5 = 2$ states. So, the hot bands involving the $\nu_4 + 2\nu_5$ $^{II}\Pi$ state in Table 3.13 were fitted apart simultaneously considering only the ℓ – type interaction. Only transitions with J up to 30 were considered to refine the parameters in Eq. (3.2). In total, 394 out of 462 transition wavenumbers were retained in the final cycle of the least–squares procedure, with a standard deviation of the fit equal to 4.0×10^{-4} cm^{-1}. The set of obtained parameters is reported at the bottom of Table 3.15.

Table 3.15: Spectroscopic parameters (in cm^{-1}) resulting from the simultaneous fit of all the levels with $v_4 + v_5 = 3$ of $^{13}C^{12}CD_2$

Parameter				Parameter			
ω_4^0		503.5544841	(771)	g_{44}^0		0.5557629	(659)
ω_5^0		536.8590584	(766)	g_{45}^0		3.373394	(815)
x_{44}^0		1.6980310	(850)	g_{55}^0		2.1493075	(562)
x_{45}^0		−1.796163	(591)	y_4^{45}		−0.157040	(810)
x_{55}^0		−1.5436945	(908)	y_5^{55}		−0.0038060	(110)
y_{445}		0.218922	(579)	r_{45}^0		−3.3048625	(443)
y_{555}		0.0082752	(142)	r_{45}^J	$\times 10^3$	0.087166	(143)
				r_{45}^{JJ}	$\times 10^6$	0.003335	(120)
B_0		0.833118452	(416)	γ_{445}	$\times 10^3$	0.029001	(482)
α_4	$\times 10^3$	−1.945954	(172)	γ_{555}	$\times 10^3$	−0.0007510	(163)
α_5	$\times 10^3$	−2.073341	(107)	γ^{44}	$\times 10^3$	−0.0151602	(646)
γ_{44}	$\times 10^3$	−0.0127101	(665)	γ^{45}	$\times 10^3$	−0.125865	(781)
γ_{45}	$\times 10^3$	−0.027179	(503)	γ^{55}	$\times 10^3$	−0.0398678	(162)
γ_{55}	$\times 10^3$	0.0114502	(719)	γ_4^{45}	$\times 10^3$	0.047603	(759)
D_0	$\times 10^6$	0.772277	(183)	β_5	$\times 10^6$	0.0168805	(315)
β_4	$\times 10^6$	0.0206989	(776)	δ_{45}	$\times 10^9$	−1.1592	(725)
q_4^0	$\times 10^3$	3.247345	(261)	q_{55}	$\times 10^3$	0.0283192	(367)
q_5^0	$\times 10^3$	3.139017	(103)	q_4^J	$\times 10^6$	−0.0210648	(846)
q_{44}	$\times 10^3$	−0.080390	(225)	q_5^J	$\times 10^6$	−0.0205800	(465)
q_{45}	$\times 10^3$	−0.016761	(171)	q_4^k	$\times 10^3$	0.077396	(231)
ρ_5^0	$\times 10^9$	−2.2807	(388)				
ρ_{45}^0	$\times 10^9$	−9.528	(370)	$K_{44,55}^0$		−6.06725	(122)

Number of fitted / assigned lines	2450 / 2689
St. dev. of the fit $\times 10^4$	3.9

Parameter [a]			Parameter [a]		
G^0_{455}	1566.3588694	(454)	q^0_{455} $\times 10^3$	6.224095	(649)
B_{455}	0.839354476	(546)	q^J_{455} $\times 10^6$	–0.06831	(235)
D_{455} $\times 10^6$	1.51798	(158)	q^{JJ}_{455} $\times 10^9$	–0.32450	(199)
H_{455} $\times 10^{12}$	–7.45	(122)			
Number of fitted / assigned lines	394 / 462				
St. dev. of the fit $\times 10^4$	4.0				

[a] Fit of the bands reaching the $v_4 = 1$, $v_5 = 2$ ($^{II}\Pi$) state, see text.

The selected set, which is reported in Table 3.15, contains 42 statistically well–determined parameters. Most of the parameters are essentially uncorrelated, but, in contrast, x^0_{45}, y_{445}, y^{45}_4, and g^0_{45}, are strongly correlated.

A few parameters of the model listed in Eqs. (2.8) to (2.13) and (3.12), which are not reported in Tables 3.14 and 3.15, were nevertheless allowed to vary in the fitting procedure, but they resulted statistically undetermined and were constrained to zero. A comparison between the results of fits #1 and #2 shows that the values of the leading parameters are consistent and their signs unchanged. The largest differences (> 50%) are observed between the constants related to the characterization of the manifolds with simultaneous excitation of the ν_4 and ν_5 modes, γ_{45}, γ^{45}, q_{45}, and ρ^0_{45}. Moreover, γ_{45} and q_{45} have opposite sign. Finally, a list of the vibrational term values G^0_c of the states for $^{13}C^{12}CD_2$ is reported in Table 3.16.

Table 3.16: Vibrational term values (in cm^{-1}) on the observed levels involving bending modes of $^{13}C^{12}CD_2$

υ_4	υ_5	Symmetry	ℓ_4	ℓ_5	G_c^0
1	0	Π	±1	0	504.9732
0	1	Π	0	±1	536.6340
2	0	Σ^+	0	0	1013.2242
2	0	Δ	±2	0	1012.7273
1	1	Σ^+	1	−1	1035.1790
1	1	Σ^-	−1	1	1041.7887
1	1	Δ	±1	±1	1041.5685
0	2	Σ^+	0	0	1068.2864
0	2	Δ	0	±2	1072.8770
2	1	$^{II}\Pi$	±2	∓1	1540.5874
1	2	$^{II}\Pi$	±1	0	1566.3589
0	3	Π	0	±1	1599.7360
0	3	Φ	0	±3	1608.7466

3.3 $H^{13}C^{12}CD$, $H^{12}C^{13}CD$, $^{13}C^{12}CD_2$: 6200 – 6800 cm^{-1}

Rare acetylene isotopologues have received so far less attention compared to the others. In 2007 Hardwick *et al.* [38] recorded a diode laser spectrum of $H^{12}C^{13}CD$ and $H^{13}C^{12}CD$ in the region around 6500 cm^{-1}, studied the first overtone of ν_1 and improved the values of the ground state parameters B_0 and D_0. In the same year, Fusina *et al*. [39] reported on the high resolution IR spectra of the two isotopologues in the region 470 – 5200 cm^{-1}, whereas, more recently, the bending states up to $\upsilon_4 + \upsilon_5 = 2$ have been characterized [30]. In order to extend the observation in the region above 6000 cm^{-1} for these 3 isotopologues, whose concentration in the sample is between 20% and 30%, a more sophisticated and sensitive apparatus than the conventional FT spectrometer has been adopted in the present study. In fact the investigation of overtone spectrum, in particular, fostered the development of new instrumental techniques [40]. A femto comb based technique, supported by conventional FTIR experiments, has been employed to investigate absorption bands belonging to the rare isotopologues $H^{13}C^{12}CD$, $H^{12}C^{13}CD$, $^{13}C^{12}CD_2$ in the range 6130 – 6800 cm^{-1}.

3.3.1 Experiment

As far as the sample is concerned, the synthesis is described in Section 3.2.1.

FTIR spectra were recorded in Bologna using a BomemDA3.002 interferometer. The region 5000 – 7800 cm^{-1} was recorded by using a quartz source, a KBr beam splitter and an InSb type detector, operating at liquid nitrogen temperature. A sample pressure of 373 Pa was used, the optical path was 10 m and the instrumental resolution 0.01 cm^{-1}, the maximum achievable because of the Doppler broadening around 6500 cm^{-1}. 2000 scans were co–added in order to improve the signal–to–noise ratio. Rovibration transition of H_2O [41] were used for calibration.

The femto–Fourier transform–cavity enhanced absorption spectroscopy (femto–FT–CEAS) instrument is set in Brussels. The experimental setup, described in detail in Ref. [42–44] is shown in Figure 3.10. It is based on a Ti:Sa femtosecond laser, with a repetition rate of 80 MHz (Coherent Chamaleon Ultra II) and 140 fs laser pulse width, which is used to pump an OPO (Optical Parametric Oscillator, Coherent PP810) module, allowing for broader wavelength coverage towards the IR (generally called Laser in Fig 3.10). The output light spans the range 1000 – 1640 nm with a typical bandwidth of 100 cm^{-1}.

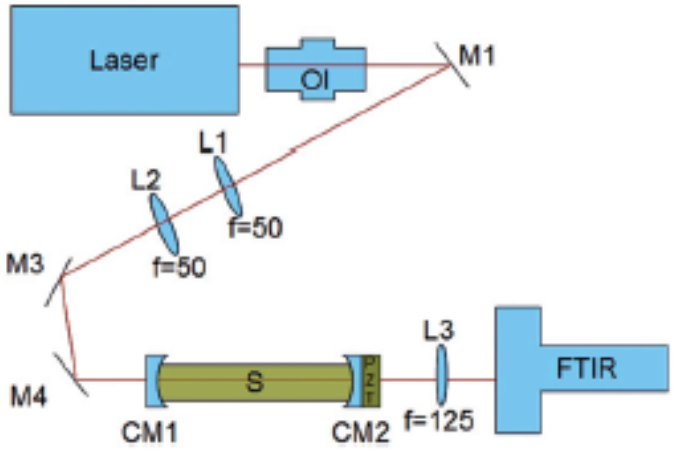

Figure 3.10: Experimental setup for femto–FT–CEAS with an OPO tunable source. Laser Ti:Sa, OPO signal or Idler; OI: HoYag optical isolator; M1, L1, L2, M3, M4, L3: steering optics; CM1 and CM2: high reflectivity cavity mirrors, PZT: piezoelectric modulator. Figure taken from Ref. [43].

The comb laser beam was sent through a HoYag type optical Faraday isolator (Thorlabs) in order to avoid optical feedback in the laser oscillator (OI in Fig 3.10), before being injected into an external cavity. Proper mode matching in the absorption cavity is achieved using a pair of lenses with focal length f = 50mm. The cavity has a length *L* of 77 cm and is made of half – inch

output couplers (CM1 and CM2, Layertec). The output cavity mirror is set on the piezoelectric translator (PZT), from Newtronics Model 200P, up to the maximum delivered frequency (20kHz). It is necessary in order to modulate the cavity length. By this way, cavity modes are jittering and every laser mode is about equally transmitted on average, and the noise level is reduced. Conditions must be adapted empirically by tuning the cell length to a slightly different value for each selected central wavelength and for each sample pressure conditions to optimise this fringing smoothing effect. The reflectivity of the mirrors is ~99.997 % in the central part of the explored spectral range. It corresponds to a finesse, defined as $F = \frac{\pi^4 \sqrt{R_1 R_2}}{1-\sqrt{R_1 R_2}}$, where R_1 and R_2 are the reflectivities of the two mirrors, equal to 90000. The equivalent pathlength L_{eq}, defined $L_{eq} = \frac{FL}{\pi}$, is about 12000 m at 6500 cm^{-1}. The laser beam exiting the absorption cavity was directed into the high resolution continuous scanning FTIR (Bruker IFS120HR) equipped with an InGaAs diode detector. The entrance FTIR iris was set to 1.5 mm, that is larger than the laser beam diameter focused to 10 μm at the FTIR entrance using a 125 mm focal lens (L3). These conditions correspond to a minimal absorption coefficient of 5×10^{-9} cm^{-1}. The FTIR resolution was 0.02 cm^{-1} and this is the main resolution–limiting factor, also accounting for the comb structure of the absorption source (80 MHz or 2.4×10^{-3} cm^{-1} free spectral range). The number of scans accumulated varied between 100 and 320, depending on the band strength and the noise conditions. Conditions for each spectrum are reported in Table 3.17.

Table 3.17: Experimental condition for each femto–FT–CEAS recorded spectrum

Spectrum	Pressure of the sample (Pa)	Range (cm^{-1})	Resolution (cm^{-1})	#Scans	Optical pathlenght (km)
1	1443.6	6530 – 6650	0.02	200	6
2	1443.6	6650 – 6800	0.02	200	6
3	1443.6	6130 – 6390	0.02	200	6
4	380.0	6300 – 6500	0.02	200	6
5	380.0	6450 – 6620	0.02	200	6
6	1333.3	6600 – 6750	0.02	200	12
7	1333.3	6320 – 6450	0.02	200	8
8	1333.3	6240-6400	0.02	200	6

The calibration of the spectra was performed using the transition wavenumbers of the $2\nu_3$ and $\nu_1 + \nu_3$ bands of $H^{13}C^{12}CH$ [45, 46].

The sensitivity achieved with the femto–FT–CEAS experiment is best illustrated when comparing spectra of the same sample recorded using conventional FTIR and femto–FT–CEAS set–ups, as shown in Fig. 3.11.

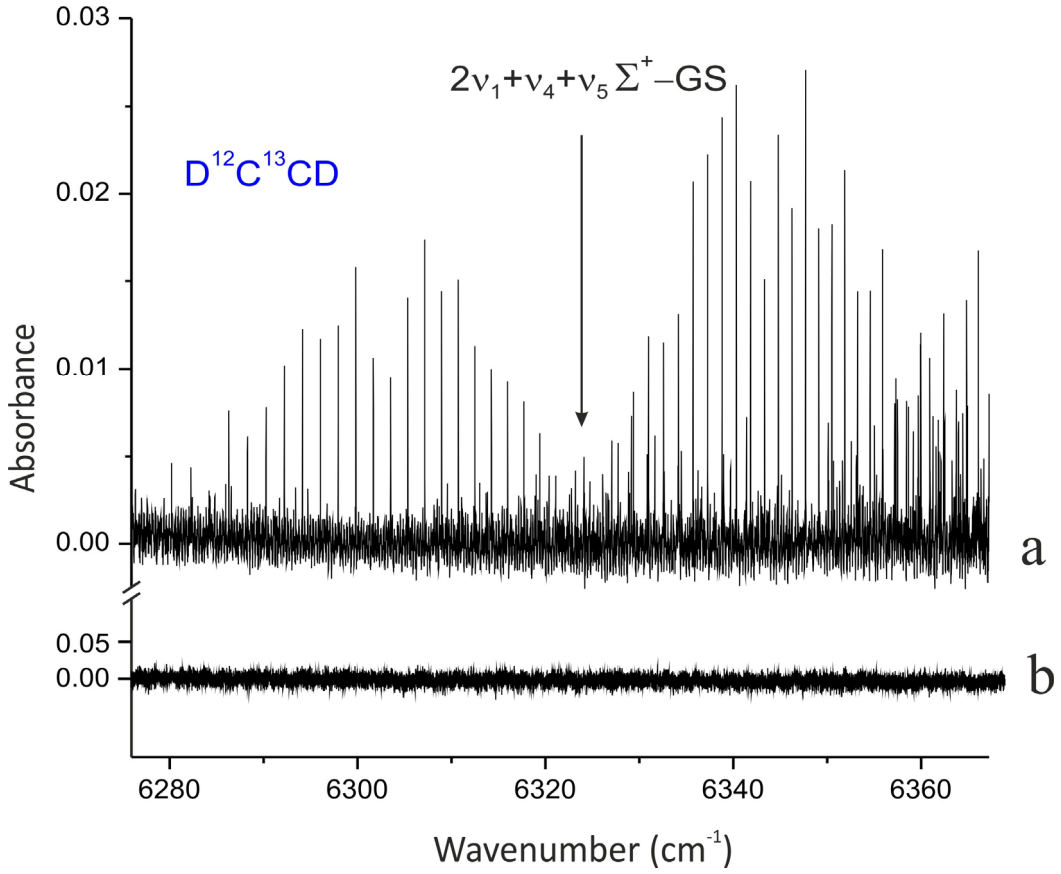

Figure 3.11: Portion of the spectrum between 6275 and 6370 cm^{-1}, showing the $2\nu_1 + \nu_4 + \nu_5 \leftarrow GS$ band of $D^{12}C^{13}CD$ centred at 6324 cm^{-1}. Experimental conditions: a) Femto–FT–CEAS apparatus, with conditions of spectrum *8* in Table 3.17, b) Bomem DA3.002 spectrum, optical path 10 m, pressure 379 Pa, resolution: 1.0×10^{-2} cm^{-1}, number of scans: 2000.

3.3.2 Analysis, Results and Discussion

The spectra appear all very congested, due to the presence of four isotopologues of acetylene. Furthermore, in some regions of the spectra the presence of traces of partially deuterated mono–^{13}C–ethylene complicates even more its interpretation, in particular in the

lower wavenumber side. The most intense lines actually belong to the $\nu_1 + \nu_3$ band of $H^{13}C^{12}CH$. An overview of the central part of the investigated region is shown in Figure 3.12.

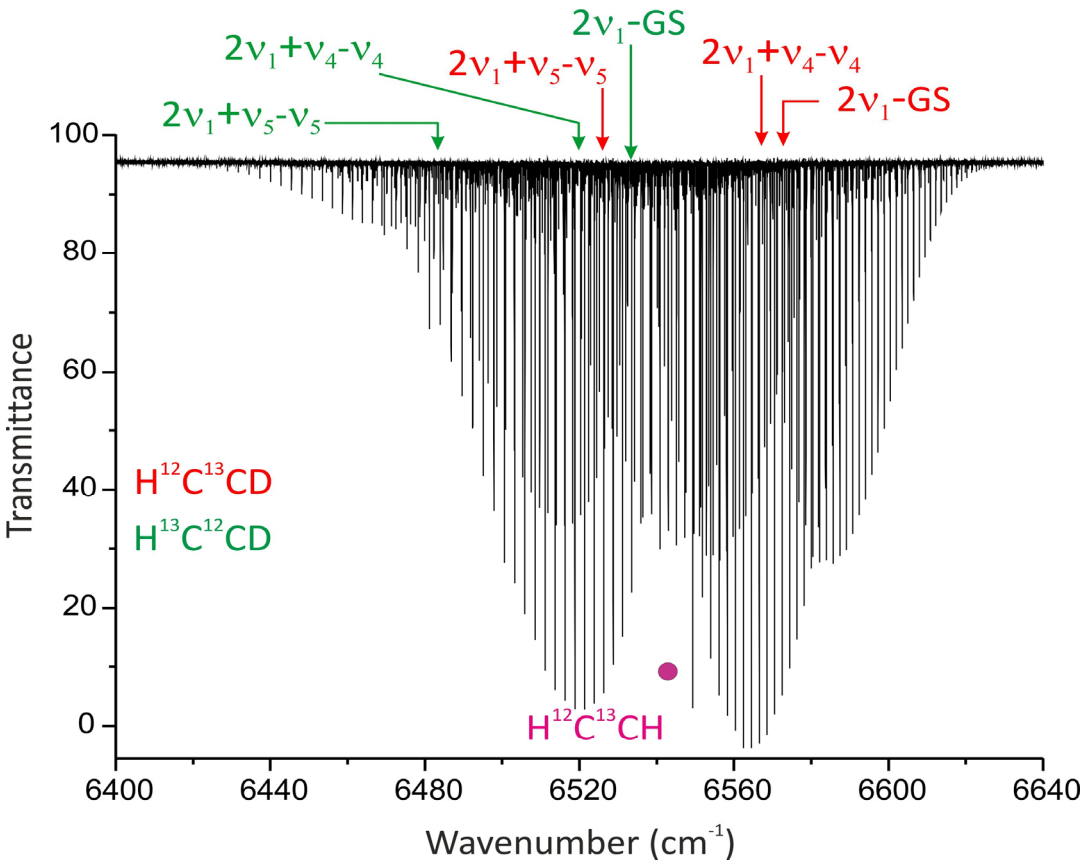

Figure 3.12: Portion of the infrared spectrum between 6400 and 6640 cm^{-1}, showing the density of signals due to the different molecules present in the sample. Experimental conditions: Bomem DA3.002 spectrum, optical path 10 m, pressure 379 Pa, resolution: 1.0×10^{-2} cm^{-1}, number of scans: 2000.

The identification of the vibrational states involved in each band and the assignment of the transitions was facilitated using precise values of the LSCD for each molecule.

Concerning the band of $^{13}C^{12}CD_2$ in Fig. 3.11, only the Σ^+ upper level of the $2\nu_1 + \nu_4 + \nu_5$ manifold has been observed. The $\Delta_{(e)}$ – GS perturbation allowed transitions are too weak to be detected in the spectrum. Three other bands belonging to the same species have been observed in the investigated region, $\nu_1 + \nu_2 + \nu_3 \leftarrow \text{GS}$ and the associated (Π–Π) hot bands $\nu_1 + \nu_2 + \nu_3 + \nu_4 \leftarrow \nu_4$ and $\nu_1 + \nu_2 + \nu_3 + \nu_5 \leftarrow \nu_5$, located at about 6780, 6755 and 6768 cm^{-1}, respectively. They are shown in Fig. 3.13.

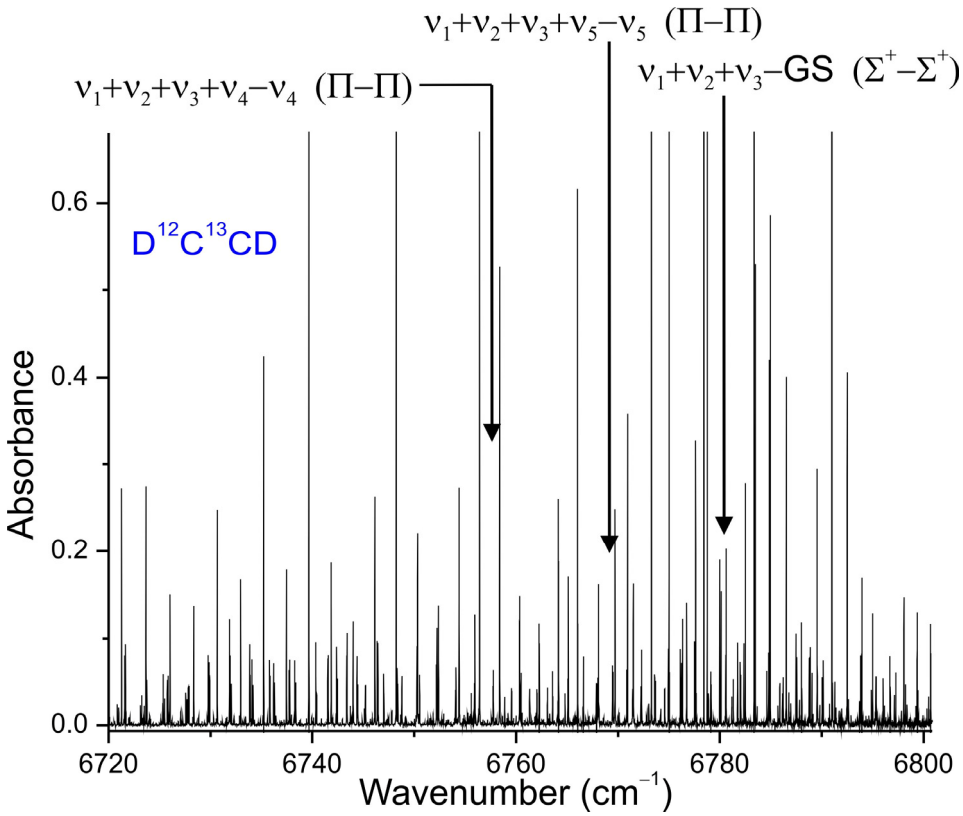

Figure 3.13: Portion of the spectrum between 6720 and 6800 cm^{-1}, showing the $\nu_1 + \nu_2 + \nu_3 \leftarrow GS$ transition with associated hot bands from ν_4 and ν_5. Experimental conditions: spectrum *2* in Table 3.17.

All the bands observed in the investigated region belonging to the three isotopologues are reported in Table 3.18, together with their band centres, the observed branches and the standard deviation of each band–by–band fit.

Table 3.18: Observed and analysed transitions for the three isotopologues

Isotopologue	Transition	Symmetry	ν_C [a]	*P*; *R*; (J_{min}, J_{max})	σ ($\times 10^3$) [b]	n. fitted/ assig. lines
$H^{12}C^{13}CD$	$2\nu_1 + \nu_5 \leftarrow \nu_5$	$\Pi \leftarrow \Pi$	6530.6125	$P_{e\text{-}e}$ (2-26); $R_{e\text{-}e}$ (1-28); $P_{f\text{-}f}$ (2-26); $R_{f\text{-}f}$ (1-29)	1.76	77/104
	$2\nu_1 + \nu_4 \leftarrow \nu_4$	$\Pi \leftarrow \Pi$	6556.8156	$P_{e\text{-}e}$ (2-31); $R_{e\text{-}e}$ (1-28); $P_{f\text{-}f}$ (2-31); $R_{f\text{-}f}$ (1-28)	1.70	93/116
	$2\nu_1 \leftarrow GS$	$\Sigma^+ \leftarrow \Sigma^+$	6565.4918	$P_{e\text{-}e}$ (1-40); $R_{e\text{-}e}$ (1-47)	0.32	74/88
$H^{13}C^{12}CD$	$2\nu_1 + \nu_5 \leftarrow \nu_5$	$\Pi \leftarrow \Pi$	6502.5194	$P_{e\text{-}e}$ (3-25); $R_{e\text{-}e}$ (1-23); $P_{f\text{-}f}$ (3-25); $R_{f\text{-}f}$ (1-23)	1.66	44/90
	$2\nu_1 + \nu_4 \leftarrow \nu_4$	$\Pi \leftarrow \Pi$	6527.4129	$P_{e\text{-}e}$ (2-24); $R_{e\text{-}e}$ (1-24); $P_{f\text{-}f}$ (2-25); $R_{f\text{-}f}$ (1-24)	1.44	62/95
	$2\nu_1 \leftarrow GS$	$\Sigma^+ \leftarrow \Sigma^+$	6536.3375	$P_{e\text{-}e}$ (1-44); $R_{e\text{-}e}$ (0-44)	0.32	65/87

$D^{12}C^{13}CD$	$2\nu_1+\nu_4+\nu_5 \leftarrow GS$	$\Sigma^+ \leftarrow \Sigma^+$	6324.4484	$P_{e\text{-}e}$ (1-24); $R_{e\text{-}e}$ (0-30)	1.12	44/55
	$\nu_1+\nu_2+\nu_3+\nu_4 \leftarrow \nu_4$	$\Pi \leftarrow \Pi$	6755.5980	$P_{e\text{-}e}$ (2-34); $R_{e\text{-}e}$ (1-28); $P_{f\text{-}f}$ (2-34); $R_{f\text{-}f}$ (1-28)	1.17	86/122
	$\nu_1+\nu_2+\nu_3+\nu_5 \leftarrow \nu_5$	$\Pi \leftarrow \Pi$	6768.1405	$P_{e\text{-}e}$ (2-35); $R_{e\text{-}e}$ (1-25); $P_{f\text{-}f}$ (2-37); $R_{f\text{-}f}$ (1-25)	1.09	91/120
	$\nu_1+\nu_2+\nu_3 \leftarrow GS$	$\Sigma^+ \leftarrow \Sigma^+$	6780.0709	$P_{e\text{-}e}$ (1-44); $R_{e\text{-}e}$ (0-34)	0.41	76/78

a In cm^{-1}.ν_C is defined by Eq.(3.3).

b σ (in cm^{-1}) corresponds to the standard deviation of the fit.

The transition wavenumbers for each band were fitted separately to the upper state rovibrational parameters by a least–squared procedure. The parameters for the lower states involved in the investigated transitions are from Ref. [30] for $H^{13}C^{12}CD$ and $H^{12}C^{13}CD$, and from Ref. [34] for $^{13}C^{12}CD_2$. The basic Hamiltonian for a linear molecule, with distortion corrections up to high power in the rotational angular momentum, was used for the analysis. In case of transitions involving doubly degenerate Π states, ℓ – doubling contribution are included. The rovibrational term values are given by Eq. (3.2), the centre energy is expressed by Eq. (3.3) and the band centre by Eq.(3.4).

Unit weights were assigned to measurements for well isolated lines, while the weights were reduced to $1/n$ if n transitions were assigned to the same wavenumber. Finally, the transitions that differed from their corresponding calculated values by more than 2.0×10^{-3} cm^{-1} or 1.0×10^{-3} cm^{-1}, depending on the S/N, were excluded from the data set in the final cycle of the refinement. The spectroscopic parameters obtained for the analysed bands are reported in Table 3.19.

Table 3.19: Band centres and spectroscopic parameters (in cm^{-1}) for the analyzed bands of $H^{12}C^{13}CD$, $H^{13}C^{12}CD$ and $D^{12}C^{13}CD$

Isotopologue	Transition	Symmetry	ν_C	B	$D\times10^6$	$H\times10^9$	$q\times10^3$	$q^J\times10^6$	$q^{JJ}\times10^9$
$H^{12}C^{13}CD$	$2\nu_1+\nu_5\leftarrow\nu_5$	$\Pi\leftarrow\Pi$	6530.61255(45)	0.9675811(29)	1.1387(38)		3.4716(33)	–0.0702(54)	
	$2\nu_1+\nu_4\leftarrow\nu_4$	$\Pi\leftarrow\Pi$	6556.81562(41)	0.9679751(25)	1.1053(30)		4.3077(30)	–0.0552(44)	
	$2\nu_1\leftarrow GS$	$\Sigma^+\leftarrow\Sigma^+$	6565.49176(65)	0.96568621(19)	1.085120(96)				
$H^{13}C^{12}CD$	$2\nu_1+\nu_5\leftarrow\nu_5$	$\Pi\leftarrow\Pi$	6502.51936(57)	0.9592614(94)	1.0791(94)		3.7325(22)		
	$2\nu_1+\nu_4\leftarrow\nu_4$	$\Pi\leftarrow\Pi$	6527.41292(63)	0.9583349(93)	0.483(36)	–0.330(37)	3.0986(96)	0.695(48)	–0.594(56)
	$2\nu_1\leftarrow GS$	$\Sigma^+\leftarrow\Sigma^+$	6536.33754(81)	0.95773678(49)	1.10171(68)	–0.0890(25)			
$D^{12}C^{13}CD$	$2\nu_1+\nu_4+\nu_5\leftarrow GS$	$\Sigma^+\leftarrow\Sigma^+$	6324.44837(38)	0.8262657(44)	2.678(12)	0.4227(89)			
	$\nu_1+\nu_2+\nu_3+\nu_4\leftarrow\nu_4$	$\Pi\leftarrow\Pi$	6755.59808(25)	0.8221048(14)	0.7873(14)		3.2574(17)	–0.0250(21)	
	$\nu_1+\nu_2+\nu_3+\nu_5\leftarrow\nu_5$	$\Pi\leftarrow\Pi$	6768.14047(22)	0.8221417(11)	0.78726(96)		3.1930(14)	–0.0264(15)	
	$\nu_1+\nu_2+\nu_3\leftarrow GS$	$\Sigma^+\leftarrow\Sigma^+$	6780.07093(98)	0.82010234(72)	0.77905(95)	0.00472(37)			

Consistent values for the rotational and quartic distortion constants are obtained, with just few exceptions. The analysis evidenced that the majority of the bands resulted unperturbed, since the values of the refined parameters are not too far from the corresponding ones in the ground state and in $\upsilon_4 = 1$ and $\upsilon_5 = 1$ states [39]. For the two bands $2\nu_1 + \nu_4 \leftarrow \nu_4$ of $H^{13}C^{12}CD$ and $2\nu_1 + \nu_4 + \nu_5 \leftarrow GS$ of $^{13}C^{12}CD_2$, *D* and *H* distortion constants had to be refined in order to reproduce the experimental data. However, their values are anomalous. This suggests the presence of some kind of perturbation, which could not be identified nor assigned from the present data. As far as $2\nu_1$ bands of mixed isotopomers are concerned, results achieved in this study can be compared to the ones from Ref. [38]. The assignment of the transitions belonging to these bands was extended up to *J"* = 47 for $H^{12}C^{13}CD$ and *J"* = 44 for $H^{13}C^{12}CD$. The new spectroscopic parameters agree with those in Ref. [38], but the *D* constants are more precise.

3.4 DCCF

Monofluoroacetylenes, HCCF and DCCF, have been the subject of spectroscopic investigations for several reasons: to verify the linearity of the molecular structure, providing also the values of the internuclear distances [47,48], to determine the energies of fundamental and multiply excited vibrational levels [49–53], and to test the suitability of the molecules for experiments using CO_2 lasers. In fact, these molecules are good candidates for laser Stark and laser microwave double resonance experiments since the ν_3 (C–F stretching) infrared fundamental band strongly absorbs at about 10 μm [54,55]. Contrary to HCCF, spectroscopic information about DCCF is really scarce. Only the fundamental stretching bands and some bands involving bending modes, namely $\nu_4 \leftarrow GS$, $2\nu_4 \leftarrow GS$ and $\nu_4 + \nu_5 \leftarrow GS$, have been analysed, and no study of the region above 3800 cm^{-1} has been performed. In Table 3.20 are listed the normal modes of vibration for DCCF.

Table 3.20: Normal modes of DCCF

Band	Symmetry	Wavenumber (cm^{-1})
ν_1	Σ^+	2645.1 [56]
ν_2	Σ^+	2088.1 [56]
ν_3	Σ^+	1045.9 [57]
ν_4	Π	439.0 [58]
ν_5	Π	364.0 [56]

As far as the bending modes are concerned, ν_4 has been investigated at a medium resolution (about 0.03 cm^{-1}) [58], while for ν_5 a rovibration analysis has not been accomplished. That is why a systematic investigation of all the bands involving bending modes detected in the region 320 – 800 cm^{-1} has been performed, including states with v_{tot} up to 3.

3.4.1 Experiment

The sample, which is a gift from Prof. I.M. Mills (Reading, UK), has been prepared by passing HCCF through a solution of NaOD in D_2O. Spectra were recorded in Wuppertal employing a Bruker 120HR interferometer. Two spectra, namely #1 and #2, were recorded by equipping the spectrometer with a Globar source, a 3.5m Mylar beamsplitter and a liquid He−cooled Cu:Ge detector operating at 4.2 K temperature. A glass cell measuring 0.280 m length and outfitted with CsBr windows was used throughout. General conditions are reported in Table 3.21.

Table 3.21: Experimental conditions for the recording of DCCF spectra

Spectrum	Pressure of the sample (Pa)	Range (cm^{-1})	Source	Detector	Resolution (cm^{-1})	#Scans	Optical pathlenght (m)
#1	950	320 – 700	Globar	Cu:Ge	0.0031	330	0.28
#2	200	350 – 850	Globar	Cu:Ge	0.0024	880	0.28

Calibration was done by comparison with lines belonging to the ν_2 band of residual CO_2 in the vacuum interferometer. The reference wavenumbers were taken from [22]. The estimated accuracy of the spectra is: spectrum #1 better than 3×10^{-4} cm^{-1}, spectrum #2 better than 2×10^{-4} cm^{-1}. The precision of isolated, medium to strong, unblended lines in spectrum #1 is better than 2×10^{-4} cm^{-1}, in spectrum #2 better than 1×10^{-4} cm^{-1}.

3.4.2 Description of the spectra

a) The 320 – 400 cm^{-1} region

The ν_5 fundamental band is located at lowest wavenumbers, and its intensity can be considered as medium if compared to the ν_4 strong band. It is shown in Figure 3.14.

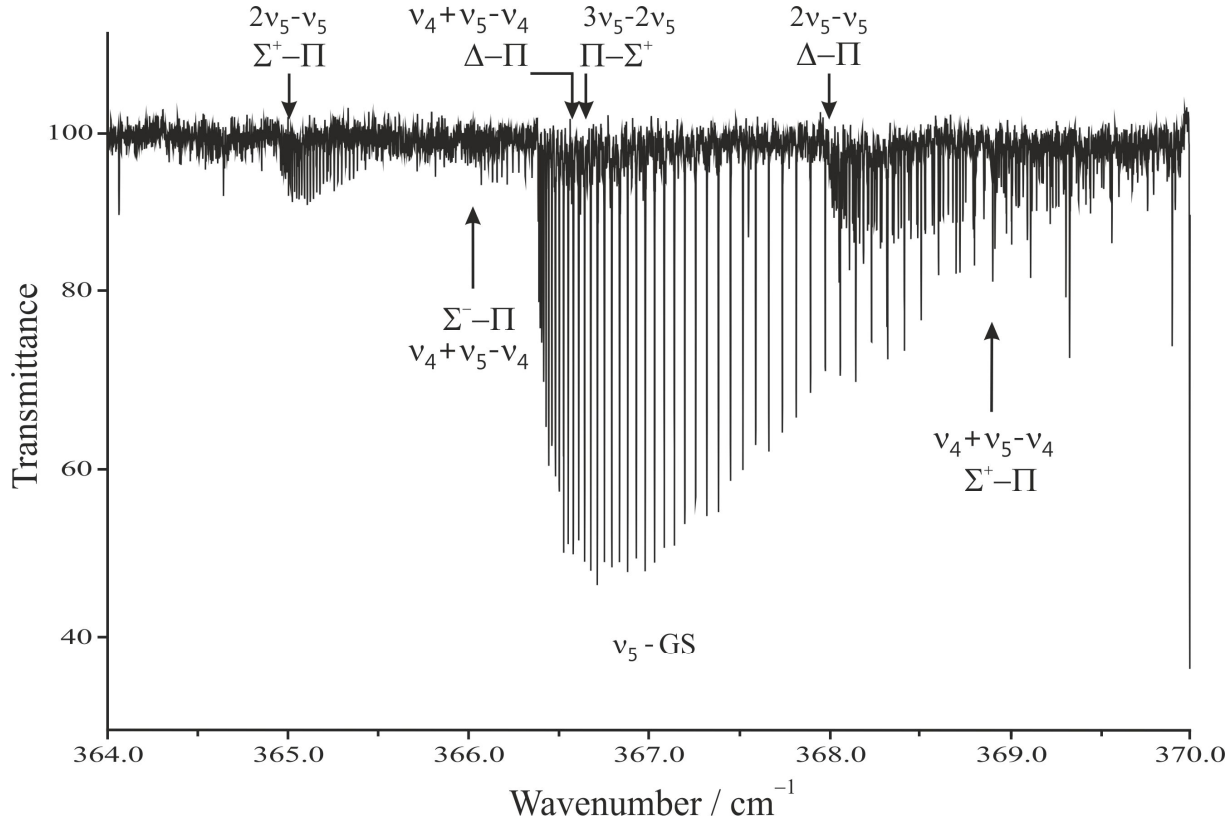

Figure 3.14: Portion of the spectrum of DCCF between 364 and 370 cm^{-1}, showing the *Q* branch transitions of ν_5 and of some associated hot bands. Experimental conditions: spectrum *#2* in Table 3.21.

Figure 3.14 is dominated by the *Q* branch of the ν_5 fundamental band ($\Pi - \Sigma^+$), which is centred at 366.4 cm^{-1}. Among the associated hot bands, the strongest are $2\nu_5 \leftarrow \nu_5$ ($\Sigma^+ - \Pi$), located at 364.9 cm^{-1}, and $2\nu_5 \leftarrow \nu_5$ ($\Delta - \Pi$) at 368.0 cm^{-1}. The $\nu_4 + \nu_5 \leftarrow \nu_4$ ($\Sigma^-, \Delta, \Sigma^+ - \Pi$) hot band has three components at 366.0, 366.5, and 368.9 cm^{-1}, respectively. In addition, the weak *Q* branch of $3\nu_5 \leftarrow 2\nu_5$ ($\Pi - \Sigma^+$) can be observed intermingled with the strong *Q*(*J*) transitions of the fundamental. The $3\nu_5 \leftarrow 2\nu_5$ ($\Pi - \Delta$) and ($\Phi - \Delta$) components were not identified even after careful inspection, being too weak to be detected. In total, 11 bands have been investigated in this region with v_{tot} up to 3.

b) The 400 – 500 cm^{-1} region

The region is dominated by the ν_4 fundamental band. This spectral range is the more crowded of the entire spectrum, due to the presence of 19 hot bands overlapping each other. Two significant portions of this spectrum are shown in Figures 3.15 and 3.16. In the first one the more intense hot bands are shown: $2\nu_4 \leftarrow \nu_4$ ($\Sigma^+ - \Pi$), whose *Q* branch starts at 431.8 cm^{-1}, and at higher wavenumbers $3\nu_4 \leftarrow 2\nu_4$ ($\Pi - \Sigma^+$) at 435.4 cm^{-1}. Between these bands the two components $2\nu_4 + \nu_5 \leftarrow \nu_4 + \nu_5$ ($^{II}\Pi - \Delta$) and ($^{II}\Pi - \Sigma^-$) can be observed at 432.8 and 433.3 cm^{-1}. It is worth to point out that the most intense lines in Fig. 3.15 are *P*(*J*) transitions of the ν_4 fundamental band, whose *Q* branch is centred at 441.1 cm^{-1} and dominates Figure 3.16.

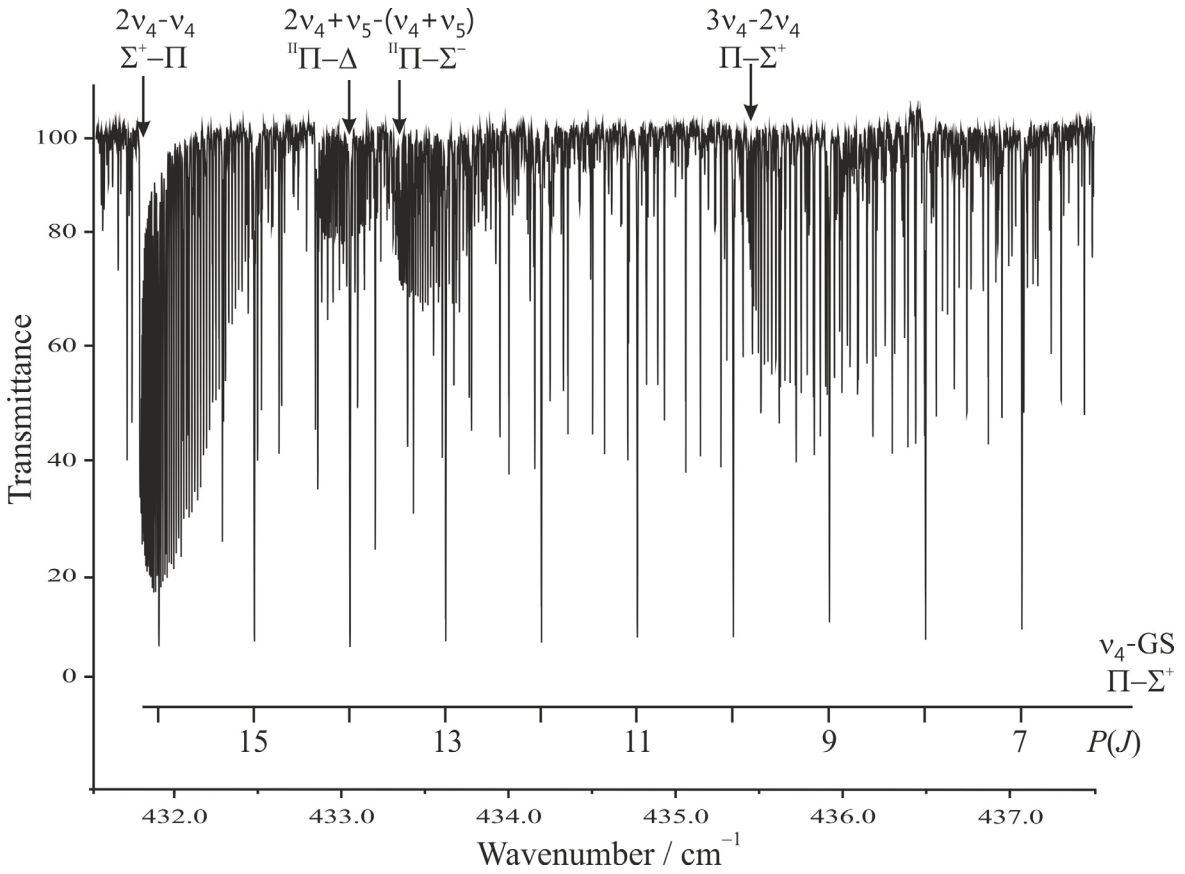

Figure 3.15: Portion of the spectrum of DCCF between 431.5 and 437.5 cm^{-1}, showing the *Q* branch transitions of $2\nu_4 \leftarrow \nu_4$ ($\Sigma^+ - \Pi$) and of some associated hot bands. Experimental conditions: spectrum *#2* in Table 3.21.

Figure 3.16, where nine hot bands are indicated, depicts very well the crowded situation around ν_4. From lower to higher wavenumbers, the Σ^-, Δ, and Σ^+ components of $\nu_4 + \nu_5 \leftarrow \nu_5$ are present at 440.7, 441.2, and 443.6 cm^{-1}, respectively and the Δ component of $2\nu_4 \leftarrow \nu_4$ at 444.4

cm^{-1}. The centre of this band is almost coincident with the intense *Q* branches of three hot bands overlapping each other: $\nu_4 + 2\nu_5 \leftarrow 2\nu_5$ ($^{I}\Pi - \Delta$), $2\nu_4 + \nu_5 \leftarrow \nu_4 + \nu_5$ ($^{I}\Pi - \Sigma^+$), and $2\nu_4 + \nu_5 \leftarrow \nu_4 + \nu_5$, ($\Phi - \Delta$). Finally, the *Q* branches of the two components $^{II}\Pi \leftarrow \Sigma^+$ and $\Phi \leftarrow \Delta$ of $\nu_4 + 2\nu_5 \leftarrow 2\nu_5$ overlap that of ν_4. In total, 20 bands have been detected in this region, three of them with upper state of Φ symmetry.

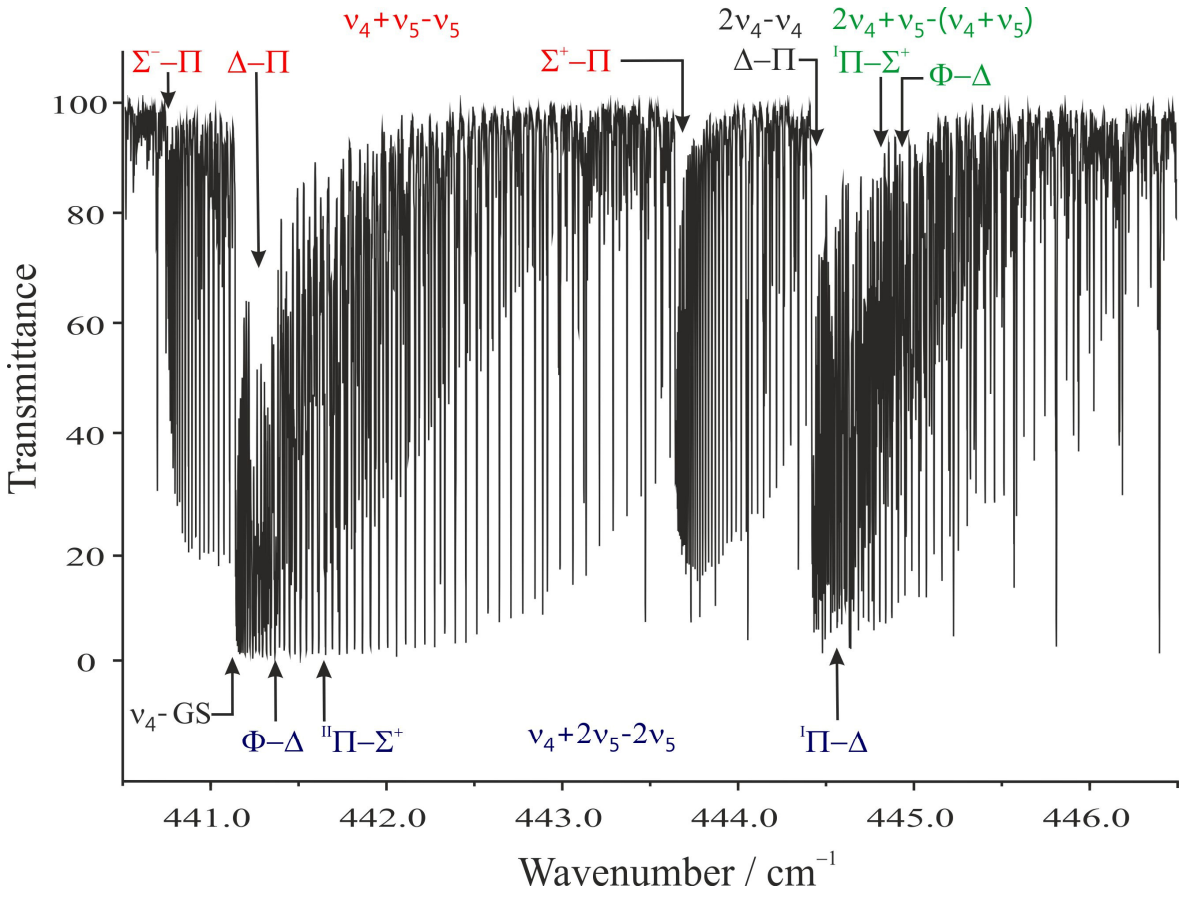

Figure 3.16: Portion of the spectrum of DCCF between 440.5 and 446.5 cm^{-1}, showing the *Q* branch transitions of $\nu_4 \leftarrow$ GS ($\Pi - \Sigma^+$) and eight associated hot bands. Experimental conditions: spectrum *#2* in Table 3.21.

c) The 600 – 850 cm^{-1} region

Just one band has been identified in the range 600 – 720 cm^{-1}: it is a difference band involving a stretching mode, namely $\nu_3 \leftarrow \nu_4$, ($\Sigma^+ - \Pi$), whose *Q* branch is centred at 605 cm^{-1}. Compared to the bending system under investigation, this band is so weak that transitions of the *P* and *R* branches could be identified and assigned only in spectrum #1 recorded at higher pressure. As shown in Figure 3.17, this weak band appears under the strong features of the ν_4 fundamental band of HCCF.

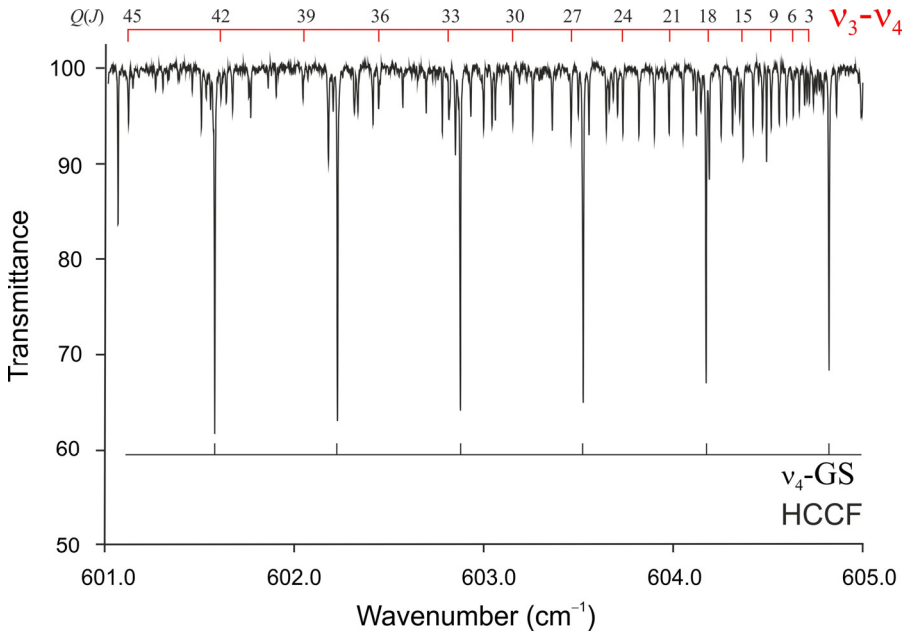

Figure 3.17: Portion of the spectrum of DCCF between 601 and 605 cm^{-1}, showing the *Q* branch transitions of $\nu_3 - \nu_4$ ($\Sigma^+ - \Pi$) difference band. Experimental conditions: spectrum *#2* in Table 3.21.

The first overtone band of ν_5 and its hot band from ν_5 appear at 731.3 and 731.6 cm^{-1}, respectively. The 780 – 840 cm^{-1} portion of the spectrum, displayed in Fig. 3.18, is dominated by the medium strong $\nu_4 + \nu_5 \leftarrow$ GS ($\Sigma^+ - \Sigma^+$) band, with origin at 810 cm^{-1}, and associated hot bands from ν_4 or ν_5. In total, 7 bands have been identified and analyzed in the 600 – 850 cm^{-1} region.

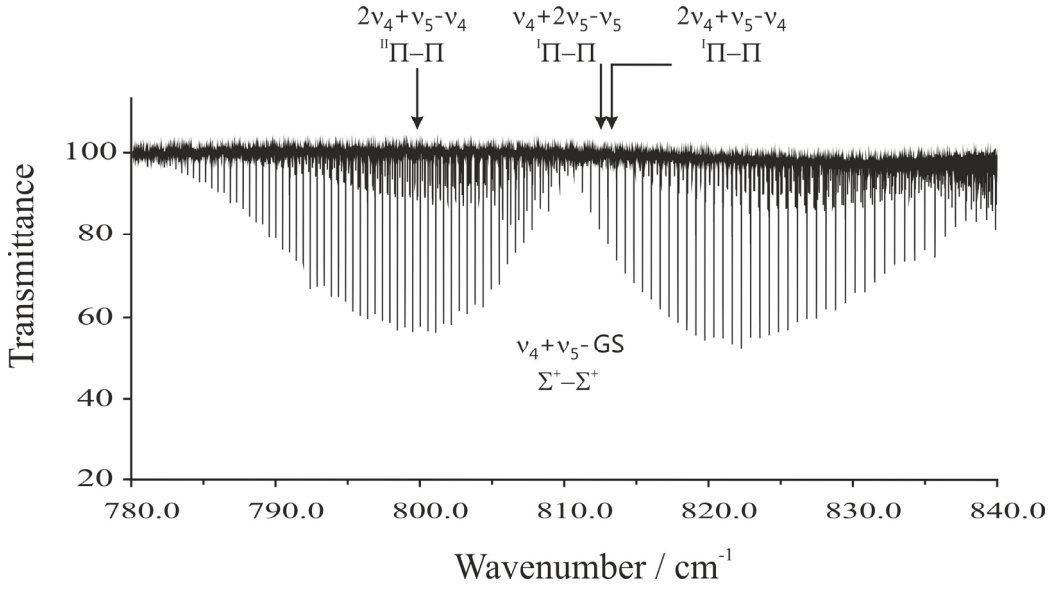

Figure 3.18: Portion of the spectrum of DCCF between 780 and 840 cm^{-1}, showing the *P* and *R* transitions of $\nu_4 + \nu_5 \leftarrow$ GS ($\Sigma^+ - \Sigma^+$) and some associated hot bands. Experimental conditions: spectrum *#2* in Table 3.21.

3.4.3 Analysis

The assignment procedure was accomplished by using the LSCD calculated on the basis of the previously reported spectroscopic parameters of DCCF [48,57,58]. They allowed the identification of the lower vibrational state and the correct identification of the *J* quantum number for each transition. The upper state of transitions, which was not previously observed, was assigned by comparison of the term values with the bending states pattern of HCCF [50]. The following step was the systematic research of all the transitions reaching the same upper level from different lower states. In total, 6791 IR transitions have been assigned to 38 vibrational bands, 37 of which involving pure bending states with v_{tot} up to 3, while one is the difference band $\nu_3 - \nu_4$. All the assigned bands are collected in Table 3.22, as well as the symmetry of the vibrational states involved in the transitions, the band centre, the observed range of *J* values for the various branches, the number of fitted and assigned lines and the RMS error resulting from the simultaneous least–squares analysis.

Table 3.22: Bands of DCCF included in the least–squares fitting procedure

Transition	Symmetry	ν_C [a]	P; R; Q (J_{min}, J_{max})	σ ($\times 10^4$) [b]	No. fitted/ assigned lines
$\nu_4 + 2\nu_5 \leftarrow \nu_4 + \nu_5$	$^{II}\Pi \leftarrow \Sigma^+$	362.7352	$P_{e\text{-}e}$ (13-20); $R_{e\text{-}e}$ (13-25); $Q_{f\text{-}e}$ (4-30)	10.46	40/52
	$^{II}\Pi \leftarrow \Sigma^-$	365.6314	$P_{f\text{-}f}$ (10-26); $R_{f\text{-}f}$ (8-22); $Q_{e\text{-}f}$ (2-34)	9.34	57/64
$2\nu_5 \leftarrow \nu_5$	$\Sigma^+ \leftarrow \Pi$	364.9503	$P_{e\text{-}e}$ (2-49); $R_{e\text{-}e}$ (5-48); $Q_{e\text{-}f}$ (2-53)	5.50	136/141
	$\Delta \leftarrow \Pi$	367.9915	$P_{e\text{-}e}$ (6-44); $R_{e\text{-}e}$ (1-61); $Q_{f\text{-}e}$ (2-46) $P_{f\text{-}f}$ (7-44); $R_{f\text{-}f}$ (3-48); $Q_{e\text{-}f}$ (2-66)	7.95	264/292
$\nu_4 + \nu_5 \leftarrow \nu_4$	$\Sigma^- \leftarrow \Pi$	365.9905	$P_{f\text{-}f}$ (3-40); $R_{f\text{-}f}$ (1-44); $Q_{f\text{-}e}$ (3-44)	5.31	116/122
	$\Delta \leftarrow \Pi$	366.4638	$P_{e\text{-}e}$ (4-36); $R_{e\text{-}e}$ (1-40); $Q_{f\text{-}e}$ (3-45) $P_{f\text{-}f}$ (4-36); $R_{f\text{-}f}$ (6-36); $Q_{e\text{-}f}$ (3-34)	6.85	178/204
	$\Sigma^+ \leftarrow \Pi$	368.8867	$P_{e\text{-}e}$ (5-37); $R_{e\text{-}e}$ (4-36); $Q_{e\text{-}f}$ (3-44)	4.97	96/105
$3\nu_5 \leftarrow 2\nu_5$	$\Pi \leftarrow \Sigma^+$	366.6679	$R_{e\text{-}e}$ (10-30); $Q_{f\text{-}e}$ (1-29)	7.94	46/49
$\nu_5 \leftarrow$ GS	$\Pi \leftarrow \Sigma^+$	366.3807	$P_{e\text{-}e}$ (2-65); $R_{e\text{-}e}$ (0-65); $Q_{f\text{-}e}$ (1-76)	3.19	201/206
$2\nu_4 + \nu_5 \leftarrow 2\nu_4$	$^{I}\Pi \leftarrow \Delta$	369.0275	$Q_{f\text{-}e}$ (3-29); $Q_{e\text{-}f}$ (3-29)	7.91	41/54
	$^{I}\Pi \leftarrow \Sigma^+$	381.6846	$Q_{f\text{-}e}$ (3-31)	9.05	25/29
$3\nu_4 \leftarrow 2\nu_4$	$\Pi \leftarrow \Delta$	422.7556	$P_{e\text{-}e}$ (2-47); $R_{e\text{-}e}$ (2-44); $Q_{f\text{-}e}$ (2-49) $P_{f\text{-}f}$ (2-44); $R_{f\text{-}f}$ (2-44); $Q_{e\text{-}f}$ (2-60)	5.50	218/262
	$\Pi \leftarrow \Sigma^+$	435.4126	$P_{e\text{-}e}$ (2-55); $R_{e\text{-}e}$ (0-55); $Q_{f\text{-}e}$ (1-68)	4.64	163/177
	$\Phi \leftarrow \Delta$	447.8723	$P_{e\text{-}e}$ (4-52); $R_{e\text{-}e}$ (2-60); $Q_{f\text{-}e}$ (3-60) $P_{f\text{-}f}$ (4-59); $R_{f\text{-}f}$ (2-58); $Q_{e\text{-}f}$ (3-60)	4.07	307/333

$2\nu_4 + \nu_5 \leftarrow \nu_4 + \nu_5$	$^{\|\|}\Pi \leftarrow \Sigma^+$	430.3939	$P_{e\text{-}e}$ (2-43); $R_{e\text{-}e}$ (1-39); $Q_{f\text{-}e}$ (1-54)	5.69	108/132
	$^{\|\|}\Pi \leftarrow \Delta$	432.8168	$P_{e\text{-}e}$ (2-60); $R_{e\text{-}e}$ (2-55); $Q_{f\text{-}e}$ (1-48) $P_{f\text{-}f}$ (2-58); $R_{f\text{-}f}$ (4-38); $Q_{e\text{-}f}$ (1-42)	4.12	249/295
	$^{\|\|}\Pi \leftarrow \Sigma^-$	433.2902	$P_{f\text{-}f}$ (2-54); $R_{f\text{-}f}$ (1-52); $Q_{e\text{-}f}$ (1-60)	4.26	145/165
$2\nu_4 \leftarrow \nu_4$	$\Sigma^+ \leftarrow \Pi$	431.7600	$P_{e\text{-}e}$ (1-81); $R_{e\text{-}e}$ (1-75); $Q_{e\text{-}f}$ (2-68)	2.99	211/214
	$\Delta \leftarrow \Pi$	444.4170	$P_{e\text{-}e}$ (3-68); $R_{e\text{-}e}$ (1-74); $Q_{f\text{-}e}$ (3-69) $P_{f\text{-}f}$ (3-72); $R_{f\text{-}f}$ (1-73); $Q_{e\text{-}f}$ (3-67)	3.27	408/412
$\nu_4 + 2\nu_5 \leftarrow 2\nu_5$	$^{\|\|}\Pi \leftarrow \Delta$	438.3823	$P_{e\text{-}e}$ (4-38); $R_{e\text{-}e}$ (4-32); $Q_{f\text{-}e}$ (7-37) $P_{f\text{-}f}$ (4-33); $R_{f\text{-}f}$ (4-29); $Q_{e\text{-}f}$ (5-43)	7.21	130/180
	$^{\|\|}\Pi \leftarrow \Sigma^+$	441.4235	$P_{e\text{-}e}$ (2-43); $R_{e\text{-}e}$ (1-49); $Q_{f\text{-}e}$ (4-45)	3.90	115/133
	$\Phi \leftarrow \Delta$	441.3739	$P_{e\text{-}e}$ (4-41); $R_{e\text{-}e}$ (2-45); $Q_{f\text{-}e}$ (4-48) $P_{f\text{-}f}$ (4-57); $R_{f\text{-}f}$ (2-58); $Q_{e\text{-}f}$ (4-42)	6.24	217/272
	$^{\|}\Pi \leftarrow \Delta$	444.5193	$P_{e\text{-}e}$ (3-48); $R_{e\text{-}e}$ (2-43); $Q_{f\text{-}e}$ (3-54) $P_{f\text{-}f}$ (2-48); $R_{f\text{-}f}$ (3-46); $Q_{e\text{-}f}$ (3-57)	7.41	218/284
	$^{\|}\Pi \leftarrow \Sigma^+$	447.5605	$P_{e\text{-}e}$ (5-43); $R_{e\text{-}e}$ (3-43); $Q_{f\text{-}e}$ (5-42)	6.14	81/109
$\nu_4 + \nu_5 \leftarrow \nu_5$	$\Sigma^- \leftarrow \Pi$	440.7424	$P_{f\text{-}f}$ (1-63); $R_{f\text{-}f}$ (1-55); $Q_{f\text{-}e}$ (1-68)	3.56	181/185
	$\Delta \leftarrow \Pi$	441.2157	$P_{e\text{-}e}$ (3-65); $R_{e\text{-}e}$ (1-74); $Q_{f\text{-}e}$ (4-62) $P_{f\text{-}f}$ (3-63); $R_{f\text{-}f}$ (1-73); $Q_{e\text{-}f}$ (4-62)	4.40	377/388
	$\Sigma^+ \leftarrow \Pi$	443.6386	$P_{e\text{-}e}$ (2-56); $R_{e\text{-}e}$ (1-55); $Q_{e\text{-}f}$ (4-68)	4.17	171/175
$\nu_4 \leftarrow$ GS	$\Pi \leftarrow \Sigma^+$	441.1326	$P_{e\text{-}e}$ (2-81); $R_{e\text{-}e}$ (0-82); $Q_{f\text{-}e}$ (1-95)	4.57	244/256
$2\nu_4 + \nu_5 \leftarrow \nu_4 + \nu_5$	$^{\|}\Pi \leftarrow \Sigma^+$	444.5578	$P_{e\text{-}e}$ (2-58); $R_{e\text{-}e}$ (0-62); $Q_{f\text{-}e}$ (1-53)	4.36	154/169
	$\Phi \leftarrow \Delta$	444.6302	$P_{e\text{-}e}$ (4-50); $R_{e\text{-}e}$ (2-53); $Q_{f\text{-}e}$ (4-52) $P_{f\text{-}f}$ (4-50); $R_{f\text{-}f}$ (2-56); $Q_{e\text{-}f}$ (4-51)	4.74	254/294
	$^{\|}\Pi \leftarrow \Sigma^-$	447.4541	$P_{f\text{-}f}$ (3-46); $R_{f\text{-}f}$ (2-49); $Q_{f\text{-}e}$ (1-53)	4.56	134/145
$\nu_3 \leftarrow \nu_4$	$\Sigma^+ \leftarrow \Pi$	604.7915	$P_{e\text{-}e}$ (4-47); $R_{e\text{-}e}$ (5-53); $Q_{e\text{-}f}$ (3-50)	4.63	131/141
$2\nu_5 \leftarrow$ GS	$\Sigma^+ \leftarrow \Sigma^+$	731.3310	$P_{e\text{-}e}$ (4-42); $R_{e\text{-}e}$ (3-42)	3.85	77/77
$3\nu_5 \leftarrow \nu_5$	$\Pi \leftarrow \Pi$	731.6182	$P_{e\text{-}e}$ (7-39); $R_{e\text{-}e}$ (5-38) $P_{f\text{-}f}$ (5-39); $R_{f\text{-}f}$ (2-39)	8.21	116/132
$2\nu_4 + \nu_5 \leftarrow \nu_4$	$^{\|\|}\Pi \leftarrow \Pi$	799.2806	$P_{e\text{-}e}$ (5-41); $R_{e\text{-}e}$ (3-38) $P_{f\text{-}f}$ (6-41); $R_{f\text{-}f}$ (3-37)	7.90	126/138
$\nu_4 + \nu_5 \leftarrow$ GS	$\Sigma^+ \leftarrow \Sigma^+$	810.0193	$P_{e\text{-}e}$ (1-58); $R_{e\text{-}e}$ (0-58)	3.00	114/116
$\nu_4 + 2\nu_5 \leftarrow \nu_5$	$^{\|}\Pi \leftarrow \Pi$	812.5108	$P_{e\text{-}e}$ (5-42); $R_{e\text{-}e}$ (3-38) $P_{f\text{-}f}$ (5-42); $R_{f\text{-}f}$ (3-38)	3.81	145/148
$2\nu_4 + \nu_5 \leftarrow \nu_4$	$^{\|}\Pi \leftarrow \Pi$	813.4445	$P_{e\text{-}e}$ (5-41); $R_{e\text{-}e}$ (3-38) $P_{f\text{-}f}$ (5-44); $R_{f\text{-}f}$ (3-41)	3.65	136/141

[a] In cm^{-1}. ν_c is defined in Eq. (3.4).

[b] σ (in cm^{-1}) corresponds to the RMS value of the residuals for the various assigned lines resulting from the simultaneous fit.

The analysis is similar to the one previously described for the bending states of the acetylene isotopologue $^{13}C^{12}CD_2$ in Section 3.2.3, with the exception that the Darling–Dennison

interaction is not effective among the analysed vibrational states of DCCF. Initially the transition wavenumbers for each band were fitted separately to effective upper state rovibrational parameters in order to check the correctness of the assignments and to extend the data set to higher J transitions. The basic Hamiltonian of a linear molecule, with distortion corrections up to high power in the rotational angular momentum was adopted for the analysis. For the transitions involving doubly degenerate states, the ℓ – doubling coefficients, namely q_v, q_v^J, and q_v^{JJ}, were taken into account. The rovibrational energies are given by Eqs. (3.2) and (3.3). Once this preliminary phase was completed, all the transition wavenumbers were fitted simultaneously by using the model Hamiltonian adopted for the analysis of acetylene isotopologues. The term values of the rotation vibration levels of the transitions were obtained by diagonalizing the appropriate energy matrix which contains the vibration and rotation term values, G^0 and F, respectively, whose diagonal contributions are defined in Eqs. (2.8) and (2.10) – (2.13). Vibration and rotation ℓ – type resonances contributions for the bending levels are expressed by off–diagonal matrix elements, see Eqs. from (2.32) to (2.34) and (3.5). First, the parameters of the $v_4 = 1$ and $v_5 = 1$ states were refined. Then, the transitions involving the $v_{tot} = 2$ manifolds, i.e. $v_4 = 2$, $v_5 = 2$, and $v_4 = v_5 = 1$, were added to the data set one at a time. Using the same strategy, the data of each level of the $v_{tot} = 3$ manifolds, $v_4 = 3$, $v_5 = 3$, $v_4 = 2$ $v_5 = 1$, and $v_4 = 1$ $v_5 = 2$, and those of the $\nu_3 - \nu_4$ difference band were considered. New parameters or the coefficients of the rotation and/or vibration dependences of the previously determined constants, characterizing the investigated manifold, were refined. Finally, 91 pure rotational transitions in vibrational states with v_{tot} up to 3 [48,57] were added to the data set. The refinement of the higher order parameters which were needed to satisfactorily reproduce the experimental observations had to meet the requirements a), b), c), d), e) illustrated in Section 3.2.4.

3.4.4 Results and Discussion

Two fits were performed: fit #1 was preliminary and included only the IR data (6791), in order to obtain a consistent set of parameters before including the much more accurate rotational transitions. In the final global fit, fit #2, 91 MW and mmW transitions were added to the dataset. The weights of the experimental data were chosen proportional to the inverse of their squared estimated uncertainties, with the exception of overlapping transitions, which were given zero weight. An uncertainty equal to 1.0×10^{-4} cm^{-1} was assigned to each IR measurement, despite the fact that the lines had different S/N depending on their intensity and on the different experimental conditions of the two recorded spectra. The uncertainty of the MW and mmW

transitions was set equal to 1.0×10^{-7} cm^{-1} for isolated lines, whereas blended lines were given an uncertainty of 1.0×10^{-6} cm^{-1}. 661 IR data, about 9.7%, were not included in the final fit because they were overlapping (418) or their observed – calculated values exceeded (243) the chosen tolerance for rejection, 2.0×10^{-3} cm^{-1}, 10 – 20 times the precision of the data. The discarded lines are randomly scattered over most of the bands. For the $2\nu_4$, $2\nu_5$ and $\nu_4 + \nu_5$ Δ states, the $J'' = 2$ *e/f* components of the rotational lines were not resolved. Their observed – calculated values were derived from the comparison of the experimental frequency with the average of the frequencies calculated for the two components.

The 57 spectroscopic parameters determined in the last cycle of fit #2 are listed in Table 3.23. They are all statistically well determined and reproduce 6130 observed IR transitions with an RMS error of 5.3×10^{-4} cm^{-1}, and 90 MW and mmW frequencies with RMS = 77 kHz. Most of the parameters are essentially uncorrelated, apart from q_t^0 and q_{tt} with $t = 4,5$ in Eq. (2.33), which are 100% correlated. However, if only the q_t^0 parameters are refined the fit quality degrades: the number of rejected IR lines increases to 803 (11.8%) and the RMS is 5.5×10^{-4} cm^{-1}. Nearly all the 140 additional rejected transitions belong to the $v_4 = 3$ and $v_5 = 3$ Π states.

Table 3.23: Spectroscopic parameters (in cm^{-1}) of the bending modes and of the $v_3 = 1$ state of DCCF

Parameter		Parameter	
ω_4^0	439.5472335(889)	$\gamma_4^{(55)} \times 10^6$	−0.5538(224)
ω_5^0	365.4684847(784)	$\gamma_5^{(44)} \times 10^6$	−0.7076(138)
x_{44}^0	−1.6567668(695)	$\gamma_5^{(45)} \times 10^6$	0.8753(281)
x_{45}^0	0.416350(110)	$\gamma_{444} \times 10^6$	0.51016(834)
x_{55}^0	0.0984956(331)	$\gamma_{454} \times 10^6$	0.2242(179)
g_{44}^0	3.5051182(408)	$\gamma_{455} \times 10^6$	−0.5171(217)
g_{45}^0	0.1471499(816)		
g_{55}^0	1.1585161(993)	$D_0 \times 10^6$	0.0889017(285)
y_{444}	0.0531452(154)	$\beta_4 \times 10^9$	1.15681(769)
y_{445}	0.1248306(342)	$\beta_5 \times 10^9$	2.58533(684)
y_{455}	0.0869928(414)	$\delta_{44} \times 10^9$	0.04177(388)
y_4^{44}	−0.0242316(141)	$\delta^{(44)} \times 10^9$	−0.08758(334)
y_4^{45}	−0.0143438(343)		
y_4^{55}	−0.0125995(762)	r_{45}^0	0.906608(522)
y_5^{44}	−0.0437386(467)	$r_{45}^J \times 10^6$	−6.3016(194)
y_5^{45}	−0.0347545(575)	r_{454}	0.084438(248)

y_5^{55}	−0.0525975(480)	r_{455}	0.186317(121)
		$q_4^0 \times 10^3$	0.4495625(123)
B_0	0.2914023717(174)	$q_5^0 \times 10^3$	0.5253172(230)
$\alpha_4 \times 10^3$	−0.5147993(567)	$q_{44} \times 10^6$	1.7614(124)
$\alpha_5 \times 10^3$	−0.8257296(329)	$q_{45} \times 10^6$	0.3113(385)
$\gamma_{44} \times 10^6$	−4.8944(417)	$q_{55} \times 10^6$	−1.6865(230)
$\gamma_{45} \times 10^6$	−1.545(532)	$q_4^J \times 10^9$	−0.98161(142)
$\gamma_{55} \times 10^6$	−12.7781(121)	$q_5^J \times 10^9$	−1.42191(128)
$\gamma^{(44)} \times 10^6$	−5.8473(284)	$\rho_4^0 \times 10^9$	−0.06879(633)
$\gamma^{(45)} \times 10^6$	−1.5873(632)	$\rho_5^0 \times 10^9$	−2.2480(613)
$\gamma^{(55)} \times 10^6$	5.9389(102)	$\rho_5^J \times 10^{12}$	1.5032(217)
$\gamma_4^{(44)} \times 10^6$	−0.81880(841)	$\rho_{45}^0 \times 10^9$	−0.1732(190)
$\gamma_4^{(45)} \times 10^6$	0.3667(237)		
		G_3^0	1045.924109(113)
		B_3	0.290361167(226)
		$D_3 \times 10^6$	0.0890150(918)
No. of fitted / assigned lines	6220 / 6882		
RMS / cm^{-1} (IR data)	0.00053		
RMS / MHz (MW data)	0.077		

The parameters in Table 3.23 are consistent with those from fit #1 and their signs unchanged, the largest differences being in the range 0 – 1 % (33 parameters), 1 – 10 % (12 parameters), 10 – 30 % (12 parameters). However, the inclusion of the rotational transitions in the data set reduces drastically the correlation coefficients between some of the parameters and decreases the uncertainties of several rotational parameters. Moreover, only 16 additional IR transitions exceeding the rejection limit of 0.002 cm^{-1} had to be discarded when the MW/mmW data were added to the IR data. This is a fairly good result since the MW and mmW transitions are more accurate than IR ones and have been attributed a larger weight in the fit procedure.

The Fermi interaction effective between the $v_3 = 1$ and $v_4 = 2^0$ states in HCCF, with k_{344} = 17.766 cm^{-1}, which has been reported in [3–6,17], has less effect on the energy of the corresponding states in DCCF owing to the different energy pattern of the vibrational levels in the two molecules. In fact, the term value difference between $v_3 = 1$ and $v_4 = 2^0$ is 95 cm^{-1} in HCCF and 173 cm^{-1} in DCCF. Qualitative indications of Fermi resonance in the spectra are present. Even if in DCCF it will be therefore weak and absorbed by the effective rovibrational state parameters, a proof for that is the nonzero but very small intensity of the $\nu_3 - \nu_4$ band at 604

cm^{-1}. This may be indicative of some $v_4 = 2^0$ character in the $v_3 = 1$ state, the difference band thus adopting some $2\nu_4 - \nu_4$ hot band properties. A further indication is that the $2\nu_4 \leftarrow \nu_4$ ($\Sigma^+ - \Pi$) hot band is redshifted more than 10 cm^{-1} with regard to ν_4 and $2\nu_4 - \nu_4$ ($\Delta \leftarrow \Pi$). This shift is accounted for by the substantial and positive value of $g_{44}^0 = 3.5$ cm^{-1}, Table 3.23.

In total, 19 components of the various manifolds up to $v_{tot} = 3$ were characterized, with the exception of the $v_5 = 3$, $\ell_5 = 3$ Φ state, and their term values are reported in Table 3.24.

Table 3.24: Vibrational term values, G_C^0, (in cm^{-1}), of the levels involving bending modes and the $v_3 = 1$ state in DCCF

v_4	ℓ_4	v_5	ℓ_5	Sym.	G_C^0
0	0	1	± 1	Π	366.3807
1	± 1	0	0	Π	441.1326
0	0	2	0	Σ^+	731.3310
0	0	2	± 2	Δ	734.3721
1	–1	1	1	Σ^-	807.1231
1	± 1	1	± 1	Δ	807.5964
1	1	1	–1	Σ^+	810.0193
2	0	0	0	Σ^+	872.8926
2	± 2	0	0	Δ	885.5496
0	0	3	± 1	Π	1097.9989
0	0	3	± 3	Φ	1104.0742[a]
1	± 1	2	0	$^{II}\Pi$	1172.7545
1	± 1	2	± 2	Φ	1175.7461
1	∓ 1	2	± 2	$^{I}\Pi$	1178.8914
2	0	1	± 1	$^{II}\Pi$	1240.4132
2	± 2	1	± 1	Φ	1252.2266
2	± 2	1	∓ 1	$^{I}\Pi$	1254.5771
3	± 1	0	0	Π	1308.3052
3	± 3	0	0	Φ	1333.4219
v_3	v_4	v_5		Sym.	G_C^0
1	0	0		Σ^+	1045.9241

[a] Calculated value of a state not observed experimentally in the IR spectra.

3.5 DC_4H

Diacetylene has a great importance in astrophysics: it has been observed in the proto−planetary nebulae CRL618 and CRL 2688 [59], and also outside our galaxy in a similar object embedded in the Large Magellanic Cloud [60]. It is a well known constituent of the stratosphere of giant planets and their moons [61−63]. Mono−deuterated acetylene has been recently detected in Titan by Cassini/CIRS [64]. Diacetylene produces one of the strongest emission features of Titan below 1000 cm^{-1}, thus it is expected that also its monodeuterated isotopologue DC_4H could be identified, providing further insight into the origin of Titan's atmosphere.

DC_4H, because of the D substitution, does not own a centre of symmetry, so it belongs to $C_{\infty v}$ point group, acquiring a small permanent dipole moment in its ground vibrational state, which allows the detection of pure rotational spectrum in the millimetre wave spectral region. The molecule has 13 vibrational degrees of freedom, originating 5 vibrations of Σ^+ symmetry and 4 double degenerate of Π symmetry, as shown in Table 3.25.

Table 3.25: Vibrational normal modes of DC_4H

Band		Symmetry	Wavenumber (cm^{-1})[a]
ν_1	Stretching C–H	Σ^+	3332
ν_2	Symmetric Stretching C≡C	Σ^+	2146
ν_3	Stretching C–C	Σ^+	854
ν_4	Stretching C–D	Σ^+	2600
ν_5	Antisymmetric Stretching C≡C	Σ^+	1938
ν_6	Bending C–H	Π	627
ν_7	Symmetric Bending C≡C-C	Π	471
ν_8	Bending C–D	Π	499
ν_9	Antisymmetric Bending C≡C–C	Π	210

[a] From Ref. [65].

The IR spectrum of DC_4H has only been studied at high resolution at wavelength shorter than 10 μm [65]. No high resolution study was performed below 1000 cm^{-1}, where the

fundamental bending bands are located. That is why an intensive investigation of the 450 – 1100 cm^{-1} has been undertaken.

3.5.1 Experiment

The sample of DC_4H has been synthesised by using the method described by Armitage *et al*. [66], i.e. by reaction of 1,4–dichloro–2–butyne (purchased by Aldrich) with sodium hydroxide dissolved in a nearly equimolar mixture of H_2O and D_2O.

$$ClH_2C-C\equiv C-CH_2Cl \xrightarrow{NaOH} ClHC=C=C=CHCl \xrightarrow[H_2O/D_2O]{NaOH} DC\equiv C-C\equiv CH$$

The synthetic outcome of this procedure is a mixture of about 50% DC_4H, 25% HC_4H and 25% DC_4D.

Spectra were recorded in Bologna using a Bomem DA3.002 Fourier transform spectrometer. It was equipped with a Globar source, a KBr beam splitter and a HgCdTe detector operating at liquid nitrogen temperature. Spectra were recorded at different pressures in a cell 0.18 m long. The attained resolution was 0.004 cm^{-1}. Up to 880 scans were co–added in order to improve the S/N ratio of the spectra. Experimental conditions for each recorded spectrum are reported in Table 3.26.

Table 3.26: Experimental conditions for the recording of DC_4H spectra

Spectrum	Pressure of the sample (Pa)	Range (cm^{-1})	Source	Detector	Resolution (cm^{-1})	#Scans	Optical pathlenght (m)
a	306.5	450 – 1100	Globar	MCT	0.004	880	0.18
b	66.7	450 – 1100	Globar	MCT	0.004	800	0.18
c	1333.3	450 – 1100	Globar	MCT	0.004	800	0.18

In order to calibrate the spectra, rovibrational transitions of H_2O [20] and CO_2 [67] were used. The precision of the measurements was estimated to be 4×10^{-4} cm^{-1}.

In addition, rotational spectra of DC_4H in the ground and excited bending states have been recorded between 85 and 615 GHz in collaboration with the group of the Department "G. Ciamician", using a mm–wave spectrometer.

3.5.2 Description of the spectra

Due to the small value of the rotational constant B (B_0 is about 0.136 cm^{-1}) and to the various isotopologues that are present in the sample, the spectrum is rather congested. An overview of the investigated spectral zone is shown in Figure 3.19.

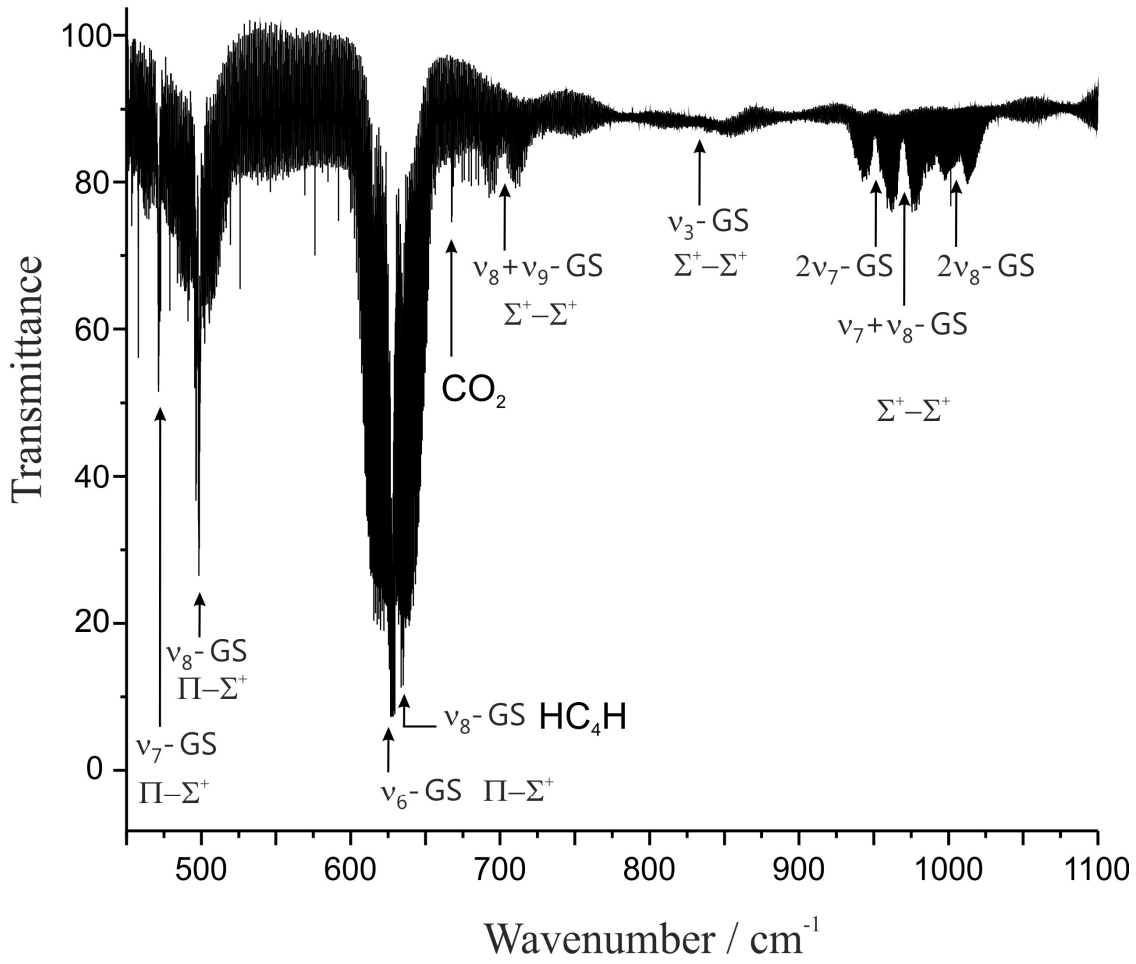

Figure 3.19: Overview of the investigated region of the spectrum, between 450 and 1100 cm^{-1}. Experimental conditions: see spectrum *a*) in Table 3.26.

Three fundamental bending bands $\Pi - \Sigma^+$, namely ν_6, ν_7 and ν_8, have been observed and analysed. The strongest band present in the spectrum is assigned to ν_6 partially overlapping the ν_8 of HC_4H. Luckily, the HC_4H fundamental bands have been already analysed [68], simplifying the assignment procedure and the identification of the weaker transitions belonging to the isotopologue under investigation. Besides, several hot, combination and overtone bands have been identified. The ν_6 region is the most crowded, due to the presence of many Q branches of hot bands, the strongest of them arising from ν_9, which is located at about 290 cm^{-1}. Towards

higher wavenumbers the spectrum appears less congested. Between 800 and 900 cm^{-1} it is possible to detect the very weak ν_3 band. Finally, in the range 900 – 1100 cm^{-1} the first overtones of ν_7 and ν_8 are observed, together with the combination band $\nu_7 + \nu_8$. For these three bands only the Σ^+ component has been identified.

3.5.3 Analysis, Results and Discussion

The list of the investigated bands in the infrared is reported in Table 3.27, together with the symmetry of the transitions, the value of the band centre, the observed range of *J* values for the various branches, the number of assigned lines and the root mean square (RMS) error.

Table 3.27: Observed and analysed transitions for DC_4H

Transition	Symmetry	ν_C [a]	*P*; *R*; (J_{min}, J_{max})	σ ($\times 10^4$) [b]	n. assign. lines
$\nu_7 \leftarrow GS$	$\Pi \leftarrow \Sigma^+$	471.2648	$P_{e\text{-}e}$ (3-81); $R_{e\text{-}e}$ (1-75); $Q_{f\text{-}e}$ (12-75)	3.5	246
$\nu_8 + \nu_9 \leftarrow \nu_9$	$\Sigma^+ \leftarrow \Pi$	497.8842	$P_{e\text{-}e}$ (6-79); $R_{e\text{-}e}$ (3-79);	5.3	132
$\nu_8 \leftarrow GS$	$\Pi \leftarrow \Sigma^+$	498.2591	$P_{e\text{-}e}$ (11-96); $R_{e\text{-}e}$ (5-95); $Q_{f\text{-}e}$ (24-81);	3.4	184
$\nu_6 + \nu_9 \leftarrow \nu_9$	$\Sigma^+ \leftarrow \Pi$	625.7766	$P_{e\text{-}e}$ (6-79); $R_{e\text{-}e}$ (3-79);	5.0	184
$\nu_6 \leftarrow GS$	$\Pi \leftarrow \Sigma^+$	626.8209	$P_{e\text{-}e}$ (2-117); $R_{e\text{-}e}$ (4-115); $Q_{f\text{-}e}$ (18-73);	3.5	246
$\nu_8 + \nu_9 \leftarrow GS$	$\Sigma^+ \leftarrow \Sigma^+$	708.5023	$P_{e\text{-}e}$ (6-57); $R_{e\text{-}e}$ (9-65)	3.6	109
$2\nu_7 \leftarrow GS$	$\Sigma^+ \leftarrow \Sigma^+$	950.1728	$P_{e\text{-}e}$ (1-97); $R_{e\text{-}e}$ (0-84)	3.6	170
$\nu_7 + \nu_8 \leftarrow GS$	$\Sigma^+ \leftarrow \Sigma^+$	969.4633	$P_{e\text{-}e}$ (1-87); $R_{e\text{-}e}$ (0-90)	3.1	175
$2\nu_8 \leftarrow GS$	$\Sigma^+ \leftarrow \Sigma^+$	1005.1905	$P_{e\text{-}e}$ (1-83); $R_{e\text{-}e}$ (0-85)	3.5	169

[a] In cm^{-1}. ν_C is defined by Eq. (3.3).

[b] σ (in cm^{-1}) corresponds to the standard deviation of the fit.

A band–by–band fitting procedure was accomplished to analyse the assigned bands. The transition wavenumbers for each band were fitted separately to the upper state rovibrational parameters by a least–squares procedure. The basic Hamiltonian for a linear molecule, with distortion corrections up to high power in the rotational angular momentum, was used for the

analysis. In case of transitions involving doubly degenerate Π states, ℓ – doubling contribution are included. The rovibrational term values are given by Eq. (3.2), the centre energy is expressed by Eq. (3.3) and the band centre by Eq. (3.4). In this case, $k = \ell_t + \ell_{t'}$ with *t,t'* = 6, 7, 8, 9.

Unit weights were assigned to measurements for well isolated lines, while the weights were reduced to 1/*n* if *n* transitions were assigned to the same wavenumber. Finally, the transitions that differed from their corresponding calculated values by more than 2.0×10^{-3} cm^{-1} or 1.0×10^{-3} cm^{-1}, depending on the S/N, were excluded from the data set in the final cycle of the refinement.

The fit of the transitions of the υ_6 = 1 bending state showed anomalous residuals. Considering that the excited state υ_9 = 3 is only 3 cm^{-1} apart, it has been guessed that a quartic anharmonic interaction was effective between these two states. Since no experimental information about υ_9 = 3 was available, its spectroscopic parameters were calculated in the following way: the vibrational energy was assumed to be three time that one of the υ_9 = 1 state, *B* and *D* were linearly extrapolated from the corresponding values of the ground and υ_9 = 1, whereas the ℓ – doubling constants were constrained to the values determined from υ_9 = 1. The value of the interaction parameter W_{6999} has been determined. In addition, the resonant system near υ_3 = 1 has been taken into account. A diagram illustrating the interacting system centred on the υ_3 = 1 state is reported in Fig. 3.20. The dashed lined indicates the position of the unperturbed energy levels, while the large arrows indicate the energy displacement due to the anharmonic interactions. The six states resonant system deeply affects the analysis and, as a consequence, a global rovibrational analysis of all the bands has been performed. A detailed description of the model adopted for the analysis is in Ref. [69,70]. The off–diagonal matrix elements for the cubic interactions were inserted in the Hamiltonian:

$$\left\langle \upsilon_3, \upsilon_t^{\ell_t}, \upsilon_{t'}^{\ell_{t'}}, \ell \middle| H_{30} + H_{32} \middle| (\upsilon_3+1)^{\ell_t \pm 1}, (\upsilon_t - 1)^{\ell_t \pm 1}, (\upsilon_{t'}+1)^{\ell_{t'} \mp 1}, \ell \right\rangle = \frac{\sqrt{2}}{2}\left[C_{30}^{(3tt')} + C_{30J}^{(3tt')} J(J+1) \right] \left[(\upsilon_3+1)(\upsilon_t \mp \ell_t)(\upsilon_{t'} \pm \ell_{t'}) \right]^{1/2} \tag{3.14}$$

$$\left\langle \upsilon_3, \upsilon_t^{\ell_t}, \ell \middle| H_{30} + H_{32} \middle| (\upsilon_3+1)^{\ell_t \pm 1}, (\upsilon_t - 2)^{\ell_t}, \ell \right\rangle = \sqrt{2}\left[C_{30}^{(3tt)} + C_{30J}^{(3tt)} J(J+1) \right] \left[(\upsilon_3+1)(\upsilon_t - \ell_t)(\upsilon_{t'} + \ell_t) \right]^{1/2} \tag{3.15}$$

The model adopted allowed the identification of transitions not previously observed.

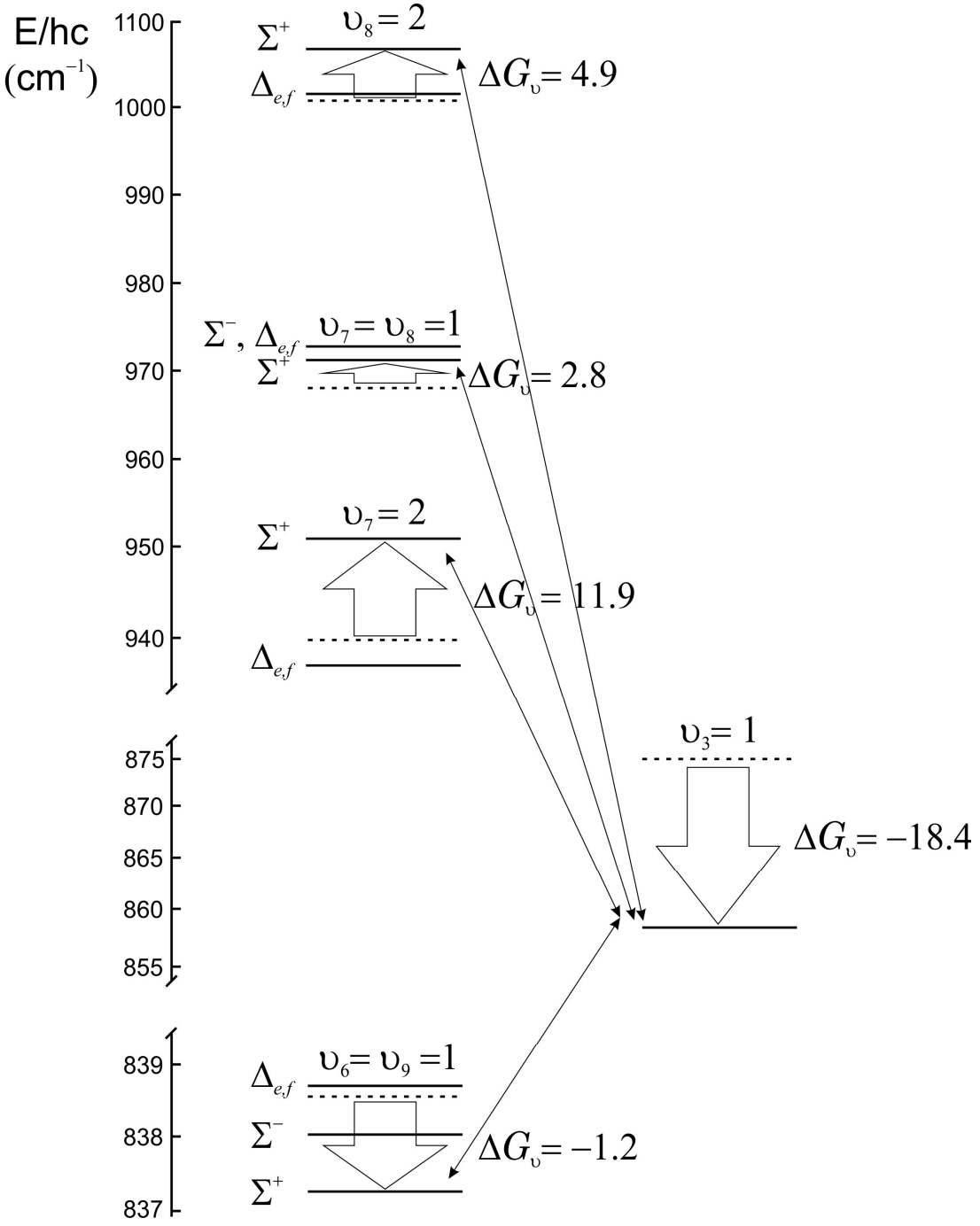

Figure 3.20: Vibrational energy levels diagram of the resonance system centred on the $v_3 = 1$ state. Anharmonic interactions producing the displacement of the levels are indicated, as well as the value of the energy shift. The diagram in not to scale.

The obtained spectroscopic parameters as well as the interaction parameters are reported in Table 3.28. In most cases, the observed wavenumbers were well fitted by adjusting the band centre, *B*, *D* and *H*, but in the hot bands, namely $\nu_8 + \nu_9 \leftarrow \nu_9$ and $\nu_6 + \nu_9 \leftarrow \nu_9$, there are more prominent centrifugal trends which required the refinement of the octic parameter *L*.

Table 3.28: Band centres and spectroscopic parameters for DC_4H

Band	Symmetry	ν_C (cm^{-1})	B (MHz)	D (kHz)	H (mHz)	L (μHz)	q (MHz)	q_J (Hz)
$\nu_7 \leftarrow GS$	$\Pi \leftarrow \Sigma^+$	471.264817(80)	4090.6301(42)	0.4071(18)	0.60(21)		3.0392(24)	–3.20(56)
$\nu_8+\nu_9 \leftarrow \nu_9$	$\Sigma^+ \leftarrow \Pi$	497.88416(15)	4100.854(12)	1.3266(86)	107.6(21)	–5.07(17)		
	$\Sigma^- \leftarrow \Pi$	498.00022(19)	4100.923(10)	0.5547(42)	6.02(47)			
	$\Delta_e \leftarrow \Pi$	498.58134(20)	4100.763	–0.556(16)	–124.5(45)	6.60(41)		
	$\Delta_f \leftarrow \Pi$	498.58133(18)	4100.8094	0.2633(44)	–7.28(57)			
$\nu_8 \leftarrow GS$	$\Pi \leftarrow \Sigma^+$	498.259142(67)	4089.6482(23)	0.39577(66)	0.089(		2.6321(17)	–0.88(34)
$\nu_6+\nu_9 \leftarrow \nu_9$	$\Sigma^+ \leftarrow \Pi$	625.77660(23)	4096.9474(90)	0.8889(62)	35.0(15)	–1.13(12)		
	$\Sigma^- \leftarrow \Pi$	626.54962(21)	4097.428(14)	0.6358(87)	19.6(18)	–0.72(12)		
	$\Delta_e \leftarrow \Pi$	627.02090(18)	4097.563(14)	0.0176(98)	–31.5(23)	1.08(18)		
	$\Delta_f \leftarrow \Pi$	627.02116(11)	4097.5867(57)	0.2338(24)	–8.70(28)			
$\nu_6 \leftarrow GS$	$\Pi \leftarrow \Sigma^+$	626.820869(50)	4086.2057(16)	0.39835(35)	0.173(15)		2.1259(20)	–2.04(46)
$\nu_8+\nu_9 \leftarrow GS$	$\Sigma^+ \leftarrow \Sigma^+$	708.502320(97)	4100.7709(71)	1.2278(41)	67.60(67)			
$\nu_3 \leftarrow GS$	$\Sigma^+ \leftarrow \Sigma^+$	855.89272(18)	4081.1133(67)	0.3907(16)				
$2\nu_7 \leftarrow GS$	$\Sigma^+ \leftarrow \Sigma^+$	950.172799(57)	4093.5899(23)	0.36703(76)	0.685(65)			
$\nu_7+\nu_8 \leftarrow GS$	$\Sigma^+ \leftarrow \Sigma^+$	969.463268(50)	4095.2028(22)	0.56660(75)	5.898(66)			
$2\nu_8 \leftarrow GS$	$\Sigma^+ \leftarrow \Sigma^+$	1005.190519(30)	4094.0138(14)	0.35758(54)	0.207(53)			
Interaction parameters								
	W_{6999}(cm^{-1})	0.10804(89)	$C_{30J}^{(369)}$ (MHz)	0.2381(82)				
	$C_{30}^{(377)}$ (cm^{-1})	–12.113	$C_{30}^{(388)}$ (cm^{-1})	–8.141				
	$C_{30J}^{(377)}$ (MHz)	0.495	$C_{30}^{(378)}$ (cm^{-1})	7.1559				
	$C_{30}^{(369)}$ (cm^{-1})	–2.498						

References

[1] Y. Xiao, D.J. Jacob, and S. Turquety, *J. Geophys. Res.* **112**, D12305, doi:10.1029/2006JD008268.

[2] A. Coustenis, R.K. Achterberg, B.J. Conrath, D.E: Jennings, A. Marten, D. Gautier, C.A. Nixon, F.M. Flasar, N.A. Teanby, B. Bézard, R.E. Samuelson, R.C. Carlson, E. Lellouch, G.L. Bjoraker, P.N. Romani, F.W. Samuelson, P.G.J. Irwin, T. Fouchet, A. Hubert, G.S. Orton, V.G. Kunde, S. Vinatier, J. Mondellini, M.M. Abbas, and R. Courtin, *Icarus* **189**, 35 (2007).

[3] E. Herbst, *Annu. Rev. Phys. Chem.* **46**, 27 (1995).

[4] H.M. Randall and E.F. Barker, *Phys. Rev.* **45**, 124 (1934).

[5] F. Stitt, *J. Chem. Phys.* **8**, 56 (1940).

[6] B.D. Saksena, *J. Chem. Phys.* **20**, 95 (1952).

[7] E.D. Tidwell and E.K. Plyler, *J. Opt. Soc. Am.* **52**, 656 (1962).

[8] S. Ghersetti and K. Narahari Rao, *J. Mol. Spectrosc.* **28**, 373 (1968).

[9] S. Ghersetti, J. Pliva and K. Narahari Rao, *J. Mol. Spectrosc.* **38**, 53 (1971).

[10] H. Fast and H.L. Welsh, *J. Mol. Spectrosc.* **41**, 203 (1972).

[11] A. Baldacci, S. Ghersetti, S.C. Hurlock and K. Narahari Rao, *J. Mol. Spectrosc.* **42**, 327 (1972).

[12] E. Kostyk and H.L.Welsh, *Can. J. Phys.* **58**, 912 (1980).

[13] D.B. Braund and A.R.H. Cole, *Aust. J. Chem.* **33**, 2053 (1980).

[14] T.R. Huet, M. Herman and J.W.C. Johns, *J. Chem. Phys.* **94**(5), 3407 (1990).

[15] M. Herman, M.I. El Idrissi, A. Pisarchik, A. Campargue, A.C. Gaillot, L. Biennier, G. Di Lonardo and L. Fusina, *J. Chem. Phys.* **108**(4), 1377 (1997).

[16] S. Ghersetti and K. Narahari Rao, *J. Mol. Spectrosc.* **28**, 27 (1968).

[17] D. Bermejo, G. Di Lonardo, J.L. Doménech, and L. Fusina, *J. Mol. Spectrosc.* **209**, 259 (2001).

[18] S. Yu, B.J. Drouin, J.C. Pearson, H.M. Pickett, V. Lattanzi, and A. Walters, *Astrophysical Journal*, **698**, 2114 (2009).

[19] G. Weirauch, M.I. El Idrissi, J. Vander Auwera, M. Herman and A. Campargue, *Mol. Phys.* **99**(11), 969 (2001).

[20] R.A. Toth, *J. Opt. Soc. Am.* **B 8**, 2236 (1991).

[21] R.A. Toth, *J. Opt. Soc. Am.* **B 10**, 2006 (1993).

[22] G. Guelachvili and K. Narahari. Rao, *Handbook of Infrared Standards II*, Academic Press, Inc. Orlando, Florida, 1986.

[23] V.–M. Hornemann, *J. Opt. Soc. Am*. B **21** (5), 1050 (2004).

[24] R.A. Toth, *Applied Optics* **30**(36), 5289 (1991).

[25] B. Amyay, M. Herman, A. Fayt, L. Fusina, A. Predoi–Cross, *Chem. Phys. Letters* **491**, 17 (2010).

[26] A. Predoi–Cross, M. Herman, L. Fusina, G. Di Lonardo, *Mol. Phys.* **110**, 2621 (2012).

[27] G. Di Lonardo, A. Baldan, G. Bramati and L. Fusina, *J. Mol. Spectrosc.* **213**, 57 (2002).

[28] A. Predoi–Cross, M. Herman, L. Fusina, G. Di Lonardo, *Mol. Phys.* **109**, 559 (2011).

[29] C. Degli Esposti, L. Dore, L. Fusina, F. Tamassia, *Mol. Phys.* **111**(7), 896 (2013).

[30] L. Fusina, E. Canè, F. Tamassia, A. Baldan, G. Di Lonardo, *J. Mol. Spectrosc.* **268**, 226 (2011).

[31] M. Villa, E. Canè, F. Tamassia, G. Di Lonardo, L. Fusina, *J. Chem. Phys*. **138**, 134312 (2013).

[32] E. Canè, G. Cazzoli, G. Di Lonardo, L. Dore, R. Escribano and L. Fusina, *J. Mol. Spectrosc.* **216**, 447 (2002).

[33] R.E. Colborn, K.P.C. Volhardt and J. Label, *Comp. Radiopharm.* **20**, 257 (1983).

[34] G. Di Lonardo, L. Fusina, A. Baldan, R.Z. Martinez and D. Bermejo, *Mol. Phys.* **109**, 2533 (2011).

[35] K.F. Palmer, S. Ghersetti, K. Narahari Rao*, J. Mol. Spectrosc.* **30**, 146 (1969).

[36] S. Ghersetti, A. Baldacci, S. Giorgianni, R.H Barnes and K. Narahari Rao, *Gazz. Chim. It.* **105**, 875 (1975).

[37] M. Huhanantti, J. Hietanen, R. Anttila and J. Kauppinen, *Mol. Phys.* **37**, 905 (1979).

[38] J.L. Hardwick, Z.T. Martin, M.J. Pilkenton and E.N. Wolf, *J. Mol. Spectrosc.* **243**, 10 (2007).

[39] L. Fusina, E. Cané, F. Tamassia and G. Di Lonardo, *Mol. Phys.* **105**, 2321 (2007).

[40] B. Bernhardt, A. Ozawa, P. Jacquet, M. Jacquey, Y. Kobayashi, T. Udem, R. Holzwarth, G. Guelachvili, T.W. Haensch, N. Picque, *Nat. Photonics* **4**, 55 (2009).

[41] R.A. Toth, *Applied Optics* **33**(21), 4851 (1994).

[42] X. De Ghellinck d'Elseghem Vaernewijck, D. Golebiowski and M. Herman, *Mol. Phys.* **110**, 2735 (2012).

[43] X. De Ghellinck d'Elseghem Vaernewijck, K. Didriche, C. Lauzin, A. Rizopoulos, M. Herman and S. Kassi, *Mol. Phys.* **109**, 2173 (2011).

[44] X. De Ghellinck d'Elseghem Vaernewijck, S. Kassi and M. Herman, *Mol. Phys.* **110**, 2665 (2012).

[45] S. Robert, B. Amyay, A. Fait, G. Di Lonardo, L. Fusina, F. Tamassia and M. Herman, *J. Phys. Chem*. **A 113**, 13251 (2009).

[46] A. Fayt, S. Robert, G. Di Lonardo, L. Fusina, F. Tamassia and M. Herman, *J. Chem Phys*. **126**, 1143030 (2007).

[47] J.K. Tyler and J. Sheridan, *Trans. Faraday Soc.* **59**, 2661 (1963).

[48] H. Jones and H.D. Rudolph, *Z. Naturforsch. A* **34**, 340 (1979).

[49] J.K. Holland, D.A. Newnham, I.M. Mills and M. Herman, *J. Mol. Spectrosc.* **151**, 346 (1992).

[50] J.K. Holland, W.D. Lawrance and I.M. Mills, *J. Mol. Spectrosc.* **151**, 369 (1992).

[51] J.K. Holland, D.A. Newnham and I.M. Mills, *Mol. Phys.* **70**, 319 (1990).

[52] A.F. Borro, I.M. Mills and A. Mose, *Chem. Phys*. **190**, 363 (1995).

[53] O. Vaittinen, M. Saarinen, L. Halonen and I.M. Mills, *J. Chem. Phys*. **99**, 3277 (1993).

[54] K. Matsumura, K. Tanaka, C. Yamada and T. Tanaka, *J. Mol. Spectrosc*. **80**, 209 (1980).

[55] H. Jones, *J. Mol. Spectrosc*. **102**, 498 (1983).

[56] R. Anttila and M. Huhanantti, *J. Mol. Spectrosc*. **54**, 64 (1975).

[57] M. Niedenhoff, K.M.T. Yamada, J. Lindenmayer and H. Jones, *J. Mol. Spectrosc*. **152**, 213 (1992).

[58] M. Huhanantti, R. Anttila and J. Kauppinen, *J. Mol. Spectrosc*. **66**, 46 (1977).

[59] J. Chernicaro, A.M. Heras, A.G.G.M. Tielens, J.R. Pardo, F. Herpin, M. Guélin and L.B.F.M. Waters, *Astrophys. J.* **546**, L123 (2001).

[60] J. Bernard−Salas, E. Peeters, G.C. Sloan, J. Cami, S. Guiles and J.R. Houck, *Astrophys. J.* **652**, L29 (2006).

[61] T. De Graauw, H. Feuchtgruber, B. Bezard, P. Drossart, T. Encrenaz, D.A. Beintema, M. Griffin, A. Heras, M. Kessler, K. Leech, E. Lellouch, P. Morris, P.R. Roelfsema, M. Roos−Serote, A. Salama, B. Vandenbussche, E.A. Valentijn, G.R. Davis and D.A. Naylor, *Astron. Astrophys*. **321**, L13 (1997).

[62] T. Fouchet, B. Bézard and T. Encrenaz, *Space. Sci. Rev*. **119**, 123 (2005).

[63] A. Coustenis, R.K. Achterberg, B.J. Conrath, D.E. Jennings, A. Marten, D. Gautier, C.A. Nixon, F.M. Flasar, N.A. Teanby, B. Bézard, R.E. Samuelson, R.C. Carlson, E. Lellouch, G.L. Bjoraker, P.N. Romani, F.W. Taylor, P.G.J. Irwin, T. Fouchet, A. Hubert, G.S. Horton, V.G. Kunde, S. Vinatier, J. Mondellini, M.M. Abbas and R. Courtin, *Icarus* **189**, 35 (2007).

[64] A. Coustenis, D.E: Jennings, A. Jolly, Y. Bénilan, C.A. Nixon, S. Vinatier, D. Gautier, G.L. Bjoraker, P.N. Romani, R.C. Carlson and F.M. Flasar, *Icarus* **197**, 539 (2008).

[65] N.L. Owen, C.H. Smith and G.A. Williams, *J. Mol. Struc*t. **161**, 33 (1987).

[66] J.B. Armitage, R.H. Jones and M.C. Whiting, *J. Chem. Soc*., 44 (1951).

[67] V. –M. Hornemann, *J. Opt. Soc. Am*. B **241**, 45 (2007).

[68] L. Bizzocchi, F. Tamassia, C. Degli Esposti, L. Fusina, E. Cané and L. Dore, *Mol. Phys.* **109**, 2181 (2011).

[69] F. Tamassia, L. Bizzocchi, C. Degli Esposti, L. Dore, M. Di Lauro, L. Fusina, M. Villa and E. Cané, *Astron. Astrophys.* **549**, A38 (2013).

[70] L. Bizzocchi, F. Tamassia, C. Degli Esposti, L. Dore, L. Fusina, M. Villa and E. Cané, *J. Chem. Phys.* **139**, 154308 (2013).

CHAPTER 4

ANALYSIS OF SYMMETRIC TOP MOLECULES

The symmetric top molecules analysed belong to C_{3V} point group.

4.1 CH_3CCH

Propyne, or methylacetylene, is a prolate symmetric top molecule and it has a large value of the axial rotational parameter. As a consequence, the excitation energies of the levels increase rapidly with the *K* quantum number. Nevertheless, the *K* – components of a specific sub–branch lie in a fairly narrow wavenumber range, in particular for low *J* values. These spectral structures are thus ideal probes for the kinetic energy of the interstellar medium [1]. In addition, propyne exhibits prototype behaviour for the investigation of intramolecular vibrational redistribution (IVR), induced by the methyl group rotation [2–11]. Propyne has $3N - 6 = 15$ vibrational degrees of freedom, giving rise to 9 normal modes, as illustrated in Table 4.1.

Table 4.1: Description of the normal modes of CH_3CCH

Mode	Symmetry		Band origin (cm^{-1})
ν_1	A_1	Acetylenic CH stretch	3335.1 [7]
ν_2	A_1	Symmetric methyl CH stretch	2941.0 [11]
ν_3	A_1	C≡C stretch	2142.0 [12]
ν_4	A_1	Methyl deformation	1385.6 [13]
ν_5	A_1	Stretching C–C	930.3 [14]
ν_6	E	Antisymmetric methyl CH stretch	2980.9 [3]
ν_7	E	Methyl skeletal deformation	1450.3 [13]
ν_8	E	Methyl rocking	1036.1 [14]
ν_9	E	C≡C–H bend	638.6 [15]
ν_{10}	E	C–C≡C bend	330.9 [16]

The region of the first overtone of ν_1 is quite complex, because of a network of Coriolis and anharmonic interactions. That is why an accurate re–investigation of the range 6200 – 6700 cm^{-1} is needed.

4.1.1 Experiment

Spectra were recorded both in Bologna and in Brussels using different techniques.

a) Supersonic expansion – CRDS: FANTASIO+

Low temperature spectra were recorded in specific ranges by Cavity Ring Down Spectroscopy (CRDS). Briefly, CRDS is a highly sensitive technique that enables measurements of samples which can absorb electromagnetic radiation. The principle is quite simple: a laser is used to illuminate a high–finesse optical cavity. When the laser is in resonance with a cavity mode, intensity builds up in the cavity due to constructive interference. The laser is turned off in order to allow the measurement of the exponentially decaying light intensity leaking from the cavity. During this decay, light is reflected back and forth thousands of times between the mirrors of the cavity giving a considerable effective path length. If something that absorbs the light is present inside the cavity, the decay of the radiation is even faster. A CRDS setup measures how long it takes for the light to decay to 1/e of its initial intensity. The instrumental system built up for recording the spectra is shown in Figure 4.1.

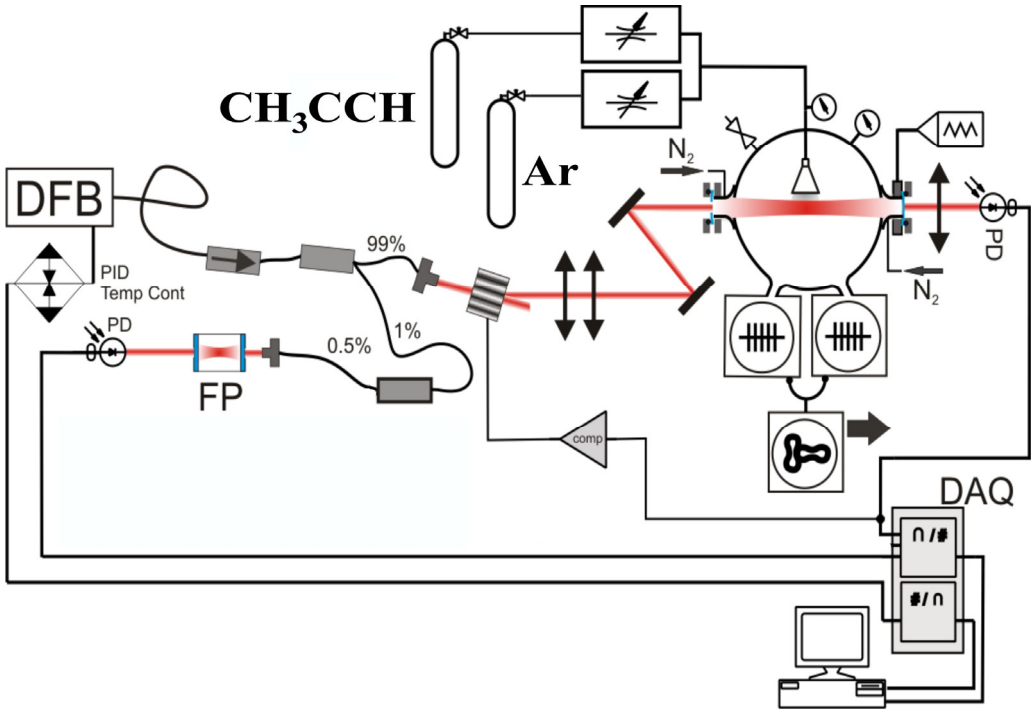

Figure 4.1: Experimental setup of the FANTASIO+ instrumentation.

The CW – CRDS spectrometer uses DFB tunable diode lasers (TDL) emitting in the 1.5 μm range (e.g. ILX light wave, 1 MHz line width). The TDL beam is sent through an optical isolator and then split by a coupler. Some 1% of the light intensity is sent via a fibre collimation package (f = 8 mm) into a Fabry – Pérot interferometer made of two 50% reflectivity flat mirrors positioned on an Invar bar. The remaining 99% of the light is focused by a fibre collimation package (f = 4.5 mm) onto an acousto – optical modulator (AOM) from AA Opto – Electronic (MGAS 80 – A1). The first order diffraction from the AOM is injected into the TEM_{00} mode of a linear ring–down cavity through two lenses (f_1 = 30 mm, f_2 = 50 mm) and two steering mirrors. The cavity is composed of two concave mirrors (Radius = 1000 mm) with reflectivity R = 99.9986% (Layertec), separated by about 540 mm. The ring down time was about 130 μs [17], corresponding to about 72000 passes below the 1 cm slit, i.e. some 720 m effective absorption path in the cooled gas. The TDL frequency can be continuously tuned by sweeping the temperature using a home – made PID stabilizer. The temperature tuning from about 60 °C to –5 °C corresponds approximately to 30 cm^{-1} of spectral range for each diode. 50 measured ring down times for each spectral point of the present recordings have been averaged. For linearization of the spectra, the transmittance of a Fabry – Pérot interferometer was recorded simultaneously, as described in [17]. FTIR spectra previously recorded [2] with an estimated precision of 10^{-3} cm^{-1} were used for calibration.

The free supersonic jet expansion is produced using two identical, large turbomolecular pumps (Leybold MAG W3200 CT; 3200 l/s). They are directly mounted below the cylindrical expansion cell, about 32 cm in diameter. The reservoir (p_0) and residual (p_∞) pressures are measured using MKS Baratron gauges (1000 and 1 torr full scale, respectively). The propyne, from Air Liquide (97 % purity) and used without further purification, and Ar carrier gas, flows were measured using MKS and Brooks flowmeters (10000 and 50000 cubic centimetre per minute at STP, respectively). The slit nozzle was about 1 cm long and 30 μm wide. As the recorded bands differ strongly in intensity, the experimental conditions, listed in Table 4.2, have been tuned for each spectrum to reach an optimal signal–to–noise ratio ($\alpha_{min} = 5 \times 10^{-8}$ cm^{-1}). The rotational temperature is estimated to be about 20 K, in each case.

Table 4.2: Experimental conditions used to record the propyne spectra with supersonic expansion

Band	p_0 (kPa)	p_∞ (Pa)	Ar flow (SCCM)	Propyne flow (SCCM)
$2\nu_1$	75	1.3	4600	28
$\nu_1+\nu_2$ / $\nu_1+\nu_6$	61	1.9	4500	236
$\nu_1+\nu_3+\nu_5$	80	1.7	4300	710

b) FTIR

High resolution spectra were recorded at the university of Bologna using a Bomem DA3.002 Fourier Transform spectrometer. The sample of propyne (99% of purity) was purchased by Sigma Aldrich. The instrument was equipped with a quartz source, a quartz beam splitter and a InSb detector, operating at liquid nitrogen temperature. A multipass cell was used in order to obtain a maximum path length up to 10 m. Several scans up to 2400 were co–added in order improve the signal–to–noise ratio. An instrumental resolution from 0.004 cm^{-1} to 0.016 cm^{-1} was set, achieving a resolution of 0.016 cm^{-1}, close to the Doppler limit. Experimental conditions for each spectrum are reported in Table 4.3.

Table 4.3: Experimental conditions for the recording of CH_3CCH FTIR spectra

Spectrum	Pressure of the sample (Pa)	Range (cm^{-1})	Source	Detector	Resolution (cm^{-1})	#Scans	Optical pathlenght (m)
a	267.0	6200 – 6700	Quartz	InSb	0.004	880	6
b	1333.3	6200 – 6700	Quartz	InSb	0.008	1800	10
c	2666.6	6200 – 6700	Quartz	InSb	0.016	2400	10

The calibration was performed on the basis of the already calibrated low temperature CRDS spectra recorded in Brussels and on H_2O rovibrational transitions [18,19].

c) Cavity Enhanced Absorption Spectroscopy (CEAS)

Spectra were recorded in Brussels using the apparatus already described in Section 3.3.1. Conditions needed to be adapted empirically by tuning the cell length to a slightly different value

for each selected central wavelength and for each sample pressure to optimize this fringing smoothing effect. The equivalent path length is $L_{eq} = \frac{FL_{cavity}}{\pi} \approx 12000$ m at 6500 cm^{-1}, and is reduced to a minimum value of 1500 m on the edges of the explored spectral range (at 6200 cm^{-1}). The spectra were recorded using propyne (from Air Liquide, 97 % purity) at a pressure of 267 Pa, retuning the laser output wavelength as often as necessary to cover the full range from 6200 to 6700 cm^{-1}. The pressure was kept low to reduce pressure broadening effects, actually producing a resolution most comparable to that in the conventional FTIR spectra, which benefited from a better instrumental resolution but presented more severe pressure broadening. For the range 6300 to 6700 cm^{-1}, 50 scans were accumulated, leading to $\alpha_{min} = 5 \times 10^{-9}$ cm^{-1}. In the remaining part (6200 – 6300 cm^{-1}), 200 scans were accumulated. The OPO–femto–FT–CEAS spectra were calibrated using the FTIR spectra.

4.1.2 Description of the spectra

The investigated region is between 6200 and 6700 cm^{-1}, as shown in Figure 4.2.

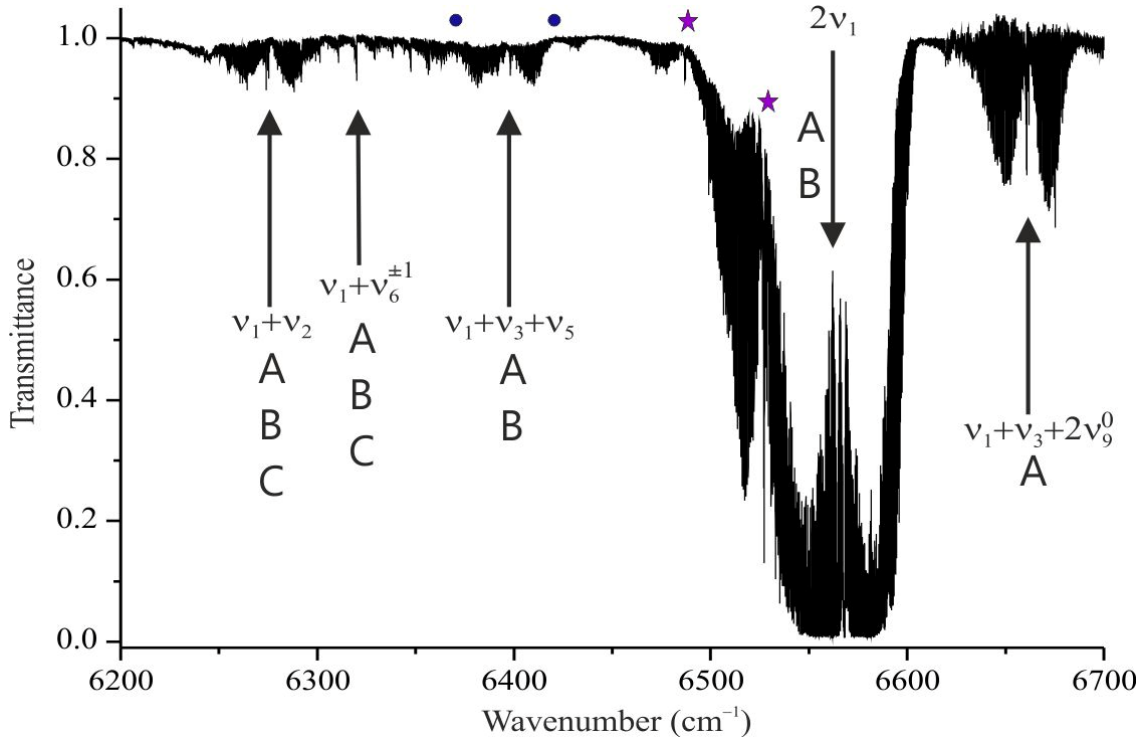

Figure 4.2: Fourier transform spectrum of propyne in the region 6200 – 6700 cm^{-1}. Hot bands associated with $2\nu_1$ are indicated with a star, whereas a dot identifies bands not included in the considered system under investigation. Letters A, B, C indicates the techniques FTIR, CRDS, CEAS (respectively), providing data used in the analysis. Experimental conditions: see spectrum *c* in Table 4.3.

Combination and overtone bands are observed in this region, namely $\nu_1+\nu_2$, $\nu_1+\nu_3+\nu_5$, $2\nu_1$, $\nu_1+\nu_3+2\nu_9^0$ (parallel) and $\nu_1+\nu_6^{\pm1}$ (perpendicular). All of them involve the acetylenic CH stretch ν_1. In addition, hot bands connected with $2\nu_1$ have been observed: they are indicated with a star in Fig. 4.2, but they are not considered in the analysis. Two new bands labelled with a dot in Figure 4.2 were identified and analysed apart and not included in the network of interaction considered during this investigation. They will be discussed in the next section. The origin of the data sets used in the analysis, in terms of one of the three instrumental techniques described in the previous section (A = FTIR; B = CRDS; C = CEAS) is indicated in the Fig. 4.2. A comparison between the spectra recorded with the three different techniques is illustrated in Fig. 4.3.

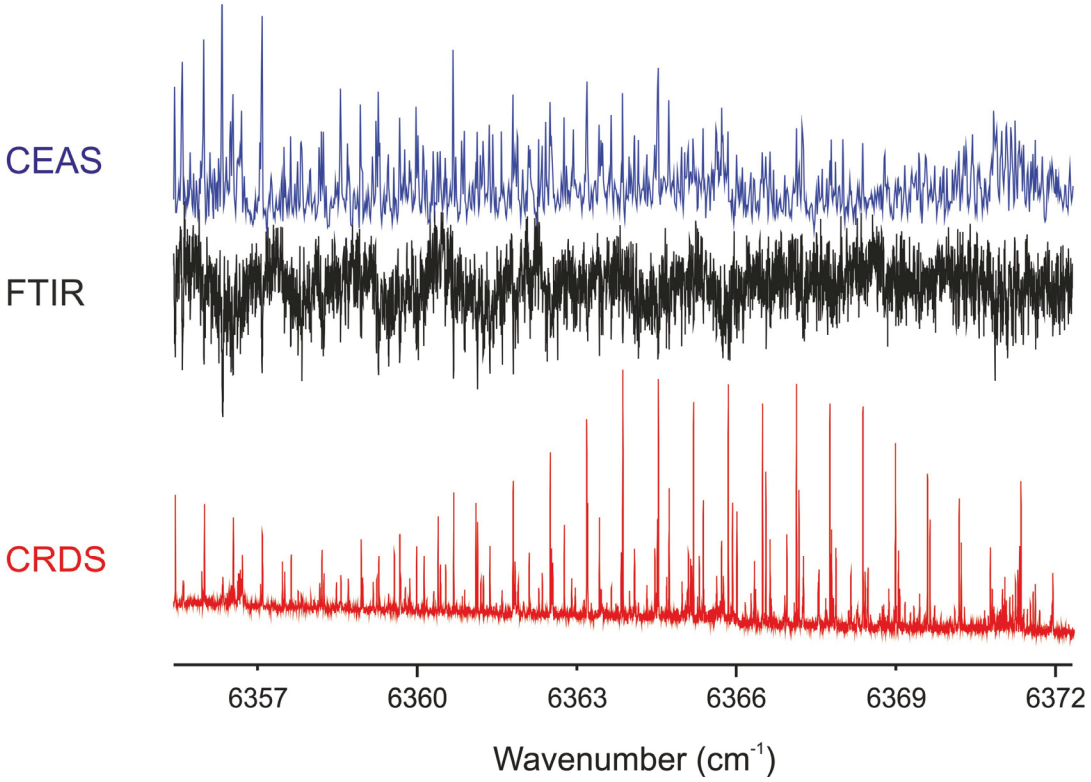

Figure 4.3: Comparison between the spectra of propyne recorded with the three different techniques, CRDS, FTIR and CEAS.

Some bands are too weak to be observed with conventional room temperature FTIR spectrum (black central trace). The CEAS spectrum (blue trace) provides additional sensitivity to highlight high *J* and *K* lines, while the jet cooled CRDS spectrum (red trace) provides a sensitive probe of simplified, low *J* and *K* structure. In fact, the recording of cold spectra was actually extremely important as they allowed the understanding and the analysis of the *K* structure of the parallel bands, unresolved in room temperature spectra. However, stronger bands are well

characterized from the conventional FTIR technique. CEAS data were recorded over the entire spectral range, but they were used only in a narrow interval around 6300 cm^{-1}, either because the bands present outside this interval were strong and the FTIR data set was already complete, or because the additional information was of poorer quality and, as a consequence, not worth to be included in the fitting process.

4.1.3 Analysis

The *K* structure of all the investigated parallel bands could not be completely resolved, since the spectrum is really complicated. For this reason the information available from cold spectra are indispensable to assign low *K* values, since the intensity of the lines decreases rapidly with increasing *K*, i.e. the *K* = 3 transitions are observable only in few cases. The *Q* branch structures for the first few *K* values are partially resolved on the cold spectra (see for instance the *Q* branches of the $\nu_1+\nu_2$ band in Fig. 4.4).

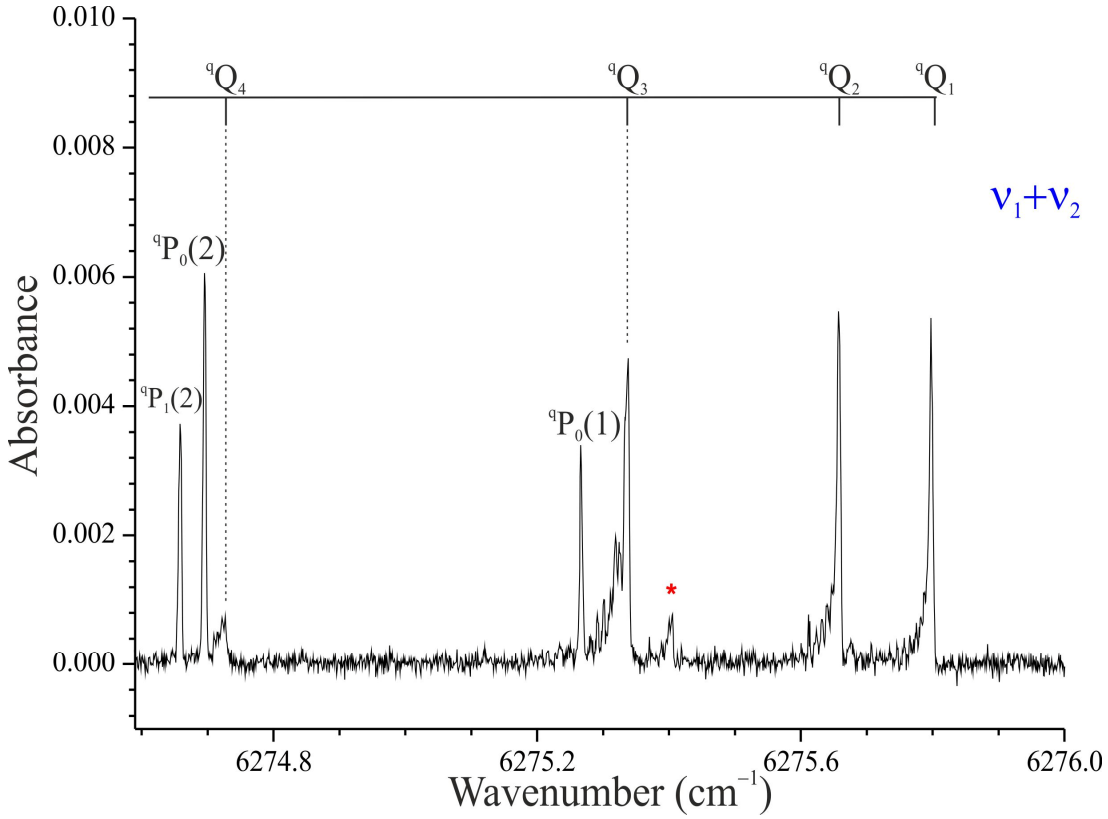

Figure 4.4: Detail of the CRDS spectrum of propyne showing the *Q* branches of the parallel band $\nu_1+\nu_2$. The red asterisk indicates a *Q* branch (presumably *K* = 1) of a band in interaction with $\nu_1+\nu_2$. Experimental conditions: see $\nu_1+\nu_2$ in Table 4.2.

The analysis of room temperature spectra was useful to extend the assignments at higher J values, using the CEAS data, in particular, for the weaker bands around 6300 cm^{-1}.

- $2\nu_1$: This is the strongest band present in the recorded range, already investigated by McIlroy *et al*. [6] under jet–cooled conditions, at a rotational temperature of 5 K, which is slightly lower compared to 20 K as in these spectra. The K and J structures of the various P and R branches are well resolved. In Figure 4.5 a portion of the CRDS spectrum between 6562.875 and 6563.025 cm^{-1} is shown. From the irregular K pattern it is immediately clear that some perturbations are present: K = 3 should indeed appear at higher wavenumbers than K = 2, rather than between K = 1 and 2, as observed. Similar anomalies have already pointed out for $J'' \leq 11$ [6]. Assignments has been extended up to J = 28 both for K = 0 and 1 and up to J = 15 and 12 for K = 2 and 3, respectively, as summarized in Table 4.4, thanks to the high quality of the present CRDS data (S/N > 10000). Although $2\nu_1$ is the strongest band, only a relatively small number of lines has been assigned. This is due to the fact that in the cold spectra only low J and K values are observable and in the room temperature spectra the overlap between sub–bands with different K values did not allow to separately identify the corresponding transitions.

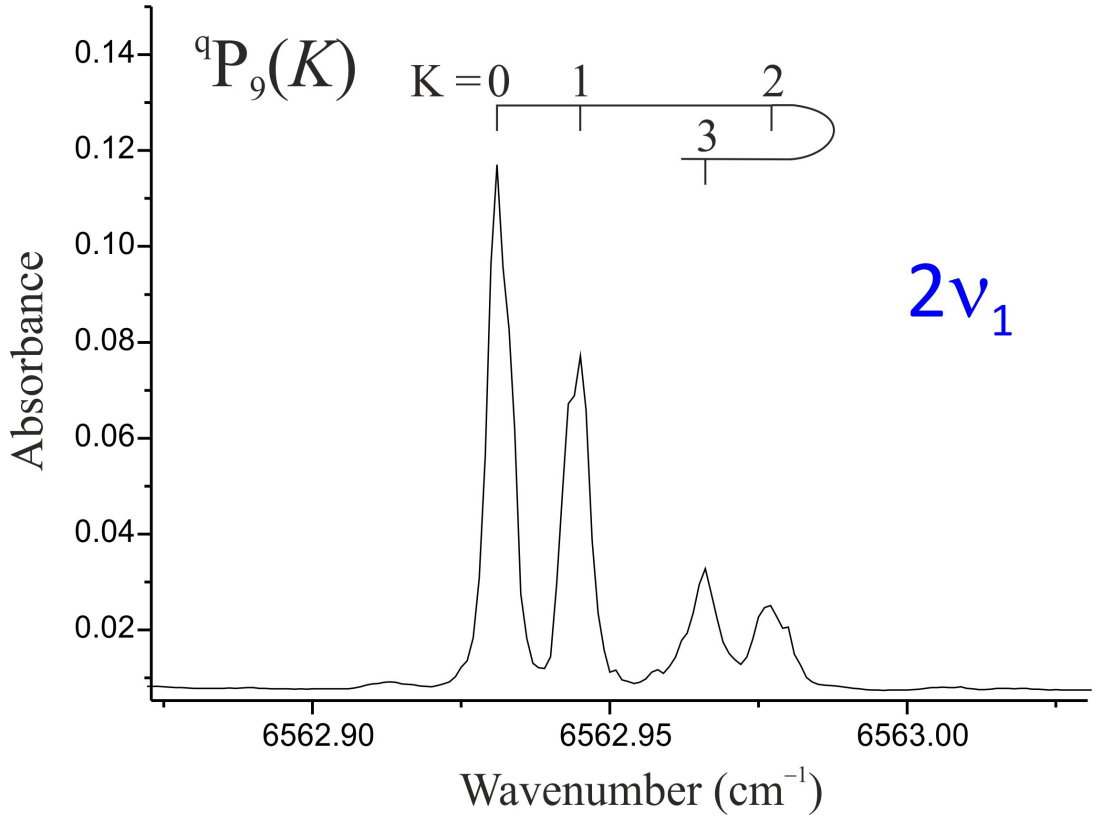

Figure 4.5: Detail of the CRDS spectrum of propyne showing the K structure of the $^qP_9(K)$. Experimental conditions: see $2\nu_1$ in Table 4.2.

- $\nu_1+\nu_2$: This band is that at lowest wavenumbers among those investigated. Transitions with K = 0 and 1, up to J = 41 and 19, respectively, K = 2 and 3 up to J = 17 have been assigned, as summarized in Table 4.4. Another parallel weak band can be observed on the low temperature spectra at about 6275.4 cm^{-1} (indicated with a red asterisk in Fig. 4.4), which is slightly redshifted with respect to the $\nu_1+\nu_2$ origin. It will be called Band 1 hereafter. Only few lines are observed (with $2 < J < 10$, presumably K = 0), which are likely to borrow intensity from $\nu_1+\nu_2$, as further discussed in Section 4.1.4.

- $\nu_1+\nu_3+\nu_5$: This band has an intensity comparable to that of $\nu_1+\nu_2$ and is redshifted and close to $2\nu_1$. It has been possible to assign the K = 0 and 1 lines, up to J = 35 and 24, respectively, and K = 2 up to J = 20, as reported in Table 4.4. Thanks to the high–resolution and low temperature conditions, two others almost overlapping series of lines could be identified, belonging to two bands, labelled 2 and 3 hereafter. For Band 2, a few J values, up to J = 12, could be assigned to P and R transitions, leading to determine the origin, the rotational constant B and the quartic centrifugal distortion parameter D_J of the upper state, as reported in Section 4.1.4. For Band 3, only four P and four R lines are observed, but no useful information could be gained from them. In addition, there are two more bands in the range, identified by blue dots in Figure 4.2, labelled Bands 4 and 5. Their origins are close to 6371 and 6421 cm^{-1}, respectively. No analysis has been performed since on the FTIR spectra they are too weak and their structure is not well resolved and no cold spectra in their ranges have been recorded.

- $\nu_1+\nu_3+2\nu_9^0$: It is the band at the highest wavenumber in the analysed spectral range. It is a strong band even if it corresponds to 4 quanta of excitation. It mainly gains intensity from the close and strong $2\nu_1$ overtone band. Also in this case cold spectra were not available and only room temperature spectra were analyzed. Only K = 0 and 1 transitions up to J = 34 could be assigned.

- $\nu_1+\nu_6^{\pm1}$: This is the only perpendicular band observed in the investigated region. It appears between $\nu_1+\nu_2$ and $\nu_1+\nu_3+\nu_5$, with slightly lower intensity. The structure of the ${}^{P}P$, ${}^{P}Q$, ${}^{P}R$ branches was initially assigned from the cold spectra, which significantly helped in the region where overlap occurs with $\nu_1+\nu_2$ in the room temperature spectrum. Many Coriolis–type perturbations could be observed, as discussed below.

The assignments and band centre for each band are listed in Table 4.4.

Table 4.4: Bands of propyne included in the least–squares fitting procedure

Vibrational transition	Symmetry	ν_0 [a]	Lines assigned			
			$K = 0$	$K = 1$	$K = 2$	$K = 3$
$\nu_1 + \nu_2$	A_1	6275.841723[b]	^{q}P (1-41) ^{q}R (0-40)	^{q}P (2-17) ^{q}R (1-19) ^{q}Q (1-14)	^{q}P (3-17) ^{q}R (2-17) ^{q}Q (2-11)	^{q}P (4-17) ^{q}R (3-17) ^{q}Q (3-14)
$\nu_1 + \nu_6^{\pm 1}$	E	6315.785910	^{r}P (2-28) ^{r}R (0-29)	^{p}P (1-29) ^{p}R (1-21) ^{p}Q (1-22) ^{r}P (3-13) ^{r}R (1-25)	^{p}P (2-24) ^{p}R (2-12) ^{p}Q (5-29) ^{r}P (6-22) ^{r}R (2-20)	^{p}P (3-26) ^{p}R (4-23) ^{p}Q (4-28) ^{r}P (7-16) ^{r}R (3-17)
$\nu_1 + \nu_3 + \nu_5$	A_1	6399.5024[b]	^{q}P (1-35) ^{q}R (0-33)	^{q}P (2-22) ^{q}R (1-24)	^{q}P (3-20) ^{q}R (2-18)	
$2\nu_1$	A_1	6567.8778[b]	^{q}P (1-28) ^{q}R (0-28)	^{q}P (2-28) ^{q}R (1-28) ^{q}Q (1-8)	^{q}P (3-15) ^{q}R (2-13)	^{q}P (4-12) ^{q}R (3-10)
$\nu_1 + \nu_3 + 2\nu_9^0$	A_1	6660.2223[b]	^{q}P (4-34) ^{q}R (2-30)	^{q}P (4-34) ^{q}R (2-30)		

[a] The band centre, ν_0 (in cm^{-1}), is defined as $\nu_0 = E^0_{\upsilon'} - E^0_{\upsilon''}$.
[b] Unperturbed value.

First, the quantum numbers for the lines in each band were assigned and fitted in a band–by–band analysis. As expected, the results were not satisfactory and a large number of higher order parameters (the distortion constants *H*) had to be refined. Most of them resulted poorly determined with anomalous values, order of magnitude larger than the corresponding ones in the ground state (GS). In addition, the number of lines discarded in the fits was rather large (in all 113 out of 616, about 14%) and the predicted position of the transitions did not allow the extension of the assignments at higher *J* and *K* values. This suggested clearly that it was necessary to analyse the bands all together, taking into account the interaction between them. Nevertheless, the outputs of this band–by–band analysis were used as input for the global fit. In each case, the assignment of the quantum numbers *J* and *K* was checked by means of ground state combination differences (GSCD), calculated using the GS parameters in Ref. [20] and reported in Table 4.5.

Table 4.5: Ground state parameters (in cm^{-1}) of propyne

A_0	5.3083046
B_0	0.28505976
$D_{0J}\times10^6$	0.09803546
$D_{0JK}\times10^6$	5.450142
$D_{0K}\times10^3$	0.09173
$H_{0J}\times10^{15}$	–2.308
$H_{0JK}\times10^{11}$	2.94212
$H_{0KJ}\times10^{10}$	1.7406
$H_{0K}\times10^7$	–1.114

In order to perform the global fit, an upgraded version of a program described in [21] was used. For each value of *J*, the program constructs two Hamiltonian matrices of dimensions $6\times(2J+1)$: one is set up for levels of A^+ and A^- symmetry, the other corresponds to one of the degenerate blocks of E symmetry. The diagonal matrix elements, containing the usual contributions up to the 6th power in the angular momentum operators, are given by:

$$\begin{aligned}E(J,K,\ell) = {} & E_\upsilon^0 + B_\upsilon\left[J(J+1)-k^2\right] + A_\upsilon k^2 - 2(A\zeta)_\upsilon k\ell - D_{\upsilon J}\left[J(J+1)\right]^2 \\ & - D_{\upsilon JK}\left[J(J+1)\right]k^2 - D_{\upsilon K}k^4 + \eta_{\upsilon J}\left[J(J+1)\right]k\ell + \eta_{\upsilon K}k^3\ell \\ & + H_{\upsilon J}\left[J(J+1)\right]^3 + H_{\upsilon JK}\left[J(J+1)\right]^2 k^2 + H_{\upsilon KJ}\left[J(J+1)\right]k^4 + H_{\upsilon K}k^6 \\ & + \tau_{\upsilon J}\left[J(J+1)\right]^2 k\ell + \tau_{\upsilon JK}\left[J(J+1)\right]k^3\ell + \tau_{\upsilon K}k^5\ell + \tau_{\upsilon K*}k^3\ell^3\end{aligned} \tag{4.1}$$

where terms containing ℓ vanish for non degenerate states.

The program can treat simultaneously up to 6 parallel and 6 perpendicular bands. In this case it has been adjusted for the bands analysed in the studied range (i.e. 4 parallel and 1 perpendicular bands). Bands 1–5 previously described were not considered in the system because the very few lines observed did not allow an improvement of the global analysis. The off–diagonal elements are reported in Table 4.6. As far as anharmonic resonances are concerned, they are defined as follows:

$$\begin{aligned}W_{a/35} &= \frac{1}{2\sqrt{2}}k_{a/35} \\ W_{5/99} &= \frac{1}{\sqrt{2}}k_{5/99} \\ D_{a/399} &= \frac{1}{2}K_{a/399}\end{aligned} \tag{4.2}$$

where k and K are the cubic and quartic Nielsen's anharmonic constants, respectively, the subscript represents the interacting vibrations, and a is 1 or 2.

Table 4.6: Off–diagonal matrix elements of the vibration–rotation Hamiltonian in propyne.

The basis functions are: $|v_s v_{s'} v_{s''} v_{s'''} v_t \ell_t v_{t'} \ell_{t'}, J, K\rangle = |v_1 v_2 v_3 v_5 v_6 \ell_6 v_9 \ell_9, J, K\rangle$

Coriolis type resonances

$$\left\langle 2\nu_1, J, K \left| (H_{21} + H_{23})/hc \right| \nu_1 + \nu_6, J, K \pm 1, \ell \pm 1 \right\rangle = \pm \left\{ \sqrt{2} \left[{}^{(1,6)}C_{11}^{(1)} + {}^{(1,6)}C_{11}^{(3a)} J(J+1) + {}^{(1,6)}C_{11}^{(3b)} (2K \pm 1)^2 \right] \right\} F_{\pm 1}$$

$$\left\langle 2\nu_1, J, K \left| H_{22}/hc \right| \nu_1 + \nu_6, J, K \pm 1, \ell \pm 1 \right\rangle = \sqrt{2}\, {}^{(1,6)}C_{11}^{(2)} (2K+1) F_{\pm 1}$$

$$\left\langle 2\nu_1, J, K \left| H_{22}/hc \right| \nu_1 + \nu_6, J, K + 2, \ell \mp 1 \right\rangle = \sqrt{2}\, {}^{(1,6)}C_{21}^{(2)} F_{\pm 2}$$

$$\left\langle \nu_1 + \nu_2, J, K \left| (H_{21} + H_{23})/hc \right| \nu_1 + \nu_6, J, K \pm 1, \ell \pm 1 \right\rangle = \pm \left\{ \sqrt{2} \left[{}^{(2,6)}C_{11}^{(1)} + {}^{(2,6)}C_{11}^{(3a)} J(J+1) + {}^{(2,6)}C_{11}^{(3b)} (2K \pm 1)^2 \right] \right\} F_{\pm 1}$$

$$\left\langle \nu_1 + \nu_2, J, K \left| H_{22}/hc \right| \nu_1 + \nu_6, J, K \pm 1, \ell \pm 1 \right\rangle = \sqrt{2}\, {}^{(2,6)}C_{11}^{(2)} (2K+1) F_{\pm 1}$$

$$\left\langle \nu_1 + \nu_2, J, K \left| H_{22}/hc \right| \nu_1 + \nu_6, J, K + 2, \ell \mp 1 \right\rangle = \sqrt{2}\, {}^{(2,6)}C_{21}^{(2)} F_{\pm 2}$$

$$\left\langle \nu_1 + \nu_3 + 2\nu_9^0, J, K \left| H_{31}/hc \right| \nu_1 + \nu_6, J, K + 1, \ell \pm 1 \right\rangle = \pm R_{3699A}^{B} F_{\pm 1}$$

$$\left\langle \nu_1 + \nu_3 + \nu_5, J, K \left| H_{31}/hc \right| \nu_1 + \nu_6, J, K + 1, \ell \pm 1 \right\rangle = \mp R_{356}^{B} F_{\pm 1}$$

Anharmonic resonances

$$\left\langle 2\nu_1, J, K \left| H_{30}/hc \right| \nu_1 + \nu_3 + \nu_5, J, K \right\rangle = W_{1/35}$$

$$\left\langle 2\nu_1, J, K \left| H_{30}/hc \right| \nu_1 + \nu_3 + 2\nu_9^0, J, K \right\rangle = D_{1/399}$$

$$\left\langle \nu_1 + \nu_2, J, K \left| H_{30}/hc \right| \nu_1 + \nu_3 + \nu_5, J, K \right\rangle = W_{2/35}$$

$$\left\langle \nu_1 + \nu_3 + \nu_5, J, K \left| H_{30}/hc \right| \nu_1 + \nu_3 + 2\nu_9^0, J, K \right\rangle = W_{5/99}$$

$$\left\langle \nu_1 + \nu_2, J, K \left| H_{40}/hc \right| \nu_1 + \nu_3 + 2\nu_9^0, J, K \right\rangle = D_{2/399}$$

Essential resonances

$$\left\langle \nu_1 + \nu_6, \ell_6, J, K \left| (H_{22} + H_{24})/hc \right| \nu_1 + \nu_6, \ell_6 \pm 2J, K \pm 2 \right\rangle = -\frac{1}{2} [q_{22}^{(6)}] F_{\pm 2}$$

$$\left\langle \nu_1 + \nu_6, \ell_6, J, K \left| (H_{22} + H_{24})/hc \right| \nu_1 + \nu_6, \ell_6 \pm 2J, K \pm 1 \right\rangle = 2(2K \pm 1)[q_{12}^{[6]}] F_{\pm 1}$$

---

[a] $F_{\pm n} = [J(J+1) - K(K \pm 1)]^{1/2} [J(J+1) - (K \pm 1)(K \pm 2)]^{1/2} \ldots . \{J(J+1) - [K \pm (n-1)](K \pm n)\}^{1/2}$

In the least–squares fits a statistical weight equal to the reciprocal of the squared estimated uncertainty has been attributed to each transition that corresponds to an isolated line, while the weight has been reduced to 1/*n* if *n* transitions are assigned to the same wavenumber. In particular, the precision of each line has been estimated as a ratio between the resolution and the signal–to–noise ratio of the corresponding spectrum, since the data derive from spectra collected in very different experimental conditions. The analysis was accomplished as an iterative process, which consisted in improving the values of the excited state parameters by means of the assigned lines, also refining new constants when necessary, predicting the wavenumbers of higher *J* and *K* unassigned transitions to be searched in the spectra and enlarging the original data set.

4.1.4 Results and Discussion

In total, 1176 rovibrational transitions have been assigned, 179 of which belong to $2\nu_1$, 254 to $\nu_1+\nu_2$, 145 to $\nu_1+\nu_3+\nu_5$, 120 to $\nu_1+\nu_3+2\nu_9^0$, and 478 to $\nu_1+\nu_6^{\pm1}$.

Once all the transitions that could be unambiguously assigned were identified, a systematic investigation to derive the set of parameters that best reproduces the experimental data was carried out. Constants up to the third order of approximation, E^0, B, A, $A\zeta$, $C_{11}^{(1)}$, $C_{11}^{(2)}$, $C_{21}^{(2)}$, $C_{11}^{(3a)}$, $C_{11}^{(3b)}$, η_J, η_K and the distortion constants D and H were refined. At the end of each fit it was checked that the newly, as well as the previously determined parameters, were statistically determined, that they improved the standard deviation of the fit and that large correlations between the parameters were not present. The parameters not fulfilling these requirements were constrained either to zero or to their corresponding GS values in the next fits.

In the final cycle 109 transitions, about 9% of the assigned transitions, were excluded from the fit since the differences between their observed and calculated values exceeded the chosen limit for rejection of 0.01 cm^{-1}. The standard deviation of the fit was 0.0029 cm^{-1}. Table 4.7 lists the parameters derived from the analyses of 1067 transitions retained in the final fit. All the parameters in Eq. (4.1) and in Table 4.6 which are not reported in Table 4.7 were set equal to zero and constrained in the refinement procedure.

Table 4.7: Spectroscopic parameters (in cm^{-1}) of propyne derived from the global analysis

	$\nu_1+\nu_2$	$\nu_1+\nu_6^{\pm1}$	$\nu_1+\nu_3+\nu_5$	$2\nu_1$	$\nu_1+\nu_3+2\nu_9^0$
$E_\upsilon^{0\,a}$	6275.840664(455)	6315.786070(388)	6399.4632(238)	6567.8778(373)	6660.2220(286)
A	5.269597(122)	5.283209(189)	5.35446(103)	5.326702(286)	5.306355(975)
B	0.28444184(274)	0.28434889(304)	0.28239875(968)	0.28353125(345)	0.28329317(545)
D_J x10^6	0.06096(196)	0.09610(428)	0.3543(234)	0.20215(349)	0.08081(533)
D_{JK} x10^6	–80.07(196)	5.450142	83.11(205)	–15.19(204)	5.450142
D_K x10^3	2.0292(102)	–2.3000(112)	1.980(231)	2.9424(310)	9.173
H_J x10^{15}	–2.308 [b]	–2.308 [b]	148193(14600)	–2.308 [b]	–2.308 [b]
H_{JK} x10^{11}	2.94212 [b]	2.94212 [b]	2.94212 [b]	2.94212 [b]	2.94212 [b]
H_{KJ} x10^{10}	1.7406 [b]	1.7406 [b]	1.7406 [b]	1.7406 [b]	1.7406 [b]
H_K x10^7	–1.114 [b]	–1.114 [b]	–1.114 [b]	–1.114 [b]	–1.114 [b]
$A\zeta$		0.360832(196)			
η_K		–0.0102251(511)			
Interaction parameters					
$^{(1,6)}C_{11}^{(1)}$	–0.01290(146)	$^{(2,6)}C_{11}^{(1)}$	–0.010053(711)	W_{135}	15.124(132)
$^{(1,6)}C_{11}^{(2)}$	–0.07861(124)	$^{(2,6)}C_{11}^{(2)}$	0.049066(577)	D_{1399}	9.886(132)
$^{(1,6)}C_{11}^{(3b)}$ x10^3	9.7249(799)				

[a] Unperturbed values.
[b] Constrained to the ground state value.

It is worth noting that while the rotational constants A and B and the quartic centrifugal distorsion constants D_J and D_K are close to the corresponding values of the GS, the refined D_{JK} values differ from the one of the GS both in order of magnitude and sign. This highlights that these parameters are effective since they absorb the effects of the interactions with unobserved dark states, which have not been taken into account in the model. An analogous explanation could be invoked for η_K and for the only sextic centrifugal distortion constant refined, H_J of $\nu_1+\nu_3+\nu_5$, whose effective value is 5 orders of magnitude larger than that of the GS and opposite in sign. The obtained results, and in particular the fact that some interaction parameters cannot be quantified in a proper way, clearly suggest that in the investigated region a large number of interacting dark states is present and that they should be taken into account in order to better understand the observed features. In the case of $2\nu_1$, for example, further interaction states are needed to explain the irregularity in the K structure. In order to identify all possible interactions between vibrational states containing ν_1, ν_2, ν_3, ν_5 and ν_9, which are involved in the analysed overtone and combination bands, we considered the polyad structure, defining $N_r = 5\nu_1+5\nu_2+3\nu_3+2\nu_5+\nu_9$ and $N_s = \nu_1 + \nu_2 + \nu_3$ [21, 22]. This could also help the assignment of the additional parallel bands 1–5. Other interactions of Coriolis–type, in addition to that between $2\nu_1$ (A_1) and $\nu_1 + \nu_6$ (E), are also possible. States of E symmetry close in energy to $2\nu_1$ are for instance $2\nu_2 + \nu_9$, $2\nu_2 + 2\nu_{10}$, and $2\nu_6 + \nu_9$. However, due to the lack of corresponding spectroscopic observations, only the pattern of anharmonic interactions between states within the same polyad has been taken into account. The polyad with $2\nu_1$ is therefore the one with $N_r = 10$, $N_s = 2$ and $\ell = 0$, *i.e.* $\{N_r, N_s, \ell\} = \{10, 2, 0\}$. The states belonging to it and the anharmonic interaction network between them up to H_{40}, are illustrated in Table 4.8.

Table 4.8: Polyad matrix for propyne involving $N_r = 10$ ($N_r = 5\nu_1+5\nu_2+3\nu_3+2\nu_5+\nu_9$) with structure: $\{N_r, N_s, \ell\} = \{10, 2, 0\}$.

$2\nu_2$	*W*2/35				*D*2/399			D11/22				
	$\nu_2+\nu_3+\nu_5$	*W*2/35	*W*1/35		*W*5/99	*D*2/399						
		$2\nu_3+2\nu_5$		*W* 1/35		*W*5/99						
			$\nu_1+\nu_2$	*W*2/35	*D*1/399					*D*2/399		
				$\nu_1+\nu_3+\nu_5$		*D*1/399	*W*1/35	*W*5/99				
					$\nu_2+\nu_3+2\nu_9$	*W*2/35					*D*2/399	
						$2\nu_3+\nu_5+2\nu_9$			*W*1/35	*W*5/99		
							$2\nu_1$	*D*1/399				
								$\nu_1+\nu_3+2\nu_9$		*D*1/399		
										$2\nu_3+4\nu_9$		

The diagonal matrix elements from top to bottom represent the vibrational states in increasing order of energy.

This scheme helped to assign Band 5, observed in the cryogenic spectrum, as $2\nu_3 + \nu_5 + 2\nu_9^0$. Consequently, the polyad size have been enlarged in order to provide further assignments, first including the vibrational mode ν_4, the only other mode of A_1 symmetry not yet included, and next including mode ν_{10}, eventually defining $N_r = 10\nu_1 + 10\nu_2 + 6\nu_3 + 4\nu_4 + 4\nu_5 + 2\nu_9 + \nu_{10}$, with adequate, additional interaction terms in the matrix Hamiltonian. This extension suggested to assign Band 4 at about 6371 cm^{-1} as $\nu_2 + 2\nu_4 + 2\nu_{10}^0$. Other bands can be tentatively assigned in the studied range, all involving A_1 upper states, on the basis of reasonable agreement between observed and predicted band origins. As a result, Bands 1 and 2 at 6275 and 6398 cm^{-1}, were assigned as $2\nu_3 + \nu_4 + 2\nu_{10}^0$ and $\nu_1 + \nu_3 + \nu_9 + \nu_{10}$ respectively. Band 3 could be assigned as $3\nu_3$, by assuming a value of $x_{3,3}$ equal to about –1.0 cm^{-1}. They would belong to polyads with N_r = 18 (Bands 1 and 3) and 19 (Band 2).

The observed rovibrational transitions for Bands 1 to 5 made it possible to analyze only $2\nu_3 + \nu_4 + 2\nu_{10}^0$ and $\nu_1 + \nu_3 + \nu_9 + \nu_{10}$. The obtained spectroscopic parameters are listed in Table 4.9.

Table 4.9: Spectroscopic parameters (in cm^{-1}) of propyne for $2\nu_3 + \nu_4 + 2\nu_{10}^0$ and $\nu_1 + \nu_3 + \nu_9 + \nu_{10}$

	Band 1	Band 2
	$2\nu_3 + \nu_4 + 2\nu_{10}^0$	$\nu_1 + \nu_3 + \nu_9 + \nu_{10}$
ν_0	6275.40954(101)	6398.33755(300)
B	0.2842307(779)	0.284268(111)
$D_J \times 10^6$	–0.0001410(164)	1.727(757)

4.2 $^{15}ND_3$

Ammonia and its isotopologues are oblate symmetric top molecules and have been studied for many years as it is a prototype molecule of the hindered inversion motion at the pyramidal nitrogen atom. In fact, the equilibrium configuration of ammonia is pyramidal but, for large amplitude motion in vibrational mode, the molecule may go through the planar configuration to a pyramidal configuration which is identical with the initial one except that the pyramid has been inverted. The two pyramidal configurations correspond to two identical minima in the potential energy curve and the planar configuration to an energy maximum. This behaviour is illustrated in Figure 4.6. The potential energy curve is illustrated in the case of ν_2, where the barrier is about 2020 cm^{-1}.

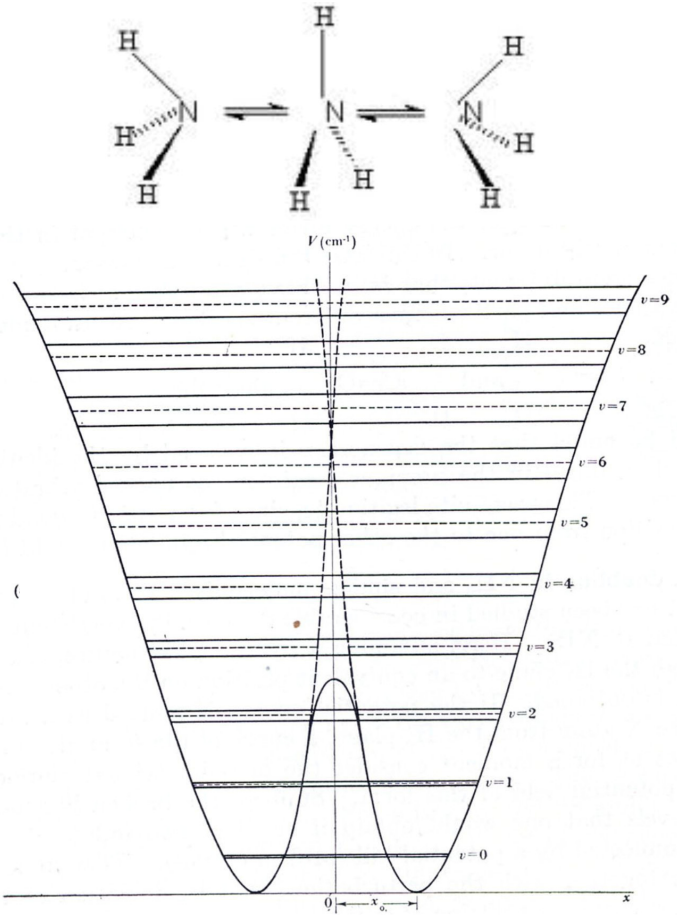

Figure 4.6: Potential energy curve for the inversion vibration ν_2 of NH_3 molecule.

However, the interconversion between the two forms is possible because of a quantum–mechanical tunnelling through the barrier. If the barrier is sufficiently low or narrow, the penetration may be so great that interaction may occur between the identical sets of vibrational level split into two components: *a* and *s* (antisymmetric and symmetric with respect

to the inversion), by mixing the wavefunctions of the two identical pyramidal forms. The splitting becomes greater towards the top of the barrier [23].

Nevertheless, the interpretation of its spectroscopic behaviour still poses a difficult challenge to both experimental and theoretical approaches. Moreover, in the last 10 years the interest in computation of the energies of vibration and rovibration levels up to high excitations has increased. An accurate reproduction of the observed transitions allows reliable predictions at room and higher temperatures [25–27] and it can help the interpretation of data collected by astronomical missions [28–30]. Up to now, spectroscopic investigation of fully deuterated ammonia has been limited to fundamentals [23,31] and to the GS [32] for $^{14}ND_3$. In case of $^{15}ND_3$, only the GS and the state $\upsilon_2 = 1$ have been investigated [33,34]. The analysis of the fundamental vibration for this isotopologue is then needed, and is presented hereafter.

4.2.1 Experiment

The isotopically pure (99% atom D, 98% atom ^{15}N) was purchased by Sigma Aldrich. The spectra were recorded between 450 and 2700 cm^{-1} using a Bomen DA3.002 Fourier transform (FT) spectrometer in Bologna. A Globar source, KBr beam splitter and two high sensitivity HgCdTe detectors operating at liquid nitrogen temperature were used. The optical path was 0.18 or 10 m. The achieved resolution ranged from 0.004 to 0.009 cm^{-1}. Before recording the spectra, the cell was flushed with pure $^{14}ND_3$ several times in order to reduce as much as possible the H/D exchange with $^{15}ND_3$. The calibration was performed by comparing absorption lines of residual CO_2 [18,35] and H_2O [36] in the spectrometer. Both the wavenumber precision and accuracy of the spectra are estimated to be 0.3×10^{-3} cm^{-1}. An overview of the general conditions for each recording are reported in Table 4.10.

Table 4.10: Experimental conditions for the recording of $^{15}ND_3$ spectra

Spectrum	Pressure of the sample (Pa)	Range (cm^{-1})	Source	Detector	Resolution (cm^{-1})	#Scans	Optical pathlenght (m)
a	80.0	450 – 1600	Globar	MCT*	0.004	1000	0.18
b	1333.2	450 – 1600	Globar	MCT*	0.006	1200	0.18
c	360.0	800 – 2300	Globar	MCT*	0.006	300	10
d	546.5	1700 – 2700	Globar	MCT*	0.004	870	0.18

* MCT is a HgCdTe detector.

4.2.2 Description of the spectra

Although the cell was conditioned in order to minimize the H/D exchange, many lines belonging to $^{15}ND_2H$ and $^{15}NH_2D$ isotopologues are present all over the spectrum.

a) The 450 – 1600 cm^{-1} region

This region is dominated by the bending fundamental modes, i.e. ν_2 (parallel band) and ν_4 (perpendicular band), at 743 and 1190 cm^{-1}, respectively, as shown in Figure 4.7. Some bands belonging to other isotopologues are present. In fact it is possible to identify ν_2, ν_{4a} and ν_{4b} of $^{15}ND_2H$ and ν_2 of $^{15}NH_2D$. Their assignments has been possible on the basis of the analysis for the two asymmetric isotopologues reported in Ref. [37]

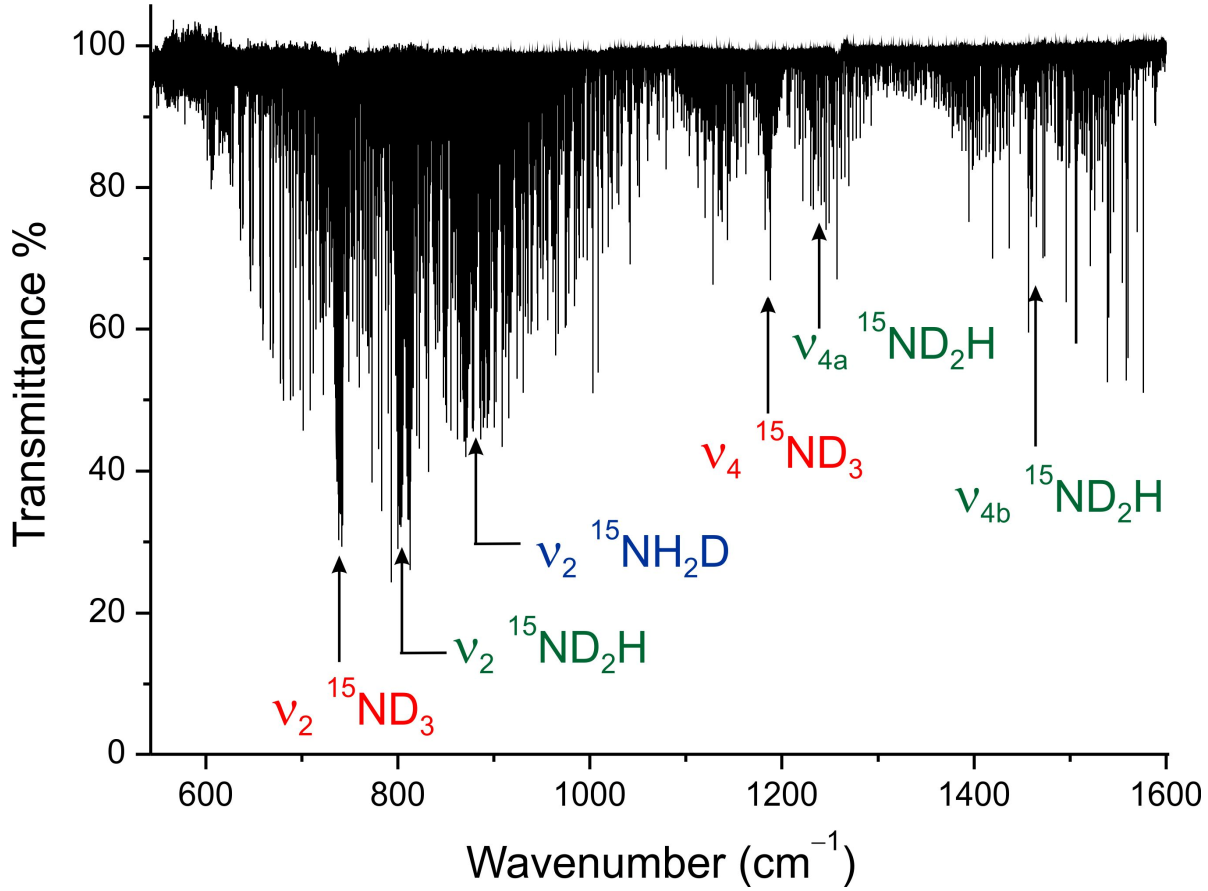

Figure 4.7: Overview of the bending region of $^{15}ND_3$ between 550 and 1600 cm^{-1}. In red are indicated the bands of the isotopologue under investigation, while in blue and green those of two impurities presents in the sample. Experimental conditions: see spectrum *a* in Table 4.10.

The parallel band ν_2 is stronger than ν_4, and its shape consists of two $s \leftarrow a$ and $a \leftarrow s$ sub–bands, centred at 739.5 and 742.8 cm^{-1}, respectively. The central Q branch region spans for about 9 cm^{-1} and is quite crowded being formed by two series of Q sub–branches, whose K–structures degrade to low wavenumbers with increasing K value. The spacing between adjacent absorptions in a given sub–branch is larger in the $s \leftarrow a$ component than in the $a \leftarrow s$ one, as illustrated in Figure 4.8.

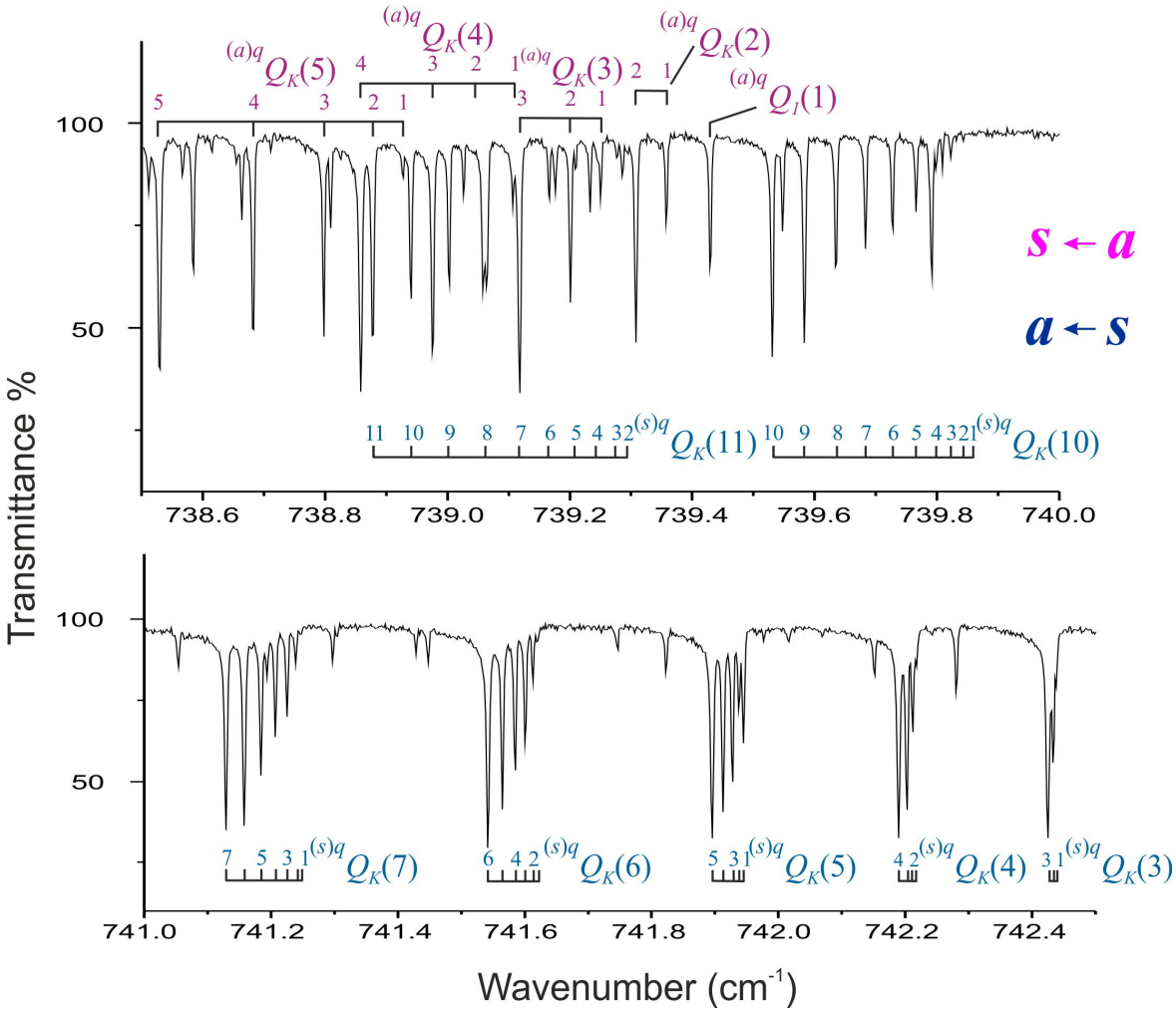

Figure 4.8: Detail of the Q branch of ν_2 for $^{15}ND_3$ near the band centre.
Experimental condition: see spectrum *a* in Table 4.10.

As far as ^qP and ^qR branches are concerned, the adjacent J manifolds are separated by about 10 cm^{-1}. The wavenumber transitions of the P branch are red–degrading, increasing K, in both the $a \leftarrow s$ and $s \leftarrow a$ components (see Figure 4.9a), while the K structure is red–degraded in the $s \leftarrow a$ but blue–degraded in the $a \leftarrow s$ sub–bands of the R branch (see Figure 4.9b). It is possible to observe in Fig. 4.9 that the intensity of absorption lines with $K = 0$ is 10 for J'' even

and 1 for J'' odd in transitions from the *s* levels of the ground state (GS). The opposite holds for transitions arising from *a* levels of GS. From the nuclear spin statistical weights of the GS levels in deuterated ammonia [31], it is possible to observe an 8, 8, 11 intensity alternation of transitions for $K'' = 3n+1$, $3n+2$ and $3n+3$ with $n = 0, 1, 2, \ldots$

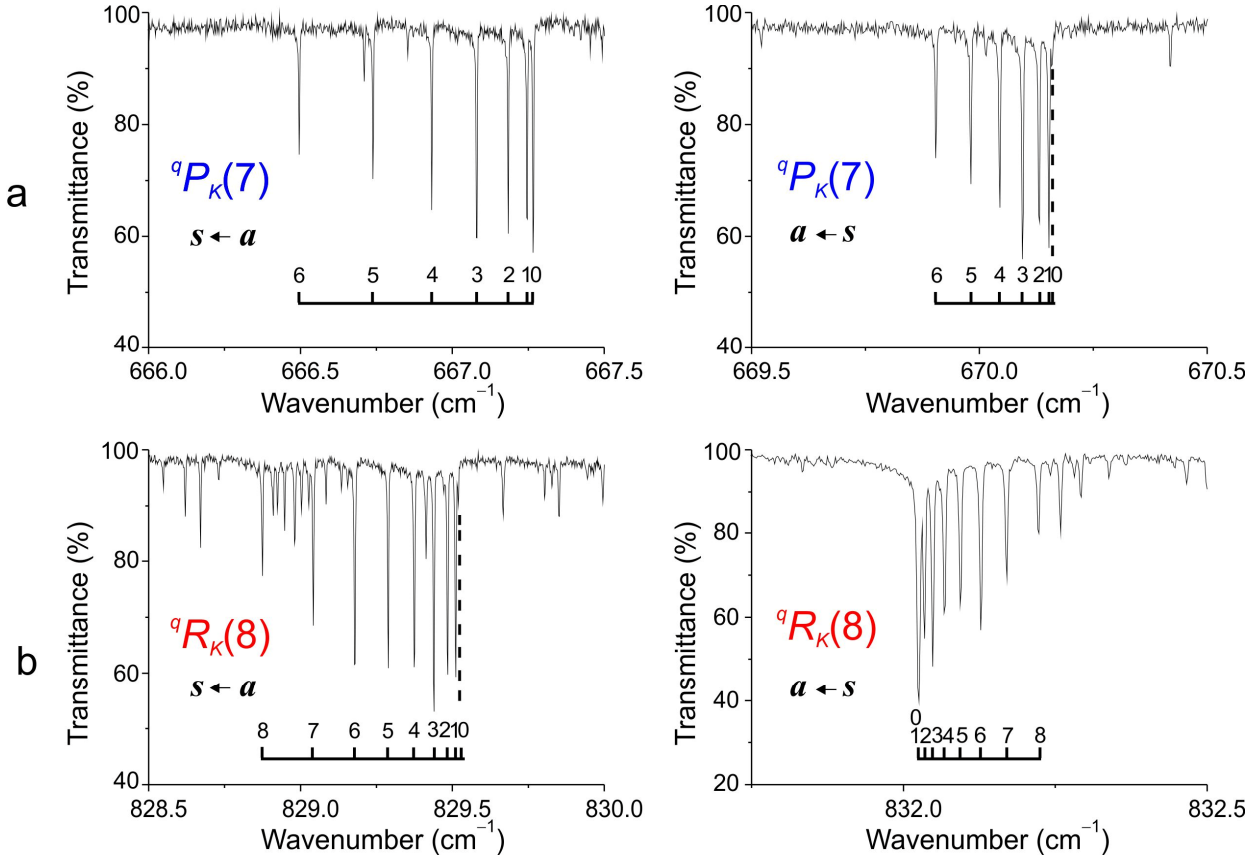

Figure 4.9: Detail of the $^qP_K(7)$ and $^qR_K(8)$ branches of ν_2 for $^{15}ND_3$. Experimental condition: see spectrum *a* in Table 4.10.

The ν_4 perpendicular band, is characterized by a strong central feature constituted by the $^pQ_K(J)$ and $^rQ_K(J)$ sub–branches, located at the higher and lower wavenumbers, respectively, with respect to $^rQ_0(J)$ at the band centre, as illustrated in Figure 4.10. The effect of the intensity alternation due to statistical weights is evident also in the $^rQ_0(J)$ sub–branch constituted by transitions that alternatively start from the *a* and *s* GS levels for $J = 1, 2, 3, \ldots$. The *J* structure of the *Q* sub–branches degrades to the blue for increasing *J*.

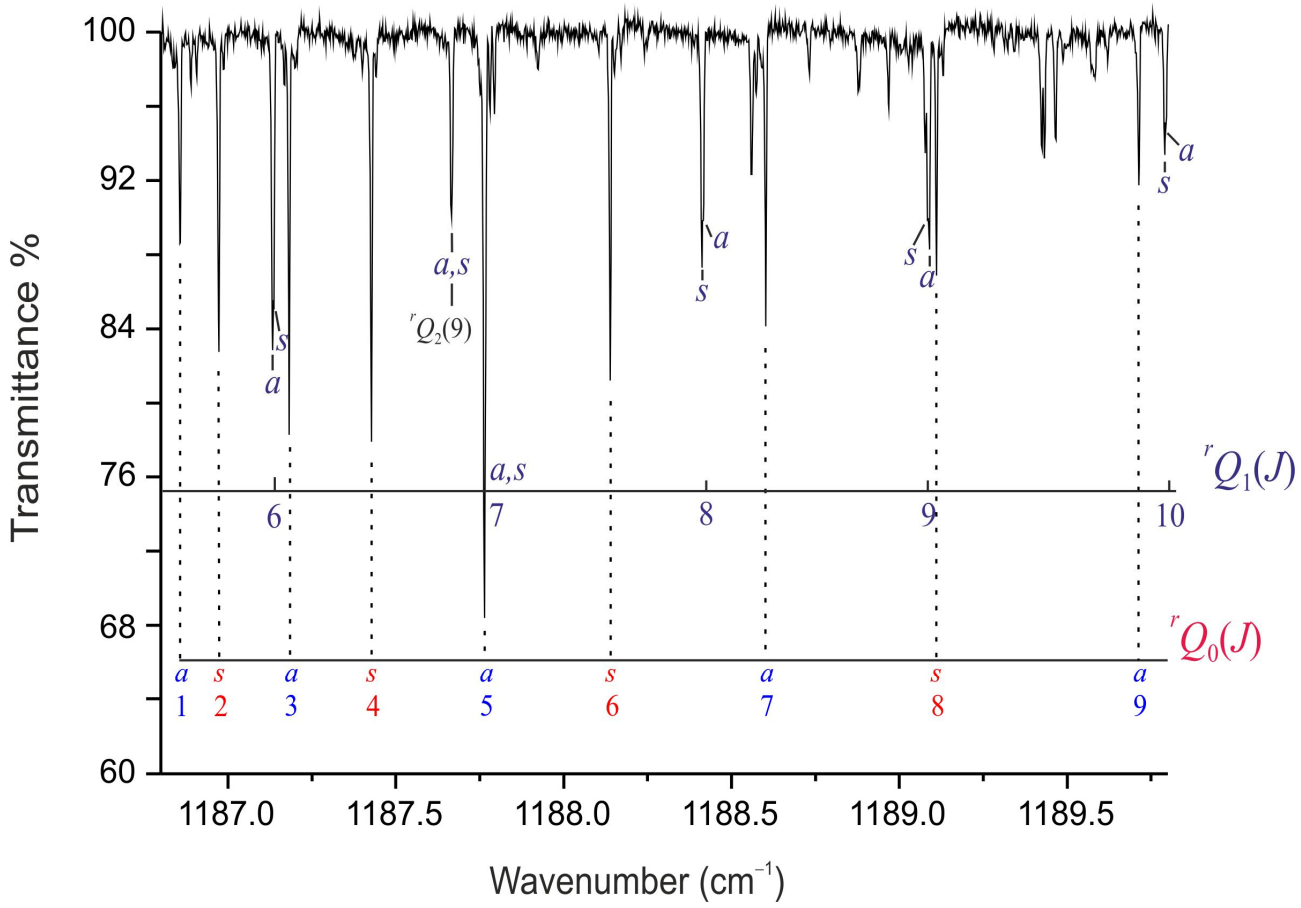

Figure 4.10: Detail of ν_4 band for $^{15}ND_3$ illustrating the ${}^{r}Q_0(J)$ and ${}^{r}Q_1(J)$ branches.
Experimental condition: see spectrum *a* in Table 4.10.

The strong ${}^{p}P_K(J)$ sub–branches are red–degraded and and ${}^{r}R_K(J)$ are blue–degraded, for increasing J. Each P and R sub–branch for a given J value degrades to high wavenumbers with increasing and decreasing K, respectively. The separation of the *a* and *s* levels of $\upsilon_4 = 1$ is very similar to that in the GS and since the selection rules allow the $s \leftarrow s$ and $a \leftarrow a$ transitions, the wavenumber difference within each *a* , *s* doublet is equal to the difference between the inversion splittings in the ground and $\upsilon_4 = 1$ states. In Fig. 4.11 it is shown that the separation of the *a* and *s* component of each doublet in the ${}^{p}P_K(7)$ sub–branch decreases from $K'' = 1$ to $K'' = 5$. For $K'' = 6$ the two absorption lines are overlapped. For $K'' = 7$ two lines are observed but with the *a* component of the doublet at higher wavenumbers. Moreover, in case of the $K'' = 3$ transitions, which are split in two doublet with the intensity ratio 10:1 due to the spin statistical weights [31], both the strong and the weak components of the quartet, rarely observed in the spectrum, are visible in Fig. 4.11.

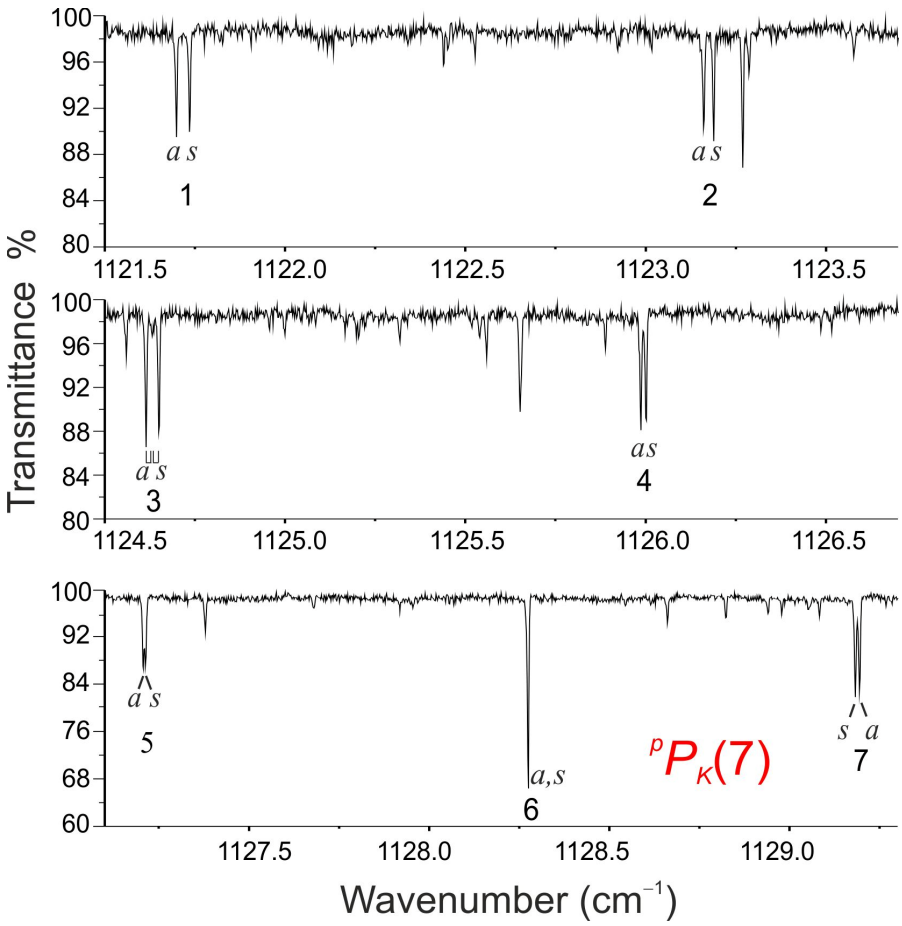

Figure 4.11: Detail of ν_4 band for $^{15}ND_3$ illustrating the $^{p}P_{K}(7)$ branch for both *a* and *s* components. Experimental condition: see spectrum *a* in Table 4.10.

b) The 2300 – 2700 cm^{-1} region

This region is dominated by the stretching fundamental bands ν_1 and ν_3 centred at about 2415 and 2552 cm^{-1}, as illustrated in Figure 4.12. These bands are much less intense than those in the bending range. The prominent feature at about 2350 cm^{-1} is CO_2, which is very useful for the calibration of the spectrum.

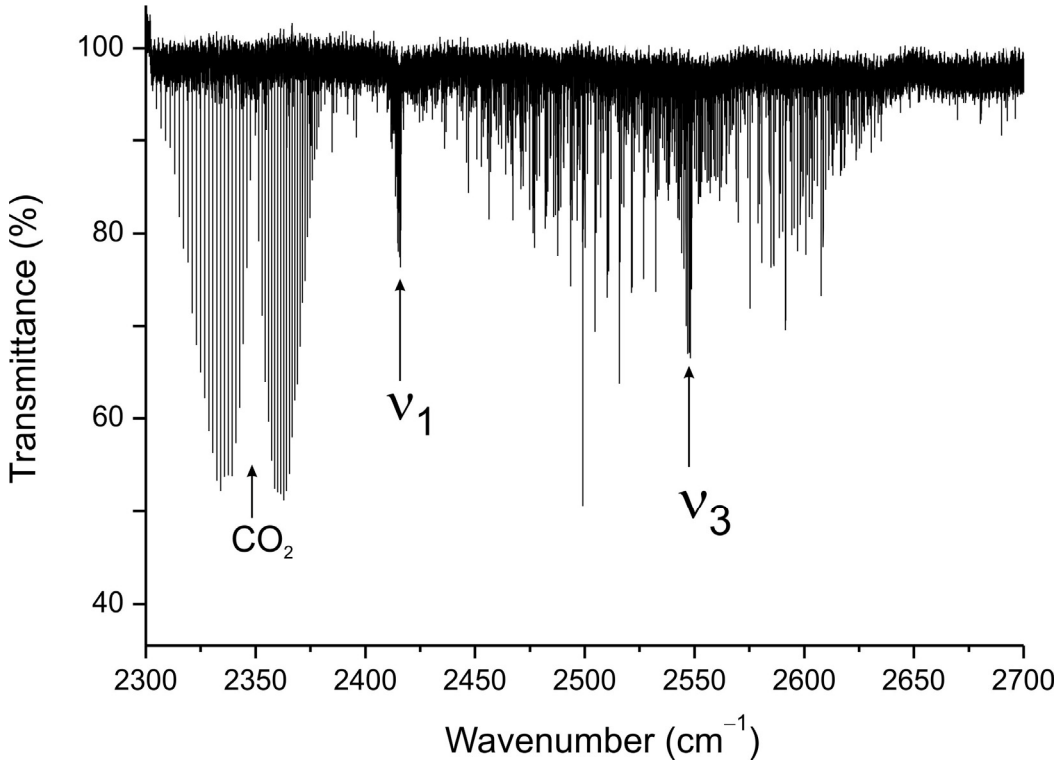

Figure 4.12: Portion of the spectrum of $^{15}ND_3$ between 2300 and 2700 cm^{-1}. The band centre of the fundamental stretching modes are indicated, as well as the presence of CO_2. Experimental conditions: see spectrum *d* in Table 4.10.

As ν_2, ν_1 is composed by two sub–bands ($s \leftarrow a$ and $a \leftarrow s$), centred at 2415.7 and 2416.4 cm^{-1}, respectively. The central *Q* branch region is much more compressed than the ν_2 one and covers about 5 cm^{-1}, being formed by two series of *Q* branches. Their *K* structure degrades towards lower wavenumbers with increasing *K*, as illustrated in Figure 4.13. It is worth noting that the *a* and *s* levels are closer than in ν_2, in fact in ν_1 they are only about 0.75 cm^{-1} apart. The spacing between adjacent absorptions in a given sub–branch is the same in the $s \leftarrow a$ and $a \leftarrow s$ components. As far as ^qP and ^qR branches are concerned, only the first few *K* values for each *J* sub–branch can be identified and assigned. The features of both *P* and *R* branches have red–degrading *K* structure with increasing *K*, in both the $a \leftarrow s$ and $s \leftarrow a$ components.

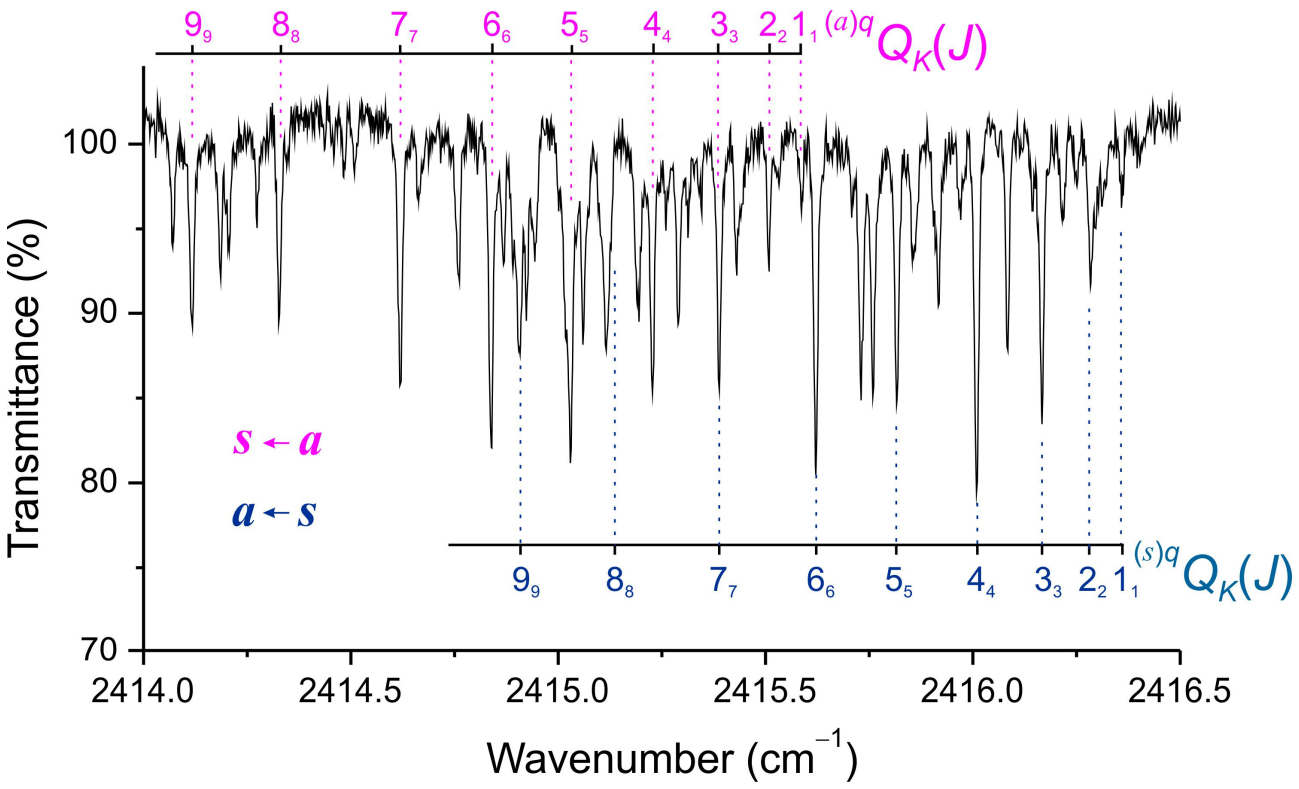

Figure 4.13: Detail of the *Q* branch of ν_1 for $^{15}ND_3$ near the band centre. Experimental condition: see spectrum *d* Table 4.10.

The perpendicular band ν_3 has the same shape of ν_4. The effect of the intensity alternation due to statistical weights is evident in the $^{r}Q_0(J)$ sub–branch. In the spectrum are visible the close doublets due to transitions from the *a* and *s* GS levels for J = 1, 2, 3,… as illustrated in Figure 4.14. The J structure of the *Q* sub–branches degrades to the red for increasing J, as well as for $^{p}P_K(J)$ and $^{r}R_K(J)$. This is opposite to what observed in ν_4. The splitting between *a* and *s* sub–levels is quite constant all over the band, and only in few cases the two components result overlapped.

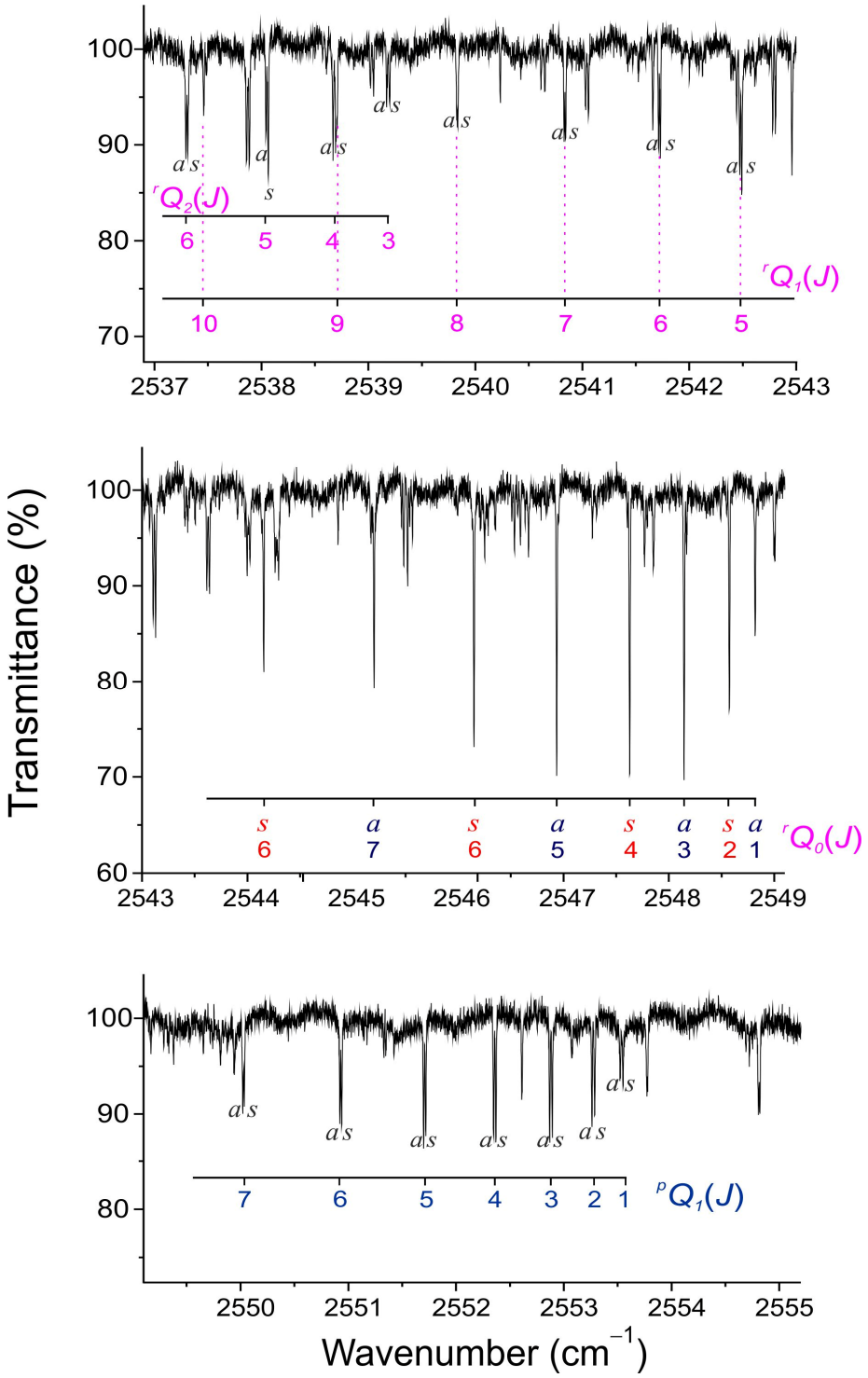

Figure 4.14: Detail of the *Q* branch of ν_3 for $^{15}ND_3$ near the band centre. Experimental condition: see spectrum *d* Table 4.10.

4.2.3 Analysis

The assignments procedure was guided by the method of GSCD, calculated from the precise ground state parameters reported in Ref. [33], and by comparison with the corresponding bands in $^{14}ND_3$. Another valuable support was provided by the relative intensity of the lines,

which is governed by the nuclear spin statistic weights, and by the very low intensity or absence of $K''=0$ lines for odd (s) or even (a) J'' in various branches. The analysis was performed fitting simultaneously the bending fundamentals, and successively the stretching modes together.

In total, 2217 transitions with $J'_{\max}=K'_{\max}=20$ were assigned for the bending modes; of these, 876 belong to ν_2, 436 and 440 to the $s \leftarrow a$ and the $a \leftarrow s$ components, respectively, whereas 1341 belong to ν_4, 668 to the $s \leftarrow s$ and 673 to the $a \leftarrow a$ component, respectively. For the stretching modes, 535 transitions with $J'_{\max}=10$, $K'_{\max}=7$ were assigned; of these, 153 belong to ν_1, 73 and 80 to the $s \leftarrow a$ and the $a \leftarrow s$ components, respectively, while 382 belong to ν_3, 193 to the $s \leftarrow s$ and 189 to the $a \leftarrow a$ component, respectively.

As the assignment procedure was guided by the pattern of the same bands in $^{14}ND_3$, the same theoretical model, described in Ref. [24], has been adopted. Four levels have been taken into account simultaneously both for the bending and the stretching analysis, namely the s and a components of $v_2 = 1$ and $v_4 = 1$ in one case and the s and a components of $v_1 = 1$ and $v_3 = 1$ in the other case, taking explicitly into account all the symmetry allowed interactions between ν_2 and ν_4 or ν_1 and ν_3, and the essential resonances active within ν_2 and ν_4, or ν_1 and ν_3. In the theoretical model the $\Delta\ell=0$, $\Delta k=\pm 3$ interaction is comprised. It connects levels with opposite inversion symmetry in the same vibration state and it results to be effective also among the rotation levels of the GS [30,31]. For each value of J, the program constructs two Hamiltonian matrices of dimensions $4 \times (2J+1)$: one is set up for levels of A_1', A_2' and A_1'', A_2'' symmetry, and the other corresponds to one of the two (degenerate) blocks of E' and E'' symmetry. The two blocks are numerically diagonalized to obtain the energy levels. The diagonal matrix elements, containing the usual contributions up to the 6th power in the angular momentum operators, were given by:

$$\begin{aligned}
{}^{(i)}E_\upsilon(J,k,\ell)/hc = {}&{}^{(i)}E_\upsilon^0 + {}^{(i)}B_\upsilon\left[J(J+1)-k^2\right] + {}^{(i)}C_\upsilon k^2 - 2\,{}^{(i)}(C\zeta)_\upsilon\, k\ell - {}^{(i)}D_{\upsilon J}\left[J(J+1)\right]^2 + \\
&- {}^{(i)}D_{\upsilon JK}\left[J(J+1)\right]k^2 - {}^{(i)}D_{\upsilon K}k^4 + {}^{(i)}\eta_{\upsilon J}\left[J(J+1)\right]k\ell + {}^{(i)}\eta_{\upsilon K}k^3\ell + \\
&+ {}^{(i)}H_{\upsilon J}\left[J(J+1)\right]^3 + {}^{(i)}H_{\upsilon JK}\left[J(J+1)\right]^2 k^2 + {}^{(i)}H_{\upsilon KJ}\left[J(J+1)\right]k^4 + \\
&+ {}^{(i)}H_{\upsilon K}k^6 + {}^{(i)}\tau_{\upsilon J}\left[J(J+1)\right]^2 k\ell + {}^{(i)}\tau_{\upsilon JK}\left[J(J+1)\right]k^3\ell + {}^{(i)}\tau_{\upsilon K}k^5\ell + {}^{(i)}\tau_{\upsilon K*}k^3\ell^3
\end{aligned} \tag{4.3}$$

The equation is similar to Eq. (4.1); the superscript (i) refers to the parity of the level, s or a, with respect to the inversion.

The off–diagonal elements are reported in Table 4.11.

Table 4.11: Off–diagonal matrix elelments of the vibration–rotation–inversion Hamiltonian

The basis functions are ${}^{s}_{a}|\nu_s,\nu_t,\ell_t,J,k\rangle = {}^{s}_{a}|\nu_2,\nu_4,\ell_4,J,k\rangle$ or ${}^{s}_{a}|\nu_1,\nu_3,\ell_3,J,k\rangle$

Coriolis type resonances

$${}^{s}_{a}\left\langle \nu_s,\nu_t,\ell_t,J,k\left|(H_{21}+H_{23})/hc\right|\nu_s-1,\nu_t+1,\ell_t\pm1,J,k\pm1,\right\rangle^{a}_{s}$$
$$=\pm\sqrt{2}\left\{{}^{(i)}C^{(1)}_{11}+{}^{(i)}C^{(3a)}_{11}J(J+1)+{}^{(i)}C^{(3b)}_{11}\left[k^2+(k\pm1)^2\right]\right\}F_{\pm1}$$

$${}^{s}_{a}\left\langle \nu_s,\nu_t,\ell_t,J,k\left|H_{22}/hc\right|\nu_s-1,\nu_t+1,\ell_t\pm1,J,k\pm1\right\rangle^{a}_{s}=\sqrt{2}\ {}^{(i)}C^{(2)}_{11}(2k\pm1)F_{\pm1}$$

$${}^{s}_{a}\left\langle \nu_s,\nu_t,\ell_t,J,k\left|(H_{22}+H_{24})/hc\right|\nu_s-1,\nu_t+1,\ell_t\mp1,J,k\pm2\right\rangle^{s}_{a}$$
$$=\sqrt{2}\left\{{}^{(i)}C^{(2)}_{21}+{}^{(i)}C^{(4a)}_{21}J(J+1)+{}^{(i)}C^{(4b)}_{21}\left[k^2+(k\pm2)^2\right]\right\}F_{\pm2}$$

$${}^{s}_{a}\left\langle \nu_s,\nu_t,\ell_t,J,k\left|H_{23}/hc\right|\nu_s-1,\nu_t+1,\ell_t\mp1,J,k\pm2,\right\rangle^{s}_{a}=\pm\sqrt{2}\ {}^{(i)}C^{(3)}_{21}\left(2k\pm2\right)F_{\pm2}$$

Essential resonances

$${}^{a}_{s}\left\langle \nu_t,\ell_t,J,k\left|\left(H_{22}+H_{24}\right)/hc\right|\nu_t,\ell_t\mp2,J,k\pm1\right\rangle^{s}_{a}=2\left\{[q_{12}+f^{J}_{12}J(J+1)](2k\pm1)+f^{K}_{12}\left[k^3+(k\pm1)^3\right]\right\}F_{\pm1}$$

$${}^{a}_{s}\left\langle \nu_t,\ell_t,J,k\left|\left(H_{22}+H_{24}\right)/hc\right|\nu_t,\ell_t\pm2,J,k\pm2\right\rangle^{a}_{s}=2\left\{{}^{(i)}q_{22}+{}^{(i)}f^{J}_{22}J(J+1)+{}^{(i)}f^{K}_{22}\left[k^2+(k\pm2)^2\right]\right\}F_{\pm2}$$

$${}^{a}_{s}\left\langle \nu_s,J,k\left|\left(H_{04}+H_{24}+H_{26}\right)/hc\right|\nu_s,J,k\pm3\right\rangle^{s}_{a}=\left\{\left[\varepsilon_2+\varepsilon_{2J}J(J+1)\right](2k\pm3)+\varepsilon_{2K}\left[k^3+\left(k\pm3\right)^3\right]\right\}F_{\pm3}$$

$${}^{a}_{s}\left\langle \nu_t,\ell_t,J,k\left|\left(H_{04}+H_{24}+H_{26}\right)/hc\right|\nu_t,\ell_t,J,k\pm3\right\rangle^{s}_{a}=\left\{\left[\varepsilon_4+\varepsilon_{4J}J(J+1)\right](2k\pm3)+\varepsilon_{4K}\left[k^3+\left(k\pm3\right)^3\right]\right\}F_{\pm3}$$

---

with $F_{\pm n}=[J(J+1)-k(k\pm1)]^{1/2}[J(J+1)-(k\pm1)(k\pm2)]^{1/2}.....\{J(J+1)-[k\pm(n-1)](k\pm n)\}^{1/2}$

In Table 4.11, if a constant is indicated without the left superscript (*i*) it corresponds to an $s \leftrightarrow a$ resonance, whereas if the superscript (*i*) is present it represents an interaction between levels of the same parity.

A weighted least–squares analysis was performed on all the assigned transitions belonging to the bending states to derive the spectroscopic parameters of the excited states. An analogous procedure was accomplished for the stretching modes. A unitary statistical weight has been attributed to each transition that corresponds to an isolated line, while the weight has been reduced to 1/*n* if *n* transitions are assigned to the same wavenumber. The GS term values were obtained using the parameters in Ref. [33] and collected in Table 4.12. The diagonal elements were calculated from the following expression:

$$
\begin{aligned}
{}^{(i)}E\left(J,k\right)/hc = {}&{}^{(i)}E^{0} + {}^{(i)}B_{0}\left[J\left(J+1\right)-k^{2}\right] + {}^{(i)}C_{0}k^{2} - {}^{(i)}D_{0J}\left[J\left(J+1\right)\right]^{2} - {}^{(i)}D_{0JK}\left[J\left(J+1\right)\right]k^{2} + \\
&- {}^{(i)}D_{0K}k^{4} + {}^{(i)}H_{0J}\left[J\left(J+1\right)\right]^{3} + {}^{(i)}H_{0JK}\left[J\left(J+1\right)\right]^{2}k^{2} + {}^{(i)}H_{0KJ}\left[J\left(J+1\right)\right]k^{4} + \\
&+ {}^{(i)}H_{0K}k^{6} + {}^{(i)}L_{0J}\left[J\left(J+1\right)\right]^{4} + {}^{(i)}L_{0JJK}\left[J\left(J+1\right)\right]^{3}k^{2} + {}^{(i)}L_{0JK}\left[J\left(J+1\right)\right]^{2}k^{3} + \\
&+ {}^{(i)}L_{0JKK}\left[J\left(J+1\right)\right]k^{6} + {}^{(i)}L_{0K}k^{8}
\end{aligned}
\tag{4.4}
$$

Table 4.12: Spectroscopic parameters (in cm^{-1}) for the GS of $^{15}ND_3$

Parameter	s [a]	a [a]
${}^{(i)}E^{0}$ [b]	0.0	0.047793490(323)
${}^{(i)}B_{0}$	5.123657150(665)	5.123494406(665)
${}^{(i)}C_{0}$	3.124569 [c]	3.124648945(154)
${}^{(i)}D_{0J}\times10^{4}$	1.975535(127)	1.972658(127)
${}^{(i)}D_{0JK}\times10^{4}$	−3.513534(502)	−3.505049(502)
${}^{(i)}D_{0K}\times10^{4}$	0.0 [c]	−0.00612448(816)
${}^{(i)}H_{0J}\times10^{8}$	2.36008(615)	2.33397(617)
${}^{(i)}H_{0JK}\times10^{8}$	−7.6191(242)	−7.4926(242)
${}^{(i)}H_{0KJ}\times10^{8}$	8.6593(308)	8.4655(308)
${}^{(i)}H_{0K}\times10^{8}$	0.0 [c]	0.096091(447)
${}^{(i)}L_{0J}\times10^{11}$	−4.1972(902)	−10.199(742)
${}^{(i)}L_{0JJK}\times10^{11}$	1.4289(411)	1.4356(411)
${}^{(i)}L_{0JK}\times10^{11}$	−1.3240(498)	−1.3240(498)
${}^{(i)}L_{0KKJ}$	0.0 [c]	0.0 [c]
${}^{(i)}L_{0K}$	0.0 [c]	0.0 [c]
	Interaction parameters	
$\varepsilon_{0}\times10^{5}$	3.7486(100)	
$\varepsilon_{0}^{J}\times10^{8}$	−0.9542(413)	
$\varepsilon_{0}^{K}\times10^{8}$	2.3055(351)	

[a] From Ref. [31]. The uncertainties as 1σ given in parentheses refer to the last significant digits.

[b] ${}^{(a)}E^{0}$ is the inversion splitting in the GS for $J = K = 0$.

[c] Fixed at the $^{14}ND_3$ value or zero.

4.2.4 Results and Discussion

The analysis was accomplished in an iterative process, which consists in improving the values of the excited state parameters by means of the assigned lines, predicting the wavenumbers of higher *J* and *K* unassigned transitions to be searched in the spectra, enlarging the data set, and so on. Once all the transitions that could be unambiguously assigned were identified, a systematic investigation to derive the set of parameters that best reproduces the experimental data was carried out. Constants up to the third order of approximation, E^0, B, C, $C\zeta$, $C_{11}^{(1)}$, $C_{11}^{(2)}$, $C_{21}^{(2)}$, $C_{11}^{(3a)}$, $C_{11}^{(3b)}$, η_J, η_K and the distortion constants D and H were refined. At the end of each fit we checked that the newly, as well as the previously determined parameters, were statistically determined, that they improved the standard deviation of the fit and that large correlations between the parameters were not present. The parameters not fulfilling these requirements were constrained either to zero or to their corresponding GS values in the next fit. Both the *J* and *K* dependences and, if present, the *s* and *a* components of a lower order coefficient, determined in the fit, i.e. f_{12}^{J} and f_{12}^{K}, were added simultaneously in the refinement.

a) $\upsilon_2 = 1$ and $\upsilon_4 = 1$

In total, 1930 transitions were retained in the last cycle of refinement with a standard deviation of the fit = 0.00071 cm^{-1}. The number of rejected transitions is 286, about 13% of the assignments, and they are mostly constituted by poorly measured, weak or blended lines randomly distributed in the experimental dataset. They were excluded since the difference between the experimental and calculated wavenumbers exceeded the rejection limit, set at 0.002 cm^{-1}.

The overall results collected in Table 4.13 comprise 20 spectroscopic parameters of υ_2 = 1, 26 of υ_4 = 1, and 11 coefficients of the off–diagonal matrix elements of the model Hamiltonian. The sextic distortion constants *H* could be significantly determined after the inclusion in the experimental dataset of transitions with *J* and *K* quantum numbers ≥ 15. All the parameters of Eq. (4.3) and of Table 4.11 not reported in Table 4.13 were constrained to zero in the refinement.

Table 4.13: Spectroscopic parameters (in cm^{-1}) of the $\upsilon_2 = 1$ and $\upsilon_4 = 1$ states of $^{15}ND_3$

Parameter	$\upsilon_2 = 1$		$\upsilon_4 = 1$	
	s	*a*	*s*	*a*
E_υ^0	739.530096(126)	742.775007(134)	1186.910962(110)	1186.9731061(113)
B	5.20781378(548)	5.19946251(545)	5.15566714(464)	5.15545837(480)
C	3.08910256(450)	3.09396727(477)	3.10548954(404)	3.10561845(405)
$D_J \times 10^3$	0.2317821(358)	0.2200535(371)	0.2088482(414)	0.2087342(435)
$D_{JK} \times 10^3$	–0.4193453(689)	–0.3813474(708)	–0.3888549(943)	–0.3863991(959)
$D_K \times 10^3$	0.0380027(500)	0.0085189(518)	0.0247095(680)	0.0225438(660)
$H_J \times 10^7$	0.297521(579)	0.205253(583)	0.27053(107)	0.27150(117)
$H_{JK} \times 10^7$	–0.92994(286)	–0.51063(265)	–0.94808(398)	–0.93440(400)
$H_{KJ} \times 10^7$	1.08400(448)	0.44913(414)	1.08345(516)	1.07014(506)
$H_K \times 10^7$	–0.13363(224)	0.18239(203)	–0.08338(231)	–0.08283(212)
$C\zeta$			–0.927345(264)	–0.959500(132)
$\eta_J \times 10^3$			–0.927427(335)	–0.927444(272)
$\tau_{JK} \times 10^6$			–0.182577(697)	–0.180181(730)
Interaction parameters				
$^{(s)}C_{11}^{(1)}$	3.3777073(685)		$^{(a)}C_{11}^{(1)}$	3.3913751(647)
$^{(s)}C_{11}^{(3a)} \times 10^3$	–0.383697(397)		$^{(a)}C_{11}^{(3a)} \times 10^3$	–0.398221(404)
$^{(s)}C_{11}^{(2)} \times 10^3$	4.6221(109)		$^{(a)}C_{11}^{(2)} \times 10^3$	4.2430(109)
$^{(s)}C_{21}^{(3)} \times 10^3$	0.28725(201)		$^{(a)}C_{21}^{(3)} \times 10^3$	0.25232(201)
q_{12}		–0.02029849(768)		
$\varepsilon_2 \times 10^5$	2.4593(253)		$\varepsilon_4 \times 10^5$	4.5720(163)
N. fitted/N. assigned lines		1930/2217		
St. dev. of the fit		0.000714		

All the parameters are statistically well determined. The values for most of them are also close to the corresponding ones in the ground state, both in sign and value. The values of the refined *s* and *a* rotation constants are very similar in the two studied vibrational states, apart from few exceptions. It is worth noting that the D_K and H_K distortion constants are effective, being constrained to 0.0 in the *s* component of GS.

b) $\upsilon_1 = 1$ and $\upsilon_3 = 1$

In total, 493 out of 535 transitions were retained in the last cycle of refinement with a standard deviation of the fit = 0.00146 cm^{-1}. The number of rejected transitions is 42, about 8% of the assignments, and they are mostly constituted by poorly measured, weak or blended lines randomly distributed in the experimental dataset. They were excluded since the difference between the experimental and calculated wavenumbers exceeded the rejection limit, set at 0.004 cm^{-1}. The overall results are collected in Table 4.14 and they comprise 18 spectroscopic parameters of υ_1 = 1, 24 of υ_3 = 1 and 5 coefficients of the off–diagonal matrix elements of the model Hamiltonian.

Table 4.14: Spectroscopic parameters (in cm^{-1}) of the υ_1 = 1 and υ_3 = 1 states of $^{15}ND_3$

Parameters	$\upsilon_1 = 1$		$\upsilon_3 = 1$	
	s	*a*	*s*	*a*
E_υ^0	2415.669376(918)	2416.389955(695)	2551.681835(358)	2551.703045(380)
B	5.115339(132)	5.1173838(857)	5.0550128(197)	5.0551173(196)
C	3.103352(214)	3.104652(178)	3.1262963(560)	3.1259504(552)
$D_J \times 10^3$	0.08340(496)	0.08334(259)	0.189463(214)	0.189166(237)
$D_{JK} \times 10^3$	–0.08389(541)	–0.04318(415)	–0.34065(161)	–0.34852(154)
$D_K \times 10^3$	–0.1000(101)	–0.03853(832)	0.0[a]	–0.621448[a]
$H_J \times 10^7$	7.205(524)	9.234(220)	0.2360[a]	0.2334[a]
$H_{JK} \times 10^7$	–0.762[a]	–0.749[a]	–1.417(122)	–1.536(123)
$H_{KJ} \times 10^7$	16.32(247)	31.80(200)	2.0701(677)	1.8935(607)
$H_K \times 10^7$	0.0[a]	0.0[a]	0.0[a]	0.0961[a]
$C\zeta$			0.3848432(679)	0.3846877(717)
$\eta_J \times 10^3$			–0.77143(716)	–0.77921(726)
$\tau_{JK} \times 10^6$			–0.5152(891)	–0.9942(867)
Interaction parameters				
		a	*s*	
$C_{11}^{(1)}$		0.442041(701)	0.444435(651)	
$C_{21}^{(2)} \times 10^3$		–7.758(267)	–8.103(218)	
q_{12}			0.0105687(349)	
N. fitted/N. assigned lines	493/535			
St. dev. of the fit	0.00146			

[a] Fixed to zero or to the GS value.

The sextic distortion constants H_K could not be determined because of the few transitions included in the dataset and the low J and K quantum numbers observed in the spectrum ($J''_{max} = 8$, $K''_{max} = 5$ for ν_1 and $J''_{max} = 10$, $K''_{max} = 7$ for ν_3), except that for the a state of $v_3 = 1$. All the parameters of Eq. (4.3) and of Table 4.11 not reported in Table 4.14 were constrained to zero in the refinement.

Differently from the bending states, in the stretching states more perturbations are present. In fact, distortion constants are quite different within the same state for s and a components, and in some case the parameters are different from the GS ones. For example, H_{KJ} of the $v_1 = 1$ state is abnormally huge. In addition, in order to reproduce in a satisfactory way the $a - a$ transitions of the ν_3 band, H_K constant is required, despite of the very few lines observed (187). The analysis of the stretching region needs to be improved taking into account also the other states close in energy, first of all $v_4 = 2^0$ and $v_4 = 2^{\pm 2}$, and, if necessary, also the $v_2 = 2$, $v_4 = 1$ state. This will be further discussed in Section 5.2.

4.3 CF_3Br

Bromotrifluoromethane, CF_3Br, commercially known as Halon 1301 or Freon 13B1, was extensively adopted as fire extinguisher and in a variety of military or industrial uses, due to its long–term storage stability, safety and effectiveness at low concentration. It has been a well suited target for investigation by infrared laser chemistry and isotopically selective multiphoton induced dissociation, since it absorbs in regions accessible to CO_2 laser radiation [38–44].

Given its adverse environmental effects (ν_4 absorbs in the atmospheric window) and the proposed potential applications, in the last decades many spectroscopic studies have been carried out on this molecule. In particular, an accurate rovibrational analysis of the bands falling in the mid–infrared region could support the quantitative detection and the temperature profile modelling of these halogenated pollutants.

CF_3Br is present in nature as two isotopologues due to the almost equal amount of bromine isotopes, ^{79}Br and ^{81}Br. The molecule, a prolate symmetric top, has 9 vibrational degrees of freedom, whose description is reported in Table 4.15.

Table 4.15: Normal modes of CF_3Br

Mode	Symmetry		Band origin (cm^{-1}) [a]	
			$CF_3{}^{79}Br$	$CF_3{}^{81}Br$
ν_1	A_1	Symmetric stretching C–F	1084.763	1084.521
ν_2	A_1	Stretching C–Br	761.9	761.9
ν_3	A_1	Symmetric bending $C–F_3$	352.4	350.4
ν_4	E	Antisymmetric stretching C–F	1208.8	1208.8
ν_5	E	Antisymmetric bending $C–F_3$	548.9	548.9
ν_6	E	Rocking $C–F_3$	302.7	302.7

[a] From Ref. [45].

4.3.1 Experiment

The sample of CF_3Br was purchased from Matheson, purity > 99 %, and used to record the spectra without further purification. The two bromine isotopologues are present in natural abundance in almost equal amount, i.e. 50.5 % $CF_3{}^{79}Br$ and 49.5 % $CF_3{}^{81}Br$.

High Resolution Free–Jet TDL Spectra

The high–resolution jet-cooled spectra, Spectra #1, were recorded in Venice with a home–built slit–jet system. Details about the experimental set up were reported in [46–48], so they are briefly reported here. The tunable IR–radiation is emitted by a Pb–salt diode laser source (Laser Components GmbH) and mode–filtered by a low resolution grating monochromator. A small fraction of the laser beam output is employed for calibration purposes, and the majority is directed through the supersonic slit–jet (path length of 1.25 cm) expansion within the vacuum chamber (stagnation pressure in the range 120 – 180 kPa, background pressure below 0.5 Pa) and finally focused on to a HgCdTe detector. A fraction (about 0.3 cm^{-1}) of a whole emission mode has been scanned within the duration of a single gas pulse (about 2 ms) by applying a 1 kHz ramp–shaped modulation to the injection current; typically 128 transmittance scans were averaged to yield the final spectrum. The TDL spectra at 200 K (dry ice), Spectra #2, were recorded with a pressure in the range 4 – 10 Pa using a homemade 0.923

m long cell. Due to the operational range of the diode lasers at disposal in the apparatus, the spectra were registered in three ranges, namely 1202.5 – 1205.0 cm^{-1}, 1208.0 – 1210.1 cm^{-1} and 1212.5 – 1214.5 cm^{-1}. Those intervals match to portions of the $\Delta J = -1$, $\Delta J = 0$, and $\Delta J = +1$ branches of ν_4, respectively.

As far as the calibration of the spectra in concerned, a solid Ge etalon (with a free spectral range of about 0.05 cm^{-1}) and reference spectra of SO_2 gas lines were employed. An accuracy better than 0.0007 cm^{-1} has been estimated for resolved single lines. Resolution up to 0.0008 cm^{-1} and 0.0015 cm^{-1} was achieved for Spectra #1 and Spectra #2, respectively.

High Resolution FTIR Spectra

The room temperature spectrum, indicated as Spectrum #3, was recorded between 1000 and 1300 cm^{-1} in Bologna using a Bomem DA3.002 Fourier transform (FT) interferometer, equipped with a Globar source, a KBr beamsplitter and a HgCdTe high sensitivity detector operating at liquid nitrogen temperature. The optical path length was 0.18 m long and the instrumental resolution was 0.004 cm^{-1}. A pressure of 13.3 Pa was introduced in the cell. In order to improve the signal–to–noise ratio and the quality of the spectrum, 660 scans were co–added. The spectral resolution is estimated to be 0.004 cm^{-1} from the convolution of the instrumental resolution and the Doppler broadening. Particular care was devoted to the calibration of the spectrum since results have to be obtained from the analysis of spectra recorded with different techniques in different conditions. Rovibration transitions of H_2O [49] were used for the calibration of Spectrum #3. The accuracy of the spectrum and the precision of isolated, medium to strong, unblended lines are better than 1×10^{-4} cm^{-1}.

The general conditions for the three spectra are reported in Table 4.16.

Table 4.16: Experimental conditions for the recording of CF_3Br spectra

Spectrum	Pressure of the sample (Pa)	Temperature (K)	Source	Detector	Resolution (cm^{-1})	#Scans	Optical pathlenght (m)
#1	0.5[a]	50	Pb – salt	MCT	0.0008	128	0.0125
#2	10.0	200	Pb – salt	MCT	0.0015	128	0.923
#3	13.3	298	Globar	MCT	0.0040	660	0.18

* MCT is a HgCdTe detector.
[a] Background pressure below 0.5 Pa.

4.3.2 Description of the spectrum

The ν_4 is a perpendicular fundamental band which absorbs between 1195 and 1220 cm^{-1}. The high–resolution infrared spectrum is very complex because of the very dense rotational structure, the simultaneous presence of absorption features due to bromine isotopologues (^{79}Br and ^{81}Br) in almost equal proportion and the absorptions of different hot bands. It is worth noting that the coarse and smoothed profile of Spectrum #3 corresponds closely to the resolved absorptions of Spectra #1 and #2. The overview of the band, together with the indication of the origin of some hot bands, is presented at the top of Figure 4.15.

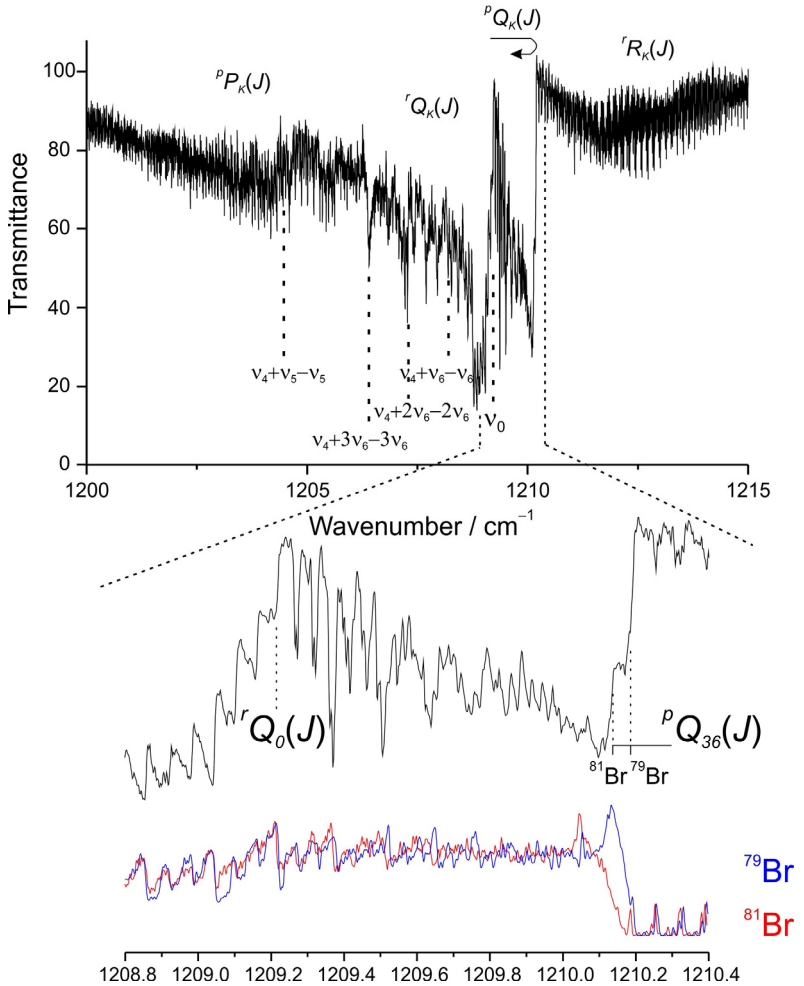

Figure 4.15: Overview of the ν_4 fundamental perpendicular band of CF_3Br from 1200.0 to 1215.0 cm^{-1}. In the middle of the figure an expansion of the *Q* branches from 1208.8 to 1210.4 cm^{-1} is shown. At the bottom of the figure, a simulation of this spectral interval is performed for both the isotopologues using PGOPHER software. Experimental conditions: see Spectrum #3 in Table 4.16.

In the figure, an expansion of the Q branch is illustrated, showing the shape of the ${}^{r}Q$ and ${}^{p}Q$ branches, the location of ${}^{r}Q_0$ and the band head for $K'' = 36$ of the ${}^{p}Q$ branches. At the bottom of the figure the simulation for both the isotopologues is reported and compared to the shape of the experimental spectrum. It is possible to see that the shape of the spectra of the two isotopologues are really very similar and so it is hard to distinguish which signal belongs to which isotopologue. The simulation was performed by using the PGOPHER software [50].

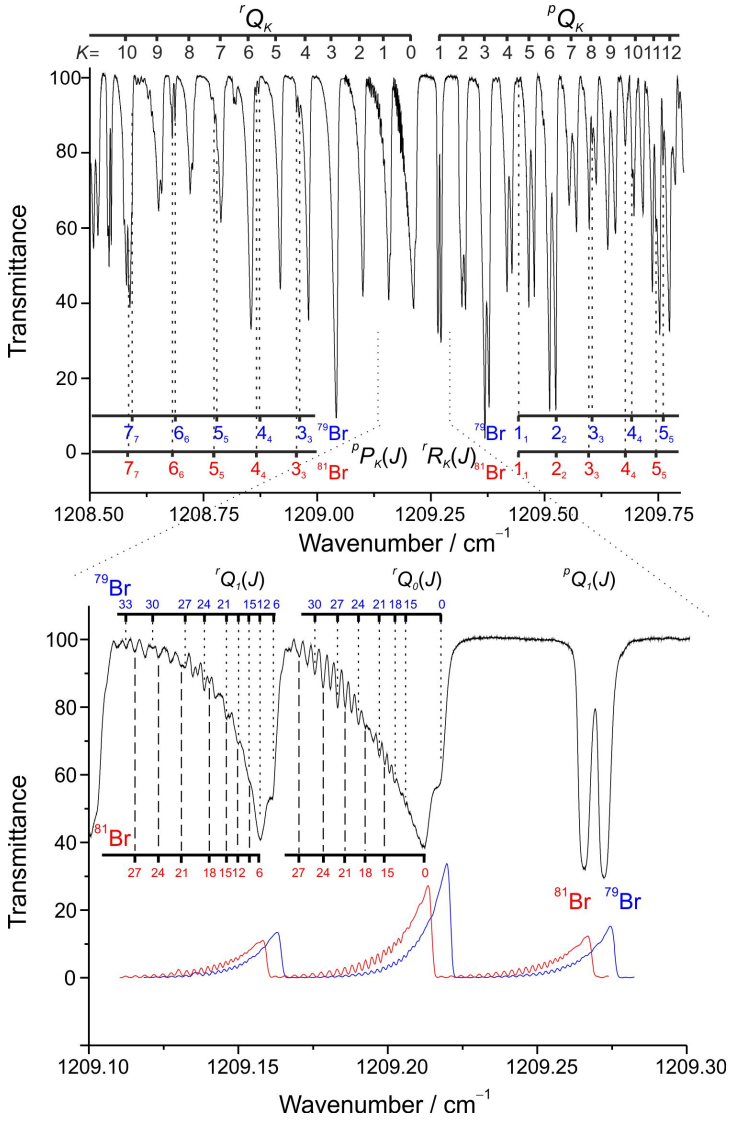

Figure 4.16: Portion of Spectrum #1 of CF_3Br from 1208.5 to 1209.8 cm^{-1} showing the Q branches of the investigated band. A focus on the ${}^{p}Q_1(J)$ ${}^{r}Q_0(J)$ and ${}^{r}Q_1(J)$ branches is presented in the bottom of the Figure, together with the simulated traces of the two isotopologues, in absorbance. Experimental conditions: see Spectrum #1 in Table 4.16.

The middle range of the free–jet TDL spectra (Spectrum #1) is shown in Figure 4.16. The adjacent ${}^{p}Q_K(J)$ and ${}^{r}Q_K(J)$ branches are not overlapped due to the low rotational temperature,

T_{rot} = 50 K. In addition, it is possible to observe the effect of the spin statistic on the intensity of branches with $K'' = 3n$, with $n = 1$ and 2, which are twice as strong as those with $K'' \neq 3n$. The structure of ${}^{p}Q_K(J)$ and ${}^{r}Q_K(J)$ branches is quite different. Whereas for ${}^{r}Q_K(J)$ it is evident that they are red–degraded for increasing J values, the structure is so packed in the case of ${}^{p}Q_K(J)$ branches that a doublet for each K value is observed, where the component at lower wavenumbers belongs to $CF_3{}^{81}Br$ and the other to $CF_3{}^{79}Br$.

The appearance of the ${}^{p}P_K(J)$ branches is shown in Figure 4.17, where two experimental traces are depicted, from Spectra #2 (red trace) and Spectrum #3 (black trace), in order to illustrate the characteristics of these branches for high J and K values. The ${}^{p}P_K(J)$ transitions degrade to higher wavenumbers for increasing K and accumulate into a band head for $J'' \geq 36$ inverting their direction.

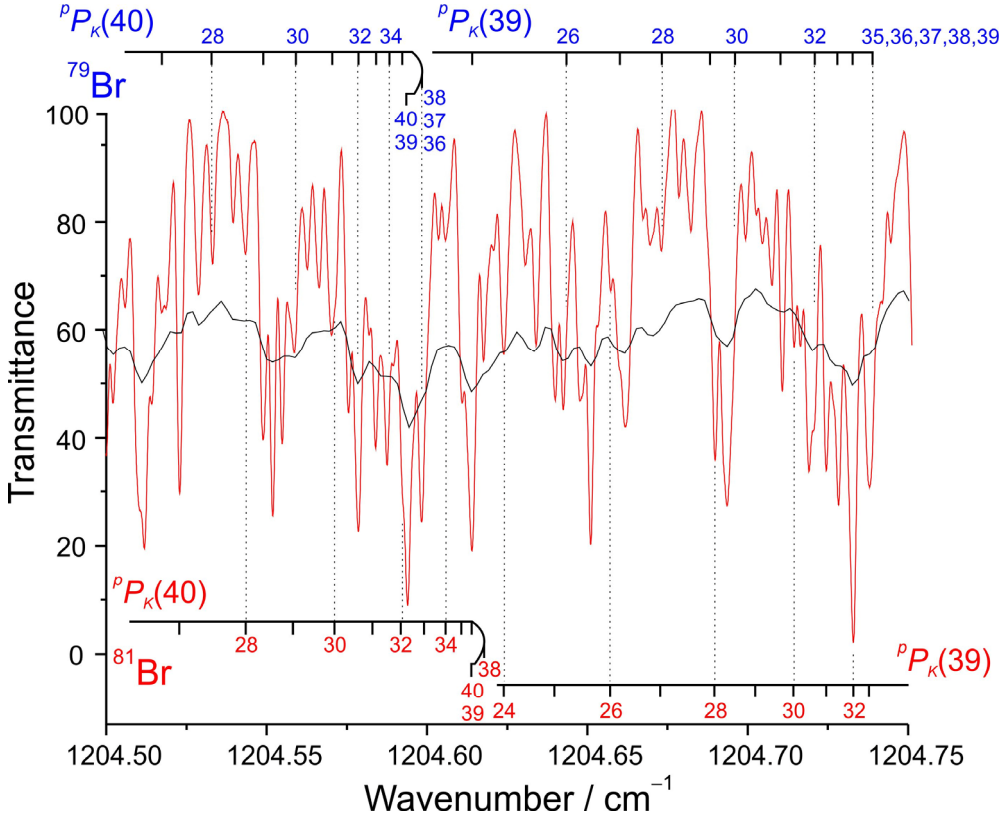

Figure 4.17: Portion of the spectrum of CF_3Br from 1204.50 to 1204.75 cm^{-1} showing the P branches of the ν_4. A focus on the ${}^{p}P_{39}(J)$ and ${}^{p}P_{40}(J)$ branches of the two isotopologues is presented. The red trace is Spectrum #2 and the black trace is Spectrum #3. See experimental conditions in Table 4.16.

Concerning the ${}^{r}R_K(J)$ branches, the K structure degrades to lower wavenumbers for increasing K. ${}^{p}P_K(J)$ and ${}^{r}R_K(J)$ transitions with low J and K values can be identified in Spectrum

#1 between the strong features of the *Q* branches. Their structure cannot be absolutely identified in Spectrum #3, as clearly represented in Figure 4.18, where $^{r}R_{K}(J)$ transitions appear.

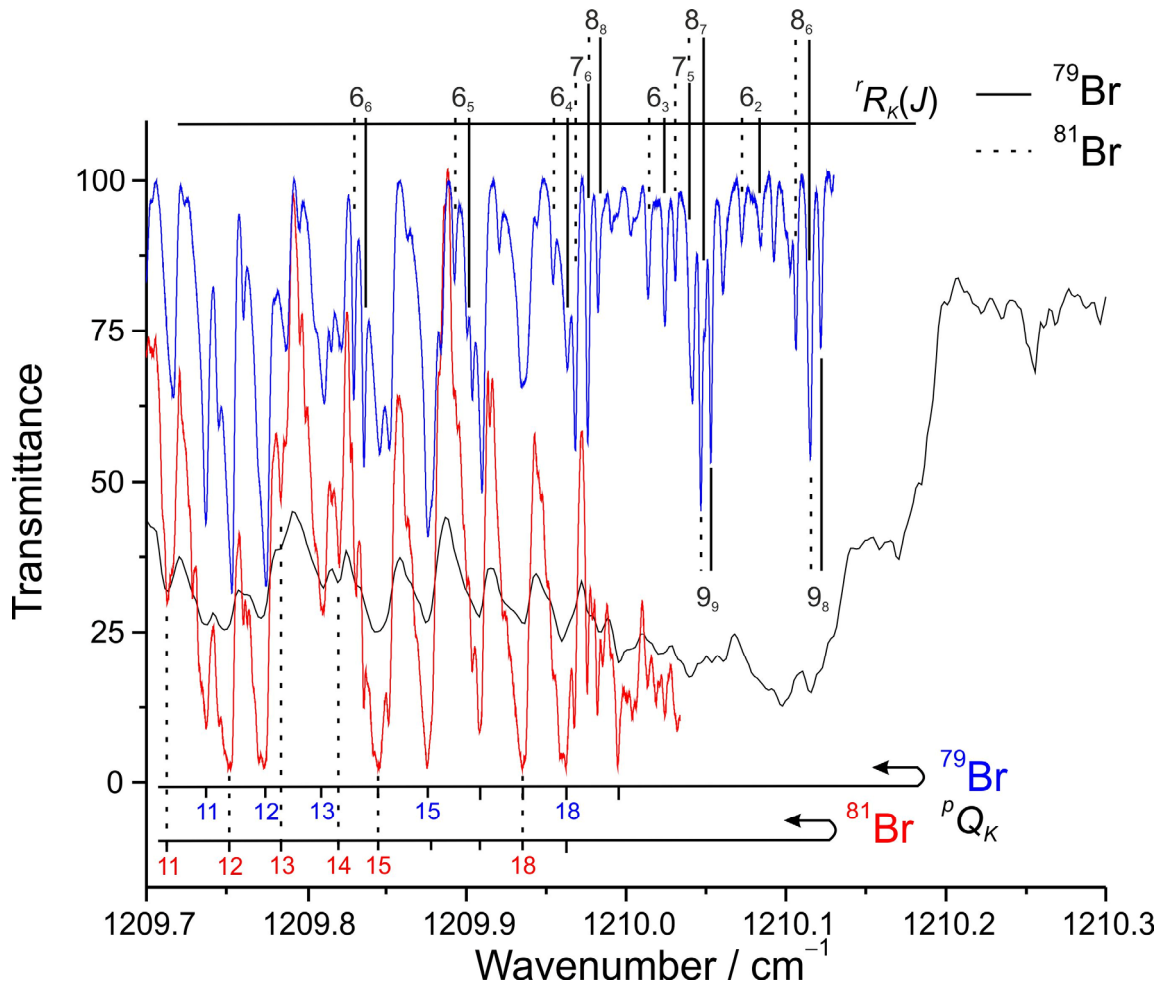

Figure 4.18: Portion of the spectrum of CF_3Br from 1209.7 to 1210.3 cm^{-1} showing some ^{r}R transitions of the ν_4 with low *J* and *K* values between the band head of the *Q* branches. The blue trace is Spectrum #1, the red trace is Spectrum #2 and the black trace is Spectrum #3. See experimental conditions in Table 4.16.

A small portion of the spectrum including the absorptions with $K'' \leq 6$ for $J = 31$, 32, and 33 is illustrated in Figure 4.19, where the red trace is from Spectra #2 and the blue trace from Spectra #1. The appearance of absorptions in the branches is rather regular but the line intensities are often quite different from what expected according to the spin statistics. This is caused by line overlapping due to the unavoidable congestion of the spectrum of the natural sample of CF_3Br.

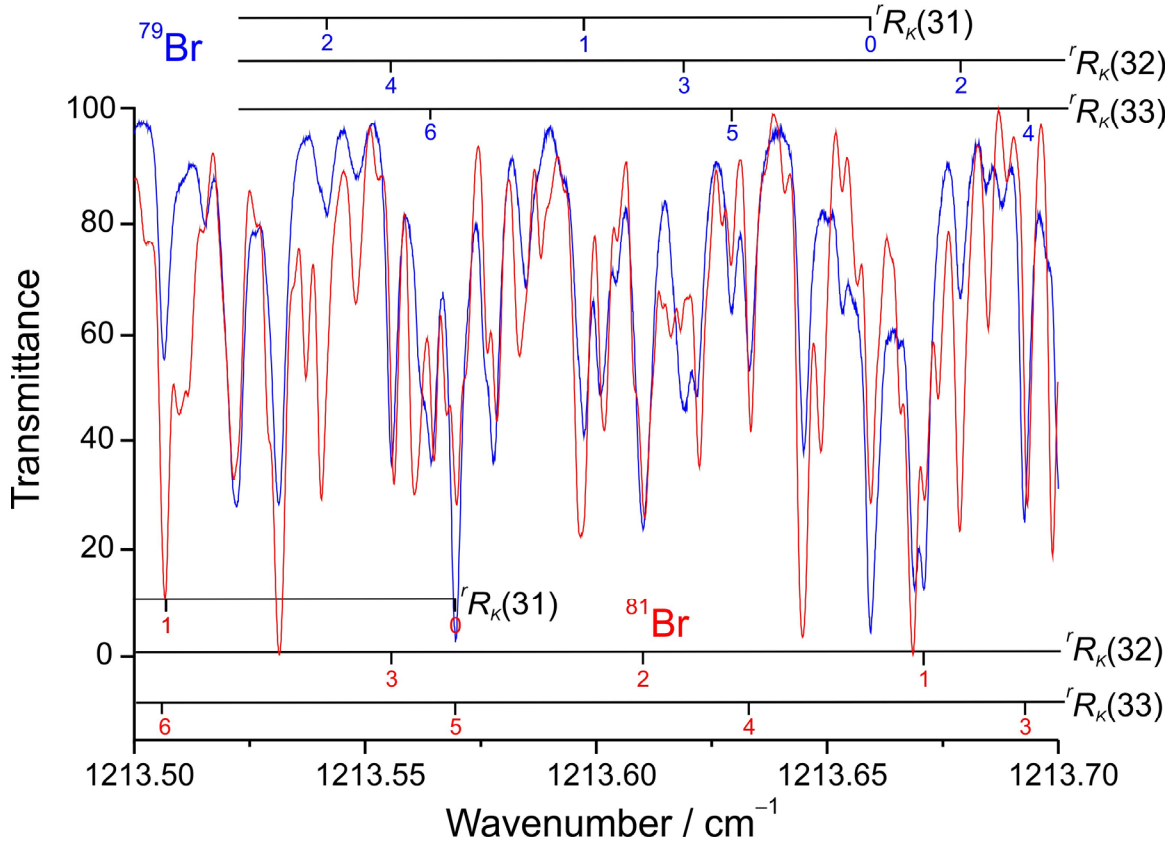

Figure 4.19: Portion of the spectrum of CF_3Br from 1213.5 to 1213.7 cm^{-1} showing the *R* branches of the ν_4. A focus on the ${}^{r}R_K(J)$ branches with $J = 31, 32, 33$ showing the lower *K* values for the two isotopologues is presented. The blue trace is Spectrum #1 and the red trace is Spectrum #2. See experimental conditions in Table 4.16.

4.3.3 Analysis, Results and Discussion

The spectrum of $CF_3{}^{79}Br$ was analysed first. The assignment procedure started from the 1208.0 – 1210.1 cm^{-1} range of the free–jet TDL spectra to take advantage from the simplification on the absorption patterns. Unfortunately, the GSCD could not be applied: ${}^{p}R_K(J-2)$ and ${}^{r}P_K(J)$ transitions connected by GSCD to ${}^{p}P_K(J)$ and ${}^{r}R_K(J-2)$, respectively, were not present in the recorded ranges of the diode laser spectra, which cover only one fifth of the ν_4 band, and GSCD from ${}^{p}P_K(J)$ and ${}^{p}Q_K(J-1)$ or ${}^{r}Q_K(J)$ and ${}^{r}R_K(J-1)$ transitions could not be used since the rotational structure of the *Q* branches is not resolved, but in ${}^{r}Q_0(J)$ and ${}^{r}Q_1(J)$ branches. Therefore, the first assignments were based on a spectrum calculated from the values of the band origin and of the rotational and distortion constants *A* [51], *B*, D_J, D_{JK} [52] and $A\zeta$ [53] reported in the literature. Once the first step was accomplished and the specific contribution to the overall spectrum of each isotopologue understood, the assignments could be extended and

some ${}^{p}P_K(J)$ and ${}^{r}R_K(J)$ transitions were identified. Next, the assignment procedure was carried on by means of Spectrum #3 to fill the two gaps of 2.5 cm^{-1} in the recorded ranges of TDL spectra. The assignments were gradually extended from the 1208.0 – 1210.1 cm^{-1} range to lower and higher wavenumbers up to the intervals 1202.5 – 1205.0 cm^{-1} and 1212.5 – 1214.5 cm^{-1} of Spectra #1 and #2.

The second step of the analysis was the identification of several ${}^{p}P_K(J)$ transitions with low J" and K" values for both the isotopologues in order to estimate the isotopic splitting and to start also the assignments of the spectral features of $CF_3{}^{81}Br$. The diagonal matrix elements, containing the usual contributions up to the 6th power in the angular momentum operators, are given by Eq. (4.1), where v = 4. The ground state energies used to calculate the transition wavenumbers were derived using the precise B_0, D_{0J} and D_{0JK} constants from MW and mmW spectra [52], the value of A_0 derived in [51] and D_K from [54]. Thanks to the extension of the assignments and the implementation of the dataset the upper state distortion constants were refined. This improved the overall quality of the fit and provided reliable predictions for transitions with higher J and K quantum numbers. Nevertheless, since the beginning of the analysis the effect of the rovibration perturbation with $\Delta\ell = \Delta k = \pm 2$ selection rule became evident, making the (k, ℓ) = (1,1) and (–1,–1) levels of the excited state appreciably split. That is why the off–diagonal matrix element $q_t^{(+)}$ (Eq. (2.43)) in the model Hamiltonian has been taken into account and refined during the fitting procedure in order to correctly reproduce the ${}^{r}Q_0$, ${}^{r}P_0$ and the ${}^{r}R_0$ transitions. Finally, the η_J and η_K spectroscopic parameters were determined from the fit including transitions with J and K values larger than 30. Other off–diagonal contributions were tempted, but they resulted statistically undetermined and were constrained to zero.

The experimental dataset includes transition wavenumbers from the three spectra at disposal. Due to the large number of assignments and the difficulty of an adequate estimate of the uncertainties of the wavenumbers from Spectrum #3 with respect to the other spectra, several weighting schemes have been tried. In Fit #1, a unitary statistical weight has been assigned to each transition that corresponds to an isolated line in the least–squares fits. The weight was reduced to 1/n if n transitions are assigned to the same wavenumber. In the last cycle of the refinements, all the experimental data that differed from the corresponding calculated values by more than 0.005 cm^{-1}, about fifty times the estimated precision of FTIR measurements and about seven times that of TDL, were excluded from the data set, Fit #1. The limit for rejection was set to such a large value compared to the precision of the data to avoid the a priori exclusion of a large number of transitions.

In Fit #2 the weights were set as follows: TDL wavenumbers, weight = 1, FTIR wavenumbers weight = 0.25. In fact, in Spectrum #3, because of its lower resolution, lines are so large that they cannot be univocally assigned. Also in this case the weight was reduced to $1/n$ if n transitions are assigned to the same wavenumber. The most appropriate rejection limit was found to be 0.004 cm^{-1}, which was the best compromise between number of rejected lines and quality of the fit. Finally, a third fitting procedure was accomplished, Fit #3, using only transitions from the diode laser spectra and giving them a weight following the criteria explained for Fit #1. In this case the limit for rejection in the last cycle of the fit was set to 0.003 cm^{-1}.

The spectroscopic parameters, the numbers of assigned and fitted transitions, and the standard deviations of Fit #1, Fit #2 and Fit #3 are collected in Table 4.17, columns 3, 4 and 5 respectively.

Table 4.17: Spectroscopic parameters (in cm^{-1}) of $CF_3{}^{79}Br$ in the ground and $\upsilon_4 = 1$ states [a]

Parameter	GS [b]	$\upsilon_4 = 1$		
		Fit #1	Fit #2	Fit #3
E_υ^0		1209.396509(66)	1209.396472(62)	1209.396418(64)
A	0.1906[c]	0.18980081(12)	0.18980093(11)	0.18980104(12)
B	0.069985970	0.06993950(11)	0.06993946(10)	0.06993947(11)
$D_J \times 10^6$	0.008989	0.007249(38)	0.007212(34)	0.007217(36)
$D_{JK} \times 10^6$	0.043393	0.040733(60)	0.040799(56)	0.040831(60)
$D_K \times 10^6$	–0.007096[d]	–0.007096[e]	–0.007096[e]	–0.007096[e]
$A\zeta$		0.1476724(19)	0.1476691(18)	0.1476692(20)
$\eta_J \times 10^6$		–0.0866(22)	–0.0898(21)	–0.0916(23)
$\eta_K \times 10^6$		0.0906(24)	0.0925(22)	0.0972(25)
$q_t \times 10^6$		9.17(42)	8.96(34)	9.59(36)
Limit for rejection		0.005	0.004	0.003
N°fitted/assigned lines		4380/4651	4123/4651	2730/3171
St. dev. of the fit $\times 10^3$		1.98	1.69	1.41

[a] The uncertainties as 1σ given in parenthesis refer to the last significant digits.
[b] From [50].
[c] From [49].
[d] From [52].
[e] Constrained to the ground state value.

The analysis of ν_4 for $CF_3{}^{81}Br$ was performed in an analogous way. The results of Fit #1, Fit #2 and Fit #3 are listed in Table 4.18, columns 3, 4 and 5 respectively.

Table 4.18: Spectroscopic parameters (in cm^{-1}) of $CF_3{}^{81}Br$ in the ground and $v_4 = 1$ states [a]

Parameter	GS [b]	$v_4 = 1$		
		Fit #1	Fit #2	Fit #3
E_v^0		1209.389652(69)	1209.389635(70)	1209.389593(76)
A	0.1906[c]	0.18982541(12)	0.18982545(11)	0.18982529(12)
B	0.069334390	0.06927592(11)	0.06927595(11)	0.06927611(11)
$D_J \times 10^6$	0.008868	0.008865(38)	0.008892(34)	0.008945(36)
$D_{JK} \times 10^6$	0.04272	0.042882(62)	0.042858(57)	0.042747(61)
$D_K \times 10^6$	–0.006279[d]	–0.006279 [e]	–0.006279 [e]	–0.006279 [e]
$A\zeta$		0.1476779(20)	0.1476788(20)	0.1476786(22)
$\eta_J \times 10^6$		–0.0896(22)	–0.0888(22)	–0.0883(24)
$\eta_K \times 10^6$		0.0886(24)	0.0889(23)	0.0870(25)
$q_t \times 10^6$		10.87(36)	10.49(30)	10.64(29)
Limit for rejection		0.005	0.004	0.003
N°fitted/assigned lines		3896/4047	3706/4047	2385/2755
St. dev. of the fit $\times 10^3$		1.93	1.69	1.40

[a] The uncertainties as 1σ given in parenthesis refer to the last significant digits.
[b] From [50].
[c] From [49].
[d] From [52].
[e] Constrained to the ground state value.

Precise values of the vibrational term values and of the spectroscopic rotational, distortion and interaction constants of $v_4 = 1$ for both $CF_3{}^{79}Br$ and $CF_3{}^{81}Br$ have been obtained. All the parameters in Tables 4.17 and 4.18 are statistically well determined and the molecular constants decrease as expected with respect to the corresponding values in the ground state. The bromine isotopic splitting of $v_4 = 1$ states obtained from the difference of their energies has been calculated and amounts to 6.9×10^{-3} cm^{-1}.

In the case of Fit #1, 6% and 4% of lines were rejected for $CF_3{}^{79}Br$ and $CF_3{}^{81}Br$, respectively. In Fit #2, 11% and 9%, and in Fit #3, 14% and 13%. They are randomly distributed in the various branches and correspond to blended lines.

Almost all the derived parameters are free from internal correlations, with the exception of D_J that resulted 91% and 92% correlated to B for $CF_3{}^{79}Br$ and $CF_3{}^{81}Br$, respectively. The three sets of parameters from Fit #1, Fit #2 and Fit #3 overlap within 1σ for both isotopologues. This indicates that the combination of the experimental wavenumbers obtained with different spectrometers do not introduce any systematic deviation in the results. The standard deviations of the fits are about ten times larger than the estimated experimental uncertainty of FTIR data and about two times that of TDL data. This reflects the crowded appearance of the spectra.

References

[1] P. Pracna, H.S.P. Müller, S. Klee, V.–M. Horneman, *Mol. Phys.* **102**, 14–15,1555 (2004).

[2] A. Campargue, L. Biennier, A. Garnache, A. Kachanov, D. Romanini, M. Herman, *J. Chem. Phys.* **111**, 7888 (1999).

[3] J. Go, D. S. Perry, *J. Chem. Phys* **97**, 6994 (1992).

[4] J. Go, T.J. Cronin, S. Perry, *J. Chem. Phys* **175**, 127 (1993).

[5] J.E. Gambogi, J. Timmermans, K.K. Lehmann, G. Scoles, *J. Chem. Phys* **99**, 9314 (1993).

[6] A. McIlroy, D.J. Nesbitt, E.R.T. Kerstel, B.H. Pate, K.K. Lehamnn, G. Scoles, *J. Chem. Phys* **100**, 2596 (1994).

[7] J.E. Gambogi, E.R.T. Kerstel, K.K. Lehmann, G. Scoles, *J. Chem. Phys* **100**, 2612 (1994).

[8] E.R.T. Kerstel, K.K. Lehmann, B.H. Pate, G. Scoles, *J. Chem. Phys* **100**, 2588 (1994).

[9] X. Chen, Y. Ganot, I. Bar, S. Rosenwaks, *J. Chem. Phys* **113**, 5134 (2000).

[10] A.L. Malinovsky, A.A. Makarov and E.A. Ryabov, *Journal of experimental and theoretical physics* **106(1)**, 34 (2008).

[11] A. Metha, A.A. Stuchebrukhov and R.A. Marcus, *J. Phys. Chem.* **99**, 2677 (1995).

[12] M.I. Idrissi, J. Liévin, M. Herman, A. Campargue, G. Graner, *Chem. Phys.* **265**, 273 (2001).

[13] A. McIlroy and D.J. Nesbitt, *J. Chem. Phys.* **91,** 104 (1989).

[14] D.R.J. Boyd and H.W. Thompson, *Trans. Faraday Soc.* **49,** 141 (1953).

[15] N.F. Henfrey and B.A. Thrush, *J. Mol. Spectrosc.* **113,** 426 (1985).

[16] P. Pracna, G. Graner, J. Cosléou, J. Demaison, G. Wlodarczak, V.–M. Horneman, and M. Koivusaari, *J. Mol. Spectrosc.* **206,** 150 (2001).

[17] K. Didriche, C. Lauzin, T. Földes, D. Golebiowski, M. Herman and C. Leforestier, *Phys. Chem. Chem. Phys.* **13**, 14010 (2011).

[18] G. Guelachvili and K. Narahari Rao, *Handbook of Infrared Standards II*, Academic Press, Inc. Orlando, Florida, 1986.

[19] R.A. Toth, *Applied Optics* **33**(21), 4851 (1994).

[20] S. Urban, P. Pracna and G. Graner, *J. Mol. Spectrosc.* **169** (1)**,** 185 (1995).

[21] M. Herman, *Mol. Phys.* **105**, 2217 (2007).

[22] M.E. Kellman, *J. Chem. Phys.* **93,** 6630 (1990).

[23] J.M. Hollas, High Resolution Spectrocopy, John Wiley & Sons, Chichester, 1998.

[24] L. Fusina, G. Di Lonardo and J.K.C. Johns, *J. Mol. Spectrosc.* **118,** 397 (1986).

[25] S.N. Yurchenko, R.J. Barber, A. Yachmenev, W. Thiel, P. Jensen and J. Tennison, *J. Phys. Chem.* **113**, 11845 (2009).

[26] X. Huang, D.W. Schwenke and T.J. Lee, *J. Chem. Phys*. **134**, 044320/1-15 (2011).

[27] X. Huang, D.W. Schwenke and T.J. Lee, *J. Chem. Phys*. **134**, 044321/1-18 (2011).

[28] A. Wotten, *Proc. SPIE* **4837**, 110 (2003).

[29] E.E. Becklin, A.G.G.M. Tielens, R.D. Gehrz and H.H.S. Callis, *Proc. SPIE* **6678**, 66780A (2007).

[30] G.L. Pilbratt, *Proc. SPIE* **7010**, 701002 (2008).

[31] M. Snels, L. Fusina, H. Hollenstein and M. Quack, *Mol. Phys.* **98**, 837 (2000).

[32] L. Fusina and S.N. Murzin, *J. Mol. Spectrosc*. **167**, 464 (1994).

[33] L. Fusina, M. Carlotti, G. Di Lonardo, S.N. Murzin, and O.N. Stepanov, *J. Mol. Spectrosc*. **147**, 71 (1991).

[34] S. Urban, D. Papousek, M. Bester, K. Yamada, G. Winnewisser and G. Guarnieri, , *J. Mol. Spectrosc*. **106**, 29 (1984).

[35] V.–M. Horneman, *J. Mol. Spectrosc*. **241**, 45 (2007).

[36] R.A. Toth, *J. Opt. Soc. Am.* **B 8**, 2236 (1991).

[37] M. Elkeurti, L.H. Coudert, J. Orphal, C.E. Fellows and S. Toumi, *J. Mol. Spectrosc*. **261**, 101 (2010).

[38] M. Takahashi, H. Kuze, H. Tashiro, M. Takami and S. Namba, *Appl. Phys. B* **41**, 91 (1986).

[39] D.W. Lupo and M. Quack, *Chem. Rev*. **87**, 181 (1987).

[40] W. Fawzy, and R.H. Schwendeman, *J. Mol. Spectrosc*. **130**, 193 (1988).

[41] V. Parthasarathy, S.K. Sarkar, N.V. Iyer, K.V.S. Rama Rao and J.P. Mittal, *Appl. Phys.* B **56**, 321 (1993).

[42] J.I. del Barrio, R. Fernández Cézar, E. Martin, F.M. G–Tablas and W. Fuss, Appl. Phys. B **63**, 51 (1996).

[43] J.I. Del Barrio, R. Fernández Cézar and F.M. G–Tablas, *Chem. Phys. Lett.* **270**, 71 (1997).

[44] Scientific Assessment of Ozone Depletion 2010, Report 52 of the World Meteorological Association's Global Ozone Research and Monitoring Project, National Oceanic and Atmospheric Administration, National Aeronautics and Space Administration, United Nations Environment Programme, World Meteorological Organization, European Commission.

[45] A. Baldacci, A. Passerini and S. Ghersetti, *J. Mol. Spectrosc*. **91**, 103 (1982).

[46] A. Pietropolli Charmet, P. Stoppa, P. Toninello, A. Baldacci and S. Giorgianni, *Phys. Chem. Chem. Phys.* **8**, 2491 (2006).

[47] A. Pietropolli Charmet, N. Tasinato, P. Stoppa, A. Baldacci and S. Giorgianni, *Mol. Phys.* **102**, 1171 (2008).

[48] A. Pietropolli Charmet, P. Stoppa, P. Toninello, S. Giorgianni and S. Ghersetti, *Phys. Chem. Chem. Phys.* **5**, 3595 (2003).

[49] R.A. Toth, *J. Opt. Soc. Am.* **B 8**, 2236 (1991).

[50] PGOPHER, C.M. Western, University of Bristol, http://pgopher.chm.bris.ac.uk.

[51] K. Burczyk, H. Bürger, A. Ruoff and A. Pinson, *J. Mol. Spectrosc*. **77**, 109 (1979).

[52] J.H. Carpenter, J.D. Muse and J.G. Smith, *J. Chem. Soc. Faraday Trans. II* **76**, 339 (1980).

[53] L.C. Hoskins and C.J. Lee, *J. Chem. Phys*. **59**, 49323 (1973).

[54] R. Tarroni, *private communication*.

CHAPTER 5

CONCLUSIONS AND PERSPECTIVES

5.1 CONCLUSIONS

A careful analysis about relevant molecules for astrochemical and astronomical purposes has been performed by means of the high–resolution infrared spectroscopy.

5.1.1 Linear molecules

As far as the *acetylene saga* is concerned, a very detailed analysis for various isotopologues has been performed.

The analysis of $^{12}C_2D_2$ was concentrated on the bending modes and stretching–bending system. The previous dataset for the bending modes [1–3] has been enlarged: the $\nu_4 + \nu_5 \leftarrow$ GS and 8 pure bending bands involving $\upsilon_{tot} = 3$ and 4 have also been analyzed at high resolution for the first time. The transitions of the former band, the IR data from the analysis of the bending modes of Huet *et al.* [1] re–calibrated, and the recent measurements in the THz region [3] were fitted simultaneously, considering only the bending states with $\upsilon_{tot} \le 2$. 92 cold and hot IR bands involving fundamentals, overtones, stretching–bending and stretching–stretching combination bands were rotationally analysed. A total of 8345 IR transitions have been assigned and fitted together with 417 Raman transitions [2] in order to characterize all the levels with $\upsilon_s = 1$ $(s = 1,2,3)$, $\upsilon_4 + \upsilon_5 \le 2$; $\upsilon_s = 2\ (s = 1,2,3)$, and $\upsilon_s = \upsilon_{s'} = 1$, $\upsilon_4 + \upsilon_5 \le 2\ (s, s' = 1,2,3)$. An accurate set of vibration and rotation parameters, including ℓ – type, and Darling–Dennison interaction constants between $\upsilon_4 = 2$ and $\upsilon_5 = 2$ levels, has been determined for each stretching mode.

A global analysis of the bending modes has been performed for the $^{13}C^{12}CD_2$ isotopologue, by recording the spectrum in the range 450 – 1700 cm^{-1} and detecting 27 bands

involving bending modes with $v_4 + v_5$ up to 3. About 3200 transitions were assigned and analyzed. Two global rotation–vibration least–squares fits were performed, one considering level with v_{tot} up to 3, without including the transitions to the $v_4 = 1$, $v_5 = 2$ $^{II}\Pi$ state, which were treated separately. The derived spectroscopic parameters reproduce the assigned transitions satisfactorily, with standard deviations of the fits very close to the quoted precision of the measurements. They adequately characterize the ground state and 13 excited bending states of the molecule.

This isotopologue, together with the rare mixed isotopomers $H^{12}C^{13}CD$ and $H^{13}C^{12}CD$, have been studied in the region 6130 – 6800 cm^{-1} using the sophisticated high–sensitivity apparatus Femto–FT–CEAS in collaboration with the ULB in Brussels. This allowed the detection and the analysis of 10 bands belonging to these isotopologues, by extending the J assignments of the first overtone of ν_1 for both $H^{12}C^{13}CD$ and $H^{13}C^{12}CD$, already reported in literature [4], and identifying combination bands involving three or four quanta of stretching and bending excitation of $D^{12}C^{13}CD$ for the first time.

The same analysis performed on bending modes for $^{13}C^{12}CD_2$ has been accomplished also for the molecule DCCF, in collaboration with the University of Wuppertal, where the spectrum was recorded in the range 320 – 850 cm^{-1}. A total of 6650 infrared transitions belonging to 38 bands up to $v_4 + v_5 = 3$ have been recorded, identified and analysed simultaneously. The ν_5 has been analysed for the first time and the global analysis allowed the characterisation of the ground state of the molecule and of 18 vibrational excited states. In addition, the difference band $\nu_3 - \nu_4$ has been identified and analysed, allowing the characterisation of the $v_3 = 1$ state. The great accuracy of the 57 spectroscopic parameters determined was achieved also by adding to the dataset MW and mmW rotational transitions from the literature [5,6].

For what concerns monodeuterodiacetylene, an intensive analysis in the region 450 – 1100 cm^{-1} has been performed. The identification and analysis of the fundamental bending modes ν_6, ν_7 and ν_8 has been accomplished, together with overtone, hot and combination bands. A dataset of more than 2500 transitions have been created, which includes 10 out of the 16 vibrational levels of DC_4H lying below 1000 cm^{-1}.

5.1.2 Symmetric top molecules

The infrared spectrum of propyne has been recorded and investigated in the range 6200 – 6700 cm^{-1} both with a FTIR and a FANTASIO+ spectrometer, in collaboration with the ULB in Brussels. Five bands in Fermi and Coriolis interaction between them have been analysed simultaneously. Cold spectra helped the beginning of the analysis, by assigning low J and K quantum numbers, while FTIR spectra were useful to extend the assignments. A large number of effective diagonal spectroscopic parameters together with the main interaction constants have been obtained. Five additional very weak bands have been observed in this region and their assignment has been tentatively suggested with the help of the polyad structure scheme. The gathered experimental information allowed the determination of the origin, the rotational constant B and the centrifugal distortion constant D_J for only two of them.

The high resolution infrared spectrum of $^{15}ND_3$ from 450 to 2700 cm^{-1} has been recorded and studied in order to analyse the fundamental bands of this isotopologue of ammonia. In particular, the bending bands ν_2 and ν_4 have been considered simultaneously, as well as the stretching bands ν_1 and ν_3. The adopted inversion–rotation–vibration Hamiltonian model has been successful in rationalizing the complicated pattern of vibration–rotation–inversion levels in the interacting states with a limited number of spectroscopic parameters. Accurate values for the spectroscopic constants and for the interaction coefficients have been obtained, together with accurate vibration tunnelling energies for $v_2 = 1$ and $v_4 = 1$. As far as the stretching modes analysis is concerned, preliminary results are quite good, even if the need for taking into account more states close in energy interacting with them is evident.

Finally, the high resolution infrared spectrum of bromotrifluoromethane has been recorded in the range 1190 – 1220 cm^{-1} to investigate the ν_4 fundamental band of this molecule, which is a fairly severe pollutant of the atmosphere and absorbs radiations efficiently in the atmospheric window. In collaboration with the Università Cà Foscari of Venezia, the free–jet diode laser technique was adopted to reduce the spectral congestion due to hot bands and the nearly coincident absorptions of $CF_3{}^{79}Br$ and $CF_3{}^{81}Br$, which are present in almost equal abundance. The assignment procedure was successful since the absorptions of the two isotopologues were disentangled and the isotopic splitting quoted. Precise spectroscopic parameters and the energy of $v_4 = 1$ for both the isotopologues have been derived from the analysis.

5.2 FUTURE PERSPECTIVES

The next step of the *acetylene saga* is to complete the analysis of the isotopologue $^{13}C^{12}CD_2$, investigating the stretching modes and the stretching–bending bands system. Once this will be accomplished, data about the ten isotopologues of acetylene involving H, D, ^{12}C and ^{13}C will be available and it will be possible to calculate experimentally the equilibrium geometry of the molecule. Until now, this has been realised by considering only 4 or 5 isotopologues [7,8], whereas the number of data for all the isotopologues and their quality have greatly improved in recent years.

As far as diacetylene is concerned, the analysis of the bending modes below 1100 cm^{-1} has to be extended to other isotopologues, in primis C_4D_2 and then C_4H_2 with one ^{13}C. This analysis is really useful for astronomical purposes, as this is the range where the spatial missions operate.

Furthermore, the analysis of the stretching modes of $^{15}ND_3$ has just started. A careful inspection of the performed fit revealed the presence of deviations and anomalous values for some parameters. This is a clear signal of the fact that other perturbations must be taken into account in order to accomplish this analysis properly. In fact, as illustrated in Figure 5.1, several states lie in a narrow region around the system $v_1 = 1$ and $v_3 = 1$ for ammonia $^{14}NH_3$.

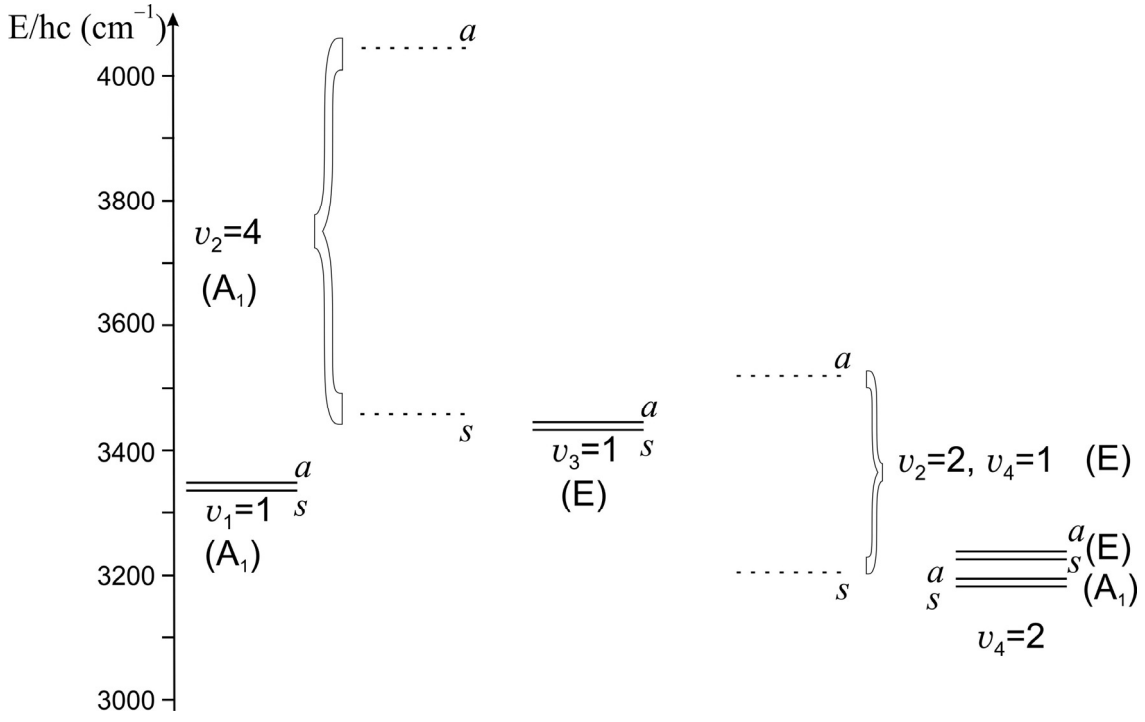

Figure 5.1: Structure of the energy states around $v_1 = 1$ and $v_3 = 1$ for $^{14}NH_3$.

The situation for the isotopologue under investigation is analogous, just shifted at lower wavenumbers between 2000 and 3000 cm^{-1}. At least four other states, namely $v_2 = 4$; $v_2 = 2$, $v_4 = 1$; $v_4 = 2^0$ and $v_4 = 2^2$ (i.e. 8 states considering the *s* and *a* components) are present and interact with $v_1 = 1$ and $v_3 = 1$ and between them both through anharmonic (states of symmetry $A_1–A_1$ or E–E) or Coriolis (states A_1–E, E–E) resonances. All these states have to be taken into account simultaneously in the analysis while analysing the stretching system, in order to obtain a satisfactory description of the absorptions observed in this spectral range.

References

[1] T.R. Huet, M. Herman and J.W.C. Johns, *J. Chem. Phys.* **94**(5), 3407 (1990).

[2] D. Bermejo, G. Di Lonardo, J.L. Doménech, and L. Fusina, *J. Mol. Spectrosc.* **209**, 259 (2001).

[3] S. Yu, B.J. Drouin, J.C. Pearson, H.M. Pickett, V. Lattanzi, and A. Walters, *Astrophysical Journal*, **698**, 2114 (2009).

[4] J.L. Hardwick, Z.T. Martin, M.J. Pilkenton and E.N. Wolf, *J. Mol. Spectrosc.* **243**, 10 (2007).

[5] H. Jones and H.D. Rudolph, *Z. Naturforsch* A **34**, 340 (1979).

[6] M. Niedenhoff, K.M.T. Yamada, J. Lindenmayer and H. Jones, *J. Mol. Spectrosc.* **152**, 213 (1992).

[7] M. Herman, A. Campargue, M.I. El Idrissi and J. Vander Auwera, *J. Chem Phys.* **32**, 921 (2003).

[8] J. Liévin, J. Demaison, M. Herman, A. Fayt and C. Puzzarini, *J. Chem Phys.* **134**, 064119 (2003).

APPENDIX

APPENDIX A

CHARACTER TABLES

Table I: $D_{\infty h}$ point group

$D_{\infty h}$	E	$2C_{\infty}^{\Phi}$	…	$\infty\sigma_{\upsilon}$	i	$2S_{\infty}^{\Phi}$	…	∞C_2		
Σ_g^+	1	1	…	1	1	1	…	1		x^2+y^2, z^2
Σ_g^-	1	1	…	-1	1	1	…	-1	Rz	
Σ_u^+	1	1	…	1	-1	-1	…	-1	z	
Σ_u^-	1	1	…	-1	-1	-1	…	1		
Π_g	2	2cos Φ	…	0	2	2cos Φ	…	0	(Rx,Ry)	(xz,yz)
Π_u	2	2cos Φ	…	0	-2	-2cos Φ	…	0	(x,y)	
Δ_g	2	2cos 2Φ	…	0	2	2cos 2Φ	…	0		(x^2-y^2,xy)
Δ_u	2	2cos 2Φ	…	0	-2	-2cos 2Φ	…	0		
Φ_g	2	2cos 3Φ	…	0	2	2cos 3Φ	…	0		
Φ_u	2	2cos 3Φ	…	0	-2	-2cos 3Φ	…	0		
…	…	…	…	…			…	0		

Table II: $C_{\infty v}$ point group

$C_{\infty v}$	E	$2C_{\infty}^{\Phi}$	…	$\infty\sigma_{\upsilon}$		
$A_1 \equiv \Sigma^+$	1	1	…	1	z	x^2+y^2, z^2
$A_2 \equiv \Sigma^-$	1	1	…	-1	Rz	
$E_1 \equiv \Pi$	2	2cos Φ	…	0	(x,y);(Rx,Ry)	(xz,yz)
$E_2 \equiv \Delta$	2	2cos 2Φ	…	0		(x^2-y^2,xy)
$E_3 \equiv \Phi$	2	2cos 3Φ	…	0		
…	…	…	…	…		

Table III: C_{3V} point group

C_{3V}	E	$2C_3$	$3\sigma_V$		
A_1	1	1	1	z	x^2+y^2,z^2
A_2	1	1	-1	Rz	
E	2	-1	0	(x,y),(Rx,Ry)	$(x^2-y^2,xy)(xz,yz)$